

AD-780 532

HIGH CHAMBER PRESSURE BLAST TUBE AND  
NOZZLE MATERIAL EVALUATION, VOLUME II

Wendell A. Stephen, et al

United Technology Center

Prepared for:

Air Force Rocket Propulsion Laboratory

17 June 1974

DISTRIBUTED BY:

**NTIS**

National Technical Information Service  
U. S. DEPARTMENT OF COMMERCE  
5285 Port Royal Road, Springfield Va. 22151

AD 780 532

# **HIGH CHAMBER PRESSURE BLAST TUBE AND NOZZLE MATERIAL EVALUATION**

## **VOLUME II**

W. A. Stephen

T. E. Frakes

T. V. O'Hara

**APPROVED FOR PUBLIC RELEASE; DISTRIBUTION UNLIMITED**

UTC 2410-FR

198

1.  
NATIONAL TECHNICAL  
INFORMATION SERVICE  
1215 JEFFERSON AVENUE  
SPRINGFIELD, VA 22151

Volume II

**VALIDATION OF THERMOCHEMICAL ANALYSIS TECHNIQUES  
FOR HIGH CHAMBER PRESSURE SOLID ROCKET NOZZLES  
WITH HIGH VELOCITY BLAST TUBES**

by

D. L. Baker  
A. J. Murphy  
M. R. Wool

The work discussed in volume II — was performed by  
Aerotherm Division of Acurex Corporation under  
subcontract to United Technology Center on contract No.  
F04611-71-C-0051. This report presents the final work of the  
project.

## ABSTRACT

The set of Aerotherm computer programs (ACE, CMA, ARGEIBL) which were validated for charring ablating and carbon/carbon materials in conventional and low velocity blast tube nozzles under Contract F04611-69-C-0065 were validated for these same materials for

- high velocity blast tube nozzles
- operation at high chamber pressures (up to 3000 psia)
- aluminized CTPB propellants which vary in aluminum content from 5 to 18 percent.

The validation was determined based on comparisons between measured and predicted surface recession and char depth thicknesses and between predicted and determined convective heat transfer coefficients. The GASKET computer program which considers kinetically controlled surface thermochemical reactions was used for predicting the performance of the bulk graphites and pyrolytic graphite materials. This code was validated for the bulk graphites but not for the pyrolytic graphite washers in this particular environment. Under Contract F04611-69-C-0081, this code had been validated for both pyrolytic graphite washers and coatings in a wide variety of environments.

The surface recession and char depth measurements used for comparisons with the analytical predictions were obtained from materials located in the aft closure, blast tube, aft entrance cap, nozzle throat, and exit cone of nozzles which were exposed to a chamber pressure of approximately 3000 psia for 10 seconds. This analysis volume summarizes the initial 13 test firings results. Three additional tests were conducted at chamber pressures up to 3500 psia using wire wound tungsten inserts. The results for these last three tests are presented in Volume I of this report. The rocket motor used for these tests had either a cylindrical or keyhole propellant grain configuration with either a 5 percent Al-CTPB or 18 percent Al-CTPB propellant. The convective heat transfer coefficient used for comparison with the analysis techniques was obtained from two total heat flux sensors installed in the blast tube of one of the rocket motor firings.

In general, the agreement between the analytical predictions and the surface recession and char depth data was either within  $\pm 25$  percent or within the experimental accuracy of the measurements with the exception of the throat. The best agreement was obtained for the analysis locations in the blast tube and exit cone. The poorest agreement occurred for the pyrolytic graphite washers in the nozzle throat region.

## TABLE OF CONTENTS

Section	Title	Page
1	INTRODUCTION	1
2	SUMMARY OF ANALYSIS TECHNIQUES	3
3	PRELIMINARY ANALYSIS	9
	3.1 Propellant Data	9
	3.2 Nozzle Geometry	10
	3.3 Flow Field Analysis	10
	3.4 Free Stream Properties	12
	3.5 Heat Transfer Boundary Conditions	13
	3.5.1 Convective Boundary Conditions	13
	3.5.2 Radiative Boundary Conditions	15
	3.6 Material Chemical and Thermal Property Data	17
4	THERMOCHEMICAL SCREENING ANALYSIS AND INDEPTH THERMAL ANALYSIS	51
	4.1 Surface Thermochemistry Data and Heat Flux Boundary Conditions	52
	4.2 Thermochemical Screening Analysis	53
	4.3 Indepth Thermal Analysis	55
	4.3.1 Analysis Assuming Steady State Ablation Surface Response	55
	4.3.2 Analysis Using Convective Heating Boundary Condition to Study Blast Tube Thermal and Ablative Response	58
5	NOZZLE THROAT PACKAGE THERMAL RESPONSE PREDICTIONS	101
	5.1 Throat Package Geometry	101
	5.2 Surface Thermochemistry and Material Property Data	101
	5.3 Thermal Response Predictions	102
	5.3.1 Two-Dimensional Analysis	103
	5.3.2 One-Dimensional Analysis Results and Their Comparison to the Two-Dimensional Analysis	103
	5.3.3 Pyrolytic Graphite Washer Backwall Insulation Effects	105
6	PRETEST NOZZLE THERMAL RESPONSE PREDICTIONS	132
	6.1 Surface Thermochemistry Data	132
	6.2 Comparison of Predicted and Measured Surface Recession, Char Depths and Material Density Profiles	133
	6.3 Pyrolytic Graphite Washer Surface Recession	135
	6.4 Char Density Profile Measurements	136

## TABLE OF CONTENTS (Continued)

Section	Title	Page
7	EXPERIMENTAL EVALUATION OF THE HEAT FLUX BOUNDARY CONDITIONS	166
	7.1 Thermal Instrumentation Systems	166
	7.2 Data Reduction Procedure	167
	7.3 Comparisons Between Measured and Predicted Surface Heat Flux	168
8	CONCLUSIONS AND RECOMMENDATIONS	177
	APPENDIX A: Thermochemical Maps for Defining Total Heat Flux	178
	References	183

## ILLUSTRATIONS

Figure		Page
2-1	Flow Chart for Screening Analysis	7
2-2	Flow Chart for Detailed Transient Analysis	8
3-1	Blast Tube Nozzle Design	23
3-2	Loaded Propellant Cartridge -- Slotted Grain	24
3-3	Blast Tube Nozzle Radius Versus Boundary Layer Streamwise Length	25
3-4	Variation of Non-Dimensional Flow Parameter with Boundary Layer Running Length for the Slotted Grain	27
3-5	Definition of Effective Flow Area in the Aft Closure -- Slotted Grain Configuration	30
3-6	Isentropic Expansion Properties for 5% Al-CTPB Propellant	31
3-7	Isentropic Expansion Properties of 18% Al-CTPB Propellant	34
3-8	Heat Transfer Distributions for 5% Al-CTPB Propellant	37
3-9	Heat Transfer Distributions for 18% Al-CTPB Propellant	39
3-10	Aft Closure Cross Sectional Area for Modified Flow Field Analysis	41
3-11	Variation of ARGEIBL Heat Transfer Coefficient with Blast Tube Area Ratio at Several Nozzle Locations	42
3-12	Heat Transfer Distributions for the Slotted Grain Port at Various Times After Startup	44
3-13	Heat Transfer Distributions for the Slotted Grain Port at Various Times After Startup	45
3-14	Effect of Keyhole Port Flow on Heat Transfer to Various Locations of the Blast Tube Nozzle (Plane of Slot)	47
3-15	Estimated Thermal Properties of MX2625 Silica Phenolic	48
3-16	Estimated Thermal Properties of Pycobond 410-65	49

# ILLUSTRATIONS (Continued)

Figure		Page
3-17	Estimated Thermal Properties for Durez 16771-1	50
4-1	Steady State Surface Response of Materials Used in Screening Analysis of Aft Closure and Blast Tube	67
4-2	Steady State Surface Response of Materials Used in Screening Analysis of Exit Cone	68
4-3	Kinetically Controlled Surface Response of Graph-i-tite G-90 Bulk Graphite at Blast Tube ( $\epsilon = 1.3$ ) Conditions	69
4-4	Kinetically Controlled Surface Response of Pyrostrand Layer Graphite at Blast Tube ( $\epsilon = 1.3$ ) Conditions	70
4-5	Blast Tube Nozzle Design	71
4-6	Comparisons of Steady State Ablation Response as a Function of Blast Tube Radius at the Blast Tube Entrance Plane	72
4-7	Aft Closure Indepth Analysis Boundary Conditions Accounting for Slotted Grain Flow	74
4-8	Aft Closure Temperature Profiles	76
4-9	Aft Closure Surface and Char Recession Histories	78
4-10	Blast Tube Indepth Analysis Boundary Conditions	79
4-11	Blast Tube Temperature Profiles	81
4-12	Blast Tube Surface and Char Recession Histories	83
4-13	Exit Plane Indepth Analysis Boundary Conditions	84
4-14	Exit Plane Temperature Profiles	86
4-15	Exit Plane Surface and Char Recession Histories	88
4-16	Convective Heat Transfer Coefficient Versus Time for Graph-i-tite G-90 Blast Tube	89
4-17	Temperature Profiles for Graph-i-tite G-90 at Blast Tube Entrance	90
4-18	Temperature Profiles for Graph-i-tite G-90 at Blast Tube Exit	92



# ILLUSTRATIONS (Continued)

Figure		Page
4-19	Response Histories for Graph-1-tite G-90 Blast Tube	94
4-20	Convective Heat Transfer Coefficient Versus Time for Pyrostrand Blast Tube	96
4-21	Temperature Profiles for Pyrostrand Blast Tube	97
4-22	Response Histories for Pyrostrand Blast Tube	99
5-1	Throat Package Geometry for two-Dimensional Analysis	106
5-2	Comparisons of Surface Removal Rates for High Pressure Nozzle Throat Package Locations, 18% CTPB Propellant	107
5-3	Transient Surface Thermochemical Response of MX4926 Carbon-Phenolic at the Throat Retaining Ring Location	108
5-4	Thermal Properties of Edge-Oriented Pyrolytic Graphite	109
5-5	Thermal Properties of ATJ Bulk Graphite	110
5-6	Estimated Thermal Properties of MX4926 Accounting for Internal Decomposition	111
5-7	Estimated Thermal Properties of Silica-Phenolic Accounting for Internal Decomposition	112
5-8	Chamber Pressure History for Throat Package Analyses	113
5-9	Isothermal Locations in Throat Package	114
5-10	Isothermal Locations in Throat Package, Accounting for Estimated Gouging Effects, Exposure Time = 11.0 Seconds	120
5-11	Comparison of Temperature Profiles in the Throat Plane	121
5-12	Comparison of Predicted Surface Temperatures at the Throat	124
5-13	Comparison of Predicted Surface Recessions at the Throat	125
5-14	Comparison of One- and Two-Dimensional Indepth Temperatures for Throat Retaining Ring	126
5-15	Temperature Profiles for MX4926 Throat Retaining Ring, Two-Dimensional Analysis	127

# ILLUSTRATIONS (Continued)

Figure		Page
5-16	Comparison of MX4926 Surface Recessions Given by the One-and Two-Dimensional Analysis	128
5-17	Comparison of MX4926 Surface Temperatures Given by the One and Two Dimensional Analysis	129
5-18	Effect of Pyrolytic Graphite Washer Backwall Boundary Condition on Throat Surface Recession	130
5-19	Effect of Pyrolytic Graphite Washer Backwall Boundary Condition on Surface and Backwall Temperatures	131
6-1	Surface Response of Durez 16771 Silica Phenolic to 5% Al-CTPB Propellant	146
6-2	Surface Response of Durez 16771 and CTPB 18% Propellant	147
6-3	Surface Response of MX2625 to 5% Al-CTPB Propellant	148
6-4	Kinetically Controlled Response of Graph-i-tite G-90 Bulk Graphite to 5% Al-CTPB Propellant	149
6-5	Surface Response of MXCE 280 Carbon-Phenolic to 5% Al-CTPB Propellant	150
6-6	Surface Response of MXCE 280 to CTPB 18% Propellant	151
6-7	Surface Response of MXCE 280 Silica-Phenolic to 5% Al-CTPB	152
6-8	Surface Response of MX4926 to 5% Al-CTPB Propellant	153
6-9	Diffusion Controlled Response Pycobond 410-65 to 5% Al-CTPB Propellant	154
6-10	Surface Response of FM5055 Carbon-Phenolic to 5% Al-CTPB Propellant	155
6-11	Surface Response of FM5055 to CTPB 18% Propellant	156
6-12	Surface Response of MX2600 Silica-Phenolic to 5% Al-CTPB Propellant	157
6-13	Chamber Pressure History for Test Firing 002	158
6-14	Chamber Pressure History for Test Firing 003	159

# ILLUSTRATIONS (Continued)

Figure		Page
5-16	Comparison of MX4926 Surface Recessions Given by the One-and Two-Dimensional Analysis	128
5-17	Comparison of MX4926 Surface Temperatures Given by the One and Two Dimensional Analysis	129
5-18	Effect of Pyrolytic Graphite Washer Backwall Boundary Condition on Throat Surface Recession	130
5-19	Effect of Pyrolytic Graphite Washer Backwall Boundary Condition on Surface and Backwall Temperatures	131
6-1	Surface Response of Durez 16771 Silica Phenolic to 5% Al-CTPB Propellant	146
6-2	Surface Response of Durez 16771 and CTPB 18% Propellant	147
6-3	Surface Response of MX2625 to 5% Al-CTPB Propellant	148
6-4	Kinetically Controlled Response of Graph-i-tite G-90 Bulk Graphite to 5% Al-CTPB Propellant	149
6-5	Surface Response of MXCE 280 Carbon-Phenolic to 5% Al-CTPB Propellant	150
6-6	Surface Response of MXCE 280 to CTPB 18% Propellant	151
6-7	Surface Response of MXCE 280 Silica-Phenolic to 5% Al-CTPB	152
6-8	Surface Response of MX4926 to 5% Al-CTPB Propellant	153
6-9	Diffusion Controlled Response Pycobond 410-65 to 5% Al-CTPB Propellant	154
6-10	Surface Response of FM5055 Carbon-Phenolic to 5% Al-CTPB Propellant	155
6-11	Surface Response of FM5055 to CTPB 18% Propellant	156
6-12	Surface Response of MX2600 Silica-Phenolic to 5% Al-CTPB Propellant	157
6-13	Chamber Pressure History for Test Firing 002	158
6-14	Chamber Pressure History for Test Firing 003	159

## ILLUSTRATIONS (Continued)

Figure		Page
6-15	Chamber Pressure History for Test Firing 005	160
6-16	Chamber Pressure History for Test Firing 006	161
6-17	Chamber Pressure History for Test Firing 009	162
6-18	Chamber Pressure History for Test Firing 013	163
6-19	Surface Temperature and Recession Rate Histories for the MSCE 280 Blast Tube of Test Firing 5	164
6-20	Comparison of Predicted and Measured Pyrolytic Graphite Washer Recession Rates	165
7-1	Schematic of Total Heat Flux Measurement System Plug	169
7-2	Schematic Drawing Showing Locations of Total Heat Flux Sensors	170
7-3	Procedure for Defining Total Heat Fluxes Using Measured Indepth Temperature Histories	171
7-4	Measured and Determined Temperatures for Forward Thermocouple Plug	172
7-5	Measured and Determined Temperatures for Thermocouple	173
7-6	Determined Blast Tube Surface Recession Rate	174
7-7	Comparison Between Measured, Determined, and Predicted Surface Recession	175
7-8	Comparison Between Predicted and Determined Heat Transfer Coefficients for Blast Tube	176

## TABLES

Table		Page
2-1	Summary of Major Features of Computer Codes	5
3-1	Summary of Material Thermal Property Data	19
3-2	MX2625 Thermal Conductivity Weighting Function	20
3-3	Durez 16771-1 Thermal Conductivity Weighting Function	20
3-4	Material Chemical Data Used for Thermal Screening Analysis and Indepth Thermal Analysis and Pretest Predictions	21
3-5	Phenolic Resin Decomposition Kinetic Constants	22
3-6	Chemical Properties of R155	22
4-1	Nozzle Location, Material Classes, and Typical Materials for the High Chamber Pressure Solid Rocket Motor	61
4-2	Summary of Materials Studied in Screening and Indepth Thermal Analysis	62
4-3	Steady State Ablation Thermal Screening Summary	63
4-4	Summary of Convective Boundary Conditions for One-Dimensional Analysis of Pyrostrand Blast Tube Entrance	66
6-1	Summary of Pretest Thermochemistry Maps	137
6-2	Measured Material Recession and Char Depths	138
6-3	Summary of Pretest Predictions and Their Comparison with Measured Data	141
6-4	Elemental Propellant Constituents	142
6-5	Elemental Propellant Constituents-Gas Only	143
6-6	Conditions for Propellant Evaluations	144
6-7	Propellant Ballistics Quoted by Manufacturer	144
6-8	Propellant Constituents (Mole Fraction)	145

# LIST OF SYMBOLS

A	area
B	pre-exponential factor
B'	non-dimensional surface removal rate
C	experimentally determined constant (used in Eq. 3-6)
C <sub>H</sub>	Stanton number
C <sub>M</sub>	non-dimensional mass transfer coefficient
D	local beam length
E <sub>a</sub>	activation energy
F	view factor
H	enthalpy
$\dot{m}$	mass flow rate
n	percent aluminum loading by mass
P	pressure
PG	pyrolytic graphite
Pr	Prandtl number
$\dot{q}$	heat rate
r	instantaneous slot radius
R	radius
t	time
T	temperature
u	velocity

# LIST OF SYMBOLS (Concluded)

$\alpha$	absorptivity
$\epsilon$	emissivity, area ratio
$\lambda$	streamwise length
$\rho$	density
$\rho_e^U C_H$	convective heat transfer coefficient
$\rho_e^U C_M$	mass transfer coefficient
$\sigma$	Stefan-Boltzmann constant

## SUBSCRIPTS

a	ambient
ARGEIBL	obtained from ARGEIBL computer code
c	char
conv	convective
e	edge
eff	effective
g	pyrolysis gas
o	chamber condition, initial
r	radial position in propellant slot, residual
R	recovery
s	free stream
slot	keyhole slot in propellant grain
w	wall

## SUPERSCRIPTS

*	throat condition, condensed phase
~	non-dimensional

## SECTION 1

### INTRODUCTION

The wide variety of mission requirements for high chamber pressure solid rocket motors result in a correspondingly wide range in the operational characteristics of the motor and nozzle. This wide range in the motor and nozzle characteristics dictates that a relatively broad material performance technology base be available in order for the engineer to efficiently design a nozzle which will satisfy the stringent thermal and structural requirements for a lightweight nozzle design. The motor performance requirements of particular interest to the nozzle design engineer are the motor ballistics and the type of propellant. Depending on the particular mission requirement, the high chamber pressure motor ballistics can range from a short to moderate single pulse motor operation to a multiple pulse or boost sustain type of motor operation. An aluminized propellant is generally used in these motors but the aluminium content in the propellant can vary from 5 to 18 percent. Typical nozzle operating characteristics can include restrictions on the nozzle configuration as well as on the nozzle performance. The nozzle configuration restrictions may require a high velocity blast tube and the nozzle performance restrictions generally include surface recession limits (particularly at the nozzle throat) and limitations on the temperature rise of the nozzle structural shell.

Because of the broad material performance technology which is required to satisfy the wide range of material and nozzle performance requirements, several Air Force programs have been conducted with the objectives of 1) obtaining experimental material performance data at high chamber pressures and 2) using these data to validate existing analytical techniques. These programs included the material performance evaluation of carbon phenolic ablators and pyrolytic graphite (PG) coatings when subjected to multiple pulse duty cycles under Contract F04611-70-C-0019 (Ref. 1), the definition and evaluation of the kinetic response of pyrolytic graphite under Contract F04611-69-C-0081 (Ref. 2) and the material performance evaluation of several charring ablators, carbon-carbons, bulk graphites, PG washers and wire wound tungsten under Contract F04611-69-C-0065 (Refs. 3 and 4). Under all of these contracts, a set of analytical techniques were validated based on comparisons between measured and predicted material performance. The objectives of this contract (F04611-71-C-0051) are to provide material performance data and to update the validation of the analytical techniques for a wide range of aluminum



loadings in the solid propellant (5 to 18 percent) and for high as well as low velocity blast tubes (blast tube area ratio from 1.3 to 2.0 with respective Mach numbers of .53 and .31).

In support of Contract F04611-71-C-0051 and under subcontract to UTC, Aerotherm performed thermochemical and thermal analyses and provided thermal instrumentation. The specific items covered in this subcontract were

Phase I Thermochemical screening calculations of ablation materials to determine their performance in a high chamber pressure solid rocket motor environment.

In-depth thermal response predictions using the results of the thermochemical screening calculations.

Phase II Definition, design, and fabrication of thermal instrumentation for installation into a high chamber pressure motor.

Transient two-dimensional heat conduction analyses of a pyrolytic graphite washer nozzle throat package.

Phase III Eighteen material performance predictions which include surface recession, char depth regression (if applicable), and in-depth transient temperature histories.

Evaluation of the method for predicting the convective heat transfer coefficient.

Phase IV Post-test experimental evaluation of the material density profile.

The analytical techniques used in Phases I through III are summarized in Section 2. The material property data, propellant property data, nozzle configuration, and the convective and radiative heat flux boundary conditions are presented in Section 3. The results obtained for the thermochemical screening and in-depth thermal response predictions and for the pyrolytic graphite washer throat package are presented in Sections 4 and 5, respectively. The analytical material performance predictions for the motor firings are presented along with comparisons with the experimental data in Section 6. The measured results from the thermal instrumentation are reported in Section 7 and finally, conclusions and recommendations are presented in Section 8.

## SECTION 2

### SUMMARY OF ANALYSIS TECHNIQUES

As mentioned previously the objectives of three previous Air Force Contracts (F04611-69-C-0065, F04611-70-C-0019 and F04611-69-C-0081) included the validation of analytical techniques for predicting the thermochemical response of materials which are typically used in high chamber pressure solid rocket motors. Under Contract F04611-69-C-0065, the comparisons between predicted and measured surface recession showed that the analytical techniques predicted the surface recession of charring ablative materials, carbon-carbon materials, and wire wound tungsten within  $\pm 25$  percent. Under Contract F04611-69-C-0081, similar comparisons showed that when the analytical techniques were modified to include kinetically controlled surface chemical reactions and if the proper kinetically controlled constants were available, then the surface recession histories for PG coatings and PG washers were generally predicted within  $\pm 50$  percent for a wide variety of thermochemical environments. These two contracts considered only single pulse motors. Under Contract F04611-70-C-0019, comparisons between the predictions and measurements showed that equally good results were obtained from multiple pulse duty cycle motors for carbon phenolic and PG coatings. Detailed results of these studies are presented in References 1 through 4. For the thermochemical analyses performed under the current contract, these same analytical techniques were used, and they are summarized briefly in the following paragraphs.

The analytical prediction techniques are in the form of computer programs and are identified by

- Aerotherm Chemical Equilibrium (ACE) Program
- Charring Material Ablation (CMA) Program
- Axisymmetric Transient Heat and Material Ablation (ASTHMA) Program
- Aerotherm Real Gas Energy Integral Boundary Layer (ARGEIBL) Program
- Aerotherm Graphite Surface Kinetics (GASKET) Program
- Boundary Layer Inversion Matrix Procedure (BLIMP) Program
- Steady State Ablation (SSA) Program

The SSA Program which predicts the steady state recession and surface temperature of a material was used along with the ACE and ARGEIBL programs for making the thermochemical screening predictions presented in Section 4. The analysis procedure for making these predictions is summarized in Figure 2-1. The first five programs were the basic ones used in making the analytical predictions which are presented in Sections 5 and 6. The analysis procedure for making these predictions is summarized in Figure 2-2. As described in Reference 3, the BLIMP program is used primarily to evaluate the heat and mass coefficients predicted by the more simplified analytical techniques. In this reference, the BLIMP program was used to confirm the heat and mass transfer coefficients predicted by the much simpler ARGEIBL program and Chilton-Colburn correlation for a typical high chamber pressure nozzle configuration. The major features of the ACE, CMA, ASTHMA, ARGEIBL, GASKET, and BLIMP computer programs are summarized in Table 2-1. For a more detailed description of the programs, the reader is referred to References 4 through 8.

Versions of the ACE, CMA, and ASTHMA computer codes which were used in making the analytical predictions are available to the rocket community. The version of ACE which is available is the EST3 code. This code, which is described in greater detail in Reference 9, treats the diffusion-controlled thermochemical response of materials, and, therefore, it is applicable to all materials for which the surface chemical reactions are not kinetically controlled or for which a surface melt layer does not develop. These materials include carbon and graphite phenolic charring ablators and carbon/carbon composites. However, EST3 is not applicable for graphites and silica phenolic charring ablators. The CMA computer code described in Table 2-1 is available as CMA3 (Reference 10). The ASTHMA and GASKET codes described in Table 2-1 were made available through Contract F04611-69-0081, and the background to these codes are presented in References 11 and 12.

TABLE 2-1

## SUMMARY OF MAJOR FEATURES OF COMPUTER CODES

Computer Program	Major Features		Typical Use	
CMA3	1	Calculation of transient thermal response of a composite slab or cylinder containing up to five in-depth charring (or noncharring) materials.	1.	Thermal analysis of ablative materials in liquid and solid rocket motors.
	2.	Calculation of surface recession rate resulting from diffusion or kinetically controlled surface chemical reactions and/or mechanical melt removal.	2.	Thermal analysis of reentry nose tips.
	3.	Considers variable thermal properties with a flexible physical model of thermal conductivity which permits the treatment of partially charred values less than the virgin material value.		
	4.	Considers in-depth and surface thermochemical effects of the pyrolysis gases being generated by both the surface and backup materials.		
GASKET	1.	Calculation of thermodynamic state for isentropic or isoenthalpic process for a closed system including condensed phase.	1.	Nozzle equilibrium isentropic expansion.
	2.	Calculation of transport properties (viscosity, thermal conductivity, and mass diffusion coefficients).	2.	Evaluation of transport coefficients for use in boundary layer analysis.
	3.	Calculation of surface state of graphite materials exposed to an environment considering kinetically controlled reactions between the material and the $H_2O$ , $CO_2$ , and $H_2$ of the combustion products.	3.	Generation of Mollier charts for any gas system.
	4.	Considers unequal diffusion coefficients.	4.	Generation of thermochemical data for use with CMA and ASTHMA computer programs

TABLE 2-1 (Concluded)

ASTHMA3	<ol style="list-style-type: none"> <li>1. Calculation of transient thermal response of a two-dimensional body.</li> <li>2. Considers surface recession</li> <li>3. General thermochemical surface boundary conditions</li> <li>4. Considers anisotropic temperature dependent thermal properties.</li> </ol>	<ol style="list-style-type: none"> <li>1. Thermal analysis of heat sink materials in liquid and solid rocket motors and reentry nose tips.</li> </ol>
ACE	<ol style="list-style-type: none"> <li>1. Calculation of thermodynamic state for isentropic or isoenthalpic process for a closed system including condensed phases.</li> <li>2. Calculation of transport properties (viscosity, thermal conductivity, and mass diffusion coefficients).</li> <li>3. Calculation of surface state of any material exposed to an environment considering all possible chemical reactions between the materials and the environment. Surface reactions may be kinetically controlled. Mechanical removal of surface melt layer may also be considered.</li> <li>4. Considers unequal diffusion coefficients.</li> </ol>	<ol style="list-style-type: none"> <li>1. Nozzle equilibrium isentropic expansion.</li> <li>2. Evaluation of transport coefficients for use in boundary layer analysis.</li> <li>3. Generation of Mollier charts for any gas system.</li> <li>4. Generation of thermochemical data for use with CMA and ASTHMA computer programs.</li> </ol>
ARGEIBL	<ol style="list-style-type: none"> <li>1. Calculation of laminar or turbulent convective heat transfer coefficients for non-ablating wall.</li> <li>2. Considers any real gas system and axial variations in wall temperature and free stream properties.</li> <li>3. Solves the energy integral equation.</li> </ol>	<ol style="list-style-type: none"> <li>1. Transfer coefficient analysis of solid and liquid rocket motors.</li> </ol>
BLIMP	<ol style="list-style-type: none"> <li>1. Calculation of laminar or turbulent convective heat transfer coefficients for ablating or nonablating wall.</li> <li>2. Considers any real gas system and axial variations in wall temperature, free stream properties, and surface recession.</li> <li>3. Considers chemical and thermal diffusion in the boundary layer.</li> <li>4. Solves nonsimilar laminar and turbulent boundary layer equations.</li> </ol>	<ol style="list-style-type: none"> <li>1. Transfer coefficient analysis of solid and liquid rocket motors and reentry nose cones.</li> </ol>

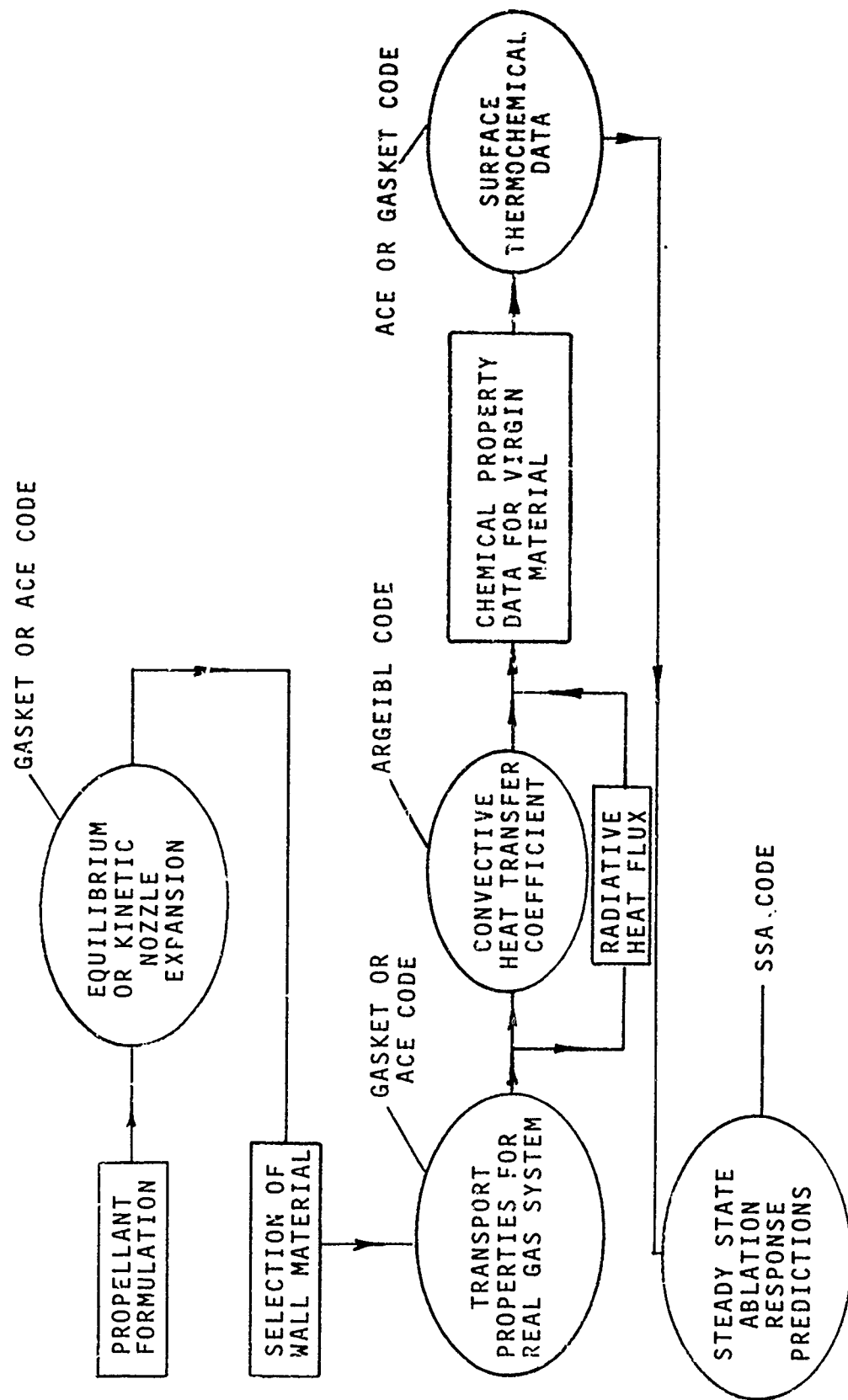


FIGURE 2-1. FLOW CHART FOR SCREENING ANALYSIS

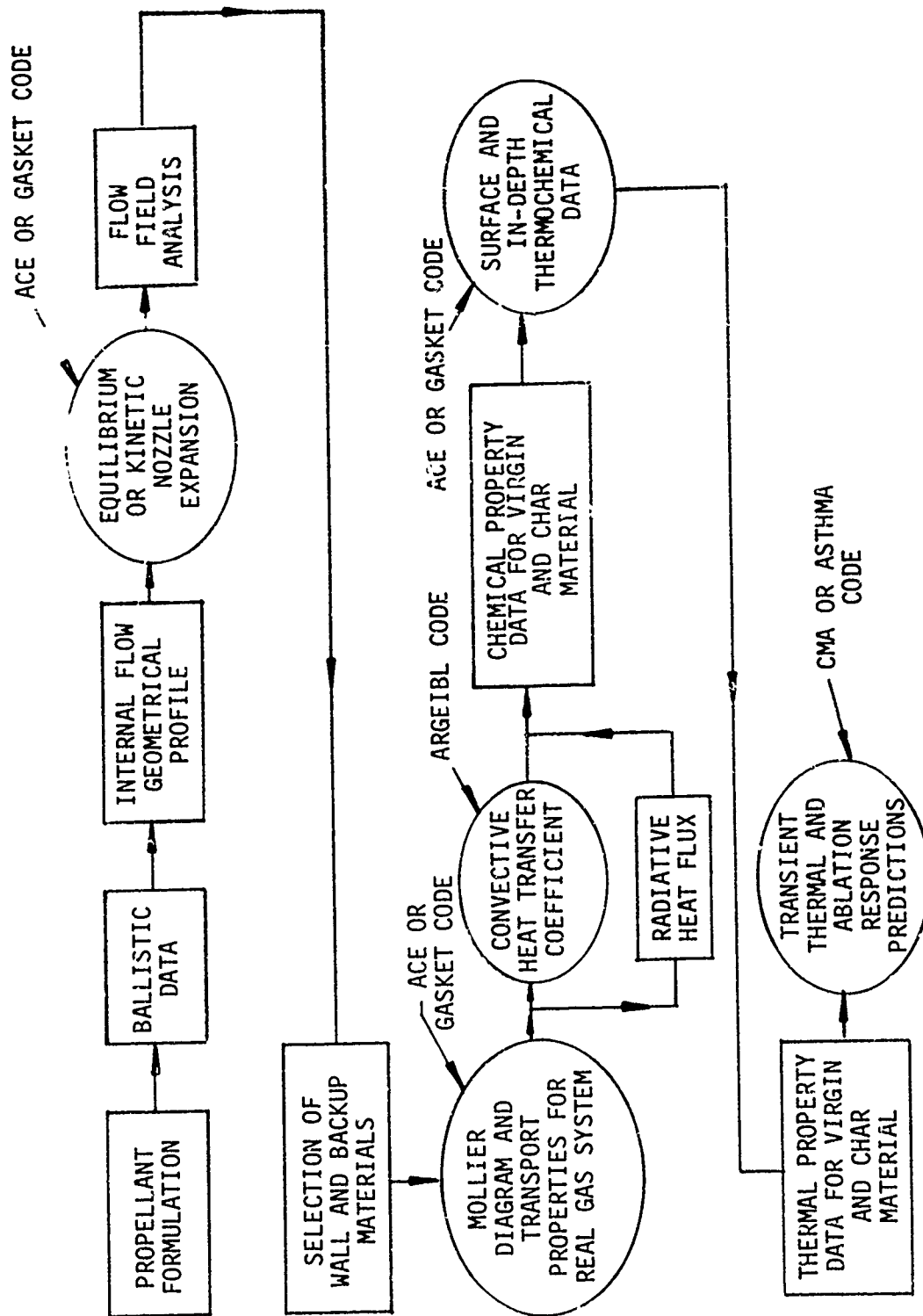


Figure 2-2. Flow Chart for Detailed Transient Analysis

### SECTION 3

#### PRELIMINARY ANALYSIS

In the previous section, the analysis techniques used to study the response of ablative rocket nozzles to high pressure combustion products were presented. The first step in the analysis procedure consists of defining the free stream properties by making computations using the ACE computer code. The next step consists of defining the convective heat transfer coefficients by making computations using the ARGEIBL code. The results of these calculations which depend only on the propellant properties and nozzle geometry are presented in this section. They were compiled for the two nozzle geometries (blast tube area ratios of 1.3 and 2.0) and the two propellants (5 and 18 percent aluminum contents) used in the test program by UTC. In later sections, more specific calculations are presented which define the material response, and these calculations use the results of this section for boundary conditions and material properties.

Propellant data and basic nozzle geometries are presented in Section 3.1 and 3.2, respectively. Section 3.3 describes the flow field analysis used for the cylindrical and keyhole port propellant cartridges. The free stream properties and heat transfer boundary conditions are presented in Sections 3.4 and 3.5, respectively. The material property data are defined in Section 3.6.

#### 3.1 PROPELLANT DATA

Two variations of a CTPB propellant were used for the following analyses. One had a 5 percent aluminum loading fraction, and the other had an 18 percent aluminum loading fraction. The chemical elements in the 5% Al-CTPB are

<u>Element</u>	<u>Atomic Wts/Unit Mass</u>
Hydrogen	0.0412
Carbon	0.0083
Nitrogen	0.0071
Oxygen	0.0287
Aluminum	0.0019
Chlorine	0.0071

The flame temperature for this propellant is 5816°R at 1000 psia. The chemical elements constituents in the 18% Al-CTPB propellant are

<u>Element</u>	<u>Atomic Wts/Unit Mass</u>
Hydrogen	0.0368
Carbon	0.0082
Nitrogen	0.0060
Oxygen	0.0242
Aluminum	0.0066
Chlorine	0.0060

The flame temperature for this propellant is 6469°R at 1000 psia.



### 3.2 NOZZLE GEOMETRY

The calculation of the heat transfer boundary conditions requires the definition of the internal nozzle contour and a nominal expected surface temperature range for the surface materials. Figure 3-1 illustrates the nozzle geometries which were used for the analyses presented in Sections 4, 5, and 6. As shown by this figure, two basic blast tube contraction ratios were considered. The nozzle geometries are identical for the aft closure, the nozzle throat diameter, and the exit cone. The primary difference in the geometries was that one had a blast tube area ratio of 1.3 and the other one had a blast tube area ratio of 2.0. This difference in the area ratio required some minor variations in the forward and aft entrance caps and in the convergence angle of the PG washers or wire wound tungsten upstream of the nozzle throat.

The materials considered for each of the nozzle components are described in Section 4 for the steady state thermochemical screening analyses, in Section 5 for the two dimensional analyses of the nozzle throat package, and in Section 6 for the post test thermochemical predictions. The surface temperature range of primary interest for these materials is between 2700 and 5400°R.

It is worth noting that the nozzle shown in Figure 3-1 was designed so that components could have more than one material exposed to the combustion products. The aft closure, for example, was divided into two sections, one encompassing the plane above the centerline of the nozzle and the other the plane below the nozzle centerline. Thus, for a single firing, two aft closure materials can be tested. In a similar manner, the aft entrance cap and the exit cone had the capability of testing two materials for any one firing, and the blast tube could contain up to three test materials.

### 3.3 FLOW FIELD ANALYSIS

The purpose of the flow field analysis was to define the mass flux as a function of boundary layer running length. This allows the free stream properties as calculated by the ACE computer program to be converted from a function of mass flux to a function of nozzle location. Two configurations of the propellant loaded cartridge were fired during the course of the program. One of these configurations had a circular port with burning both on the aft end and in the port and the other configuration had a small circular port with burning both in the port and in a slot running the length of the grain (Figure 3-2).

The flow field for the first configuration was analyzed assuming one dimensional flow and utilizing the following relationship which describes the conservation of mass for internal flows

$$\tilde{\rho}u = \frac{\rho_e u_e}{\rho_e^* u_e^*} = \frac{A^*}{A} = \text{inverse of contraction ratio} \quad (3-1)$$

where  $\rho_e u_e$  and  $A$  are the mass flux and cross sectional area, respectively. An asterisk represents nozzle throat or sonic conditions. The relationship between contraction ratio and boundary layer running length is shown in Figure 3-3. By combining this relationship with Equation 3-1, the variation of the non-dimensional flow parameter  $\tilde{\rho}u$  with the boundary layer running length was obtained, and this is shown by the  $t = \infty$  line in Figure 3-4. The slotted grain configuration, however, cannot be analyzed using one-dimensional flow theory. The flow field analysis for this configuration is described in the following paragraphs.

The flow field for the slotted propellant configuration shown in Figure 3-2 changes rapidly with time due to the increasing diameter of the circular port and the widening of the slot. One should note that the propellant is inhibited on the aft face, and, thus, the surface of the aft face of the propellant does not recede from the surface of the aft closure. Of course, the aft closure gradually becomes exposed during the motor firing due to the opening of the circular port and the widening of the slot.

One of the difficulties in performing the flow field analysis of the slotted grain is in defining the mass flux exchange between the mass of combustion products generated in the slot with those generated in the circular port. At motor ignition the surface area for the circular port is smaller than for the slot. Thus, as the flow of combustion products proceeds from the forward to the aft end of the propellant, the combustion products from the slot will feed into the circular port. At later motor burn times, the process is reversed; that is the combustion products generated at the surface of the circular port will feed into the slot. The second difficulty in performing the flow analysis is in defining the effective flow area of the slot as the combustion products in the slot are forced into the circular port at the aft end of the motor.

For the analysis presented herein, the first difficulty mentioned above was resolved by making the conservative assumption that up to the time when the combustion gases in the port starts to feed the slot, all the combustion products generated in the slot flow down the slot and that all the combustion products in the circular port flow through the circular port. To resolve the second difficulty, an engineering judgement was made in order to define the

following paragraphs for the cylindrical grain and keyhole port grains, respectively. For this analysis, a chamber pressure of 2800 psia was used.

The heat transfer coefficient distribution in nozzles fired with a cylindrical grain propellant were calculated accounting for the effects of 1) both 5 percent and 18 percent aluminum propellant, 2) blast tube area ratios of 1.3 and 2.0, 3) and wall temperatures of 2700° and 5400°R. Figure 3-8 illustrates the heat transfer coefficient distribution predicted by the ARGEIBL code for the 5 percent aluminum propellant for blast tube area ratios of 1.3 and 2.0. In each figure the sensitivity to wall temperature is shown. Figure 3-9 illustrates the heat transfer coefficient for the 18 percent aluminum propellant. Note that the 18 percent aluminum CTPB yields, in general, a lower heat transfer coefficient than the 5 percent propellant. Also, the sensitivities of each propellant to wall temperature are similar. For the case of the 1.3 blast tube area ratio, an analysis was performed to determine the sensitivity of the heat transfer coefficient on the two dimensional flow field effects in the aft closure, and this analysis is described in the following paragraph.

As mentioned previously (Section 3.3), a one dimensional flow field analysis was used for calculations involving the cylindrical port propellant cartridge. To account for the sharp convergence angle of the aft closure, an analysis was performed in which the effective flow area in the aft closure was assumed to be a spherical surface whose center is the apex of the cone created by extending the aft closure surface to the motor centerline. This surface is defined by the schematic drawing presented in Figure 3-10. Intuitively, the aft closure flow field based on the spherical surface flow area is more reasonable because the velocity vector is normal to the flow area; this is not the case for the one dimensional flow assumption. The convective heat transfer coefficients for both flow field analyses are presented in Figure 3-9A. This shows that the modified flow analysis resulted in lower heat transfer coefficients in the aft closure only. Two dimensional effects in the blast tube and further downstream were found to be insignificant.

Figure 3-11 illustrates the variation of the ARGEIBL heat transfer coefficient with blast tube area ratio at several nozzle locations. Both the 5 and the 18 percent aluminum propellants exhibit the same trends. For the blast tube entrance, the heat transfer coefficient decreases with increasing blast tube area ratio. For the throat and the exit cone entrance, the convective coefficient increases with increasing blast tube area ratio.

Figure 3-12 presents the heat transfer coefficient distribution for the slotted grain port for a nozzle with a blast tube area ratio of 2.0 and for a 5 percent aluminum propellant. These curves apply only to a portion of the nozzle which is in the same plane as the slot in the propellant

calculate the free stream properties throughout the nozzle for each propellant. These properties include static temperature, static pressure, velocity, density, molecular weight and species concentration as a function of axial distance in the nozzle. This program also calculates some of the more significant transport properties.

In calculating the free stream properties, the assumption was made that local thermodynamic and chemical equilibrium existed throughout the nozzle and that the propellant gases go through an isentropic expansion from the chamber state. This allowed a series of closed system equilibrium solutions to be performed at the various axial locations. The ACE program first calculates the entropy at the chamber state, and this entropy is held constant in subsequent solutions at different locations. The major results of this analysis are presented in Figure 3-6 for the 5 percent aluminum CTPB propellant and in Figure 3-7 for the 18 percent propellant. These results are based on a chamber pressure of 2800 psia.

### 3.5 HEAT TRANSFER BOUNDARY CONDITIONS

After the boundary layer edge or free stream properties were calculated the heat transfer boundary conditions were determined. These boundary conditions include both the convective and radiative heat transfer coefficients. The convective heat transfer coefficients apply during a motor firing (Section 3.5.1) and the radiative heat transfer coefficients apply both during the firing and during the motor cooldown (Section 3.5.2).

#### 3.5.1 Convective Boundary Conditions

To define the convective boundary conditions, the heat transfer coefficient as a function of boundary layer running length was calculated. This coefficient was defined based on an enthalpy driving potential and is given by

$$\dot{q}_{\text{conv}} = \rho_e u_e C_H (H_R - H_{ew})$$

where  $\dot{q}_{\text{conv}}$  - Total convective heat flux to the material

$\rho_e u_e C_H$  - Convective heat transfer coefficient ( $\rho_e$  - edge density,  $u_e$  - edge velocity,  $C_H$  - Stanton number)

$H_R$  - Recovery enthalpy

$H_{ew}$  - Edge enthalpy at the wall temperature.

Aside from its dependence on nozzle location and chamber pressure, the heat transfer coefficient varies with wall temperature, nozzle geometry (blast tube area ratio), and the type and configuration of the propellant grain. The heat transfer coefficients dependence on these quantities is presented in the

following paragraphs for the cylindrical grain and keyhole port grains, respectively. For this analysis, a chamber pressure of 2800 psia was used.

The heat transfer coefficient distribution in nozzles fired with a cylindrical grain propellant were calculated accounting for the effects of 1) both 5 percent and 18 percent aluminum propellant, 2) blast tube area ratios of 1.3 and 2.0, 3) and wall temperatures of 2700° and 5400°R. Figure 3-8 illustrates the heat transfer coefficient distribution predicted by the ARGEIBL code for the 5 percent aluminum propellant for blast tube area ratios of 1.3 and 2.0. In each figure the sensitivity to wall temperature is shown. Figure 3-9 illustrates the heat transfer coefficient for the 18 percent aluminum propellant. Note that the 18 percent aluminum CTPB yields, in general, a lower heat transfer coefficient than the 5 percent propellant. Also, the sensitivities of each propellant to wall temperature are similar. For the case of the 1.3 blast tube area ratio, an analysis was performed to determine the sensitivity of the heat transfer coefficient on the two dimensional flow field effects in the aft closure, and this analysis is described in the following paragraph.

As mentioned previously (Section 3.3), a one dimensional flow field analysis was used for calculations involving the cylindrical port propellant cartridge. To account for the sharp convergence angle of the aft closure, an analysis was performed in which the effective flow area in the aft closure was assumed to be a spherical surface whose center is the apex of the cone created by extending the aft closure surface to the motor centerline. This surface is defined by the schematic drawing presented in Figure 3-10. Intuitively, the aft closure flow field based on the spherical surface flow area is more reasonable because the velocity vector is normal to the flow area; this is not the case for the one dimensional flow assumption. The convective heat transfer coefficients for both flow field analyses are presented in Figure 3-9A. This shows that the modified flow analysis resulted in lower heat transfer coefficients in the aft closure only. Two dimensional effects in the blast tube and further downstream were found to be insignificant.

Figure 3-11 illustrates the variation of the ARGEIBL heat transfer coefficient with blast tube area ratio at several nozzle locations. Both the 5 and the 18 percent aluminum propellants exhibit the same trends. For the blast tube entrance, the heat transfer coefficient decreases with increasing blast tube area ratio. For the throat and the exit cone entrance, the convective coefficient increases with increasing blast tube area ratio.

Figure 3-12 presents the heat transfer coefficient distribution for the slotted grain port for a nozzle with a blast tube area ratio of 2.0 and for a 5 percent aluminum propellant. These curves apply only to a portion of the nozzle which is in the same plane as the slot in the propellant

cartridge. As shown by Figure 3-12, the predicted heating is increased substantially in the aft closure by the keyhole port grain, but the heating in the remainder of the nozzle is reduced. As time progresses the heat transfer coefficient is decreased in the aft closure and increased downstream. The steady state value shown is the same as that of a nozzle with a cylindrical grain propellant. Figure 3-13 shows the heat transfer coefficient both in the slot plane and opposite to the slot plane for the 18 percent Al-CTPB propellant and a 1.3 area ratio blast tube. Figure 3-14 normalizes the heat transfer coefficient predicted for the 5 percent Al propellant keyhole port using the circular port flow for the aft closure, blast tube entrance, throat package, and exit cone as a baseline. These results were used to determine the most severe heating conditions to be studied in the thermal screening analysis which is presented in the following section.

As mentioned earlier the heat transfer coefficient distributions given in the figures presented in this section were calculated by the ARGEIBL code. Previous experience has shown that the heat transfer coefficient predicted by the ARGEIBL code is high and should be multiplied by 0.75; that is

$$\rho_e u_e C_H = 0.75 (\rho_e u_e C_H)_{\text{ARGEIBL}} \quad (3-2)$$

where  $(\rho_e u_e C_H)_{\text{ARGEIBL}}$  - Convective heat transfer coefficient predicted by the ARGEIBL Code.

The factor of 0.75 has been used by Aerotherm in previous thermal analyses of solid rocket motors (References 3 and 4). For the transient in-depth thermal analysis presented in subsequent sections, Equation 3-2 is modified further to account for the actual chamber pressure history by using the relationship

$$\rho_e u_e C_H = 0.75 \frac{(P_0)^{0.8}}{2800} (\rho_e u_e C_H)_{\text{ARGEIBL}} \quad (3-3)$$

where  $P_0$  is the instantaneous measured (or predicted) chamber pressure in psia units.

### 3.5.2 Radiative Boundary Conditions

To model the radiative boundary conditions during nozzle firings, a parallel plate model was used. This model applies to aluminized

propellants and assumes that the particle laden stream of combustion products is optically thick and that it exchanges radiant energy with the surface as if the stream and wall were parallel plates. In this way, multiple reflections between the wall and stream were taken into account. In addition, the assumption was made that both the stream and wall behave as gray bodies and that they emit and reflect radiant energy diffusely. Based on the above assumptions, the net radiant heat flux relation is given as

$$\dot{q}_{\text{net rad}} = \epsilon_{\text{eff}} (\sigma T_s^4 - \sigma T_w^4) \quad (3-4)$$

where

$$\epsilon_{\text{eff}} - \text{Effective emissivity} = \frac{1}{\frac{1}{\epsilon_w} + \frac{1}{\epsilon_s} - 1} \quad (3-5)$$

- $\epsilon_w$  - Wall material emissivity
- $\epsilon_s$  - Particle laden stream emissivity
- $\sigma$  - Stefan-Boltzmann constant
- $T_s$  - Free stream (edge) temperature
- $T_w$  - Wall temperature.

To determine the effective emissivity using equation (3-5), the stream emissivity was defined as

$$\epsilon_s = 1 - \exp \left( -C \frac{n}{16} \rho D \right) \quad (3-6)$$

where

- C - Empirical constant (0.808)
- n - Percentage of aluminum loading
- $\rho$  - Local density of propellant combustion species (lb/ft<sup>3</sup>)
- D - Local beam length, usually taken as the diameter (in.).

To model the radiative boundary conditions during periods of nozzle cooldown, a different model was used. The nozzle surface being analyzed was considered as exchanging radiant energy with only one source which was the environment beyond the exit plane of the nozzle. This implies that the remaining interior nozzle

can be approximated as an isothermal surface which is at the same temperature as the one being analyzed. The radiant exchange with the environment beyond the exit plane of the nozzle was based on the assumption of diffuse gray body radiation. Therefore, the surface being analyzed would radiate energy to this environment in the form of

$$q \text{ net rad} = F\epsilon_w\sigma(T_a^4 - T_w^4) \quad (3-7)$$

where

- $F$  - View factor from surface to environment beyond exit plane.
- $T_a$  - Environment (ambient) temperature.

If  $T_a^4$  is neglected in relation to  $T_w^4$  Equation (3-7) reduces to

$$q \text{ net rad} = -F\epsilon_w\sigma T_w^4$$

### 3.6 MATERIAL CHEMICAL AND THERMAL PROPERTY DATA

This section summarizes the material chemical and thermal properties used for making material performance predictions using the CMA and ASTHMA computer codes.

The thermal properties include

- density - virgin material  
- char material
- material specific heat - virgin material  
- char material
- material thermal conductivity - virgin material  
- char material

and the chemical properties include

- resin mass fraction
- effective resin and reinforcement molecules
- heat of formation - virgin material  
- char material
- constants in Arrhenius type decomposition rate equation for the resin system



Material thermal properties for most materials were obtained from the references listed in Table 3-1. Thermal properties for R-155 were not available, thus limiting its analysis to steady state calculations. The thermal properties for MX2625 were estimated (Figure 3-15) from those of MX2646 (Ref. 6). The thermal conductivity weighting function is described in Table 3-2. The thermal properties of Pycobond were estimated to be those shown in Figure 3-16 and are an average of the conductivities of ATJ graphite with and against the grain. Figure 3-17 gives the estimated thermal conductivity of Durez 16771-1 which was obtained by decreasing the conductivity of MX2600 by 25%. The thermal conductivity weighting function presented in Table 3-3 was used. The nominal material density, resin mass fraction, and resin residual are presented in Table 3-4. The char density was calculated from this information. Also presented in Table 3-4 are the chemical formulas for the resin and char for each material except R-155. A heat of formation value of -1100 Btu/lb was used for the phenolic resin and a value of -6520 Btu/lb was used for the  $\text{SiO}_2$ . The decomposition kinetics for the phenolic resin are defined in Table 3-5.

The standard chemical information was not available in the literature for R-155. The values shown in Table 3-6 were obtained from Reference 16, and are sufficient for calculating both the steady state surface thermochemistry map and the steady state surface recession and temperature.

TABLE 3-1  
SUMMARY OF MATERIAL THERMAL  
PROPERTY DATA

Material	Source of Thermal Properties
MXCE 280	Ref. 13
MXSE 280	Ref. 13
MXSC 195	Ref. 13
MX2625	Figure 3-15
R-155	N/A
MX4926 <sup>b</sup>	Ref. 14
FM5055	Same as MX4926
MX2600	Ref. 14
G-90	Ref. 4
Pyrostrand	Ref. 15
Pycobond	Figure 3-16
Durez 16771-1	Figure 3-17
PG	Ref. 17
ATJ	Ref. 18

<sup>a</sup> The values of thermal conductivity used for these materials are presented in Section 5.

<sup>b</sup> Thermal properties suitable for the ASTM code are presented in Section 5.

TABLE 3-2

## MX2625 THERMAL CONDUCTIVITY WEIGHTING FUNCTION

Mass Fraction	Weighting Function	
	Virgin	Char
1.00	1.4	.0
.90	.4	.0
.60	.4	.0
.35	.0	1.0
.0	.0	1.0

TABLE 3-3

## DUREZ 16771-1 THERMAL CONDUCTIVITY WEIGHTING FUNCTION

Mass Function	Weighting Function	
	Virgin	Char
1.00	1.0	.0
.8	.5	.0
.55	.5	.0
.25	.0	1.0
.0	.0	1.0

TABLE 3-4

MATERIAL CHEMICAL DATA USED FOR THERMAL SCREENING ANALYSIS  
AND IN-DEPTH THERMAL ANALYSIS  
AND PRETEST PREDICTIONS

Material	Nominal Density Lb/Ft	Nominal Resin Mass Fraction	Resin Residual	Assumed Resin Elemental Formula	Reinforcement Elemental Formula
MXCE 280, Fibrous carbon Impregnated with an elas- tomer modified phenolic resin	78.0	0.475	0.40	$C_6H_6O$	C
MXSE 280, Fibrous silica, Impregnated with an elas- tomer modified phenolic resin	96.2	0.350	0.50	$C_6H_6O$	$SiO_2$
MXSC 195, Fibrous poly- crystalline carbon silica Impregnated with phenolic resin	96.8	0.400	0.45	$C_6H_6O$	C/ $SiO_2$
MX2625, Fibrous silica, Impregnated with phenolic resin	111.8	0.250	0.5	$C_6H_6O$	$SiO_2$
R-155, ASB/Rubber	79.5	N/A	N/A	N/A	N/A
MX4926, Carbon cloth Impregnated with phenolic resin	89.4	0.345	0.40	$C_6H_6O$	C
MX2600, Fibrous silica, Impregnated with phenolic resin	108.7	0.315	0.50	$C_6H_6O$	$SiO_2$
G-90 Bulk graphite	117.5	-	-	-	C
Pyrostrand, graphite base with graphite bond	112.0	-	-	-	C
Pycobond, graphite fiber with graphite bond	103.0	0.40			
Durez 16771-1	115.4	0.345	0.5	$C_6H_6O$	$SiO_2$
FM5055, Carbon Impregnated with phenolic resin	89.4	0.345	0.40	$C_6H_6O$	C
Pyrolytic graphite	137.3	-	-	-	C
ATJ	108.0	-	-	-	C

TABLE 3-5  
PHENOLIC RESIN DECOMPOSITION  
KINETIC CONSTANTS

Reaction, i	Pre-exponential Factor B (sec <sup>-1</sup> )	Activation Energy E <sub>a</sub> /R (°R)	Density Factor Exponent ψ	Initial Density, ρ <sub>0</sub> (lb/ft <sup>3</sup> )	Residual Density, ρ <sub>r</sub> (lb/ft <sup>3</sup> )
A	1.40 x 10 <sup>4</sup>	15,400	3	20.25	0
B	4.48 x 10 <sup>9</sup>	36,800	3	60.75	32.40 <sup>a</sup> 36.55 <sup>b</sup> 40.50 <sup>c</sup>

<sup>a</sup> Resin residual = 0.40

<sup>b</sup> Resin residual = 0.45

<sup>c</sup> Resin residual = 0.50

TABLE 3-6  
CHEMICAL PROPERTIES OF R-155

HEAT OF FORMATION (kcal/gm)	-1.96
ELEMENTAL COMPOSITION ( $\frac{\text{gm atoms}}{100 \text{ gms}}$ )	Carbon - 3.74 Hydrogen - 7.63 Oxygen - 1.59 Magnesium - 0.50 Silicone - 0.35 Aluminum -- 0.01

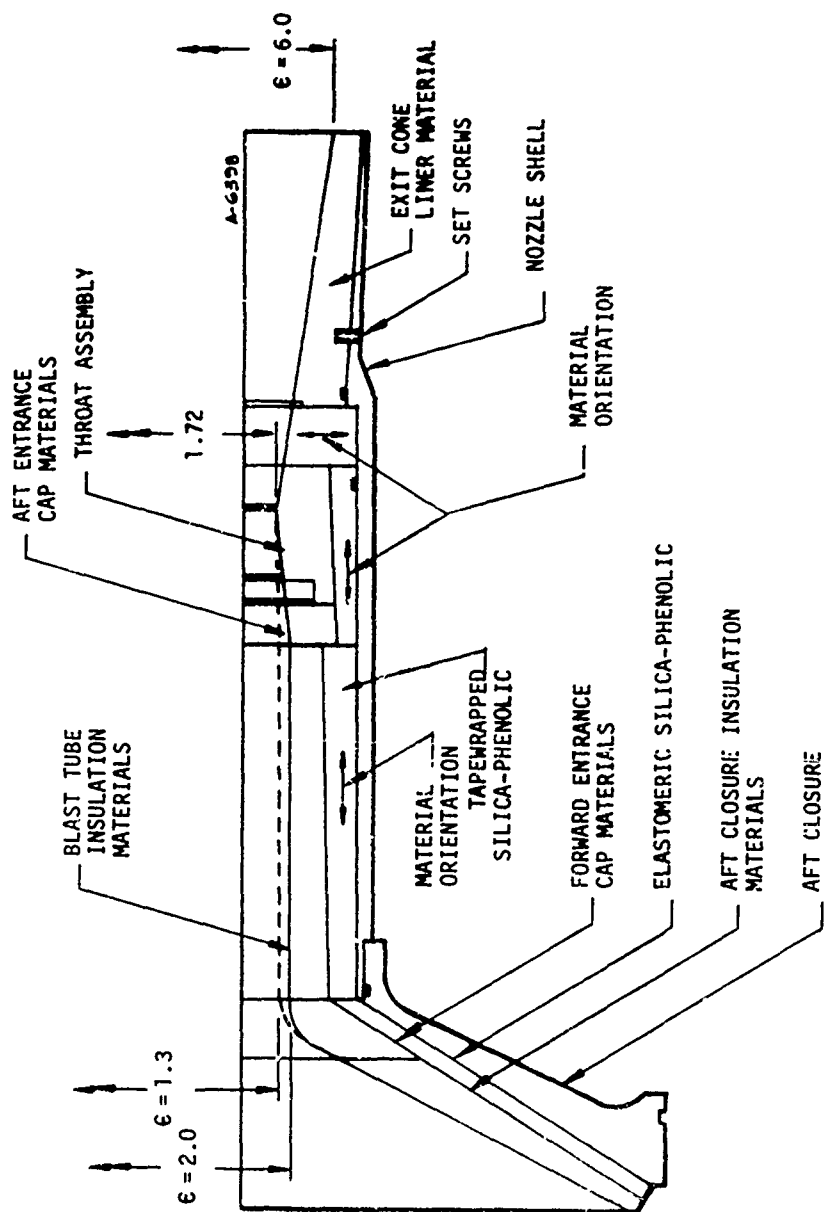


Figure 3-1. Blast Tube Nozzle Design

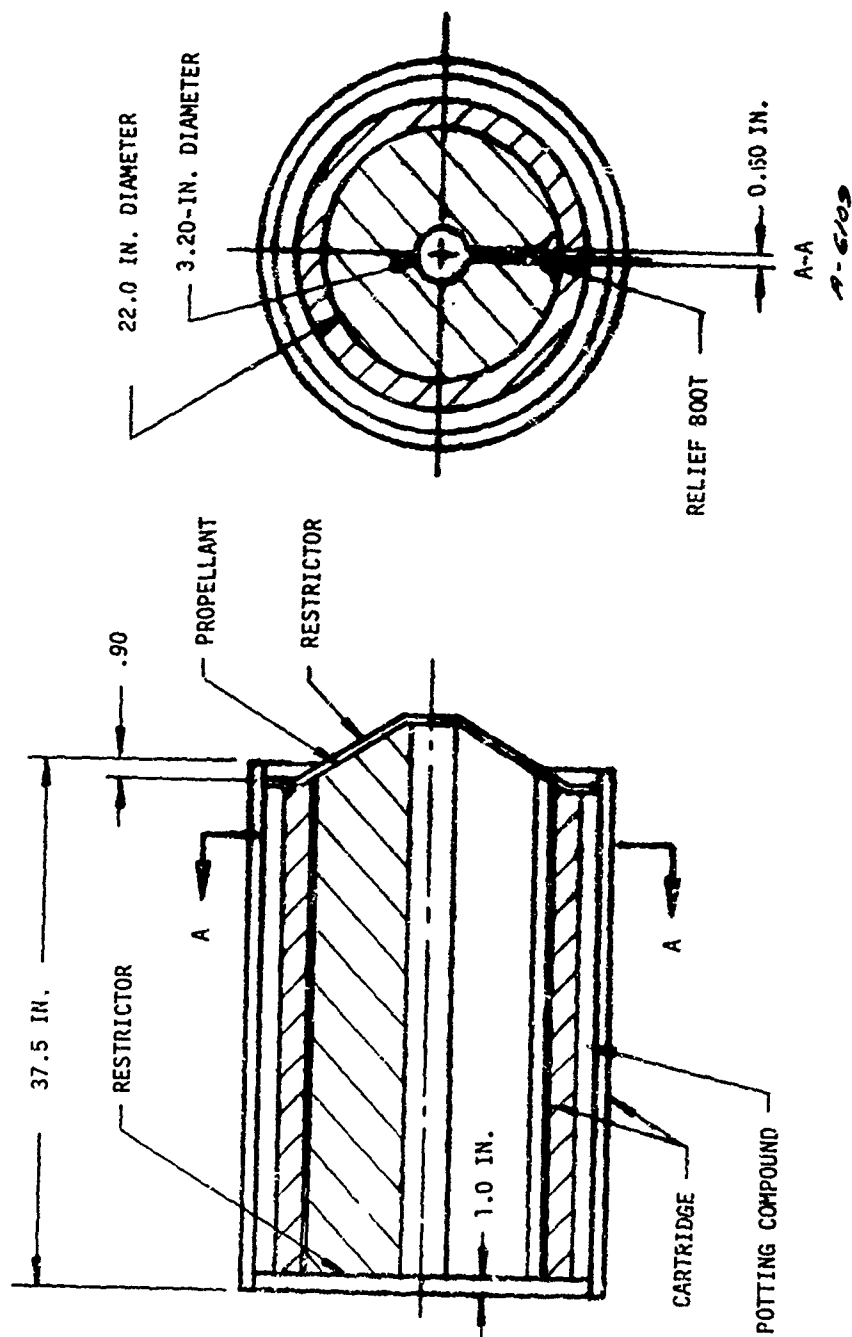


FIGURE 3-2. LOADED PROPELLANT CARTRIDGE - SLOTTED GRAIN

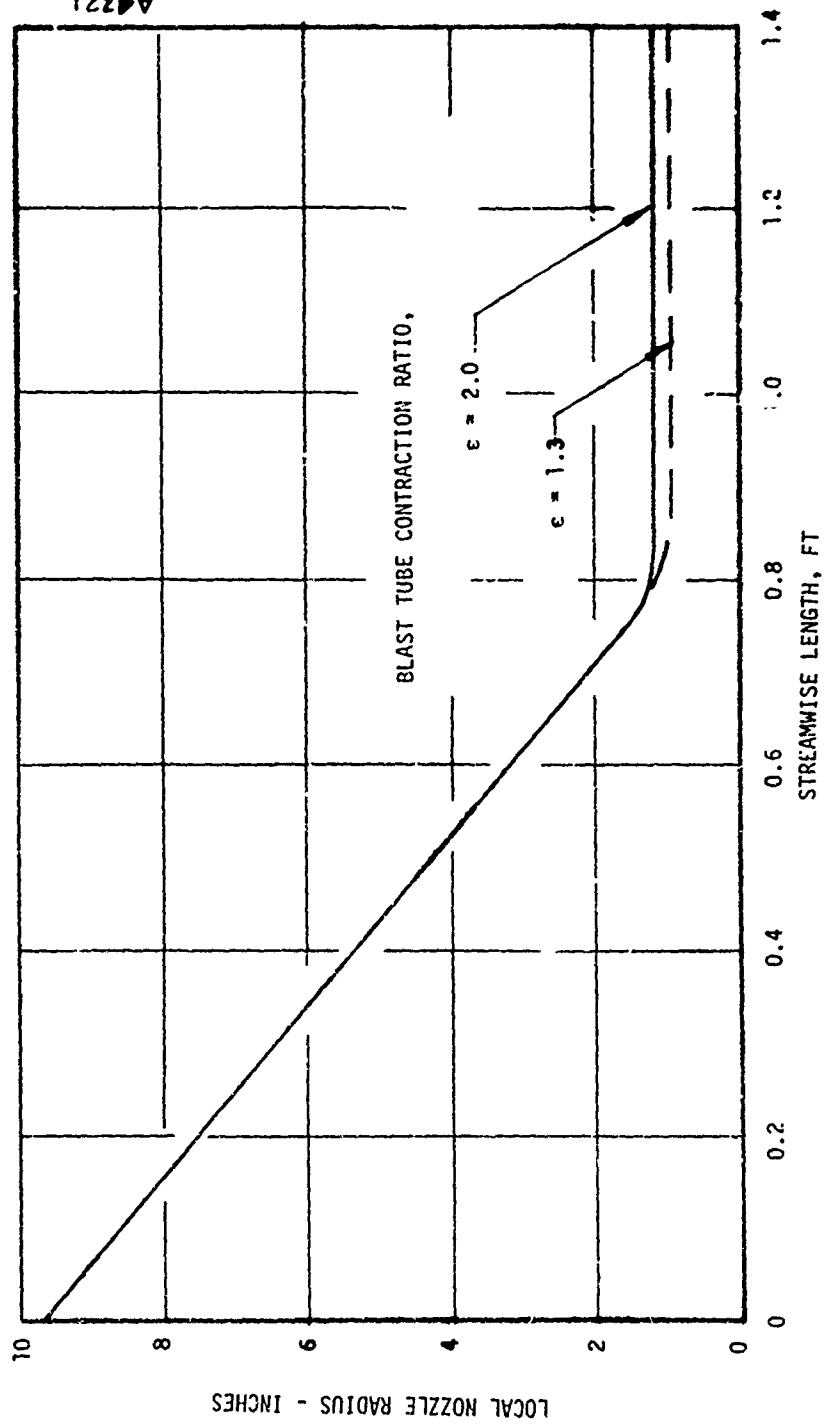


FIGURE 3-3. BLAST TUBE NOZZLE RADIUS VERSUS BOUNDARY LAYER STREAMWISE LENGTH  
A) AFT CLOSURE AND BLAST TUBE ENTRANCE



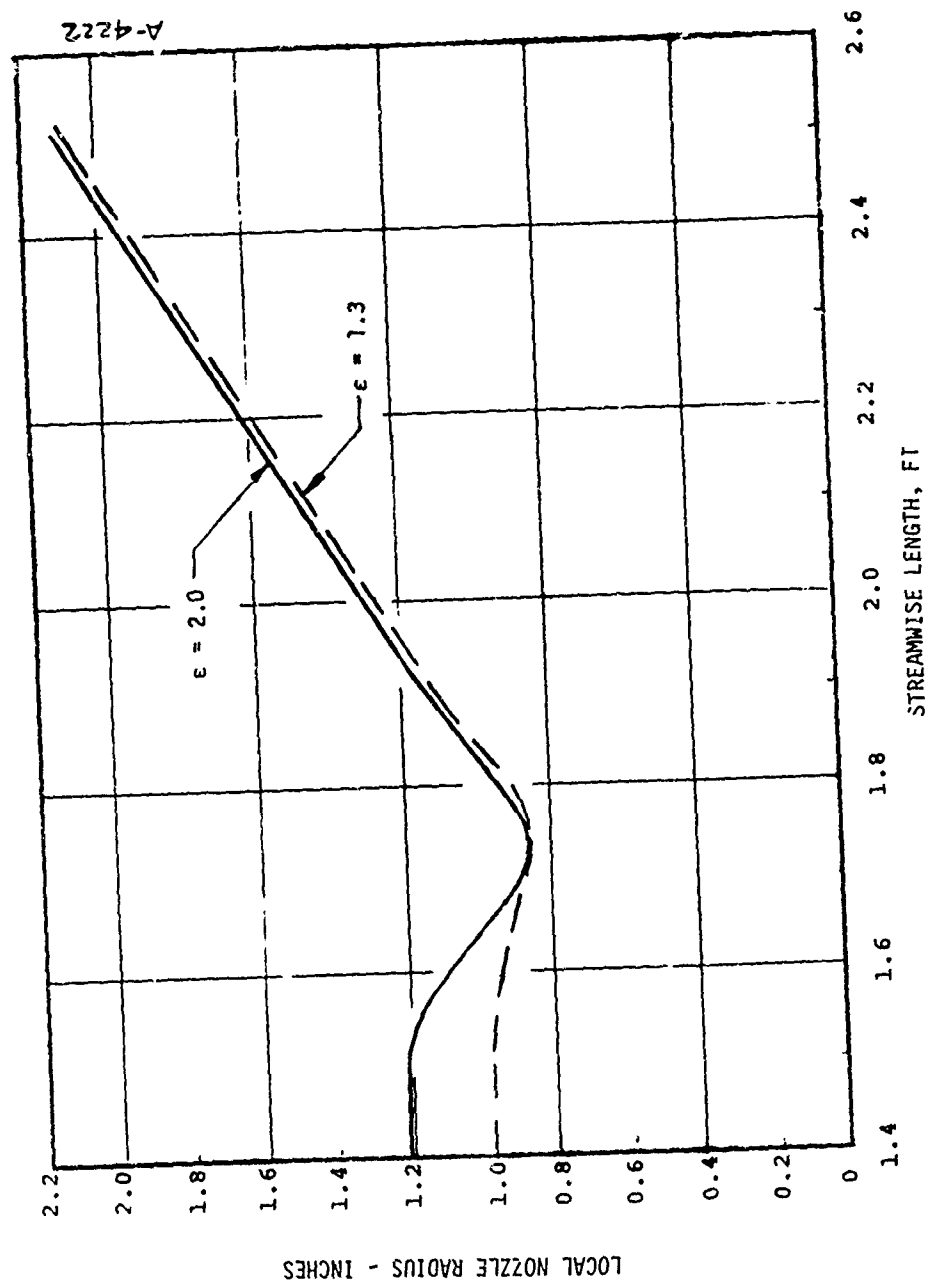


FIGURE 3-3. (CONCLUDED)  
B) THROAT PACKAGE AND EXIT CONE

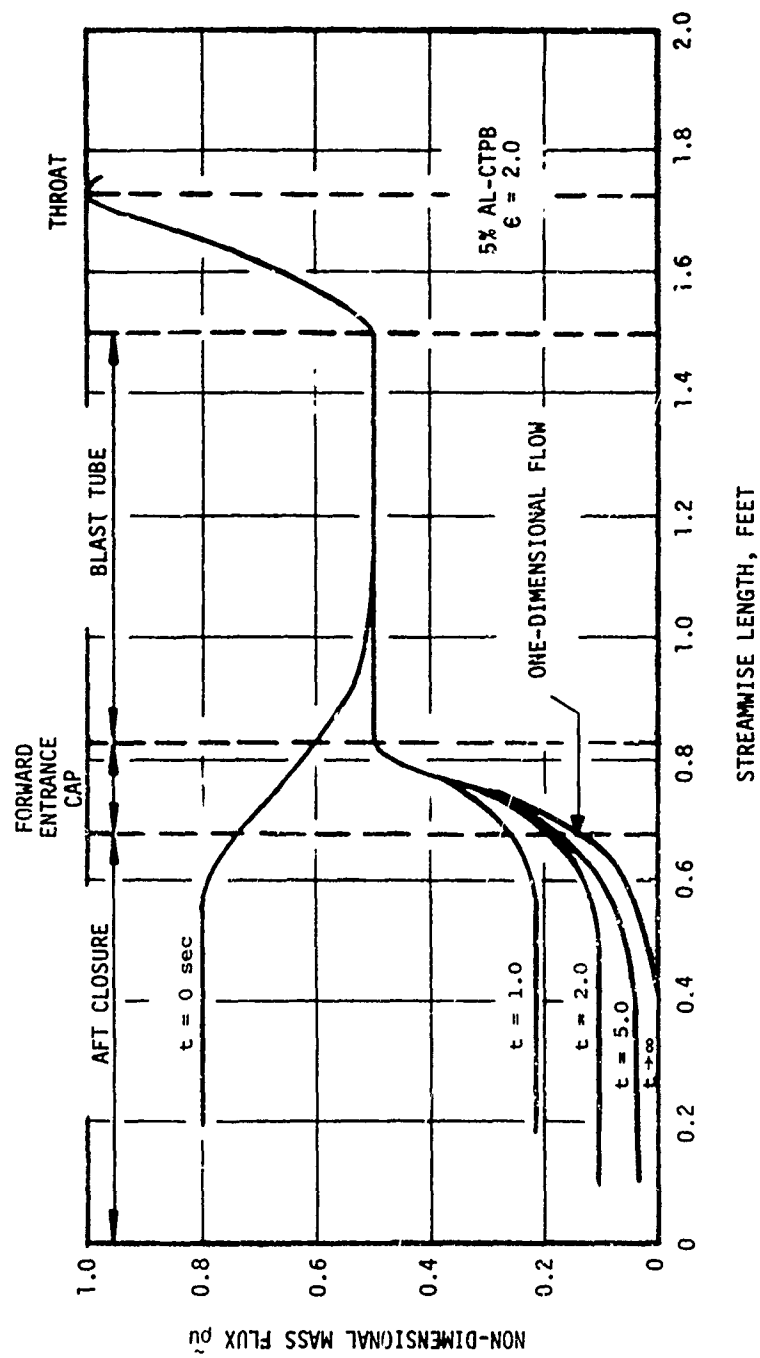


FIGURE 3-4. VARIATION OF NON-DIMENSIONAL FLOW PARAMETER WITH  
BOUNDARY LAYER RUNNING LENGTH FOR THE SLOTTED GRAIN  
A) BLAST TUBE AREA RATIO  $\approx 2.0$ , SLOT PLANE

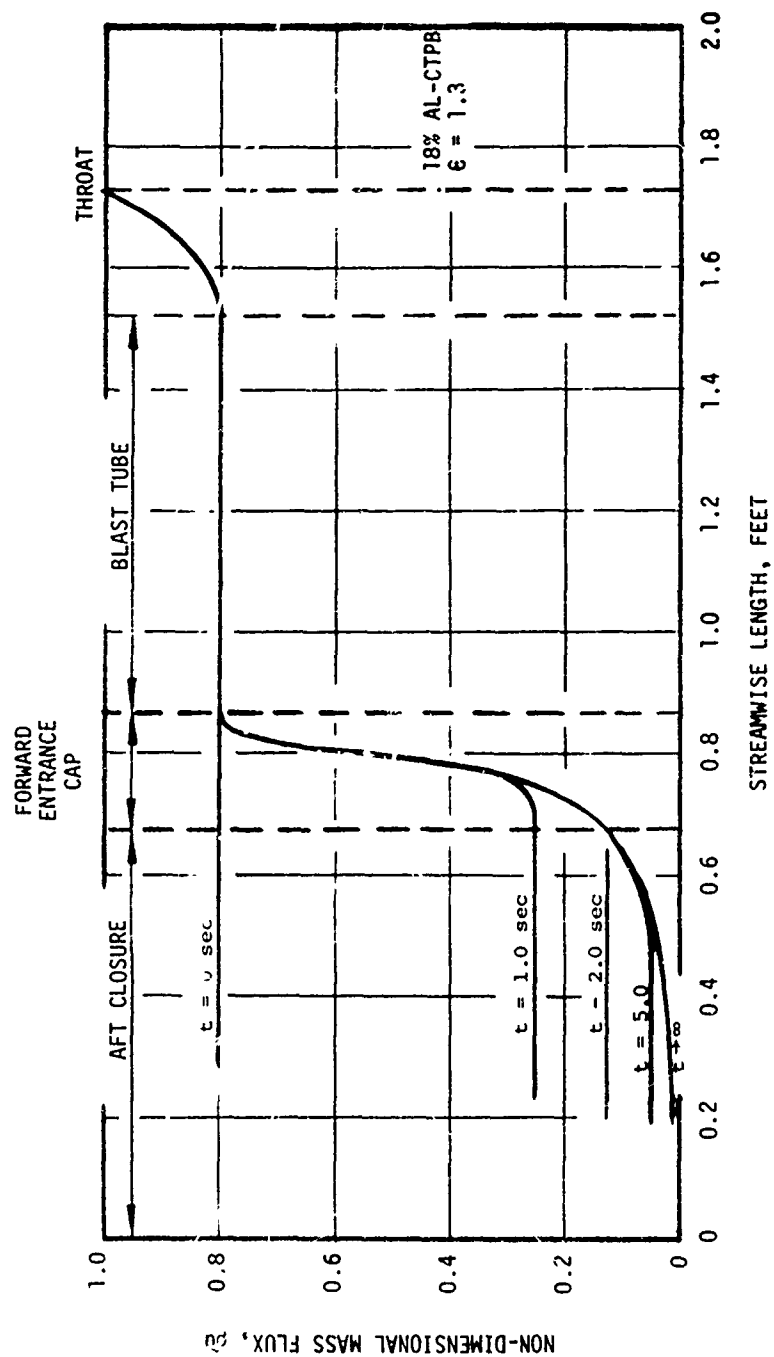


FIGURE 3-4. CONTINUED  
 B) BLAST TUBE AREA RATIO = 1.3, SLOT PLANE

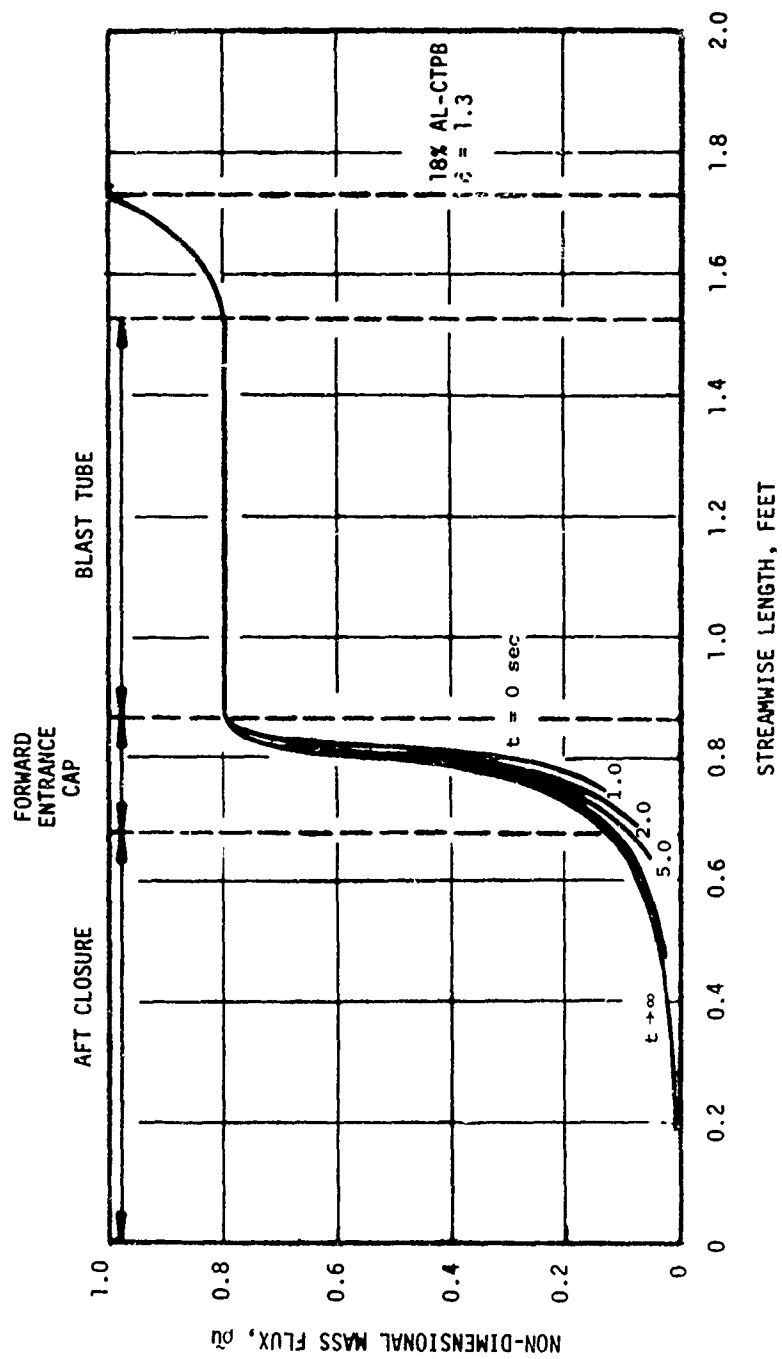


FIGURE 3-4. CONTINUED  
C) BLAST TUBE AREA RATIO = 1.3, OPPOSITE  
SLOT PLANE

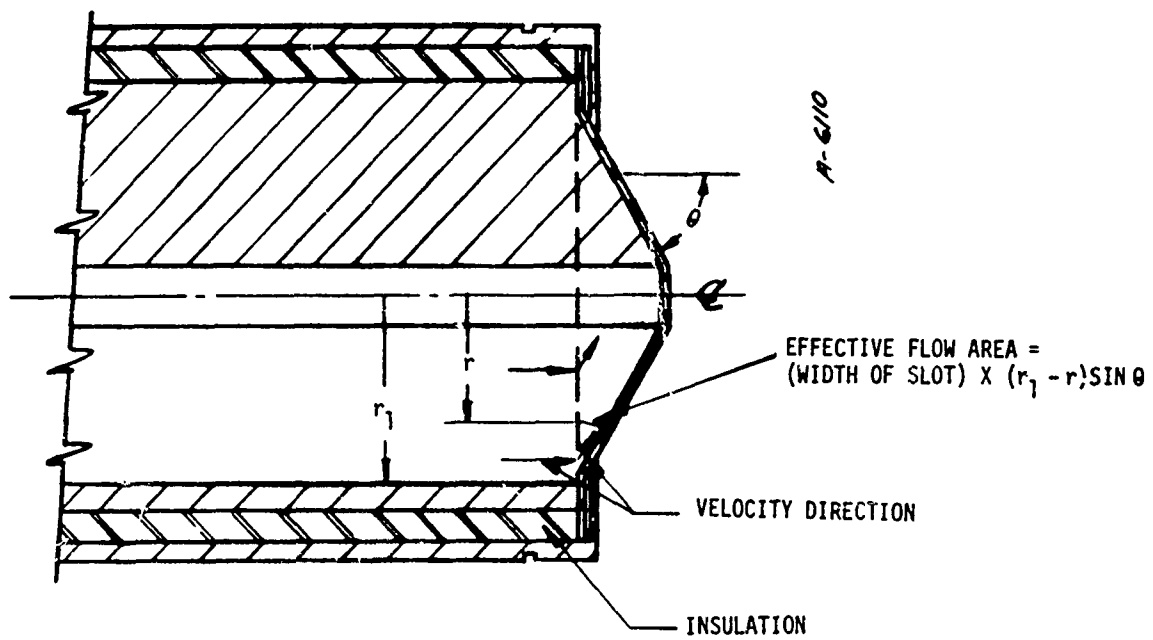


FIGURE 3-5. DEFINITION OF EFFECTIVE FLOW AREA IN THE  
AFT CLOSURE - SLOTTED GRAIN CONFIGURATION

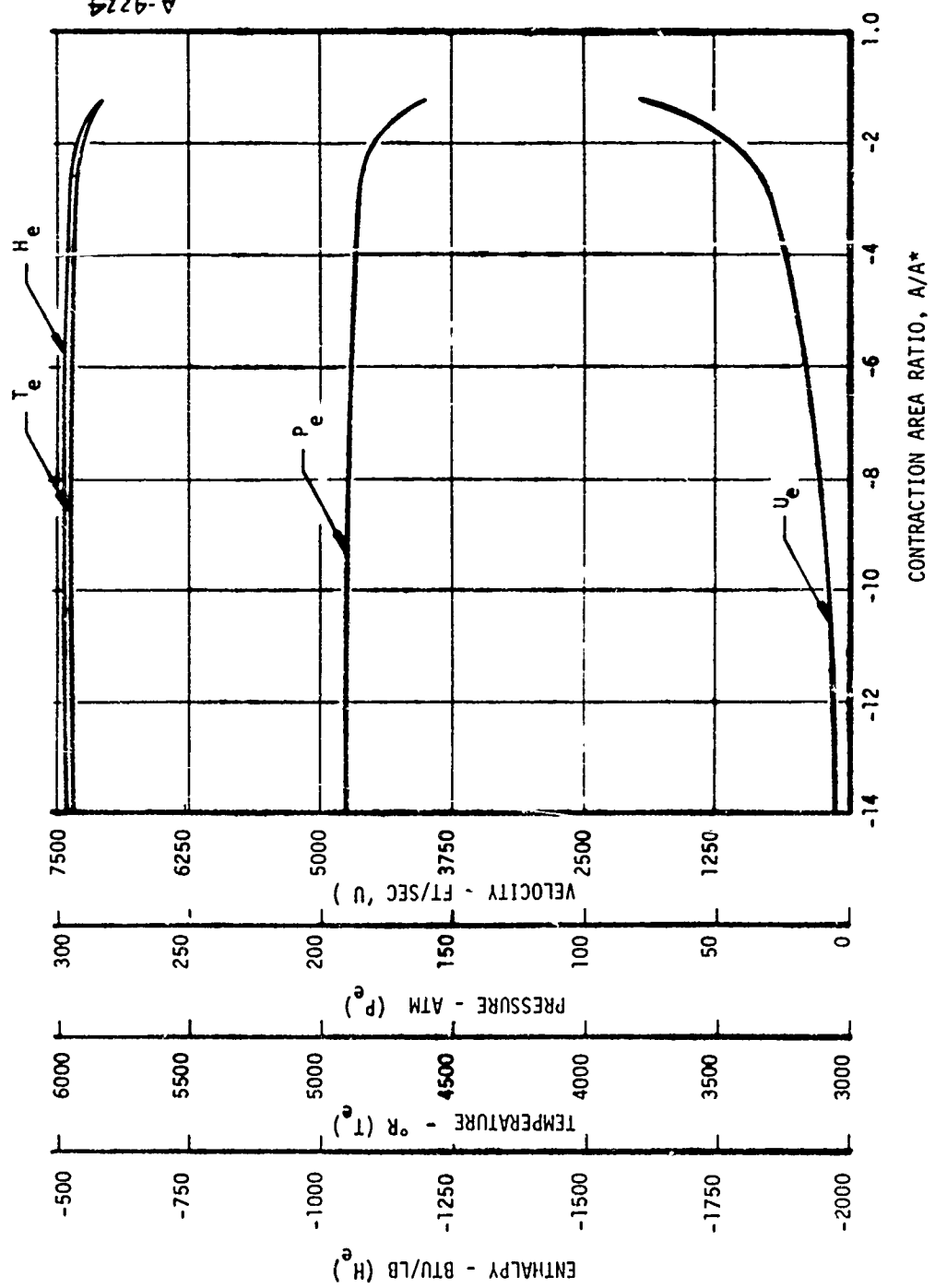


FIGURE 3-6. ISENTROPIC EXPANSION PROPERTIES FOR 5 PERCENT AL-CTPB PROPELLANT  
A) AFT CLOSURE (SUBSONIC)

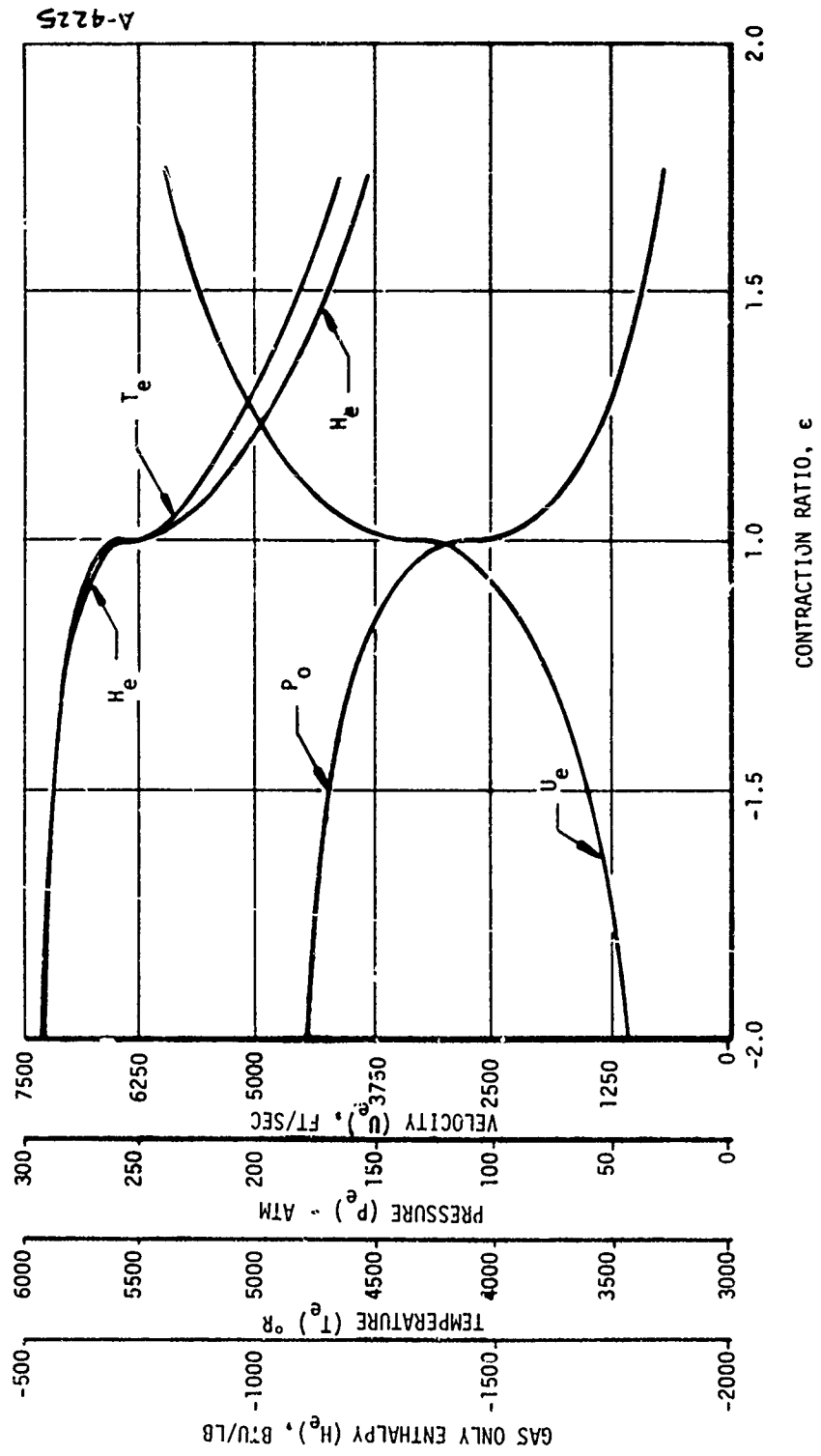


FIGURE 3-6. (CONTINUED)  
B) THROAT REGION

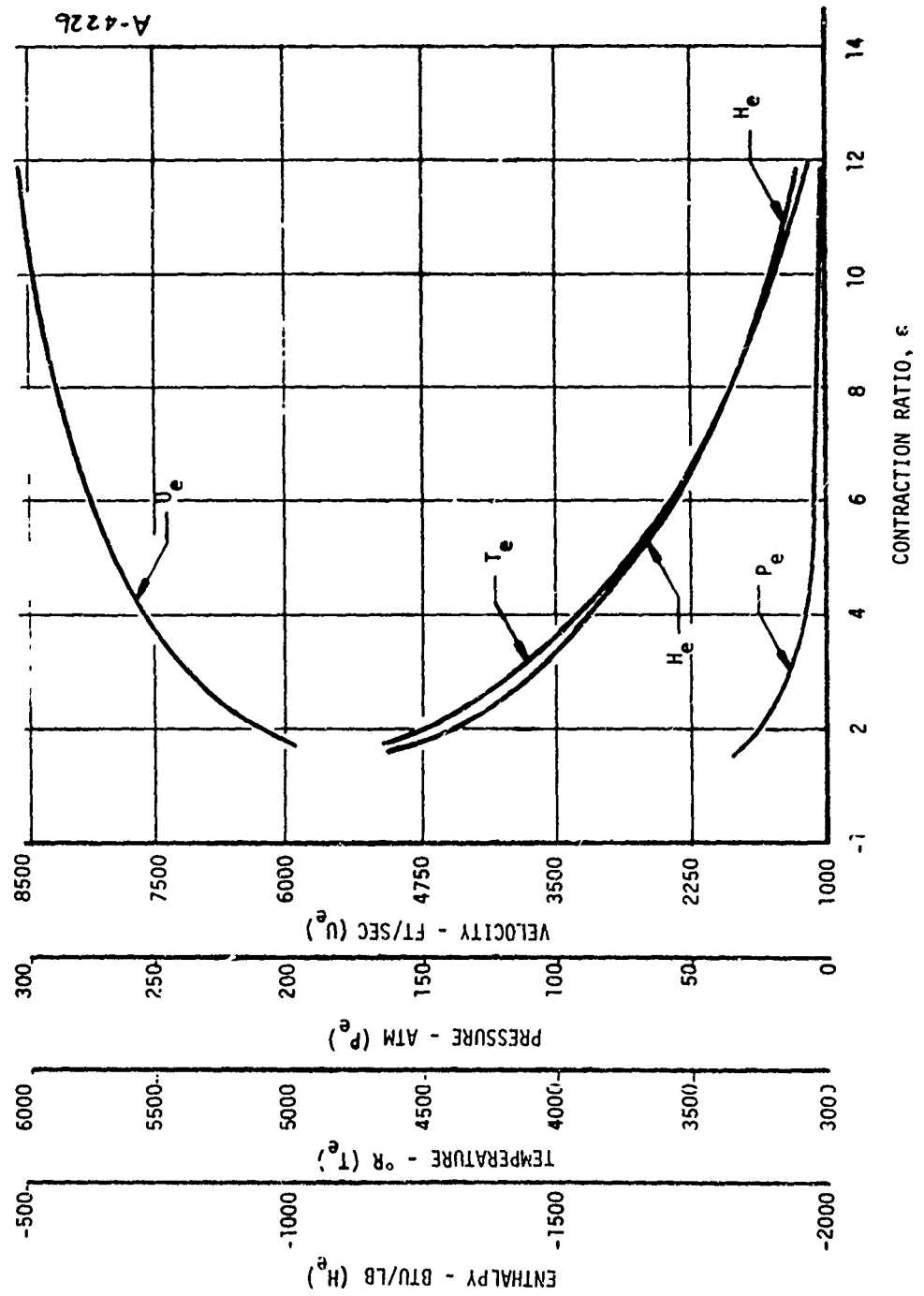


FIGURE 3-6. (CONCLUDED)  
C) EXIT CONE (SUPERSONIC)



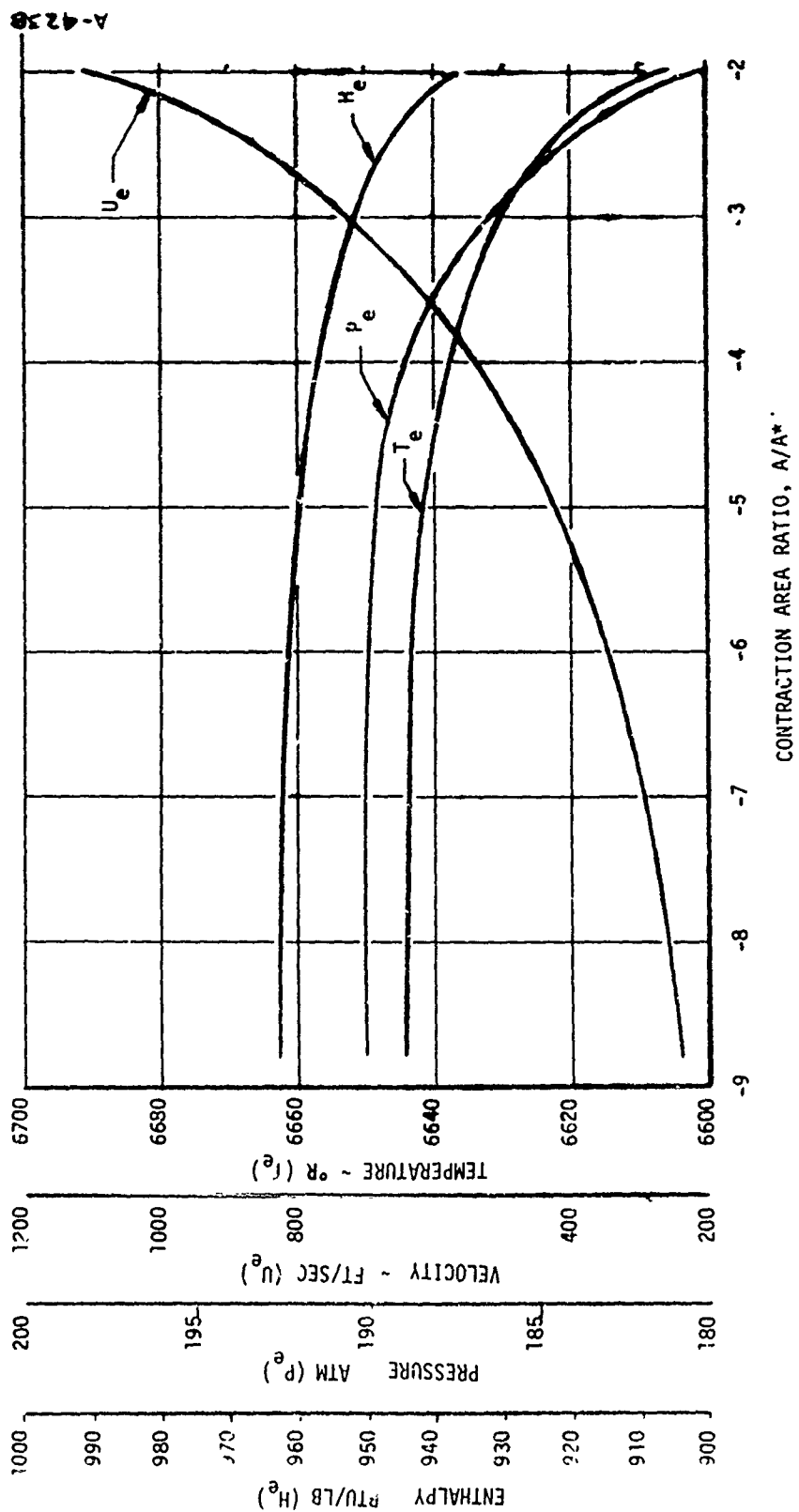


FIGURE 3-7. ISENTROPIC EXPANSION PROPERTIES OF 18 PERCENT AL-CTPB PROPELLANT  
(A) AFT CLOSURE (SUBSONIC)

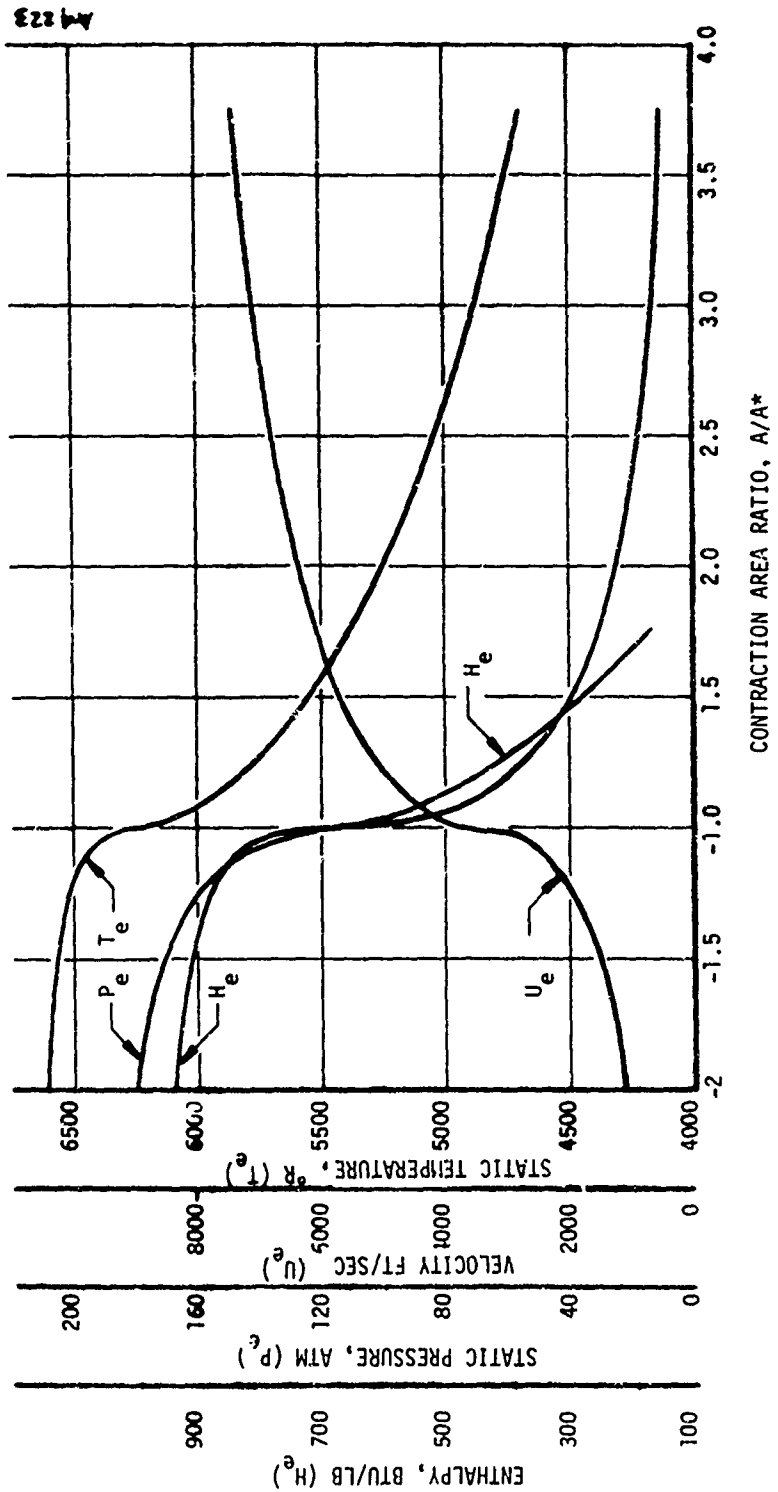


FIGURE 3-7. (CONTINUED)  
B) THROAT REGION

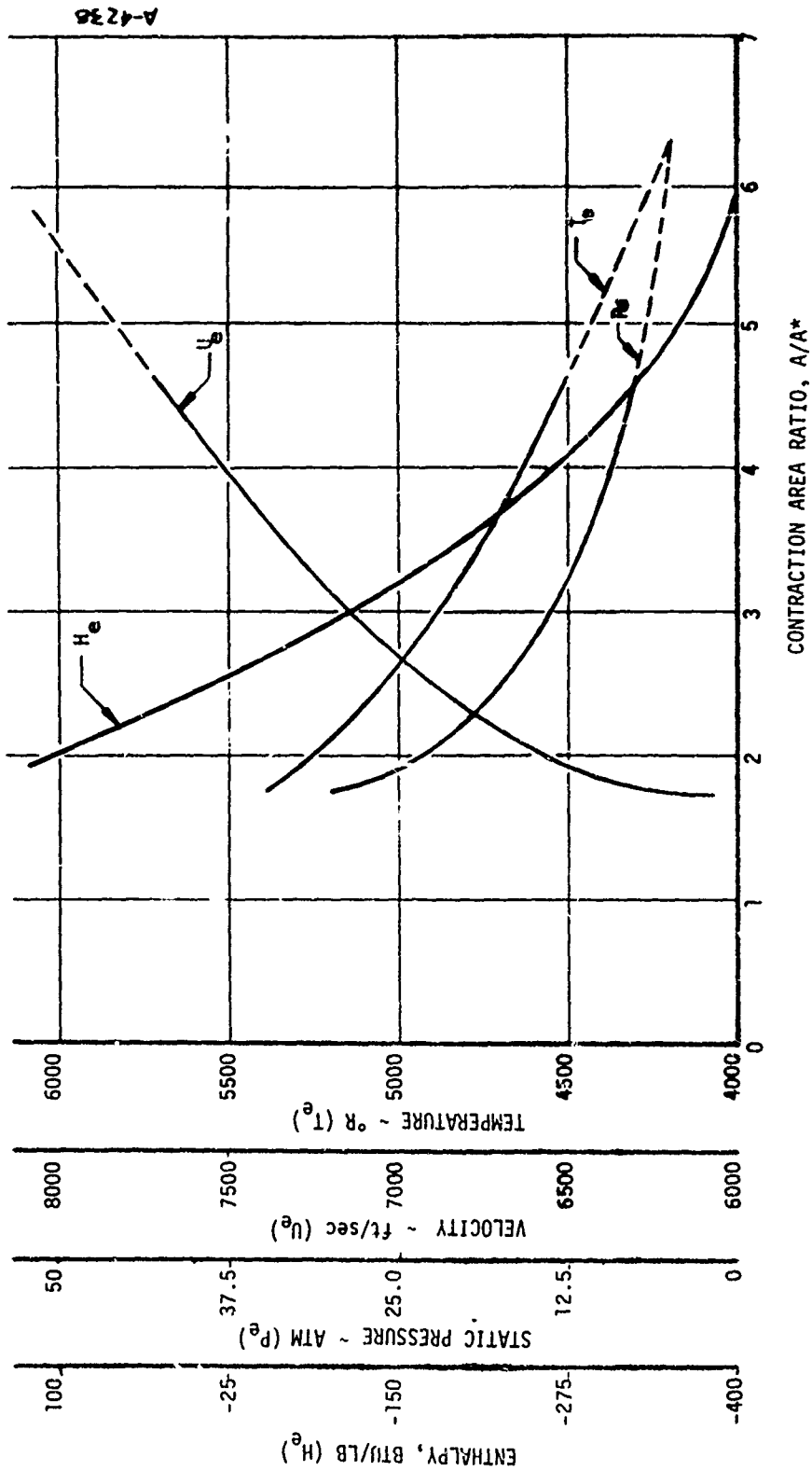


FIGURE 3-7. (CONCLUDED)  
C) EXIT CONE (SUPERSONIC)

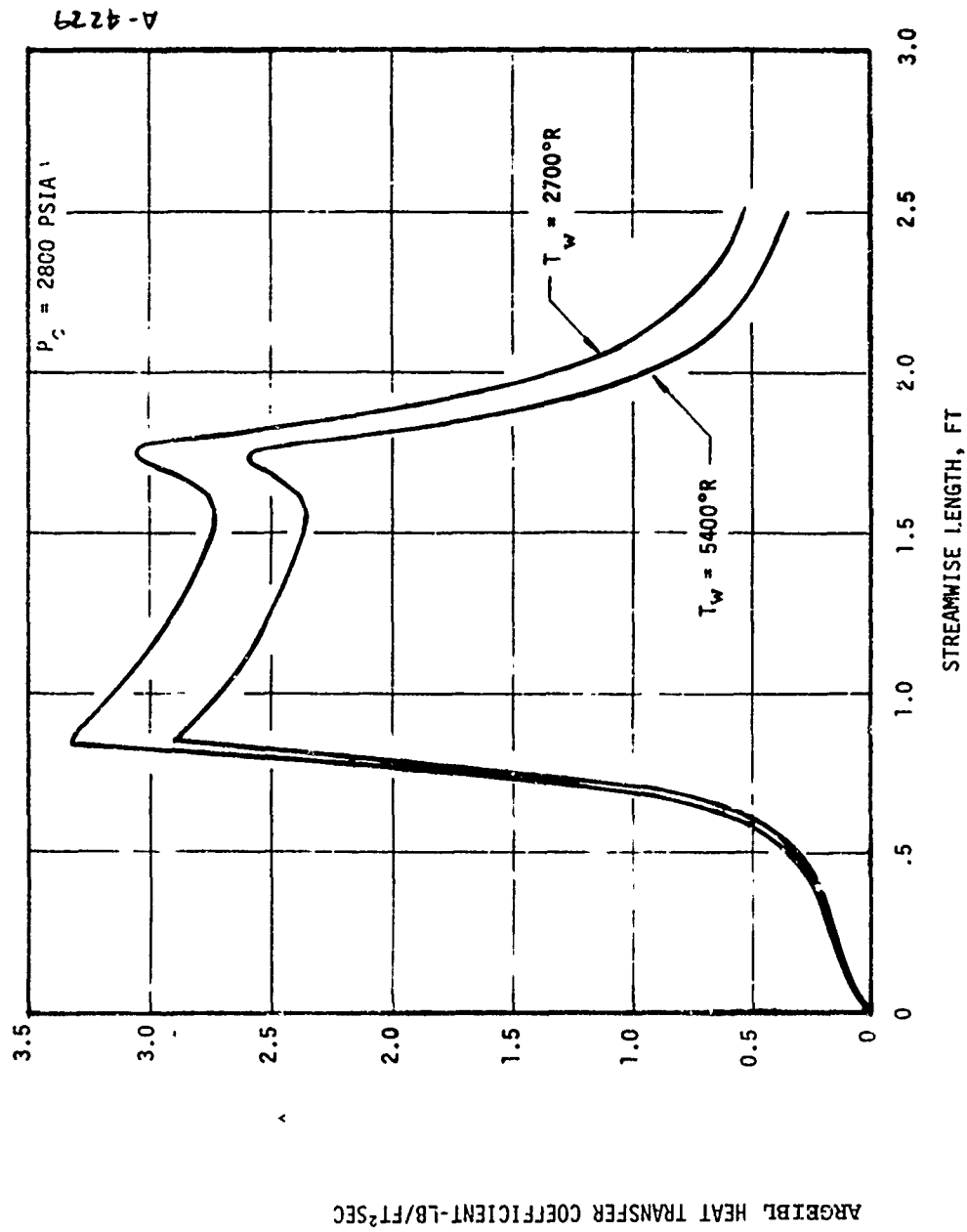


FIGURE 3-8. HEAT TRANSFER DISTRIBUTIONS FOR 5 PERCENT AL-CTPB PROPELLANT  
A) BLAST TUBE CONTRACTION RATIO = 1.3

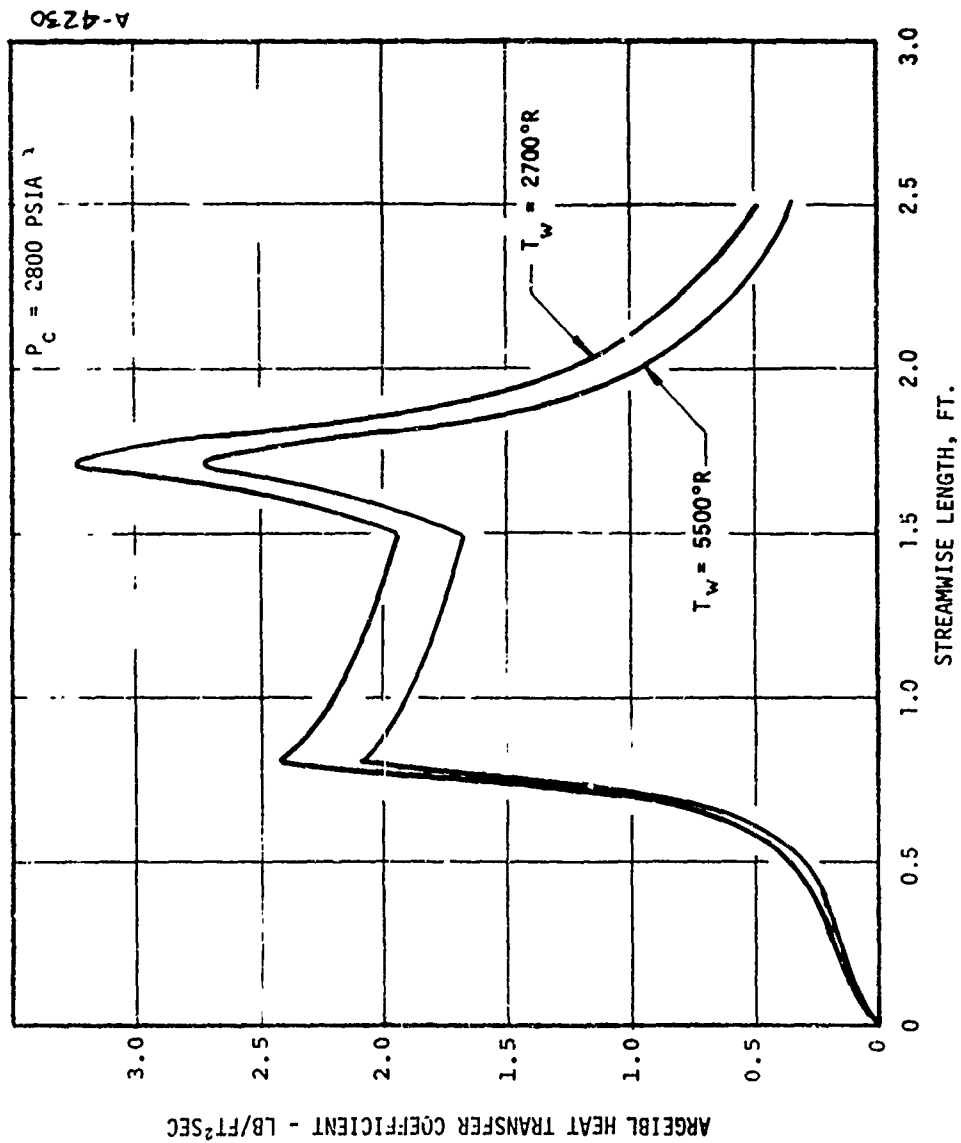


FIGURE 3-8. (CONCLUDED)  
B) BLAST TUBE CONTRACTION RATIO = 2.0

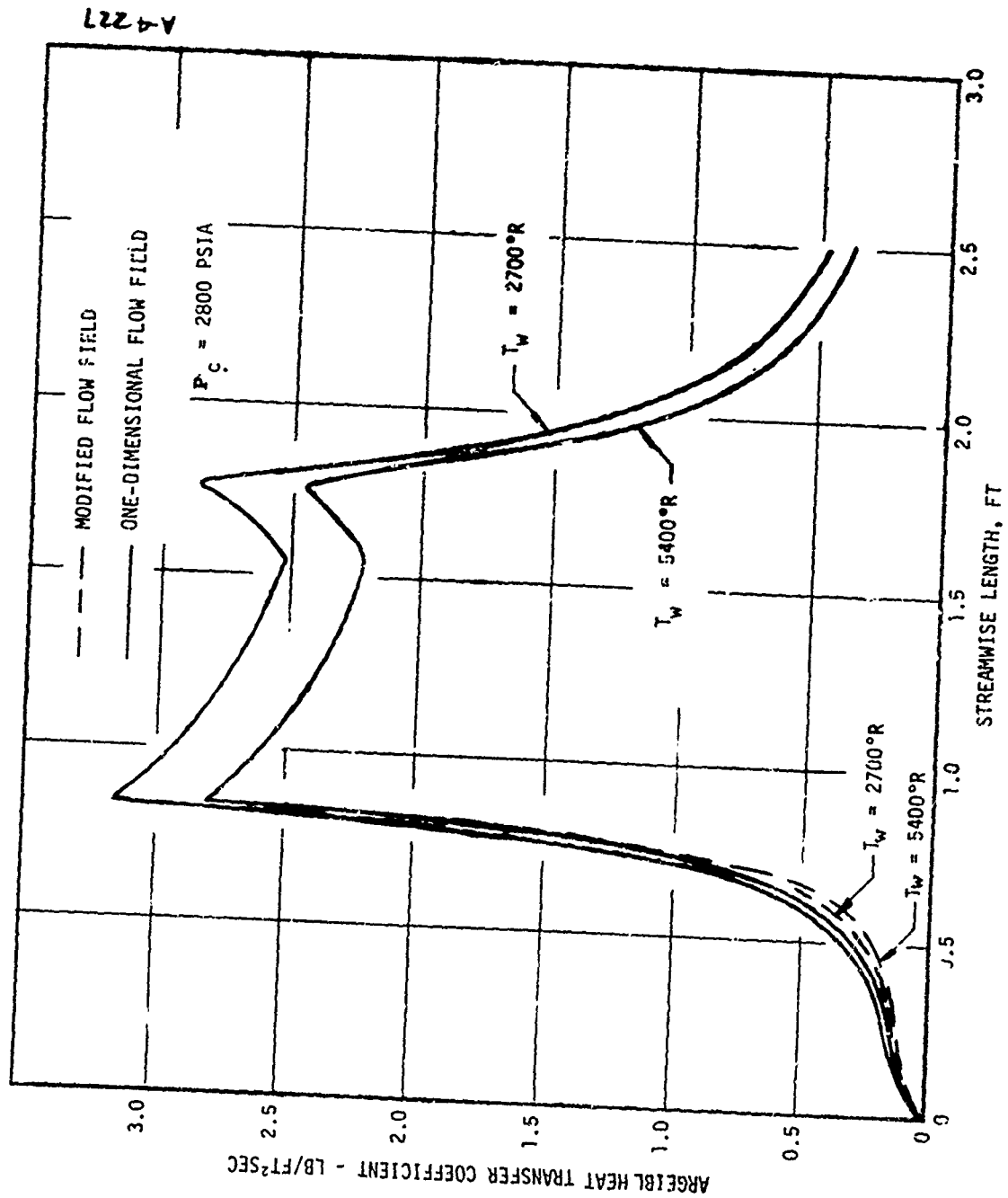


FIGURE 3-9. HEAT TRANSFER DISTRIBUTIONS FOR 18 PERCENT AL-CTPB PROPELLANT  
A) BLAST TUBE CONTRACTION RATIO = 1.3

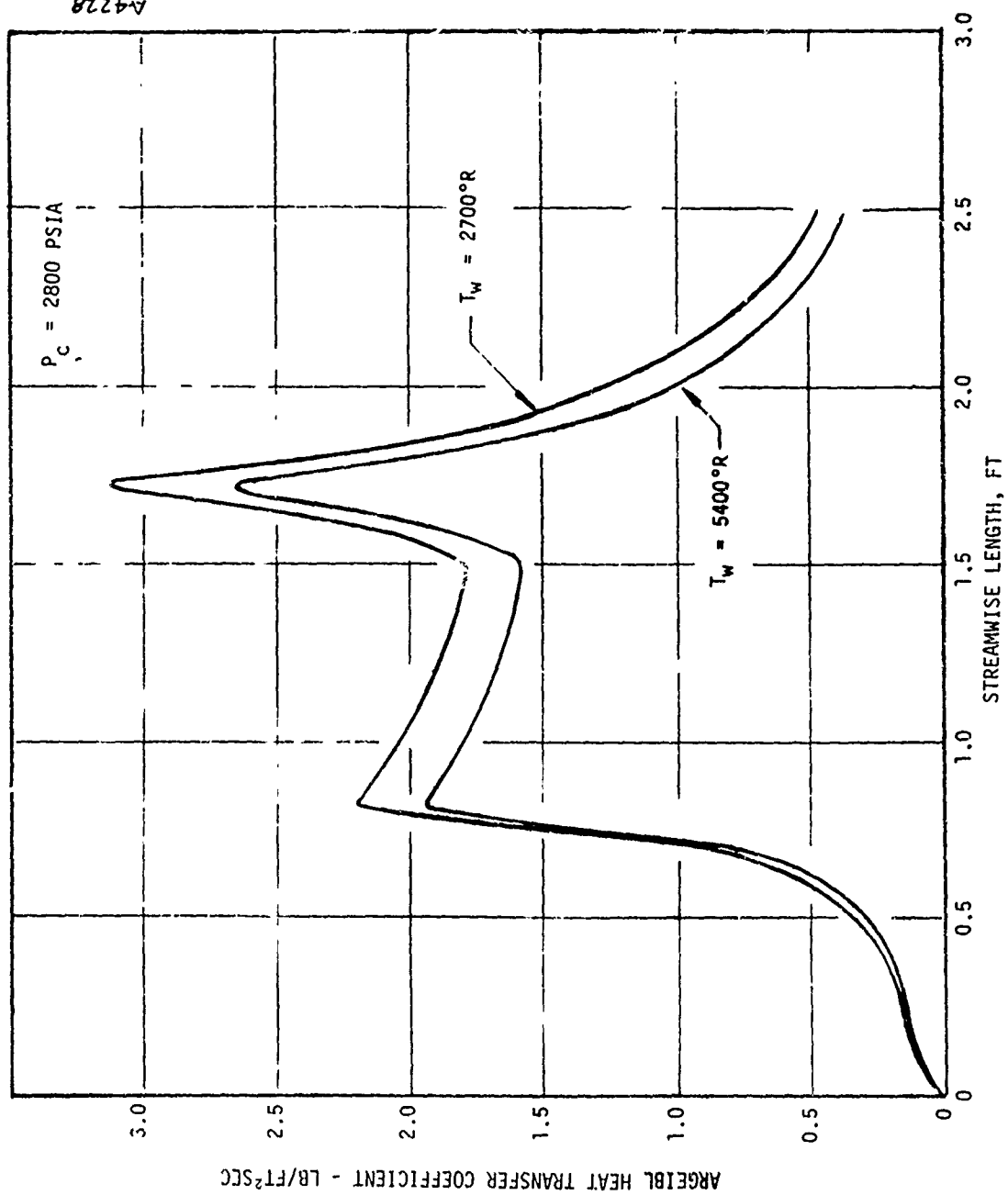


FIGURE 3-9. (CONCLUDED)  
 B) BLAST TUBE CONTRACTION RATIO = 2.0

A4228

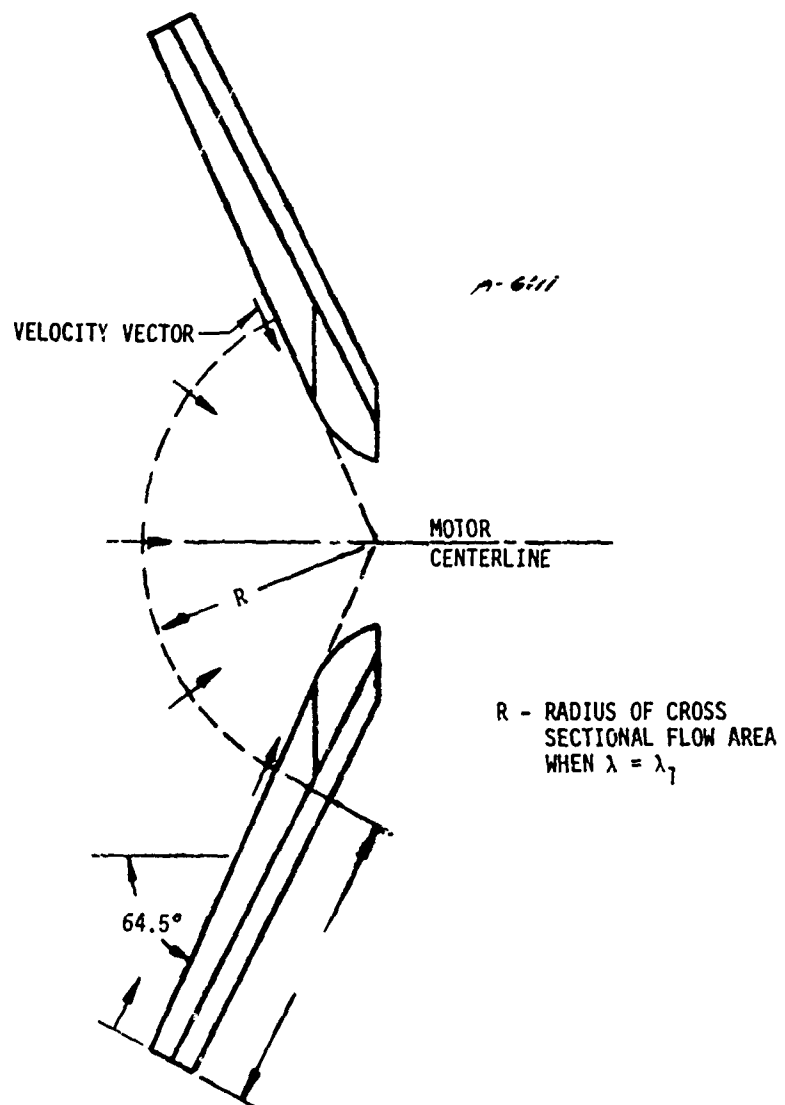


FIGURE 3-10. AFT CLOSURE CROSS SECTIONAL AREA FOR MODIFIED FLOW FIELD ANALYSIS



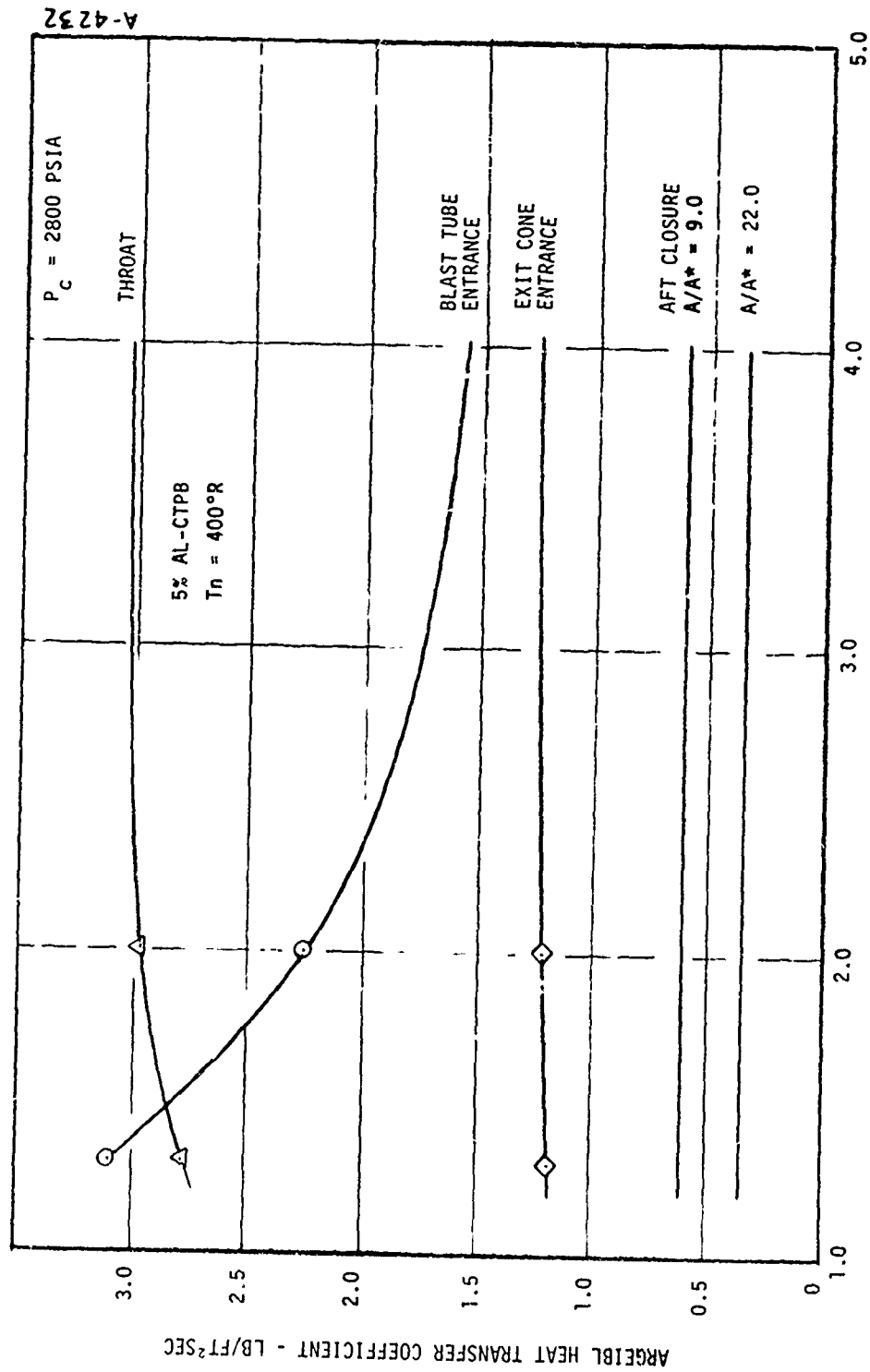


FIGURE 3-11. VARIATION OF ARGEIBL HEAT TRANSFER COEFFICIENT WITH BLAST TUBE AREA RATIO AT SEVERAL NOZZLE LOCATIONS  
A) 5 PERCENT AL-CTPB PROPELLANT

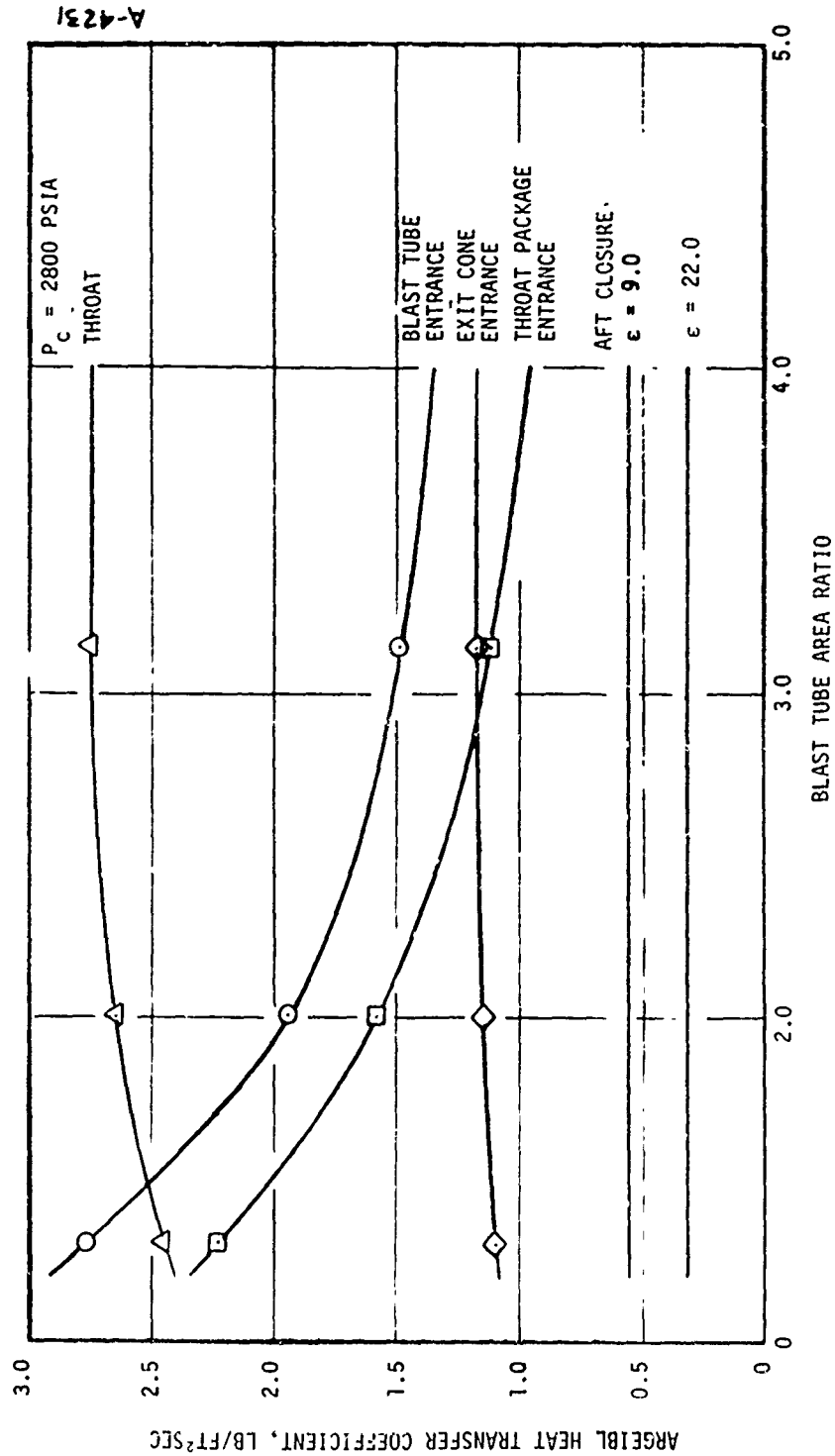


FIGURE 3-11. (CONCLUDED)  
B) 18 PERCENT AL-CTPB PROPELLANT,  $T_w = 5400^\circ R$

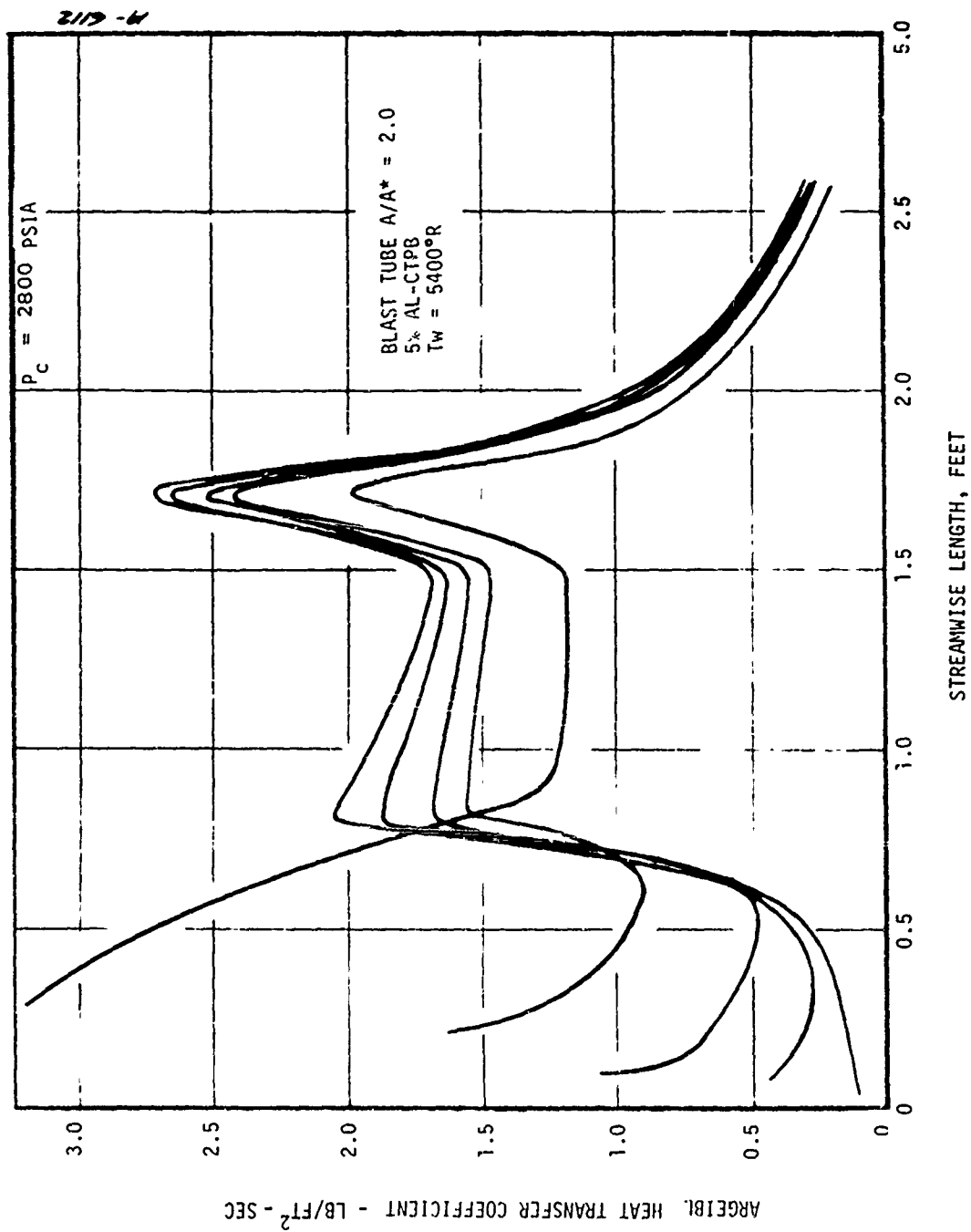


FIGURE 3-12. HEAT TRANSFER DISTRIBUTIONS FOR THE SLOTTED GRAIN PORT AT VARIOUS TIMES AFTER START-UP

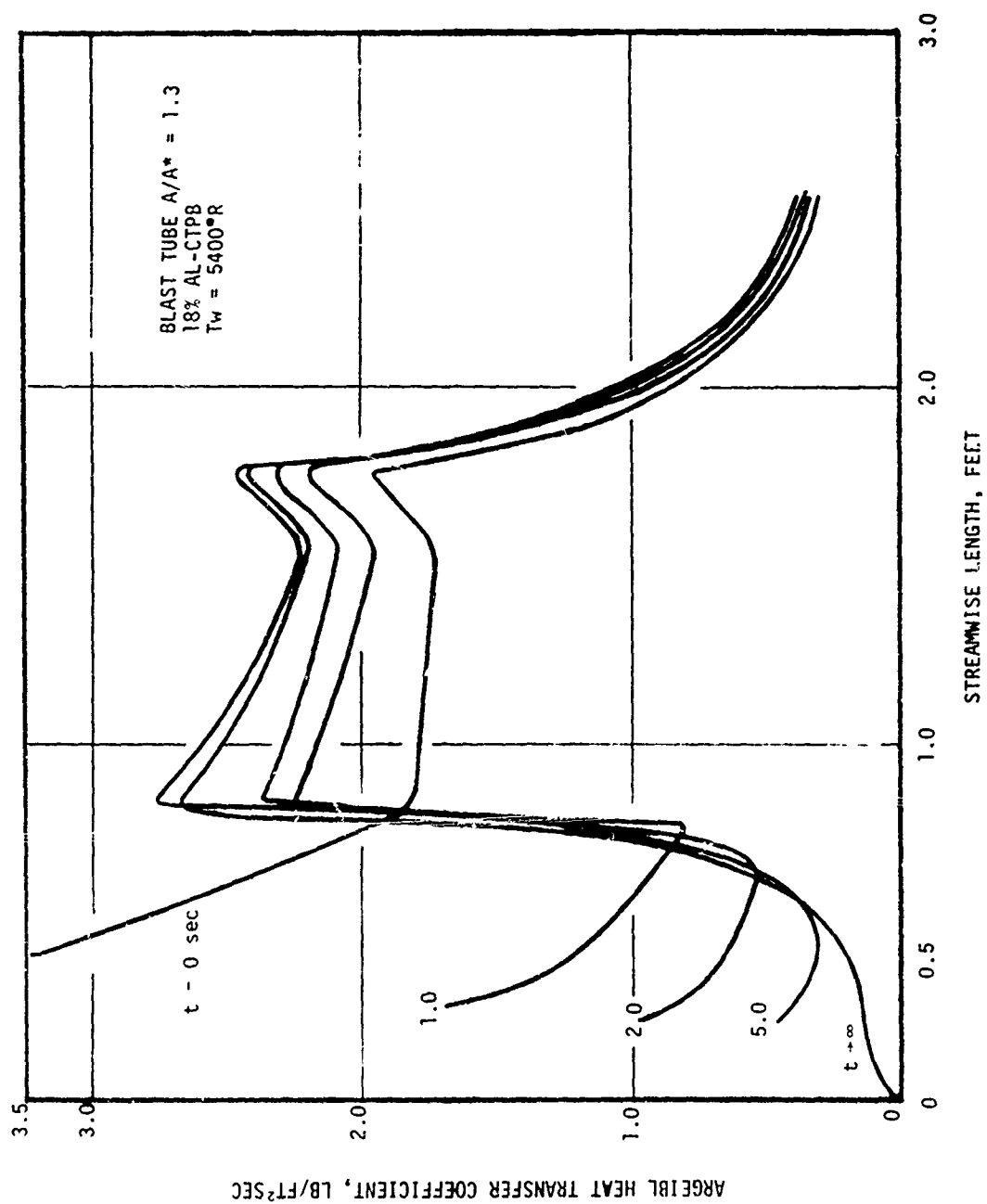


FIGURE 3-13. HEAT TRANSFER DISTRIBUTIONS FOR THE SLOTTED GRAIN  
 PORT AT VARIOUS TIMES AFTER STARTUP  
 A) IN CIRCUMFERENTIAL PLANE WITH SLOT

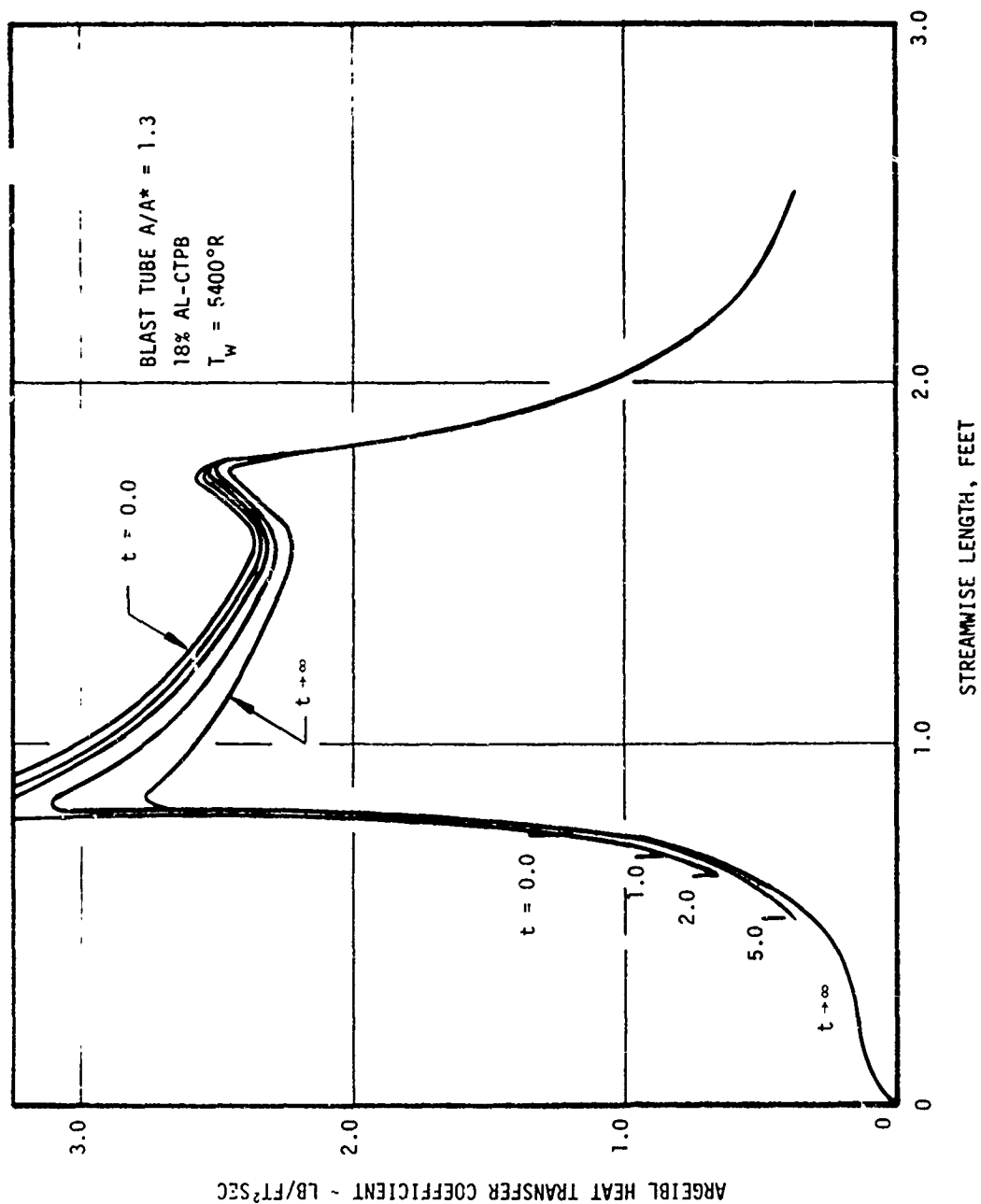


FIGURE 3-13. CONCLUDED.  
 B) IN OPPOSITE CIRCUMFERENTIAL PLANE FROM SLOT

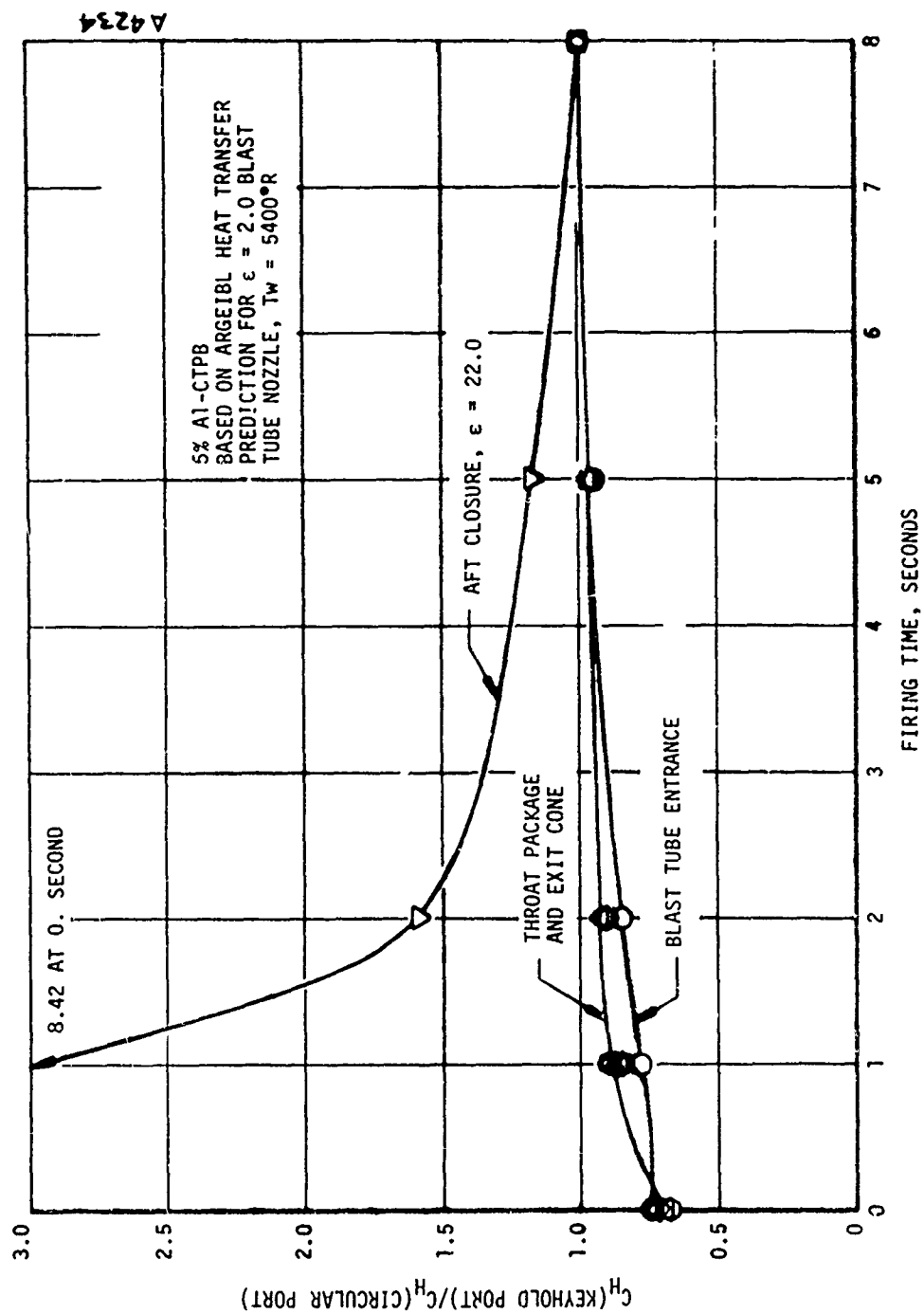


FIGURE 3-14. EFFECT OF KEYHOLE PORT FLOW ON HEAT TRANSFER TO VARIOUS LOCATIONS OF THE BLAST TUBE NOZZLE (PLANE OF SLOT)

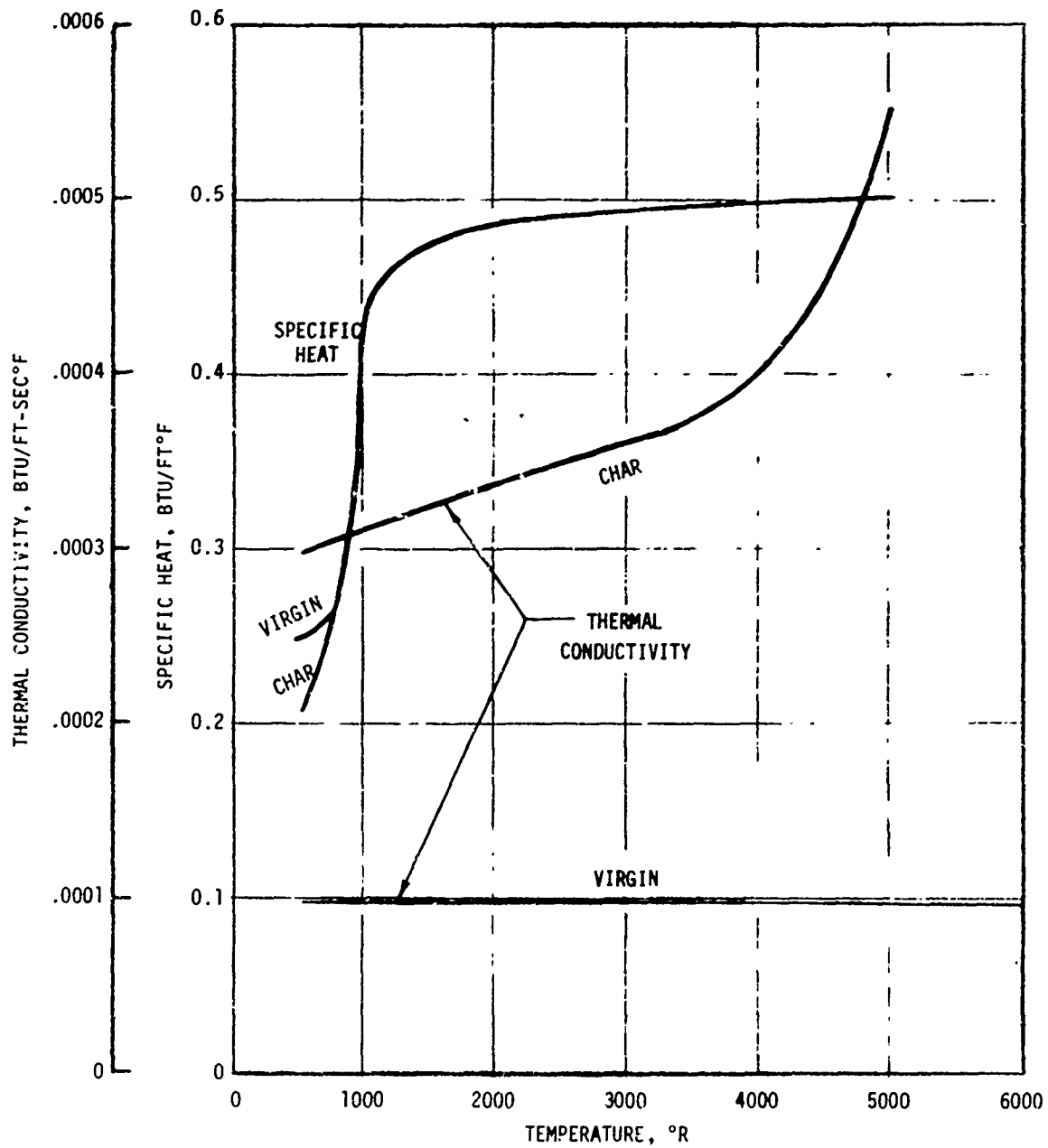


FIGURE 3-15. ESTIMATED THERMAL PROPERTIES OF MX2625 SILICA PHENOLIC

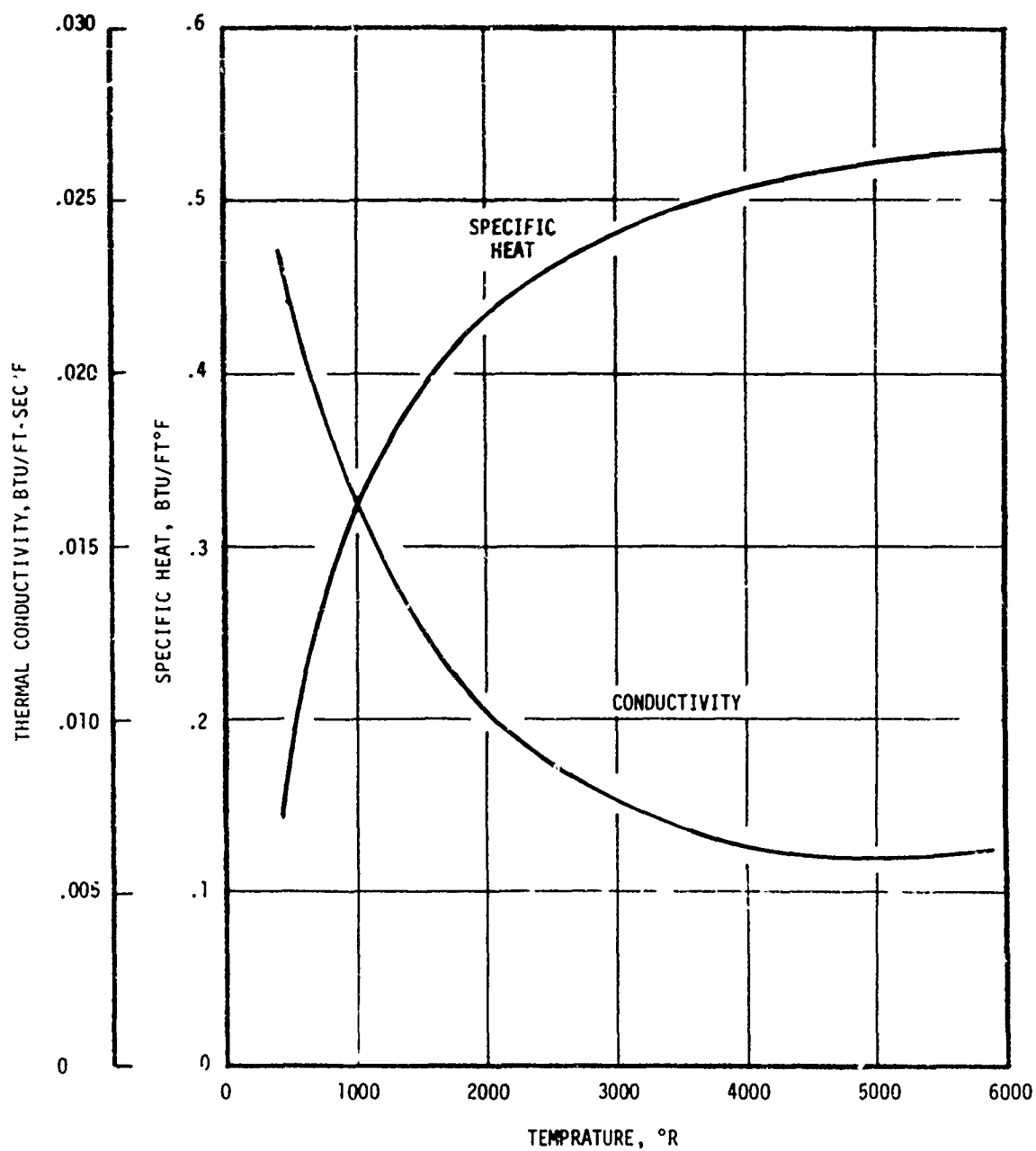


FIGURE 3-16. ESTIMATED THERMAL PROPERTIES OF PYCOBOND 410-65



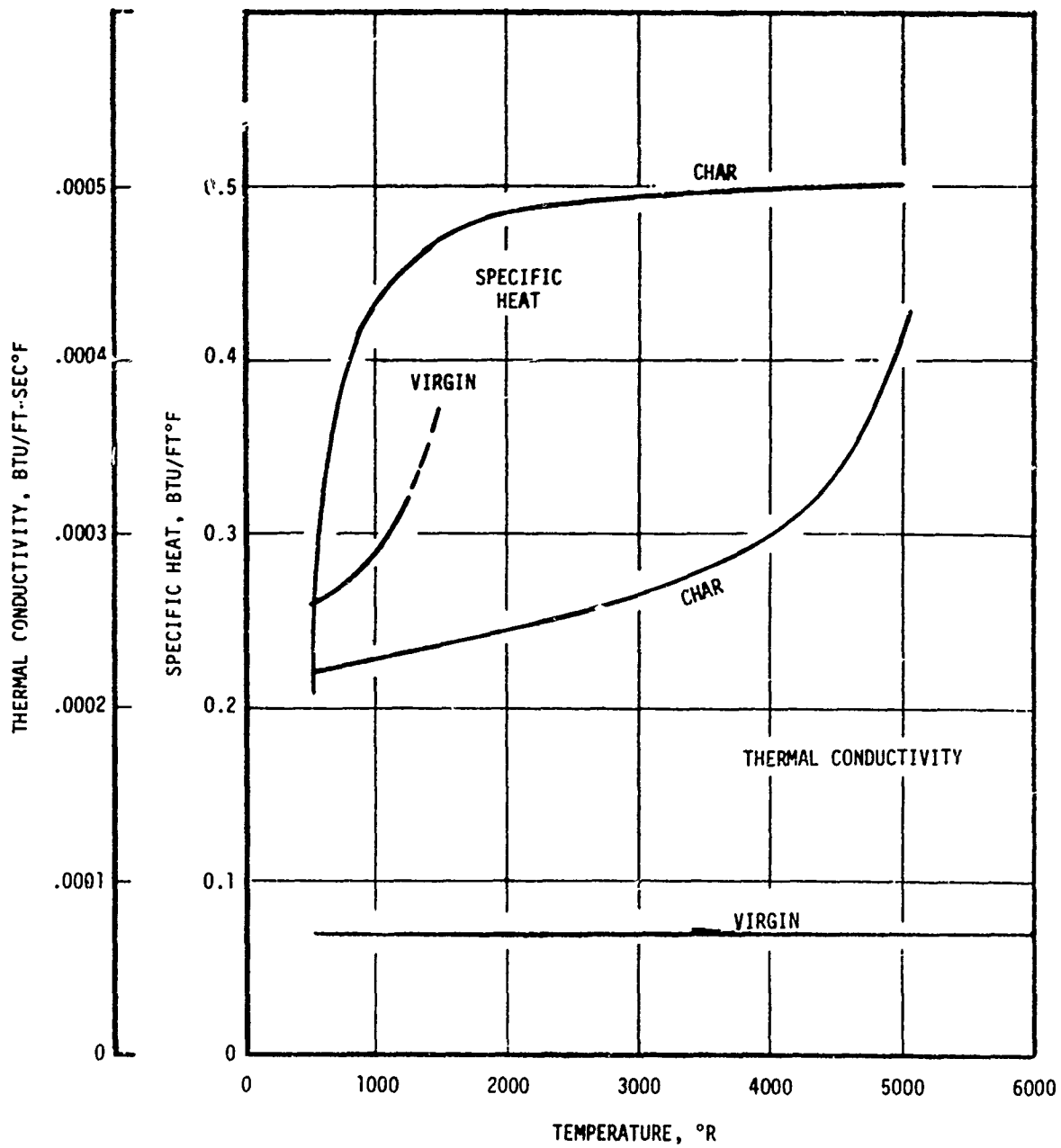


FIGURE 3-17. ESTIMATED THERMAL PROPERTIES FOR DUREZ 16771-1

## SECTION 4

### THERMOCHEMICAL SCREENING ANALYSIS AND IN-DEPTH THERMAL ANALYSIS

The objective of the thermochemical screening analysis was to predict the surface recession rate and surface temperature for classes\* of materials when subjected to the high chamber pressure environment. As described in Section 2, this screening is performed by coupling of the ACE program to a steady state energy balance solution (SSA computer program). This calculation does not require a knowledge of the material thermal properties because of the steady state assumption, but it does require a knowledge of the material chemical properties. The results of the thermochemical screening analysis provide a basis for ranking materials and also provide the surface boundary conditions for performing a conservative in-depth analysis. The parameters considered in the analysis, in addition to material class, were the aluminum loading fraction, the blast tube area ratio, the propellant grain configuration, and the nozzle location.

In performing the thermochemical screening analysis, the candidate nozzle materials being considered for the high chamber pressure nozzle were divided into categories according to material class. In addition, a typical material was selected for each material class. The selection of candidate materials and the division of these materials into material classes were performed jointly by UTC and Aerotherm. Also, the nozzle location for each material class and the particular material within each class which was considered as typical were defined by this joint effort. The material classes considered, the nozzle location, and the typical material within each material class are presented in Table 4-1. In Table 4-2 both the material location and the propellant considered are defined. The approach taken was to first make simplified calculations to determine the steady state surface recession and surface temperature of each material to both the 5 and 18 percent Al-CTPB propellants for various area

---

\* The term "material class" refers to materials which are composed of similar reinforcements; thus, all carbon and graphite reinforced ablation materials would form one class and all silica reinforced materials would form another.

ratios within the nozzle section of interest. Given this information, an in-depth thermal analysis was made as to which material, propellant, and geometry provided the most severe thermal response in each of the three nozzle components of interest: the aft closure, the blast tube, and the exit cone. These analysis results which were obtained using option 2 of the CMA program provided a basis for establishing the material thickness requirements in the nozzle design.

As shown in Table 4-2, a transient CMA analysis was performed for the G-90 and Pyrostrand blast tube configurations. A transient analysis was required for these materials because the steady state assumption does not apply for the following reasons:

- The surface recession is kinetically controlled.
- The material thermal conductivity is relatively high.

Section 4.1 presents the surface thermochemistry data and the heat flux boundary condition information obtained from Section 3 which are required in order to perform the screening and in-depth analysis. Section 4.2 presents the thermochemical screening analysis results and Section 4.3 presents more detailed in-depth thermal analysis. Also included in this section are two in-depth thermal analyses using transient convective heating (rather than steady state) boundary conditions to determine the thermal and ablative response of the G-90 and Pyrostrand materials.

#### 4.1 SURFACE THERMOCHEMISTRY DATA AND HEAT FLUX BOUNDARY CONDITIONS

Figures 4-1 and 4-2 present the surface thermochemical responses of the charring ablating materials considered in the screening analysis. For internally decomposing materials a computer code such as CMA calculates material response transients by solving iteratively a surface energy balance which requires a parametric input of both pyrolysis off-gas rates and char removal rates as a function of surface temperature. Surface thermochemistry information of this type is used in Section 5 for transient calculation of internally decomposing materials in the throat package. However, for preliminary ranking of materials, this degree of sophistication is not required, and thus the steady state assumption is warranted. For the steady state surface response of a charring material, the ratio of the mass removal rates of the pyrolysis gas and char satisfy the steady state mass conservation equation. Figures 4-1 and 4-2 are thermochemistry maps based on this steady state assumption in which the non-dimensional mass removal is a combination of both pyrolysis gas and char removal.

For the cases considered, surface response maps are functions of stream temperature, pressure, and propellant. However, since the variation of the maps with temperature and pressure is small, these maps were calculated for only one state

point for each material. This temperature and pressure was selected as the average for the locations at which each material was considered. As a result, two thermochemistry maps were calculated for each material; one for 5 and another for 18 percent Al-CTPB propellant. These maps are used in Section 4.2 to perform the thermochemical screening analysis.

Figures 4-3 and 4-4 present the surface thermochemistry maps for the two blast tube materials for which in-depth thermal analyses using a convective heating boundary condition were performed. The G-90 surface response was calculated for a blast tube pressure of 160 atm for the 18 percent Al-CTPB propellant. The Pyrostrand response was performed for a pressure of 162 atm for both the 5 and 18 percent Al-CTPB propellants.

#### 4.2 THERMOCHEMICAL SCREENING ANALYSIS

The thermochemical screening analysis was used as a means to quickly evaluate the material performance of a large number of materials at several nozzle locations. This analysis was accomplished by solving a steady state surface energy balance for each material, geometry, location, and propellant summarized in Table 4-3. The energy balance calculations were performed using the SSA computer code. Input to this code consists basically of a heat transfer coefficient, edge enthalpy, and surface thermochemistry tables for each solution. These quantities were obtained from Sections 3.5.1, 3.4, and 4.1 respectively. Table 4-3 summarizes the results of these calculations. A schematic representation of the analysis locations is presented in Figure 4-5. The results presented in this table are discussed in more detail in the following paragraphs.

As shown in Figure 4-5, analyses were performed for the aft closure for area ratios corresponding to 9.0 and 22.0. Figures 3-8 and 3-9 show that a contraction ratio of 9.0 ( $\lambda = 7.9$  inches) experiences the most thermally severe boundary conditions in the aft closure. Steady state solutions for four materials for both 5 and 18 percent Al propellants are given in Table 4-3A for the location corresponding to an area ratio of 9.0. Further studies of in-depth thermal response analysis at this location was not practical, however, due to the close proximity of the forward entrance cap. The difficulty in this analysis was that the surface recession normal to the surface was greater than the available thickness of the aft closure material, i.e., the local receding surface intersected the forward entrance cap material. For this reason further

thermochemical screening was performed at a contraction ratio of 22.0, and the results are given in Table 4-3B. The location at a contraction ratio of 22.0 is shown in Figure 4-5 to be the section at which the aft closure material is thickest. As shown in Table 4-2B, the MXSE 280 material exposed to the 5 percent Al propellant exhibited the largest recession rate.

A further step in the screening analysis was made by calculating the effect of the keyhole port grain propellant on the aft closure surface recession. The results presented in Table 4-3B shows that this grain configuration increased the steady state recession by a factor of five at conditions representing the initiation of firing but that this factor diminished to nearly the steady state condition after five seconds of firing as illustrated in Figure 3-5 and Figure 3-12. Based on these results, the thickness of the aft closure material must be sized on the surface recession for MXSE 280 material and for a slotted grain 5 percent Al-CTPB propellant. For this reason, an in-depth thermal analysis of this configuration is presented in Section 4.2.2.1.

Thermochemical screening analyses were performed at four different blast tube area ratios. Area ratios of 1.3 and 2.0 were specified as design variables for the two nozzle configurations of interest while 3.0 and 4.0 were selected to gain information concerning the effect of local area ratios resulting from accumulated surface recession on the instantaneous recession rate. Table 4-3C summarizes the results of this analysis. These calculations were made at the blast tube entrance because Figures 3-8 and 3-9 show that this location experiences the maximum heating in the blast tube.

For the materials considered in this analysis, variations in blast tube area ratio affect both the steady state surface recession and surface temperature. Figure 4-6 illustrates the fact that increasing the blast tube radius will decrease surface recession and will increase or hold constant surface temperature. This figure also shows that the propellant with a greater aluminum loading fraction (18 percent) decreases surface recession and increases surface temperature over the 5 percent Al-CTPB propellant.

The choice of the worst case combination of material, propellant, and blast tube area ratio for the in-depth thermal analysis was highly qualitative. Table 4-3C shows that for area ratios of either 1.3 or 2.0 the silica phenolic has at least a factor of 2 greater initial surface recession rates. However the greatest thermal penetration is obtained for a material which has a relatively high surface recession and high thermal conductivity. For this reason, the combination of the MXSC 195 material and the 5 percent Al-CTPB propellant were chosen for further in-depth thermal analysis. MXSC 195 has the relatively high conductivity of a carbon phenolic while exhibiting the relatively greater recession rates of a silica phenolic. A blast tube area ratio of 2.0 was chosen

due to the wall thickness being less than for a 1.3 area ratio blast tube.

In screening materials for the exit cone, two locations (expansion ratios of 2.1 and 6.0) and two materials (MX 4926 carbon phenolic) were studied. The results are summarized in Table 4-3D. For further in-depth thermal analysis, MX 4926 for an expansion ratio of 6.0 and for the 5 percent Al-CTPB propellant was chosen. Again, the choice was highly qualitative. The carbon phenolic has a higher conductivity than the silica phenolic and the expansion ratio of 6.0 had a thinner section of material than that at an expansion ratio of 2.1.

#### 4.3 IN-DEPTH THERMAL ANALYSIS

The thermochemical screening analysis presented in the previous section provided estimates of the steady state surface temperature and surface recession rate for a matrix of materials, locations, and environments in the high pressure blast tube nozzle. Both surface recession and in-depth temperatures are important parameters for design considerations, and for this reason, in-depth calculations were performed and are presented in this section. The analyses were made using option 2 of the one-dimensional CMA computer code.

Section 3.6 presents the material thermal properties used in the in-depth thermal analyses. These were not needed in the previous section since steady state calculations deal solely with the surface phenomena. Section 4.3.1 presents the analyses assuming steady state ablation response. Three locations were analyzed (the aft closure, blast tube and exit cone) using pseudo-transient surface recession and temperature boundary conditions calculated from steady state quantities. The conditions (material, propellant and location) were chosen to be those defined in Section 4.2 which would best test the adequacy of the nozzle design. Section 4.3.2 presents in-depth thermal analyses of two materials, G-90 bulk graphite and Pyrostrand fibrous PG, which were considered for use in the blast tube. These computations were performed using option 1 of the CMA computer code.

##### 4.3.1 Analysis Assuming Steady-State Ablation Surface Response

In Section 4.2, the thermochemical screening analysis was presented. From these results, a material, location and propellant were chosen in order to define the adequacy of the proposed blast tube nozzle design in each of the three nozzle sections; aft closure, blast tube and exit cone. These cases are summarized as follows:

- Aft closure - Section 4.3.2.1
  - MXSE 280 silica phenolic
  - 5 percent Al-CTPB propellant

- 22.0 contraction area ratio
- slotted grain configuration
- Blast Tube - Section 4.3.2.2
  - MXSC 195 carbon/silica phenolic
  - 5 percent Al-CTPB propellant
  - 2.0 contraction area ratio
- Exit Cone - Section 4.3.2.3
  - MX 4926 carbon phenolic
  - 5 percent Al-CTPB propellant
  - 6.0 expansion area ratio

The separate analysis for each location is presented in the following three sections.

#### 4.3.1.1 Aft Closure Analysis

The in-depth analysis in the aft closure was performed using the one-dimensional CMA code which requires as input the geometry, the time dependent boundary conditions and material chemical and thermal data. The one-dimensional in-depth geometry at a contraction ratio of 22.0 consists of 1.32 inches of MXSE 280 and 0.43 inches of steel. The material property information was obtained from Section 3.6. The time dependent boundary conditions were derived as mentioned previously, from the steady state solutions given in Table 4-2B.

Figure 4-7A shows the estimated pseudo-transient surface recession boundary condition used in the in-depth calculation. Figure 4-7B shows the surface temperature history which was used as a boundary condition. This was also taken from the steady state results presented in Table 4-3B.

The results of the aft closure analysis are presented in Figures 4-8 and 4-9. The former shows the computed in-depth thermal profiles during the exposure and during cooldown. The profiles during the motor firing which are shown in Figure 4-8A illustrate the high surface recession coupled with the relatively low thermal conductivity common silica phenolics. This results in a very small thermal penetration (about 0.10 inch) as the material recedes. The in-depth profiles calculated for the cooldown are shown in Figure 4-8B and indicate that the thermal penetration depth is only about one half of the remaining MXSE 280 thickness after 60 seconds of elapsed time. The steel casing was predicted to have a negligible temperature rise as shown in Figure 4-8B. Figure 4-9 illustrates the surface and char line recessions in relation to the total material thickness.

#### 4.3.1.2 Blast Tube Analysis

The blast tube analysis was performed at a contraction ratio of 2.0 and a location which corresponded to the entrance of the blast tube. The one-dimensional geometry consisted of 0.80 inch of MXSC 195, 0.79 inch of silica phenolic backup and 0.32 inch steel. The material property information was obtained from Section 3.6.

The time dependent boundary conditions were calculated from the steady state surface recession and surface temperature given in Table 4-2C. These values were 72.0 mils/second and 3600°R, respectively. Figure 4-10A shows the calculated pseudo-transient surface recession history used for the in-depth thermal analysis. This was derived by assuming the blast tube recession initially was at its steady state value of 72.0 mils/second. As the surface recedes with time the internal diameter gives a second point on the pseudo-transient curve. This method was continued in this time step manner to give the recession history shown. The surface temperature boundary condition as shown in Figure 4-10B remains constant at the steady state value of 3600°R.

Applying the above information to the 1-D CMA analysis led to the results shown in Figures 4-11 and 4-12. Figure 4-11A depicts the in-depth thermal response of MXSC 195 to 5 percent Al-CTPB. The relatively high conductivity of the carbon/silica phenolic would yield a large thermal penetration depth for a slowly receding surface. However, the MXSC 195 also exhibited such a severe surface erosion, the thermal penetration was kept to a minimum (about 0.10 inch). Although local thermal penetration was small, 79 percent of the material was predicted to ablate. Figure 4-11B shows that the large silica phenolic backup was adequate for insulating the steel structure. The predicted surface and char line recessions are shown in Figure 4-12.

#### 4.3.1.3 Exit Cone Analysis

The exit cone analysis was performed at an expansion area ratio of 6.0 which corresponds to the exit plane of the exit cone. The one-dimensional geometry consisted of an 0.72 inch layer of MX 4926 carbon phenolic and an 0.09 inch thick backing of steel. The material property information used as input into the CMA code was given in Section 3.6.

The time dependent boundary conditions were based on the values given in Table 4-3D. The steady state surface recession is given as 10.2 mils/second and the surface temperature as 2738°R. Similar to the blast tube calculation, the exit cone boundary conditions were derived assuming the transient response consisted of a series of steady state conditions spaced at finite time steps during the firing. This surface rate history is given in Figure 4-13A and the surface temperature is shown in Figure 4-13B.



Figure 4-14A illustrates the in-depth temperature profiles obtained using the CMA code. Due to the relatively mild environment at the exit plane of the exit cone, the surface recession was low compared to the original thickness of the MX 4926. The recession was estimated to be 17 percent of the combined material thicknesses. The thermal penetration beneath the receding surface was greater in this case than in both the previous cases. This was due to the higher conductivity of the carbon phenolic as compared to the materials considered upstream of the throat. Figure 4-11B shows that in-depth heating is felt at the steel casing at about 30 seconds. After 60 seconds of elapsed time, the steel shell is predicted to have a temperature rise of about 65°R. Figure 4-12 shows the predicted surface and char recessions during the firing.

#### 4.3.2 Analysis Using Convective Heating Boundary Condition to Study Blast Tube Thermal and Ablative Response

This section presents the additional one-dimensional analysis performed for two materials in the blast tube. The CMA code was used with a convective heating boundary condition (option 1). Variables considered are as follows:

- G-90 - Section 4.3.3.1
  - 18 percent Al-CTPB
  - contraction area ratio = 1.3
  - blast tube entrance and exit locations
- Pyrostrand - Section 4.3.3.2
  - 5 percent and 18 percent Al-CTPB
  - contraction area ratio = 1.3
  - blast tube entrance location

Section 4.3.2.1 discusses the results obtained from analyzing G-90 bulk graphite and Section 4.3.2.2 presents the results for analyzing a Pyrostrand blast tube configuration.

##### 4.3.2.1 G-90 Blast Tube Analysis

The CMA code was used to analyze the in-depth thermal response of G-90 at two blast tube locations. The one-dimensional geometry consisted of a 0.45 inch thick G-90 sleeve backed by 0.45 inches of silica phenolic (cloth reinforcement in 0° layup orientation) and 0.075 of steel casing. The chemical and thermal properties for G-90 were obtained from Section 3.6. The surface thermochemical response of G-90 to 18 percent Al-CTPB propellant was calculated using the ACE computer code and is presented in Figure 4-3. This thermochemistry map was used for both the entrance and exit locations of the blast tube.

Since the analysis uses a convective heating boundary condition, the recovery enthalpy, incident radiant heat flux and convective heat transfer coefficient as a function of time were determined. For both locations in the blast tube, the recovery enthalpy and incident radiant flux were calculated to be 942.5 Btu/lb and 865.0 Btu/ft<sup>2</sup>-second, respectively. The time dependent heat transfer coefficient was calculated from the information in Figure 3-9A. This figure shows that for a constant chamber pressure, the predicted heat transfer coefficient at the entrance of the blast tube ( $\lambda = 0.94$  ft) is 2.77 lb/ft<sup>2</sup>-sec and at the exit ( $\lambda = 1.54$  ft) is 1.54 lb/ft<sup>2</sup>-sec and that it decreases along the length of the blast tube. These coefficients were estimated for a wall temperature of 5000°R and they were applied to Eqs. 3-2 and 3-3 to obtain the heat transfer coefficients shown in Figure 4-16.

Figure 4-17 shows the in-depth thermal profiles for the G-90 blast tube entrance. After 11 seconds of exposure, the thermal penetration depth was predicted to be at about the midpoint of the silica phenolic backup. After 60 seconds, a temperature rise of 60°R was felt at the steel casing. Figure 4-18 illustrates the corresponding thermal profiles found at the exit of the blast tube. Conditions at this location were less severe (lower heat transfer coefficient) than those at the entrance. For this reason in-depth temperatures and thermal penetrations were slightly less at the exit than at the entrance. However, for both locations, the temperature rise of steel structural member was approximately the same. At the exit of the blast tube the steel housing was predicted to rise 58°R in temperature; 2°R less than the housing at the entrance. The surface recession is presented in Figure 4-19A for both cases. The entrance was calculated to recede 0.24 inch and the exit 0.194 inch. Figure 4-19B compares various temperature histories for the two locations.

#### 4.3.2.2 Pyrostrand Blast Tube Analyses

The one-dimensional CMA code was used to analyze the in-depth thermal response of a pyrostrand sleeve at the blast tube entrance with a backup of castable carbon. Calculations were made for both 5 and 18 percent Al-CTPB propellants for a blast tube contraction ratio of 1.3. The one-dimensional geometry consisted of a 0.442 inch thick Pyrostrand sleeve backed by 0.108 inches of castable carbon. Chemical and thermal properties used for Pyrostrand are presented in Section 3.6. The kinetically controlled surface response of Pyrostrand was illustrated in Figure 4-4. Reference 2 was used as a source of the surface kinetics constants. These constants were those reported for layer oriented pyrolytic graphite.

Other pertinent calculations which were input to the transient in-depth code are summarized in Table 4-4. The time dependent heat coefficients were calculated using Eqs. 3-2 and 3-3 and are presented in Figure 4-20. This illustration shows that the heat transfer coefficient at the entrance of the blast tube is higher than that at the exit.

In-depth thermal profiles due to exposure to both 5 percent and 18 percent Al-CTPB are shown in Figure 4-21. In general, 18 percent Al-CTPB results in higher surface temperatures, a greater surface recession, and greater thermal penetration than 5 percent Al-CTPB. After an elapsed time of 60 seconds, the Pyrostrand/castable carbon interface was predicted to be at a temperature of 1440°R for the 5 percent Al-CTPB propellant. Using 18 percent Al-CTPB, the interface is shown to be at a temperature of 1600°R. Figure 4-22A compares the surface recessions for both cases. The 18 percent Al-CTPB propellant results in a factor of 5 increase in surface recession as compared to the 5 percent Al-CTPB environment. However, the total surface recession amounts to less than two percent of the original pyrostrand thickness in both cases. These low surface recessions are characteristic of pyrolytic graphite materials oriented in a layer configuration. Figure 4-22B presents the surface and interface temperature calculated for both cases.

TABLE 4-1

NOZZLE LOCATION, MATERIAL CLASSES, AND  
TYPICAL MATERIALS FOR THE HIGH CHAMBER  
PRESSURE SOLID ROCKET MOTOR

Nozzle Location	Material Class	Typical Material
Aft Closure	Silica Phenolic	MXSE 280
	Elastomeric	R-155
	Carbon Phenolic	MXCE 280
	Carbon/Silica Phenolic	MXSC 195
Blast Tube	Silica Phenolic	MX 2625
		MXSE 280
	Carbon Phenolic	MXCE 280
	Carbon/Silica Phenolic	MXSC 195
	Bulk Graphite	G-90
	Pyrolytic Graphite Fiber	Pyrostrand
Exit Cone	Silica Phenolic	MX 2600
	Carbon Phenolic	MX 4926

TABLE 4-2  
SUMMARY OF MATERIALS STUDIED IN SCREENING AND  
IN-DEPTH THERMAL ANALYSIS

Material	Propellant <sup>a</sup>	Analysis Location	
		Component	Area Ratio
MXSE 280	5, 18	Blast Tube	1.3, 2.0, 3.0, 4.0
		Aft Closure	9.0, 22.0
MXCE 280	5, 18	Blast Tube	1.3, 2.0, 3.0, 4.0
		Aft Closure	9.0, 22.0
MXSC 195	5, 18	Blast Tube	1.3, 2.0, 2.0, 4.0
		Aft Closure	9.0, 22.0
R-155	5, 18	Aft Closure	9.0, 22.0
MX 2625	5	Blast Tube	1.3, 2.0, 2.0, 4.0
G-90	18	Blast Tube	1.3
Pyrostrand	5, 18	Blast Tube	1.3
MX 4926	5, 18	Exit Cone	2.1, 6.0
MX 2600	5	Exit Cone	2.1, 6.0
G-90 <sup>b</sup>	18	Blast Tube	1.3
Pyrostrand <sup>b</sup>	5, 18	Blast Tube	1.3

<sup>a</sup> 5 refers to 5 percent AL-CTPB and 18 refers to 18 percent AL-CTPB.

<sup>b</sup> Transient CMA option 1 analysis performed for these materials.

TABLE 4-3  
STEADY STATE ABLATION THERMAL SCREENING SUMMARY

A) Aft Closure, Worst Case

Material	Propellant <sup>a</sup>	Contraction <sup>b</sup> Ratio	Radius <sup>b</sup> (inches)	Heat Coeff. <sup>c</sup> (lb/ft <sup>2</sup> sec)	Surface Temperature (°R)	Recession Rate (mils/sec)
MXSE 280 Silica Phenolic	18 5	9.0	2.6	0.42 0.46	4513. 3675.	26.9 34.6
MXCE 280 Carbon Phenolic	18 5			0.42 0.46	5736. 4219.	13.8 16.0
MXSC195 Carbon/ Silica Phenolic	18 5			0.42 0.46	4773. 3802.	23.4 25.9
R-155 Asbestos Rubber	18 5			0.42 0.46	4791 3885.	23.1 21.9

<sup>a</sup> 18 is 18 percent AL-CIPB (UTP-11475), Flame Temperature = 6470°R at 1000 psia.  
5 is 5 percent AL-CIPB (UTP-13615), Flame Temperature = 5820°R at 1000 psia.

<sup>b</sup> Location is at minimum aft closure contraction ratio (Worst Environment).

<sup>c</sup> 0.75 \* ARGEIBL code coefficient prediction, assumed  $T_w = 5000^\circ\text{R}$  for 18 percent, 4000°R for 5 percent.  
CM/CH = 0.755 for 18 percent, 0.872 for 5 percent.

TABLE 4-3  
STEADY STATE ABLATION THERMAL SCREENING SUMMARY  
B) Aft Closure In-Depth Analysis Location

Material	Propellant	Contraction Ratio	Radius (inches)	Heat Coef. <sup>a</sup> (lb/ft <sup>2</sup> -sec)	Surface Temperature (°R)	Recession Rate (mils/sec)
MXSE 280 Silica Phenolic	18 5	22.	4.0	0.24	4684.	17.7
				0.26	3985.	21.2
				1.99 (0.)	3600.	107.5
				0.71 (1.)	3600.	47.4
				0.32 (2.)	3766.	29.3
MXCE 280 Carbon Phenolic	18 5			0.29 (5.)	3917.	23.3
				0.24	5922.	8.8
MXSC 195 Carbon/Silica Phenolic	18 5			0.26	4569.	9.3
				0.24	4991.	18.0
R-155 Asbestos Rubber	18			0.26	4165.	15.5
				0.24	4963.	16.7
				0.26	3885.	16.1

<sup>a</sup> 0.75 ARGEIBL code coefficient prediction; assumed  $T_w = 5000^\circ\text{F}$  for 18 percent,  $4000^\circ\text{R}$ , for 5 percent; numbers in parentheses are firing times in seconds  $t_w$  for locations behind the keyhole post, all others heat coefficients are late time or circular port values.

TABLE 4-3  
STEADY STATE ABLATION THERMAL SCREENING SUMMARY  
C) Blast Tube Entrance Location

Material	Propellant <sup>a</sup>	Contraction Ratio	Radius (inches)	Heat Coeff. (lb/ft <sup>2</sup> sec)	Surface Temperature (°R)	Recession Rate (mils/sec)
MXSE 280 Silica Phenolic	18	1.3	0.98	2.10	3781.	105.1
		2.0	1.22	1.50	3922.	77.1
		3.0	1.49	1.17	4046.	61.6
		4.0	1.72	1.04	4115.	55.5
		1.3	0.98	2.32	3600.	120.3
MXCE 280 Carbon Phenolic	15	4.0	1.22	1.69		90.0
		3.0	1.49	1.31		71.9
		4.0	1.72	1.18		66.1
		1.3	0.98	2.10	5269.	55.0
		2.0	1.22	1.50	5363.	40.6
MXSC 195 Carbon/Silica Phenolic	18	3.0	1.49	1.17	5418.	32.6
		4.0	1.72	1.04	5448.	29.4
		1.3	0.98	2.32	3152.	88.2
		2.0	1.22	1.69	3222.	64.4
		3.0	1.49	1.31	3300.	50.1
MX2625 Silica Phenolic	5	4.0	1.72	1.18	3354.	45.2
		1.3	0.98	2.10	4469.	82.2
		2.0	1.22	1.50	4500.	60.5
		3.0	1.49	1.17	4529.	48.5
		4.0	1.72	1.04	4545.	43.8
MX2625 Silica Phenolic	5	1.3	0.98	2.32	3600.	96.2
		2.0	1.22	1.69		72.0
		3.0	1.49	1.31		57.6
		4.0	1.72	1.18		53.1
		1.3	0.98	2.32	3600.	125.4
MX2625 Silica Phenolic	5	2.0	1.22	1.69		93.8
		3.0	1.49	1.31		75.1
		4.0	1.72	1.18		69.2



TABLE 4-4

SUMMARY OF CONVECTIVE BOUNDARY CONDITIONS FOR ONE-DIMENSIONAL ANALYSIS  
OF PYROSTRAND BLAST TUBE ENTRANCE

Propellant	Recovery Enthalpy (Btu/lb)	Incident Radiation (Btu/ft <sup>2</sup> -sec)	Heat Transfer Coefficient From ARGEIBL (lb/ft <sup>2</sup> -sec)
5% Al-CTPB	-520.7	552.1	2.96 <sup>a</sup> ( $\lambda = 0.84$ ft)
18% Al-CTPB	942.5	865.	2.60 <sup>b</sup> ( $\lambda = 0.84$ ft)
<sup>a</sup> estimated wall temperature = 4000°R			
<sup>b</sup> estimated wall temperature = 5000°R			

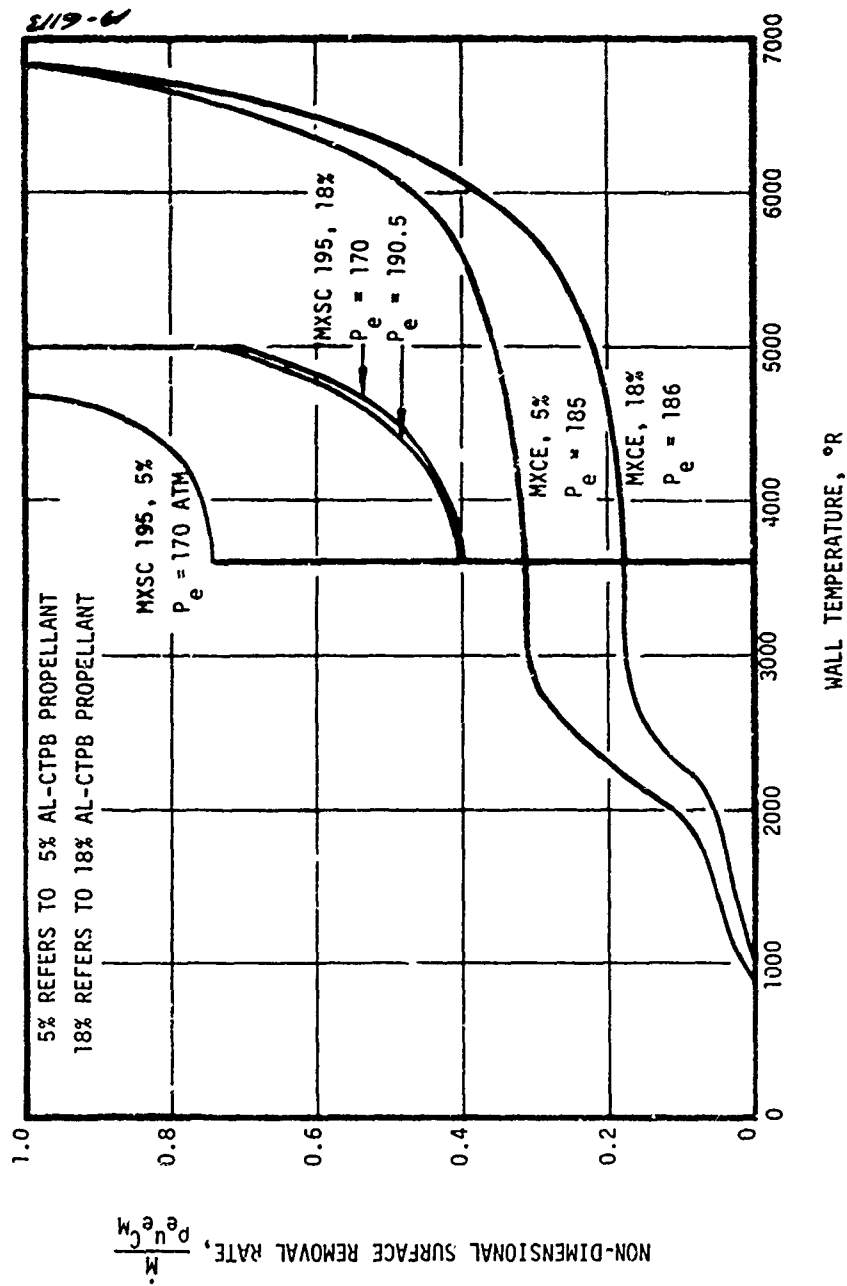


Figure 4-1. Steady State Surface Response of Materials Used in Screening Analysis of Aft Closure and Blast Tube

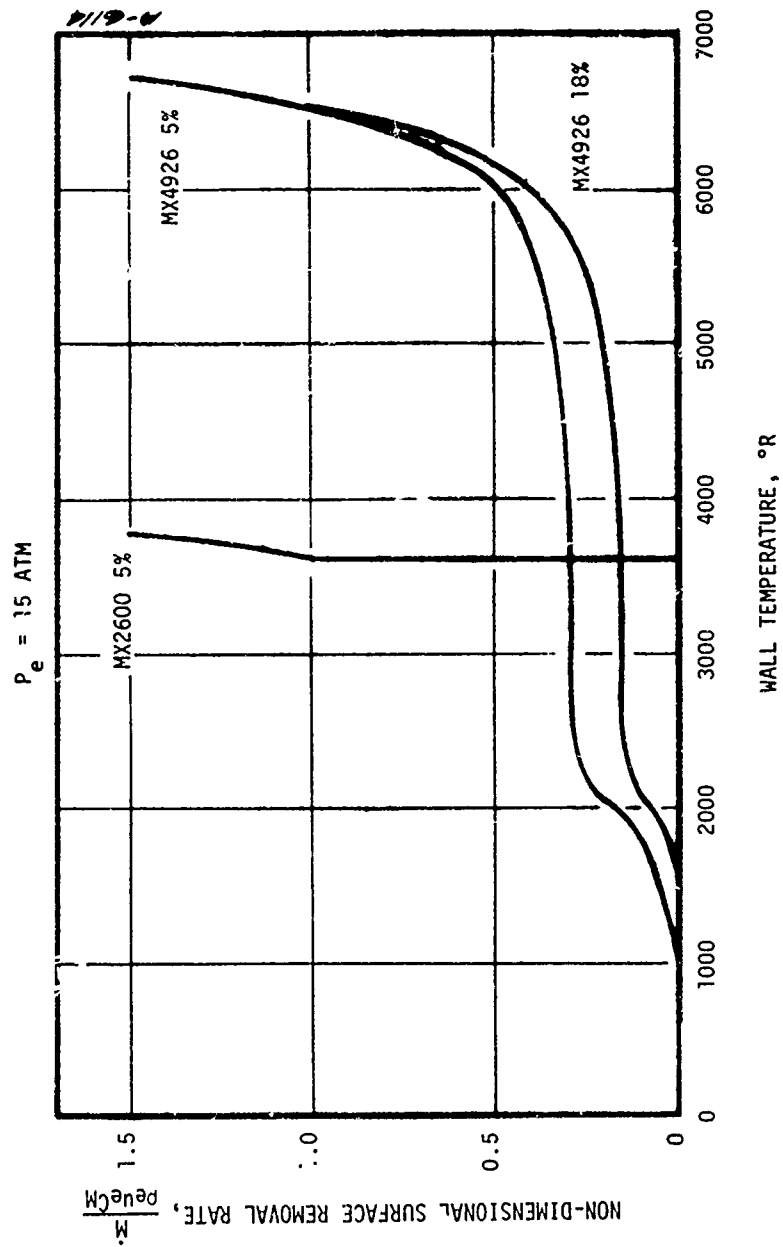


Figure 4-2. Steady State Surface Response of Materials Used in Screening Analysis of Exit Cone

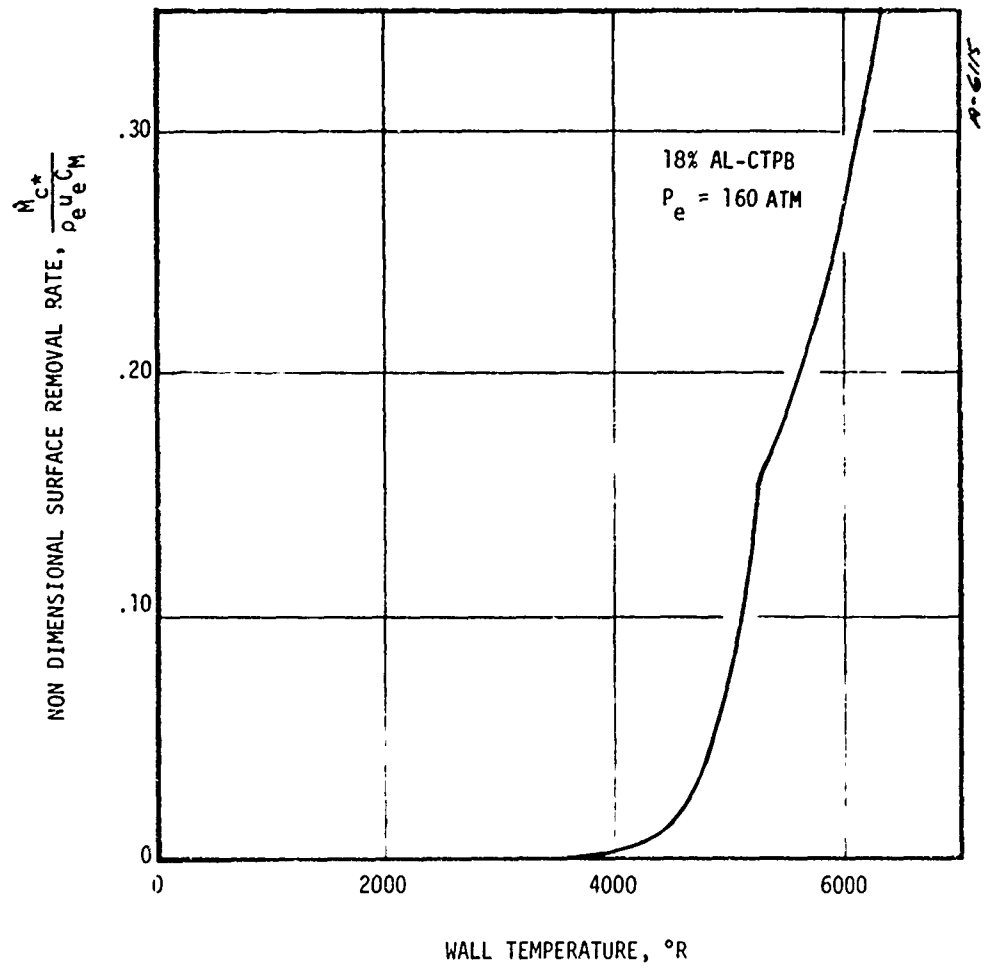


Figure 4-3. Kinetically Controlled Surface Response of G-90 Bulk Graphite at Blast Tube ( $\epsilon = 1.3$ ) Conditions

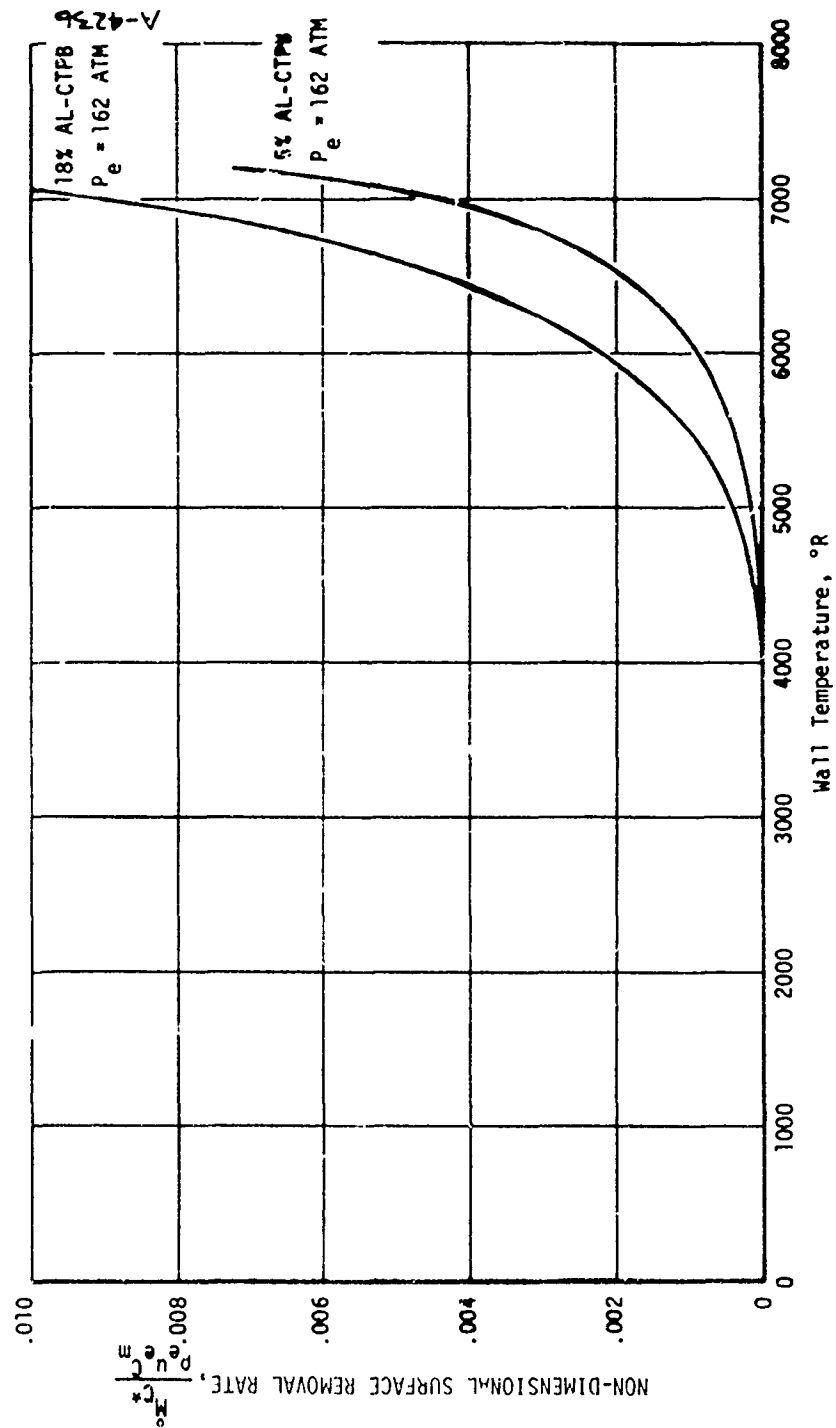
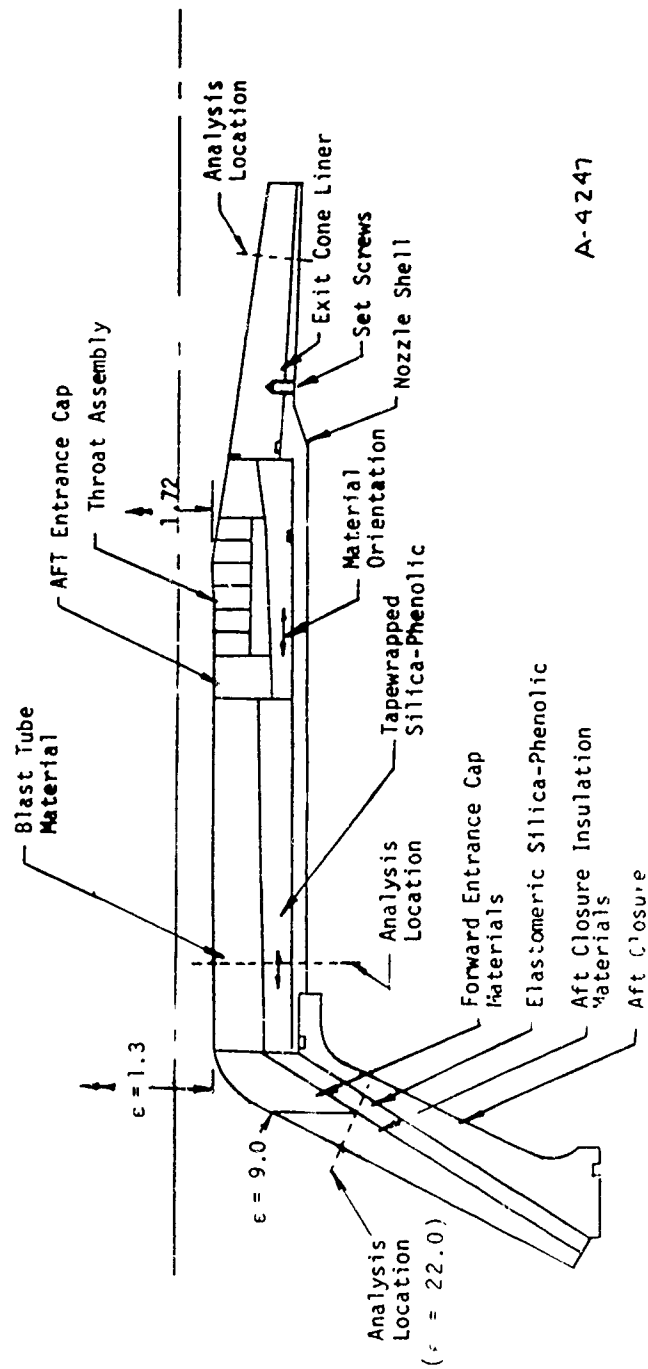


Figure 4-4. Kinetically Controlled Surface Response of Pyrostrand Layer Graphite at Blast Tube ( $\epsilon = 1.3$ ) Conditions



A-4247

Figure 4-5. Blast Tube Nozzle Design

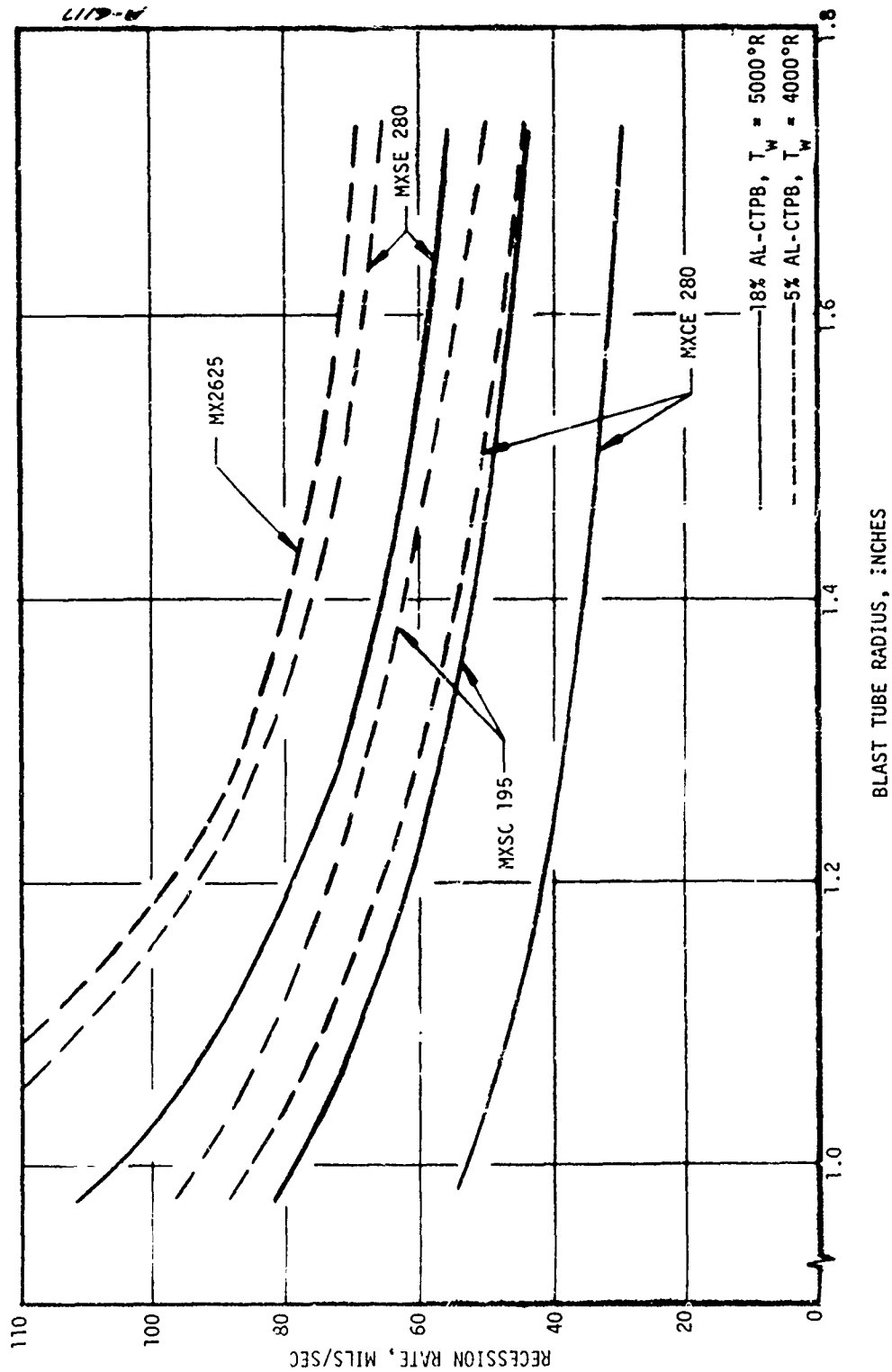


Figure 4-6. Comparisons of Steady State Ablation Response as a Function of Blast Tube Radius at the Blast Tube Entrance Plane

A) Recession Rate

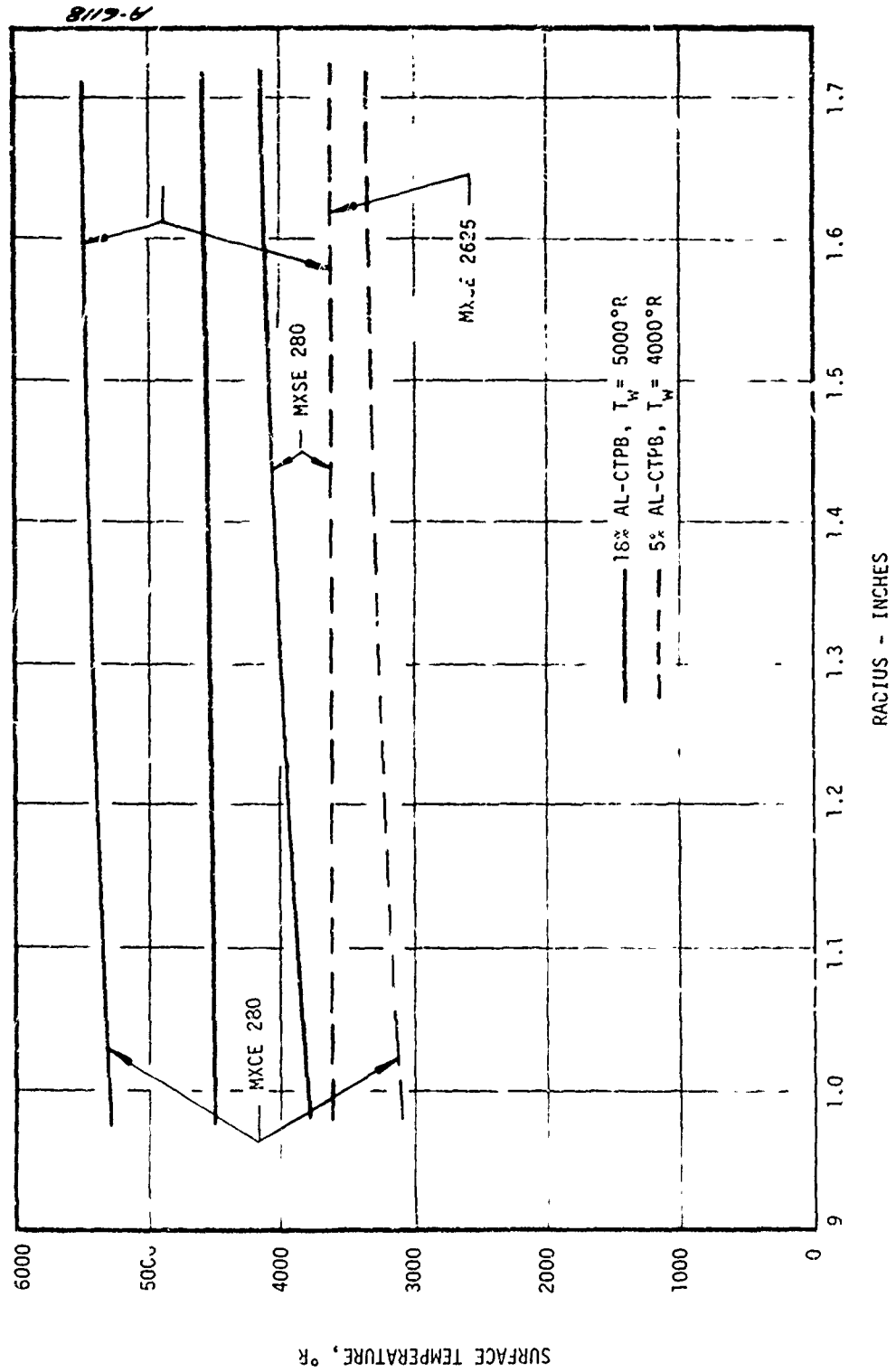


Figure 4-6. Concluded  
B) Surface Temperature



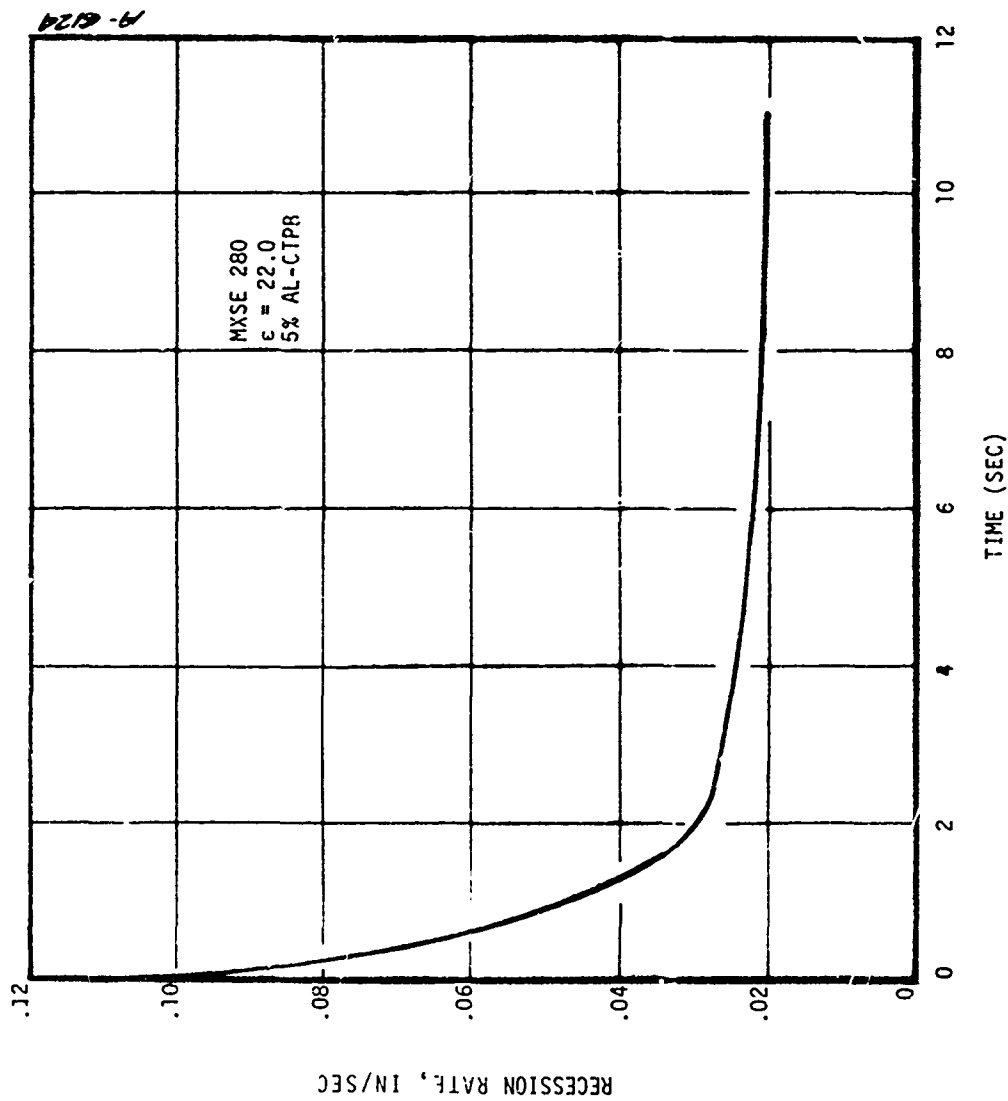


Figure 4-7. Aft Closure In-Depth Analysis Boundary Conditions Accounting for Slotted Grain Flow  
 A) Recession Rate History

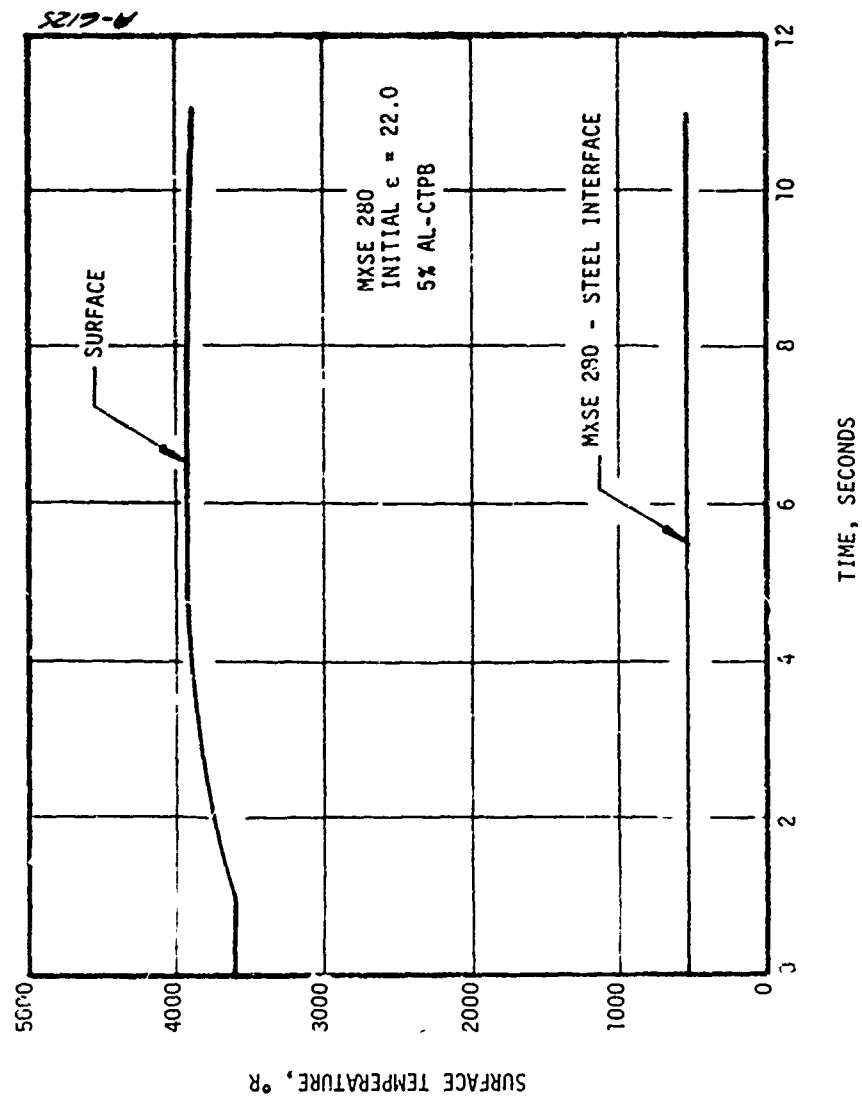


Figure 4-7. Concluded

B) Surface and Computer Backwall Temperature Histories

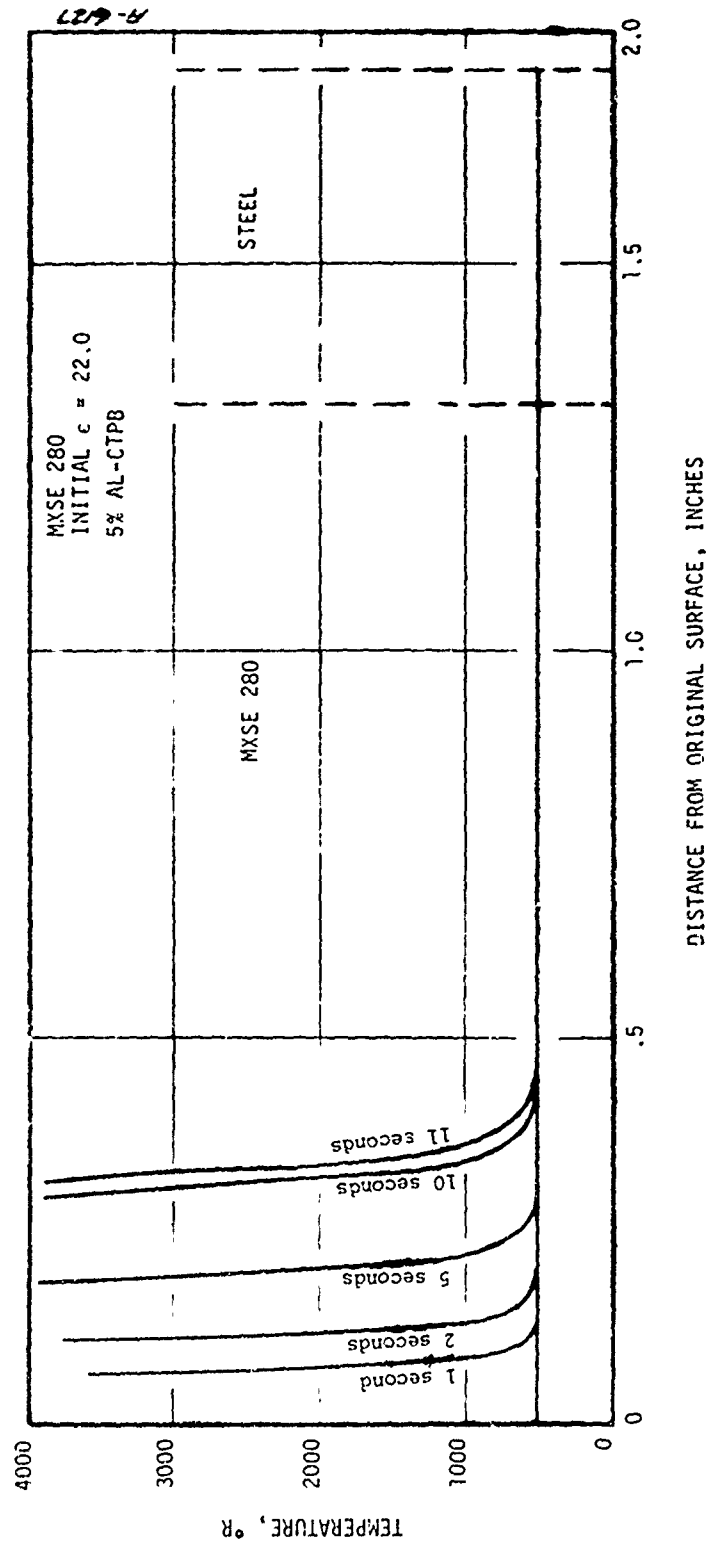


Figure 4-8. Aft Closure Temperature Profiles  
 A) For Specified Surface Temperatures and recession Rates During Exposure

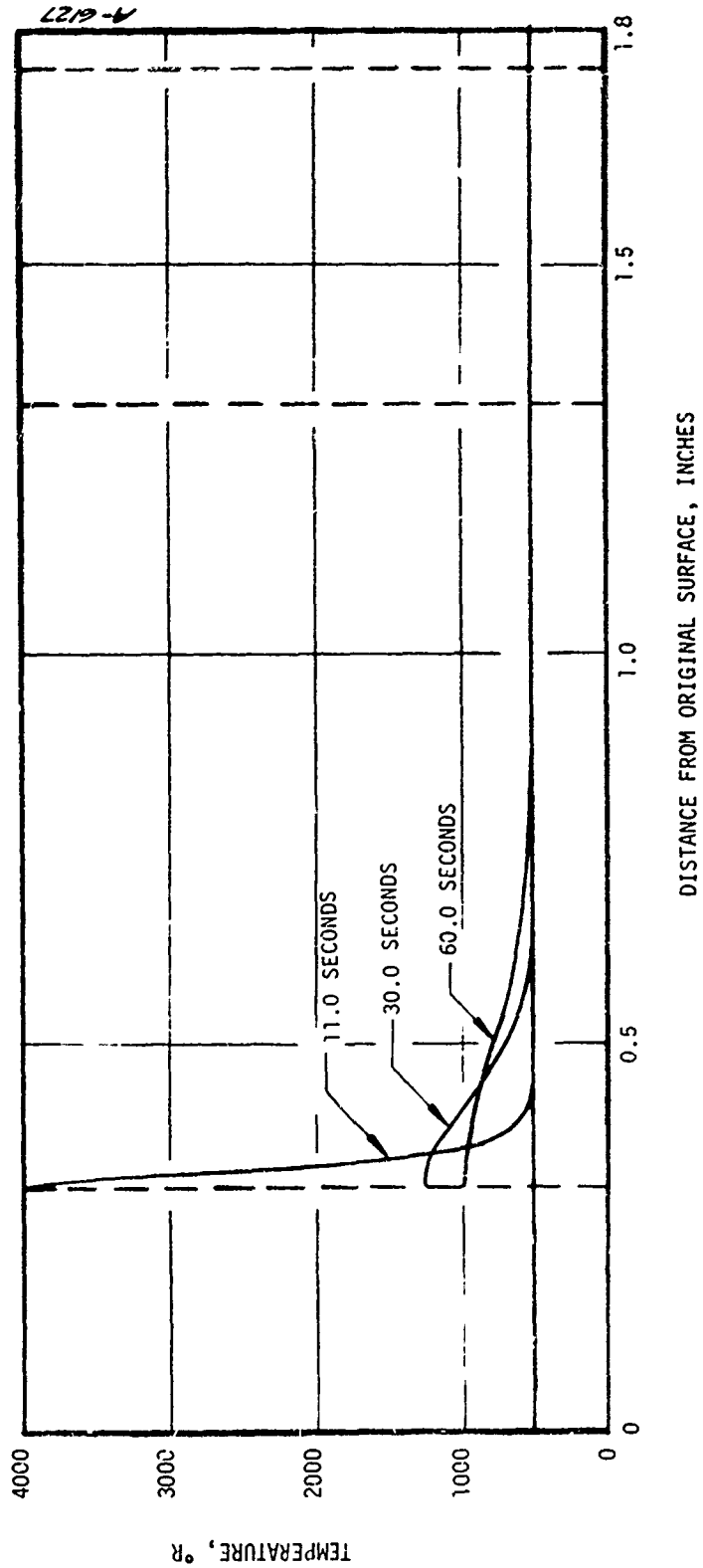


Figure 4-8. Concluded.  
B) During Cooldown

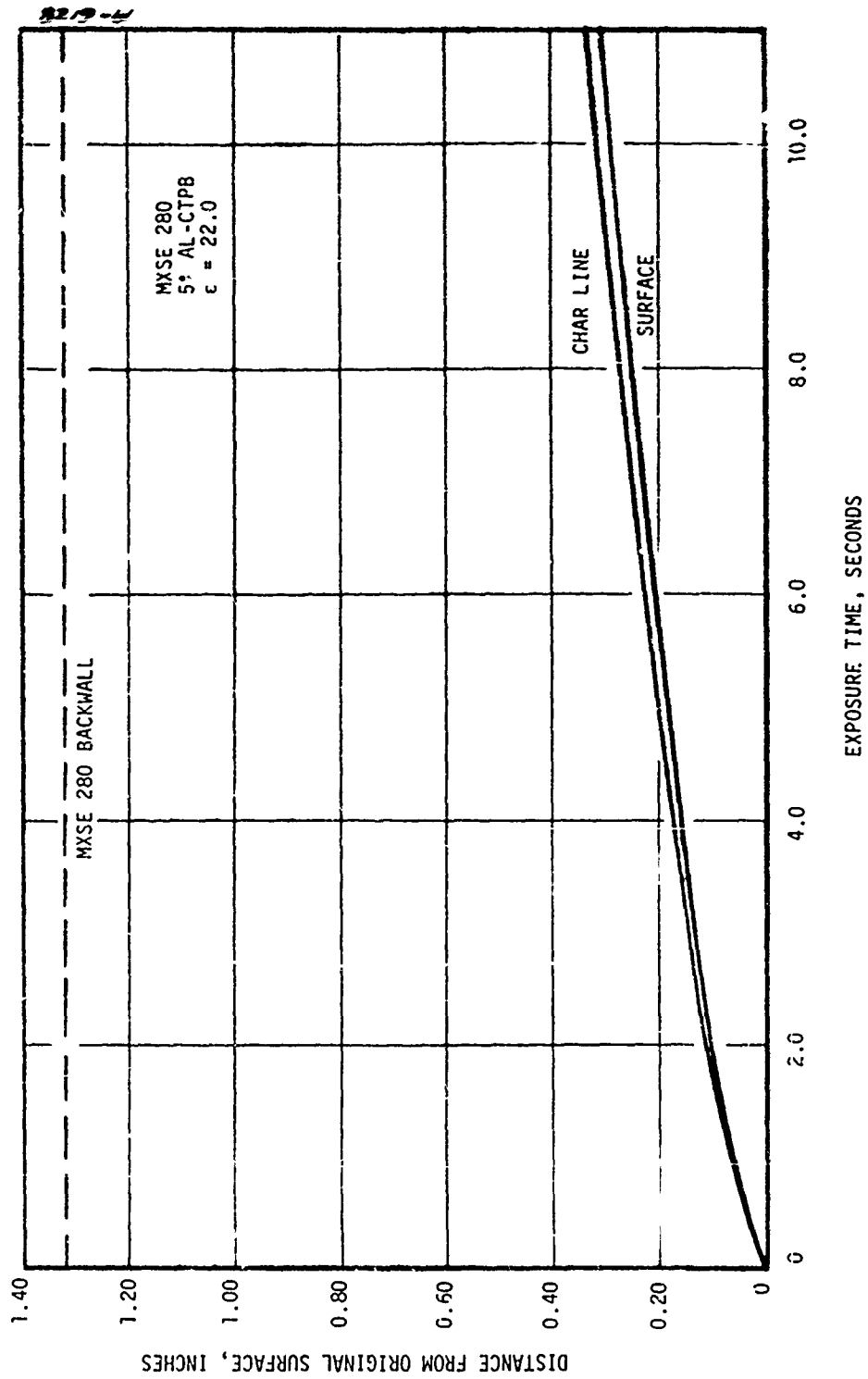


Figure 4-9. Aft Closure Surface and Char Recession Histories

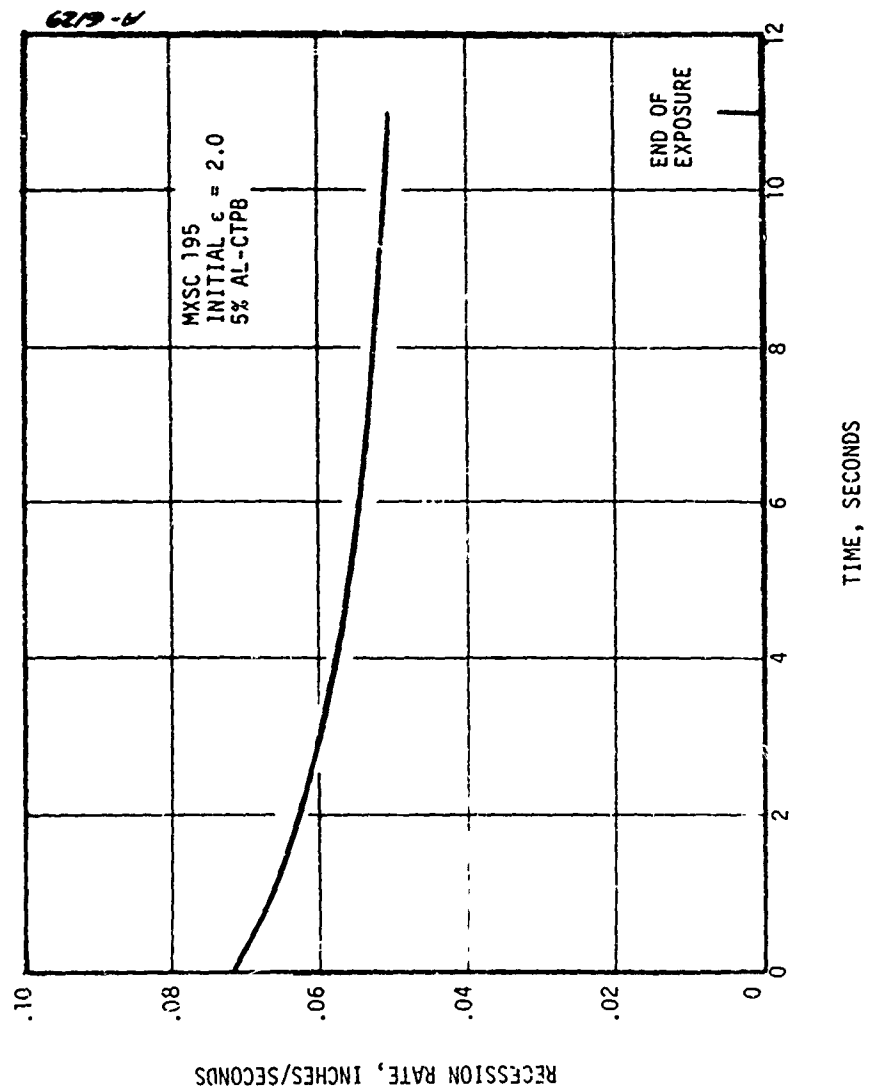


Figure 4-10. Blast Tube In-Depth Analysis Boundary Conditions  
A) Recession Rate History

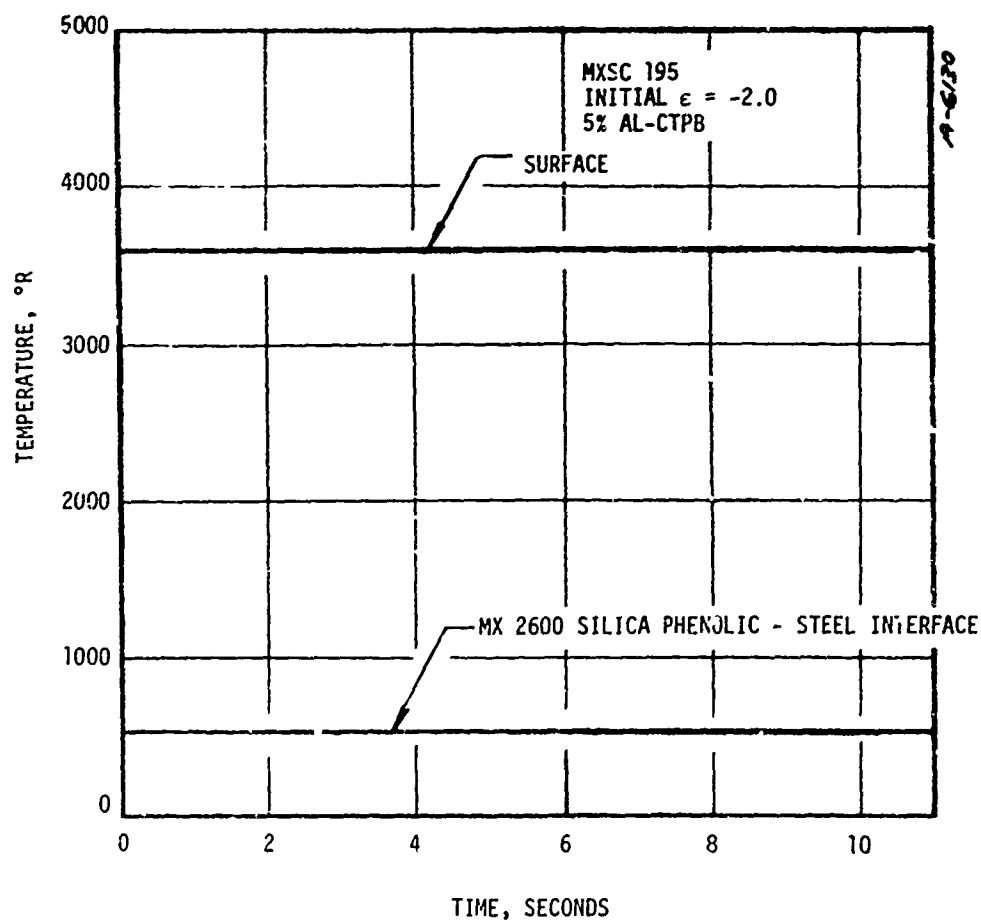


Figure 4-10. Concluded.

B) Surface and Computed Backwall Temperature Histories

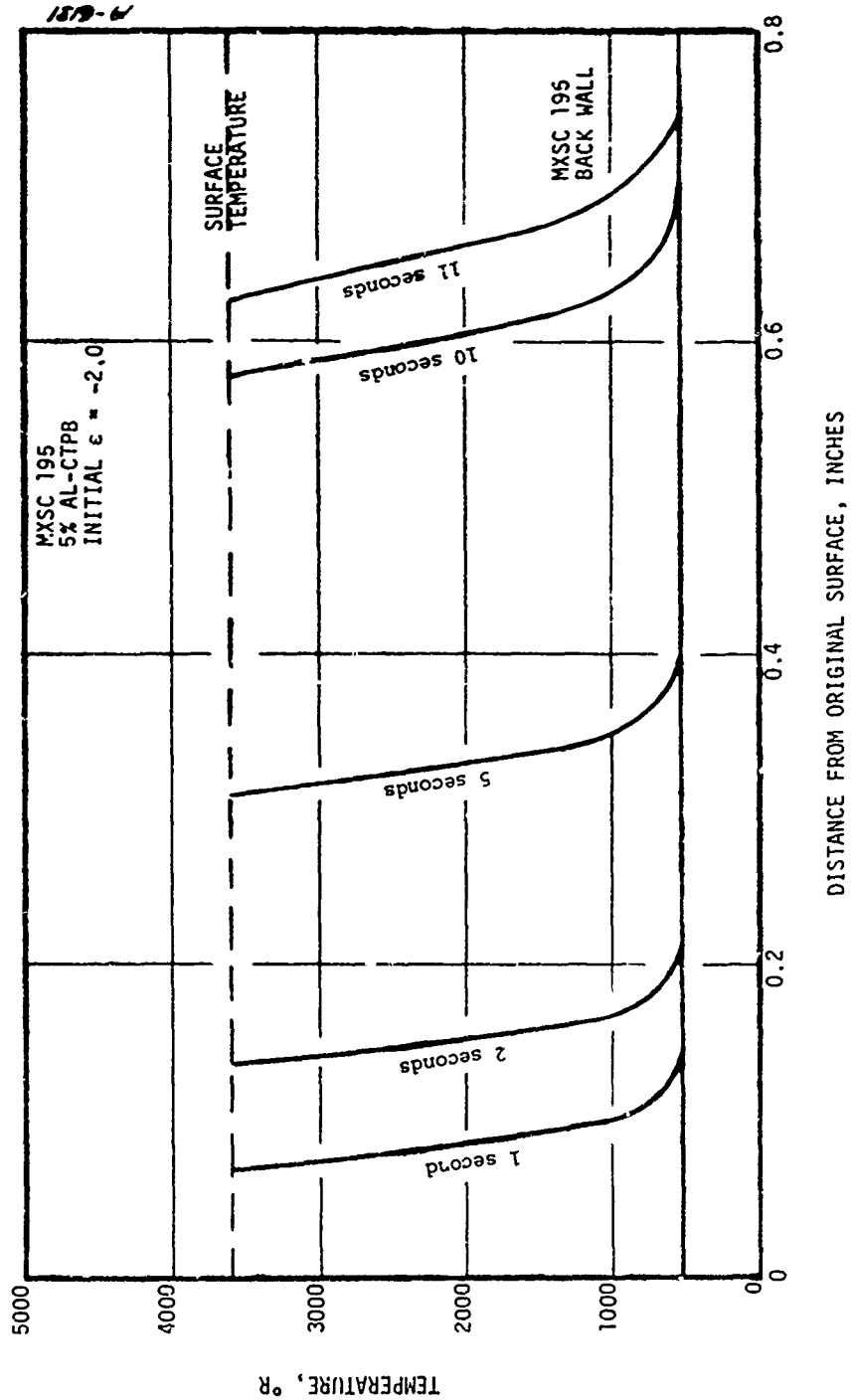


Figure 4-11. Blast Tube Temperature Profiles  
A) Specified Wall Temperature and  
Recession Rate





1.0



1.1



1.45

1.56

1.75

1.95

2.15

2.35

2.55

2.75

2.95



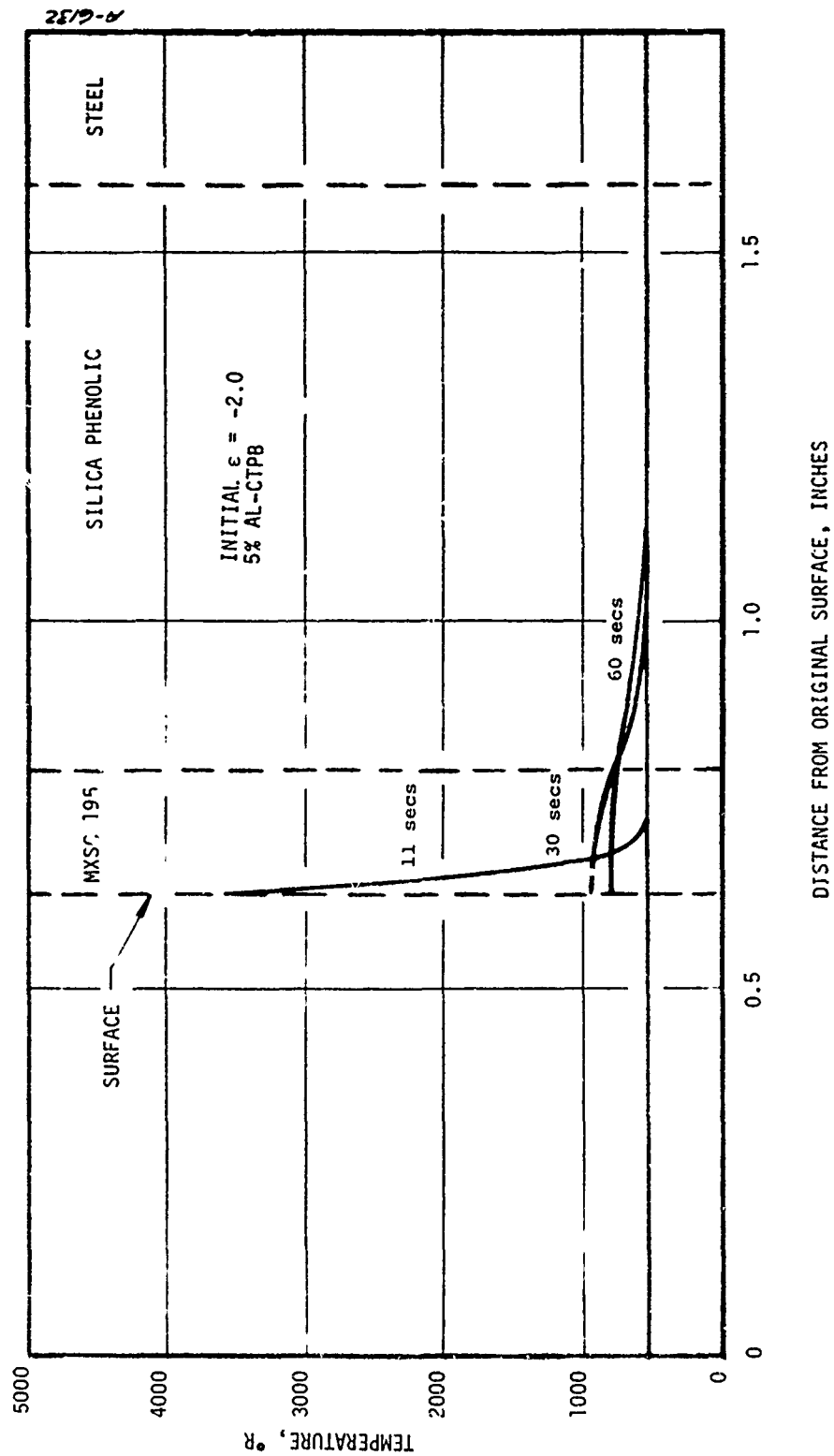


Figure 4- 11. Concluded  
B) Radiation Cooldown

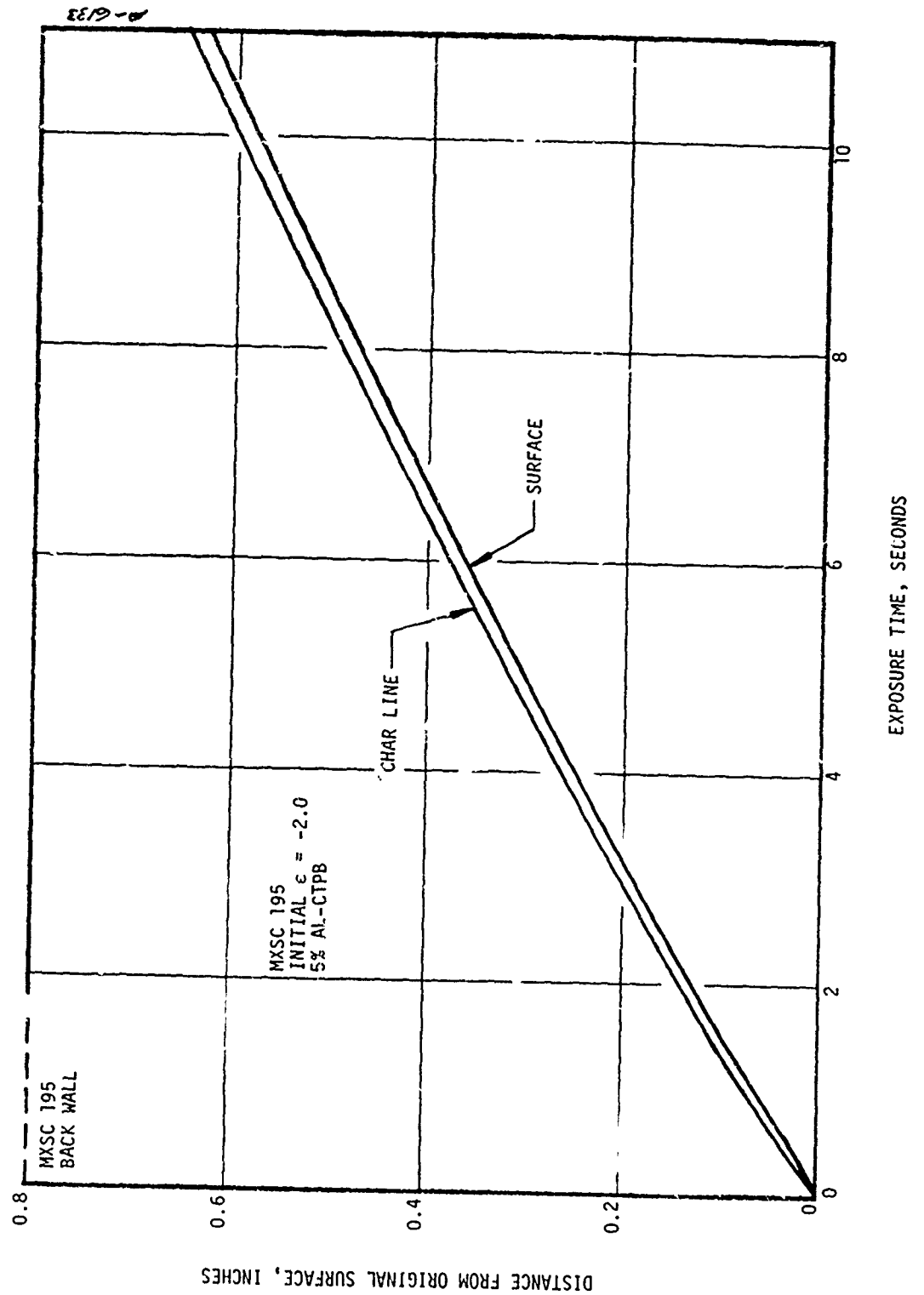


Figure 4-12. Blast Tube Surface and Char Recession Histories

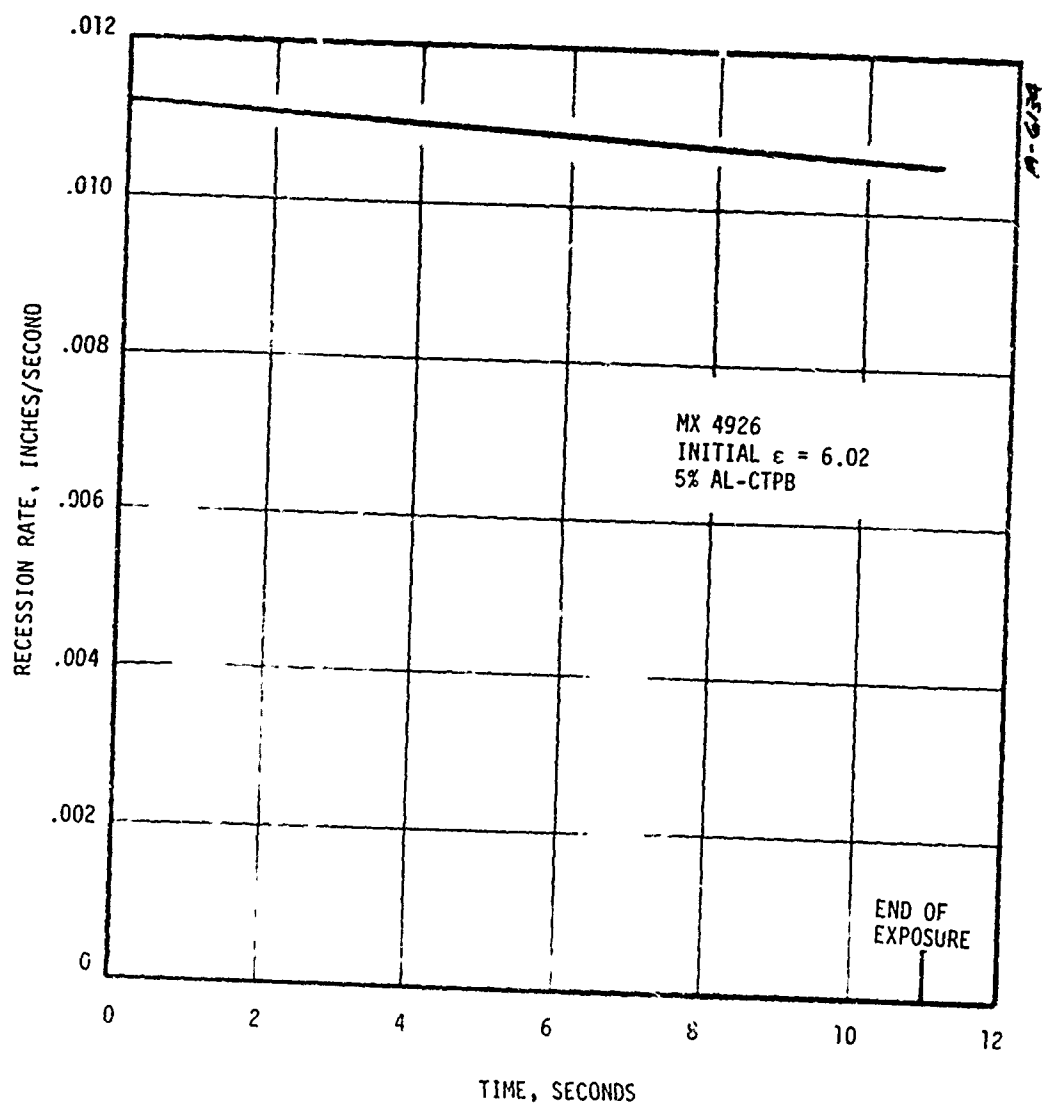


Figure 4-13. Exit Plane In-Depth Analysis Boundary Conditions  
A) Recession Rate History

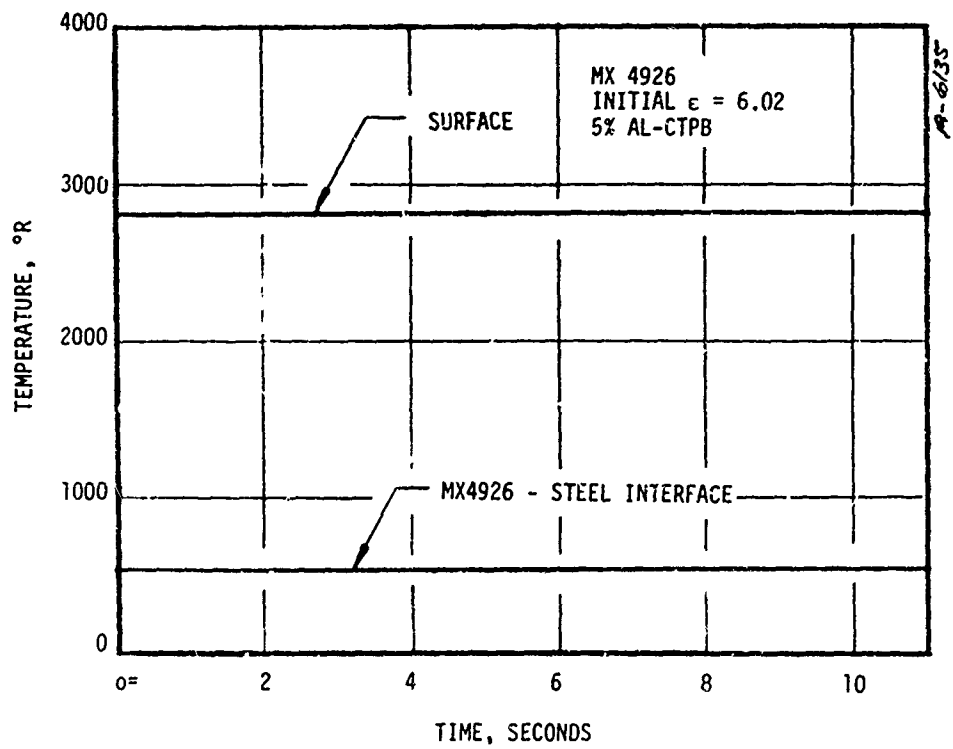


Figure 4-15. Concluded.

B) Surface and Computed Backwall  
Temperature Histories

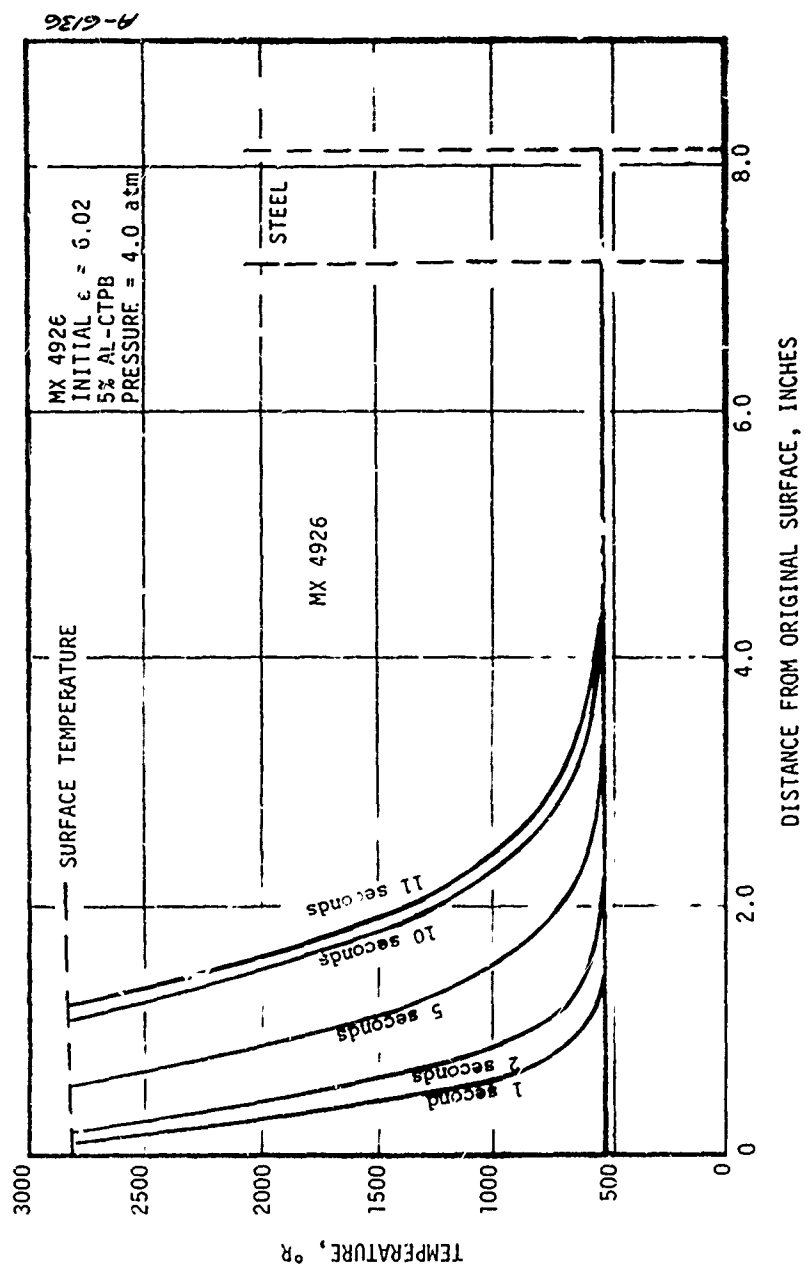


Figure 4-14. Exit Plane Temperature Profiles

A) For Specified Surface Temperatures and Recession Rates During Exposure

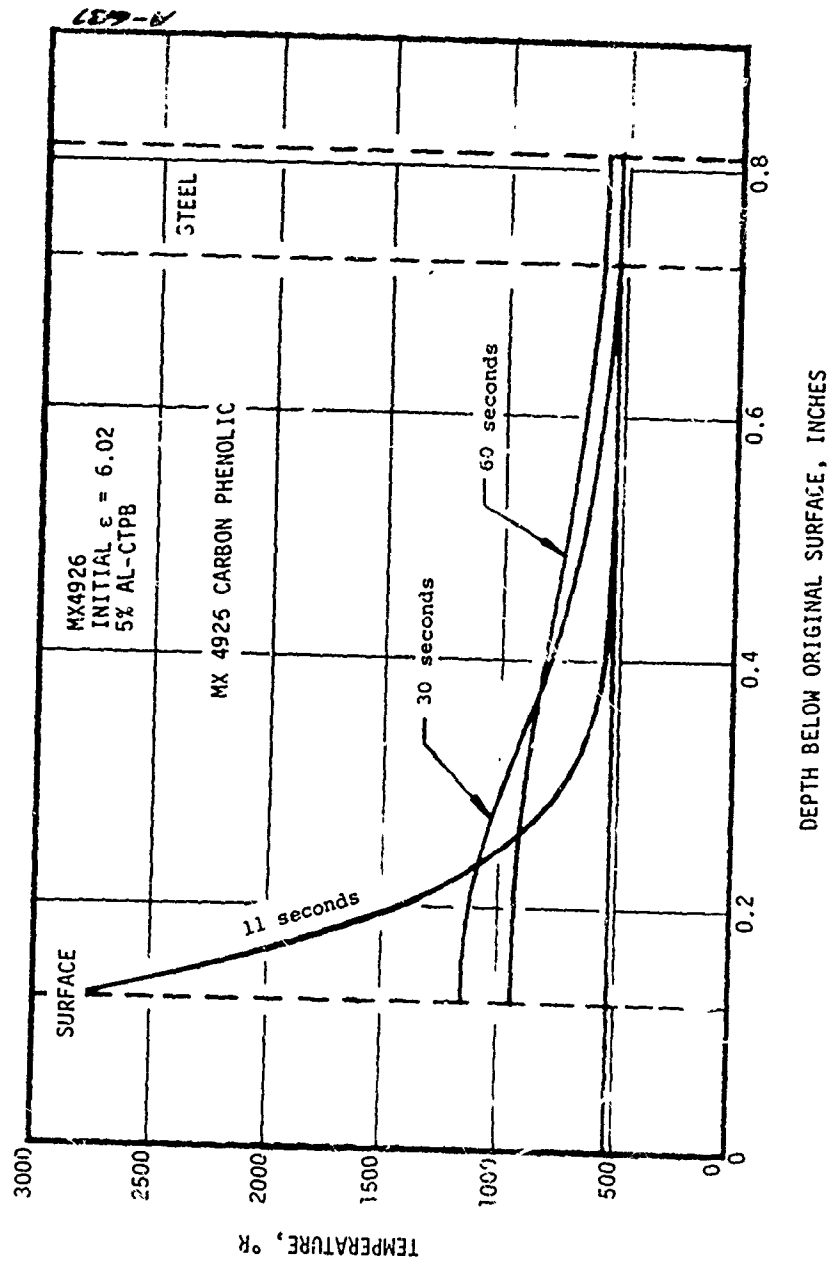


Figure 4-14. Concluded  
B) During Cooldown

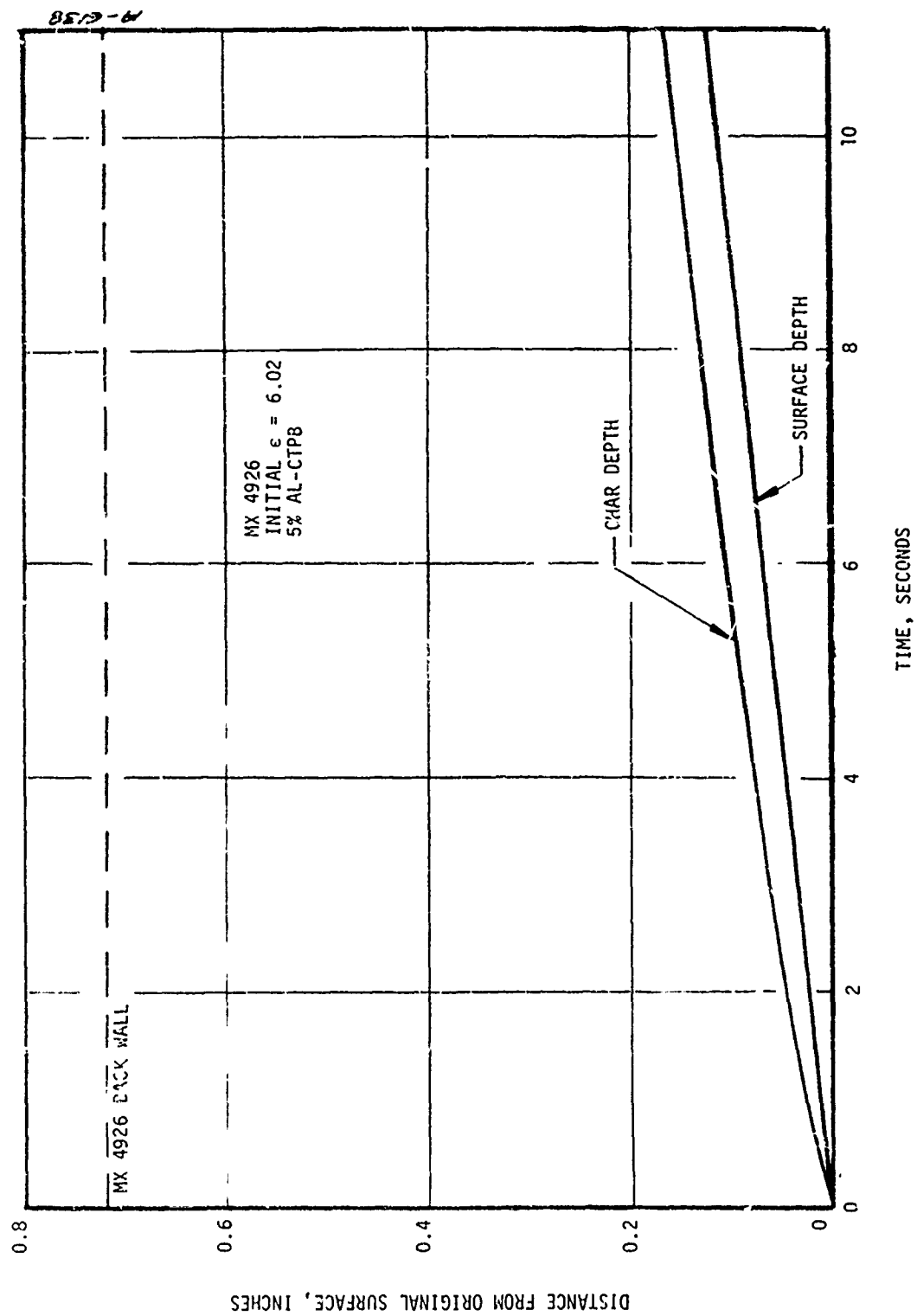


Figure 4-15. Exit Plane Surface and Char Recession Histories



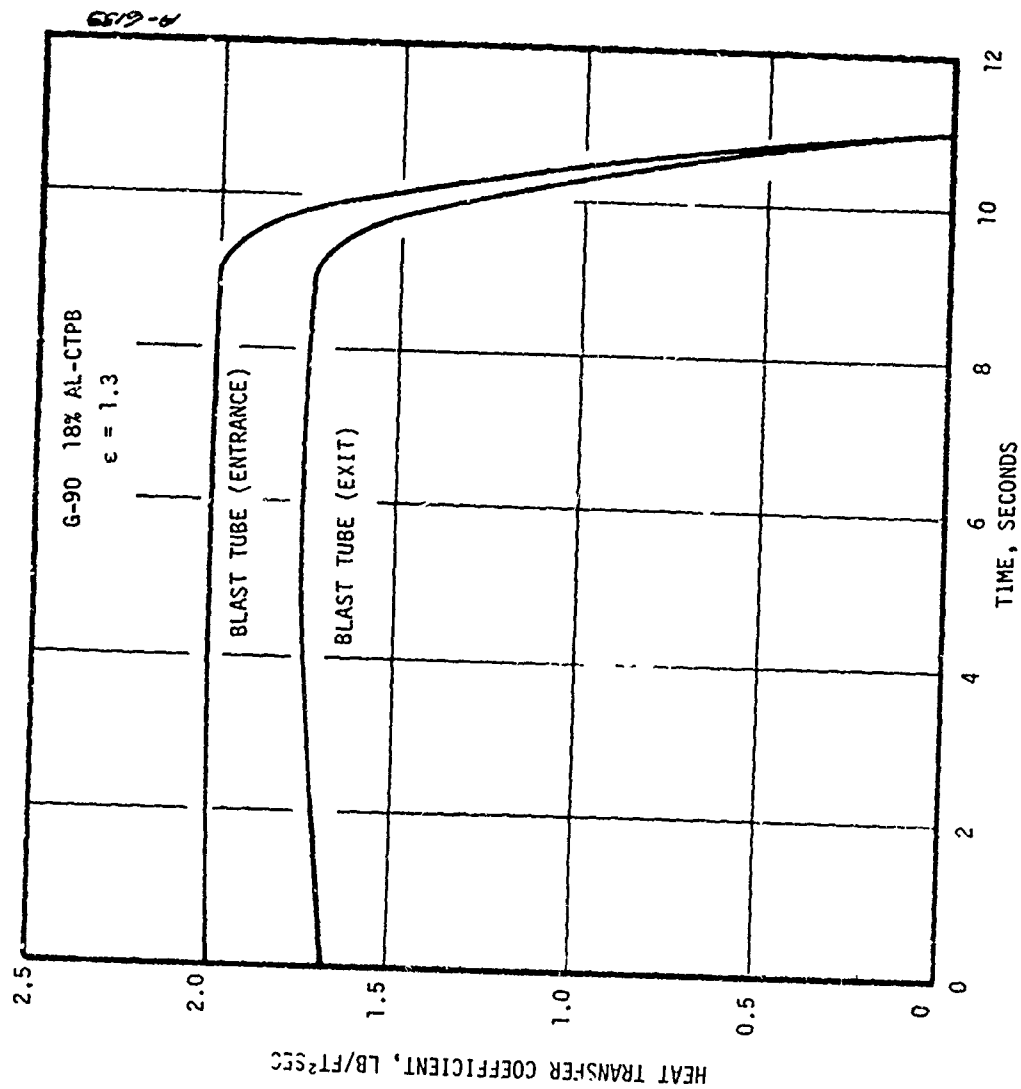


Figure 4-16. Convective Heat Transfer Coefficient Versus Time for G-90 Blast Tube

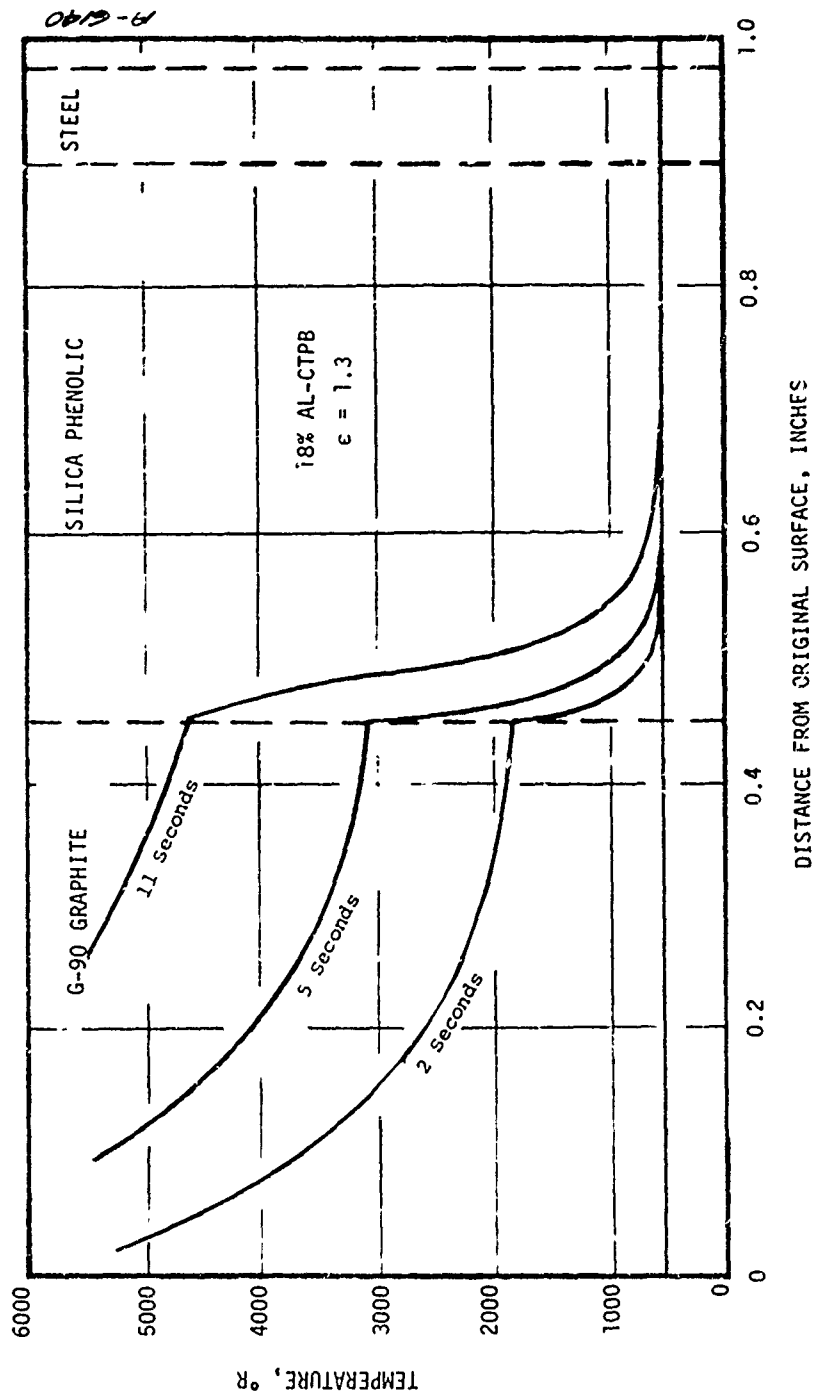


Figure 4-17. Temperature Profiles for C-90 at Blast Tube Entrance  
A) During Exposure

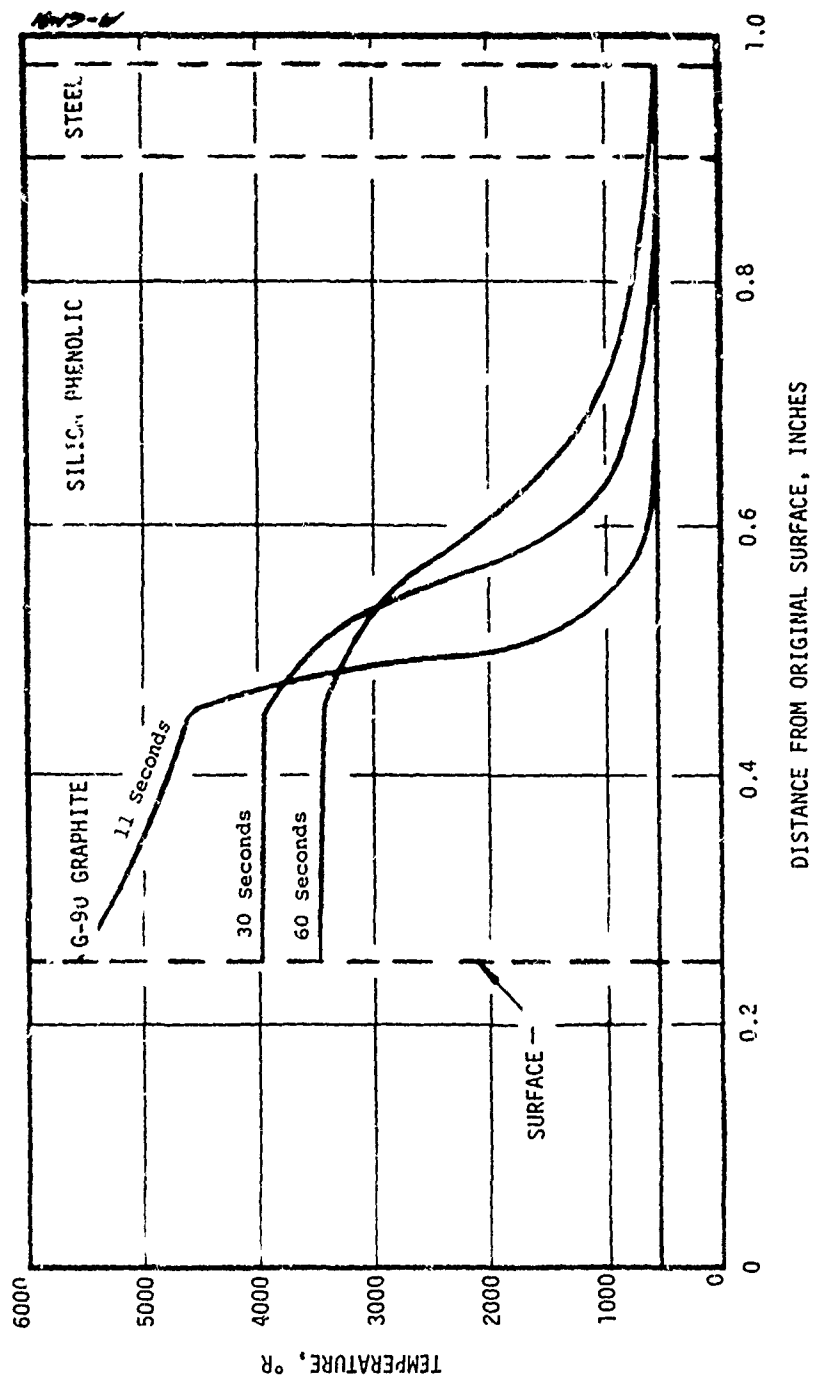


Figure 4-17. Concluded  
B) During Cooldown

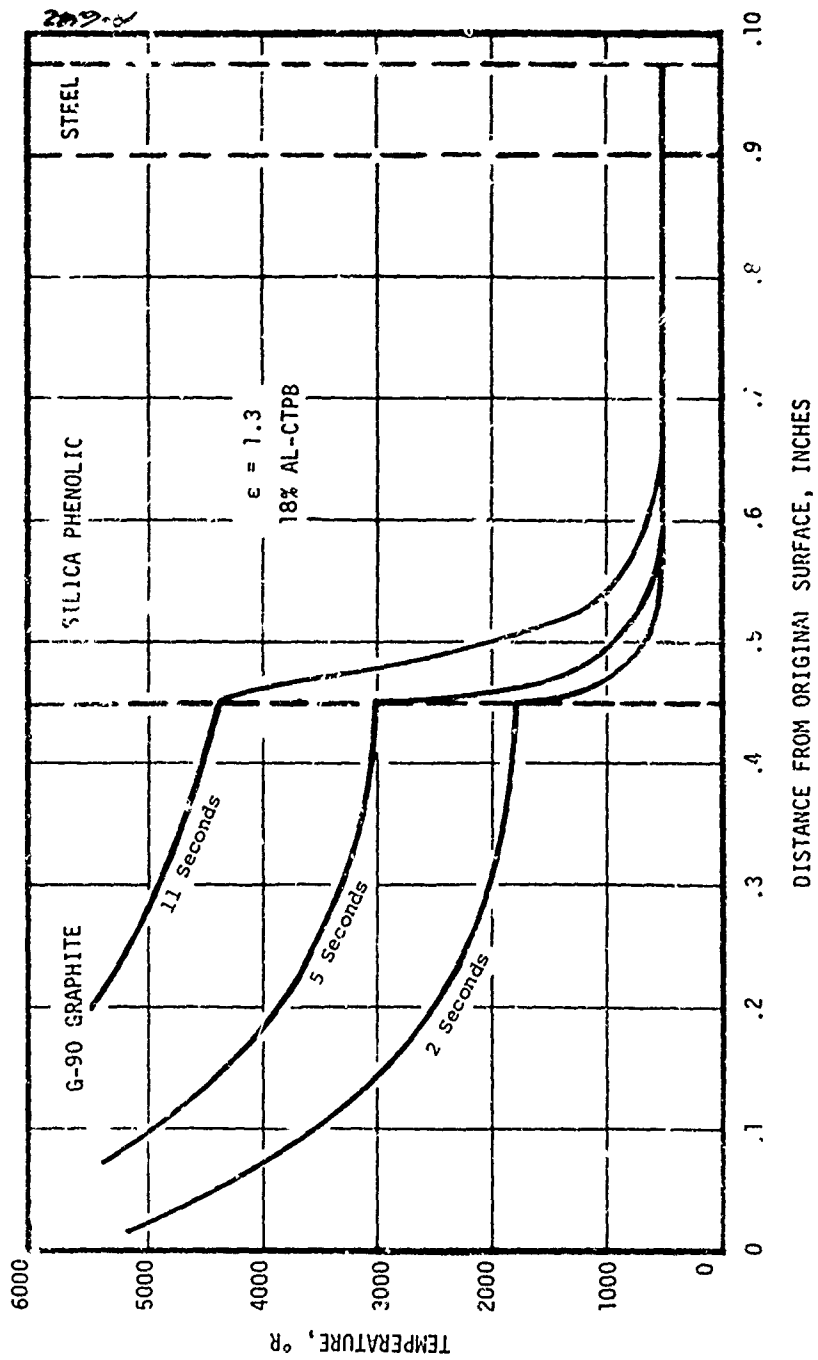


Figure 4-18. Temperature Profiles for G-90 at Blast Tube Exit

A) During Exposure

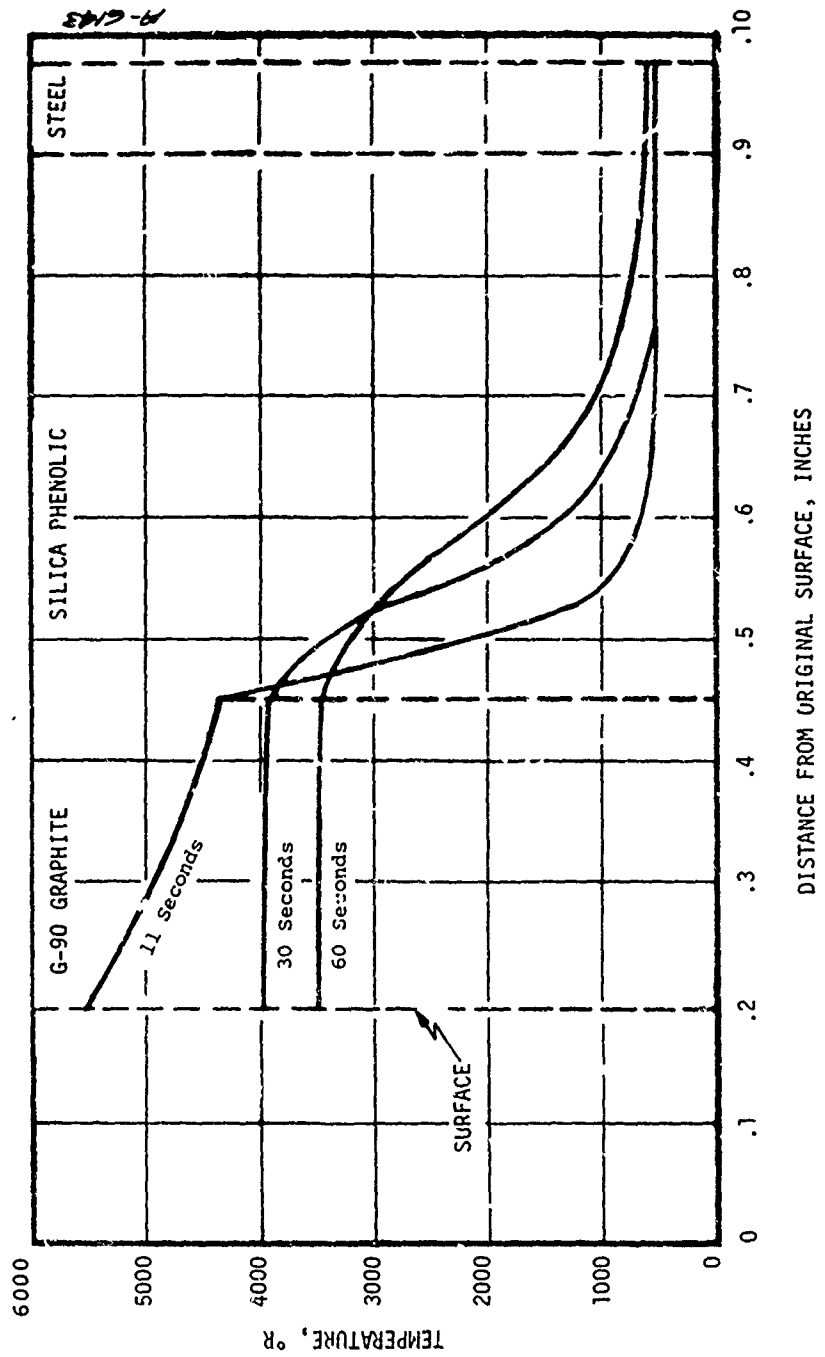


Figure 4-18. Concluded  
B) During Cooldown

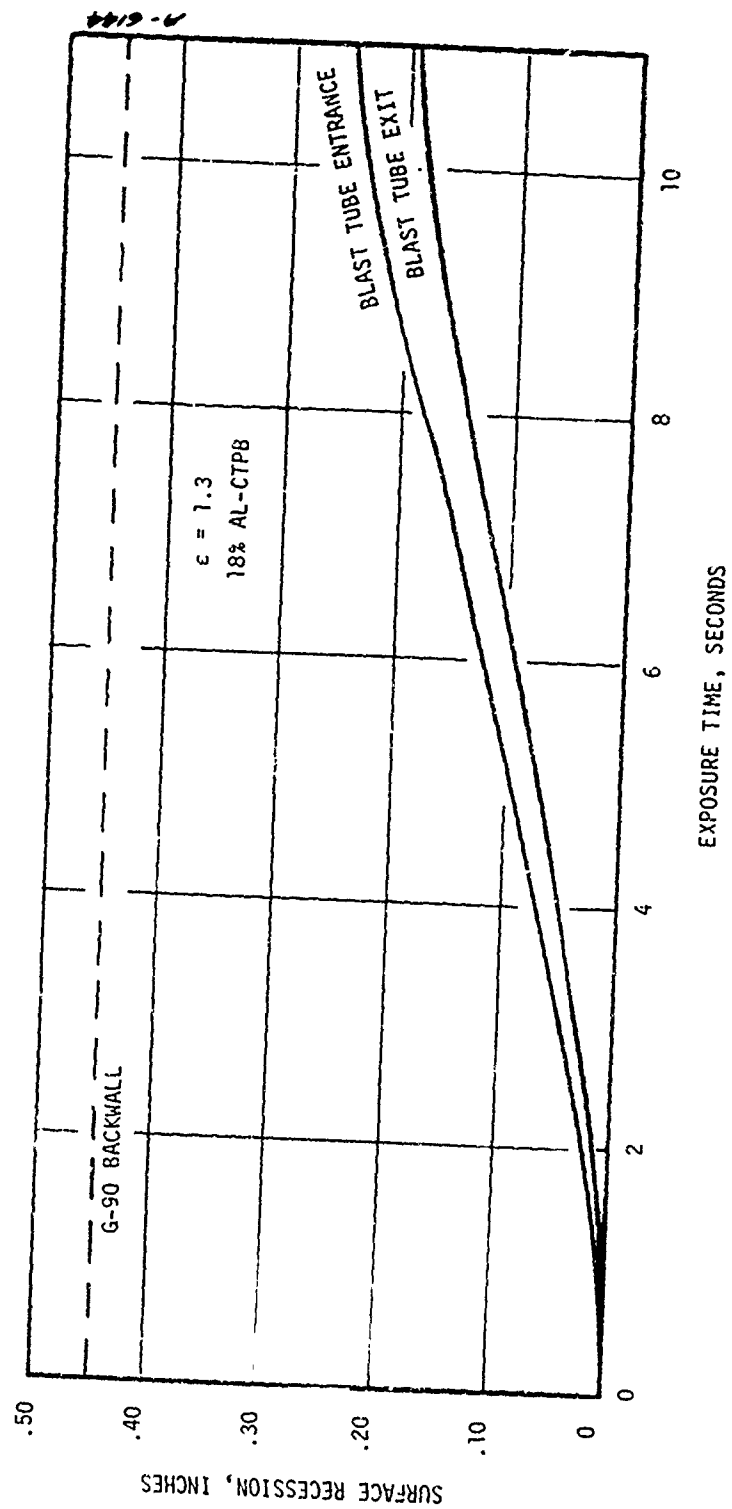


Figure 4-19. Response Histories for G-90 Blast Tube  
A) Surface Recession

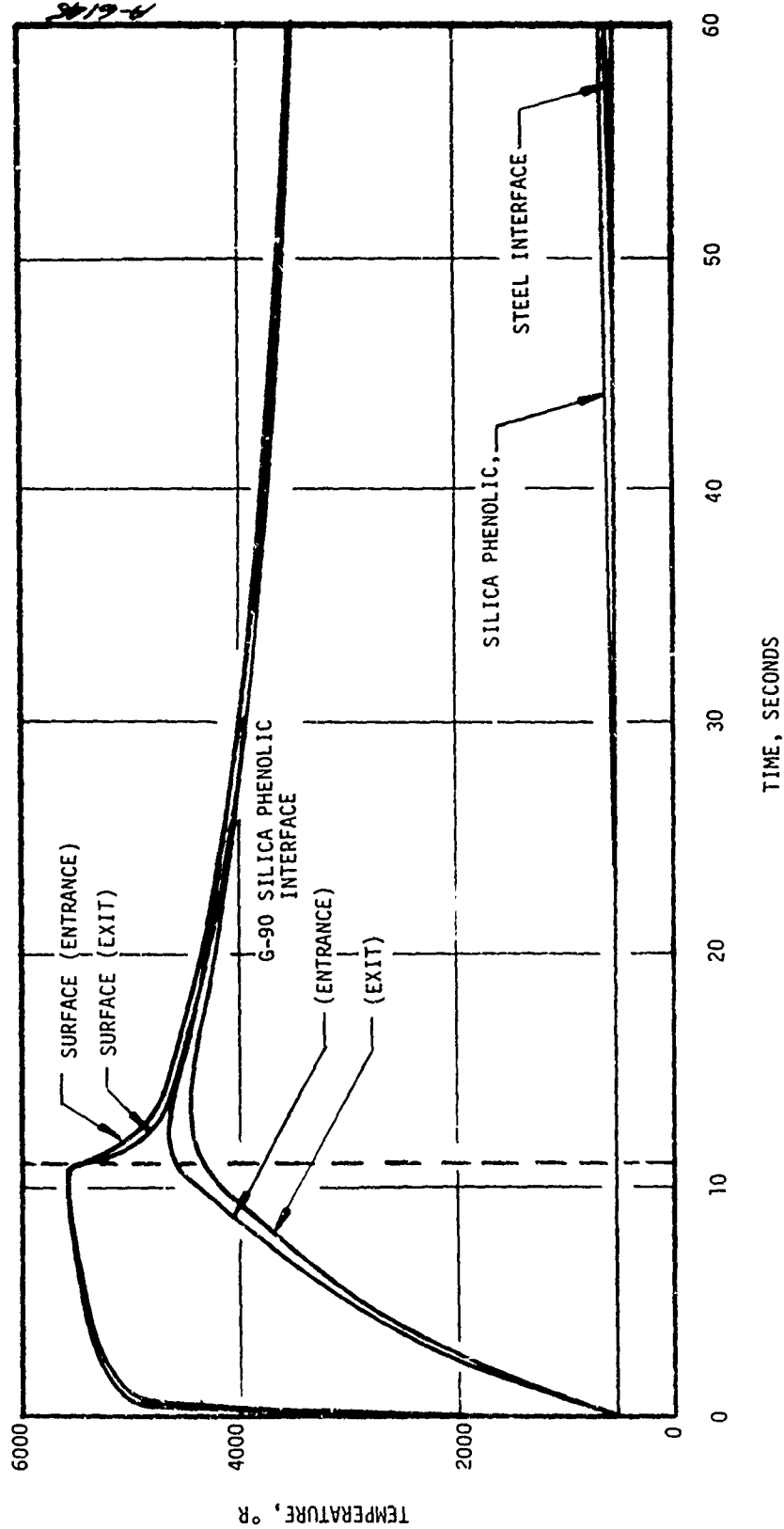


Figure 4-19. Concluded  
B) Surface and Interface Temperatures

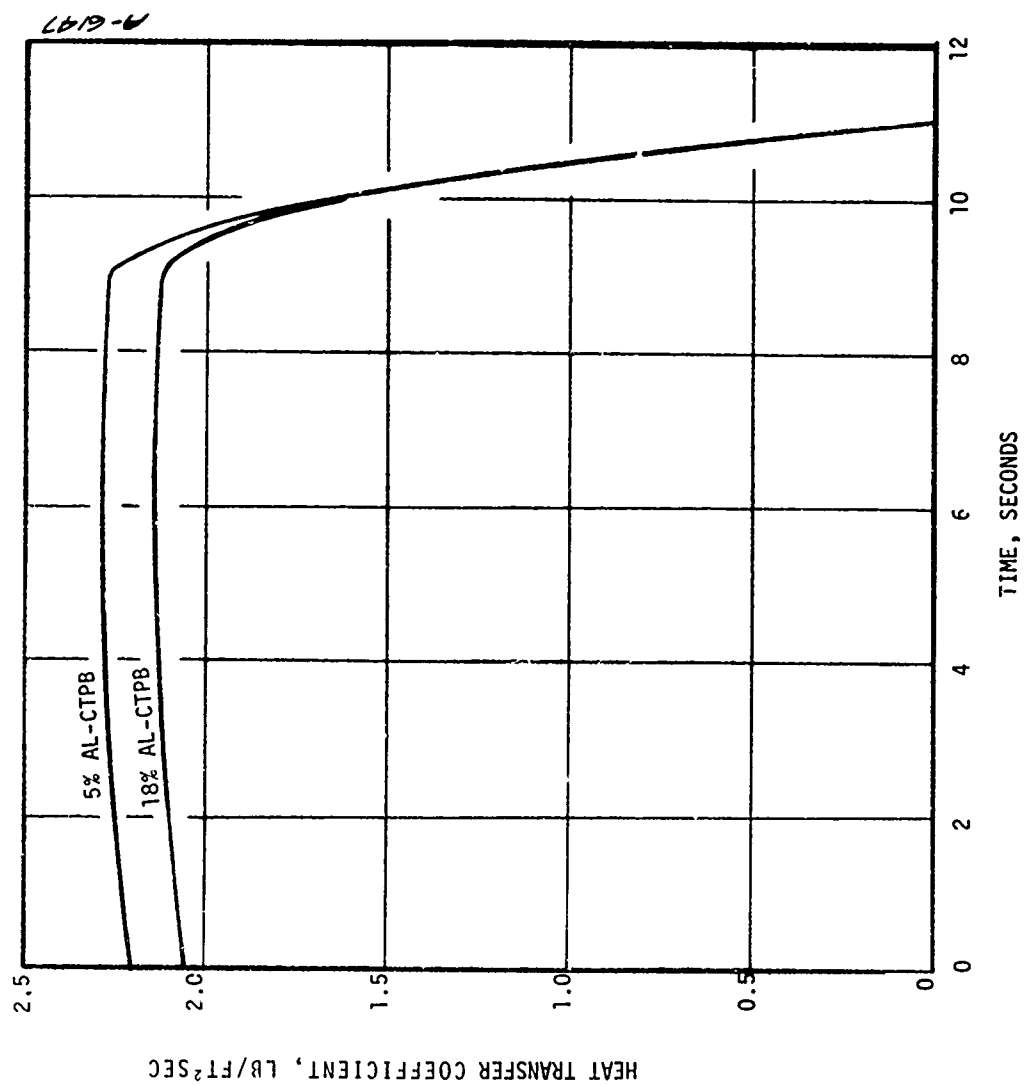


Figure 4-20. Convective Heat Transfer Coefficient Versus Time for Pyrostrand Blast Tube



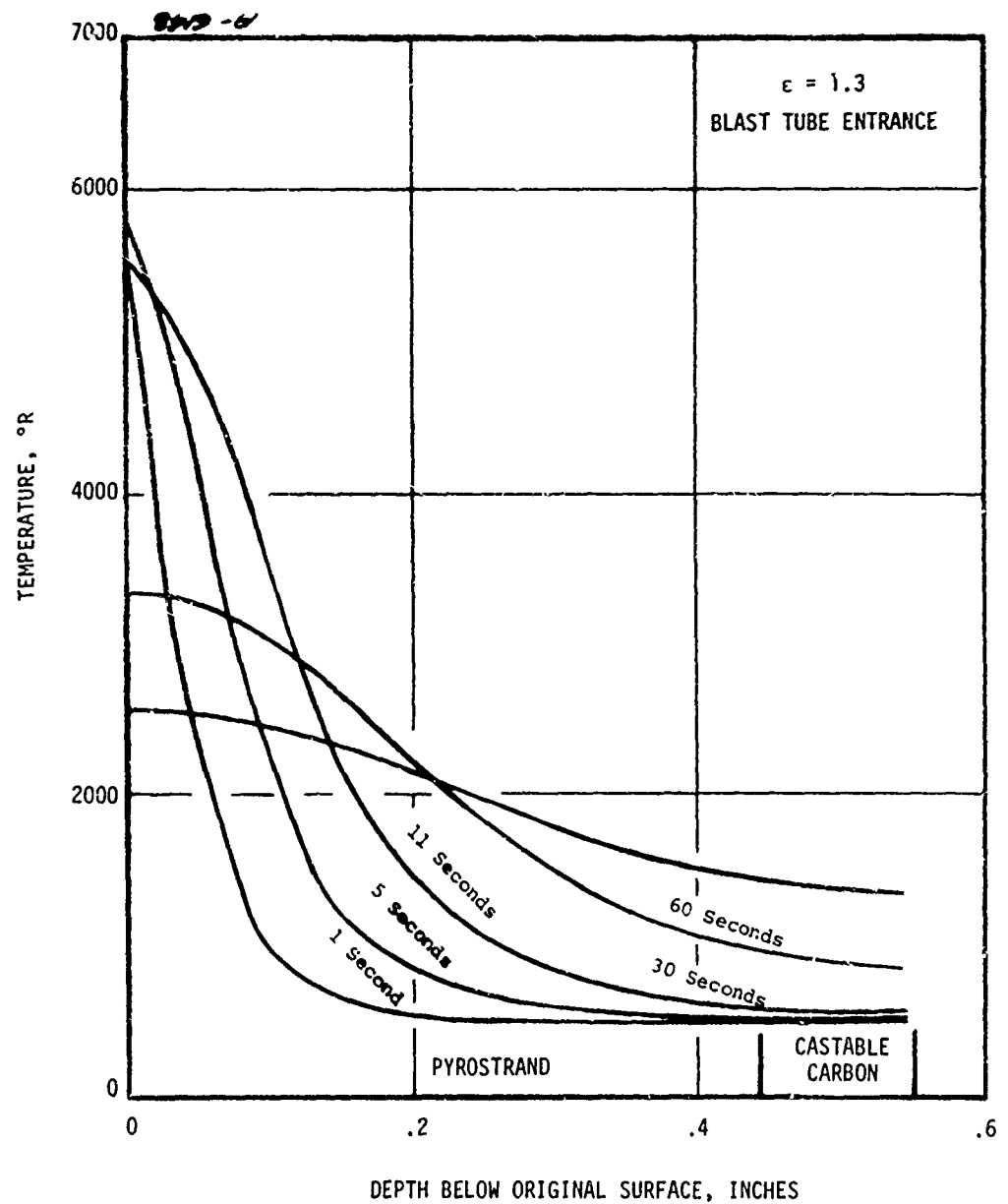


Figure 4-21. Temperature Profiles for Pyrostrand Blast Tube  
A) Exposed to 5 Percent AL-CT?B Propellant

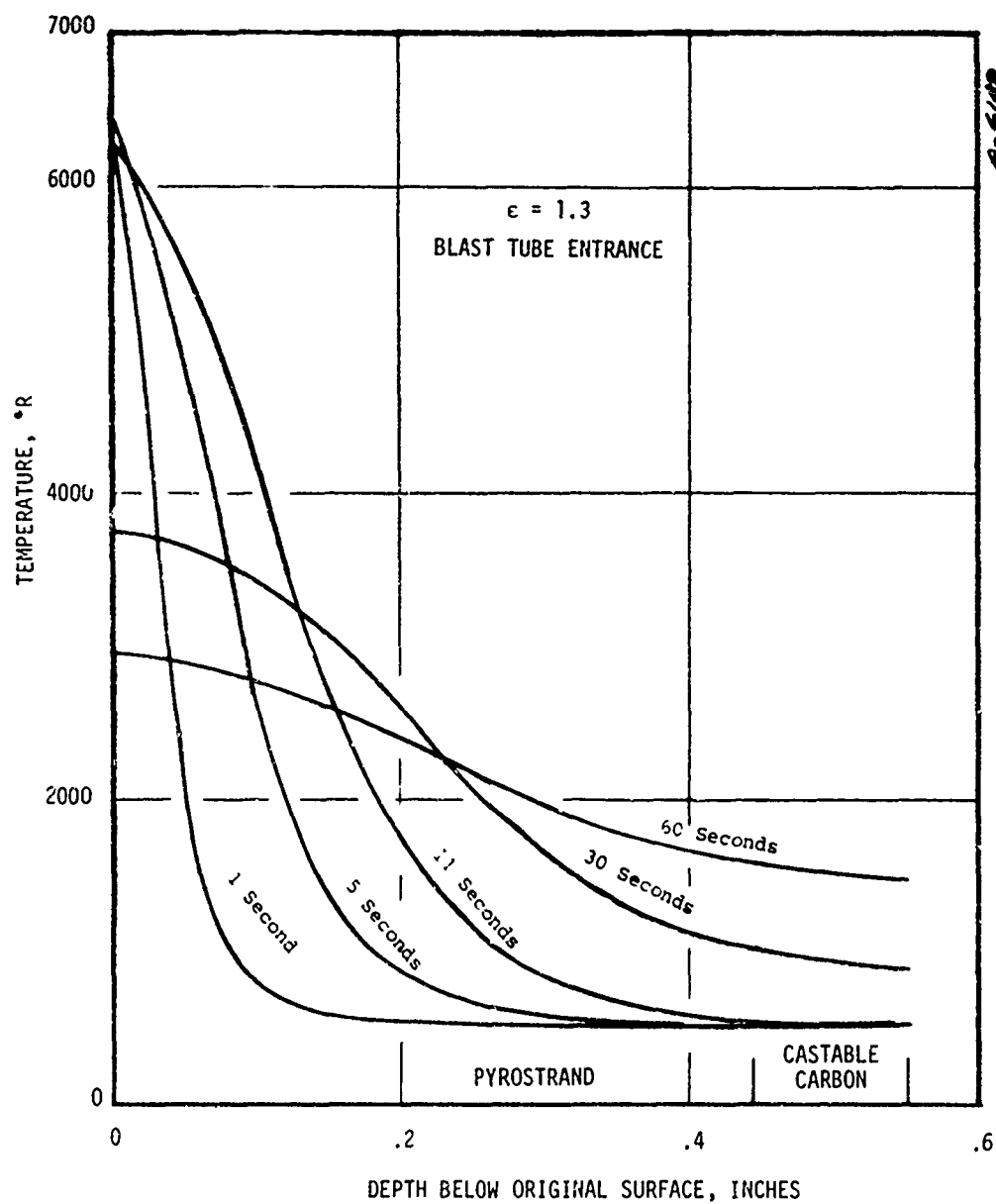


Figure 4-21. Concluded  
B) Exposed to 18 Percent AL-CTPB Propellant

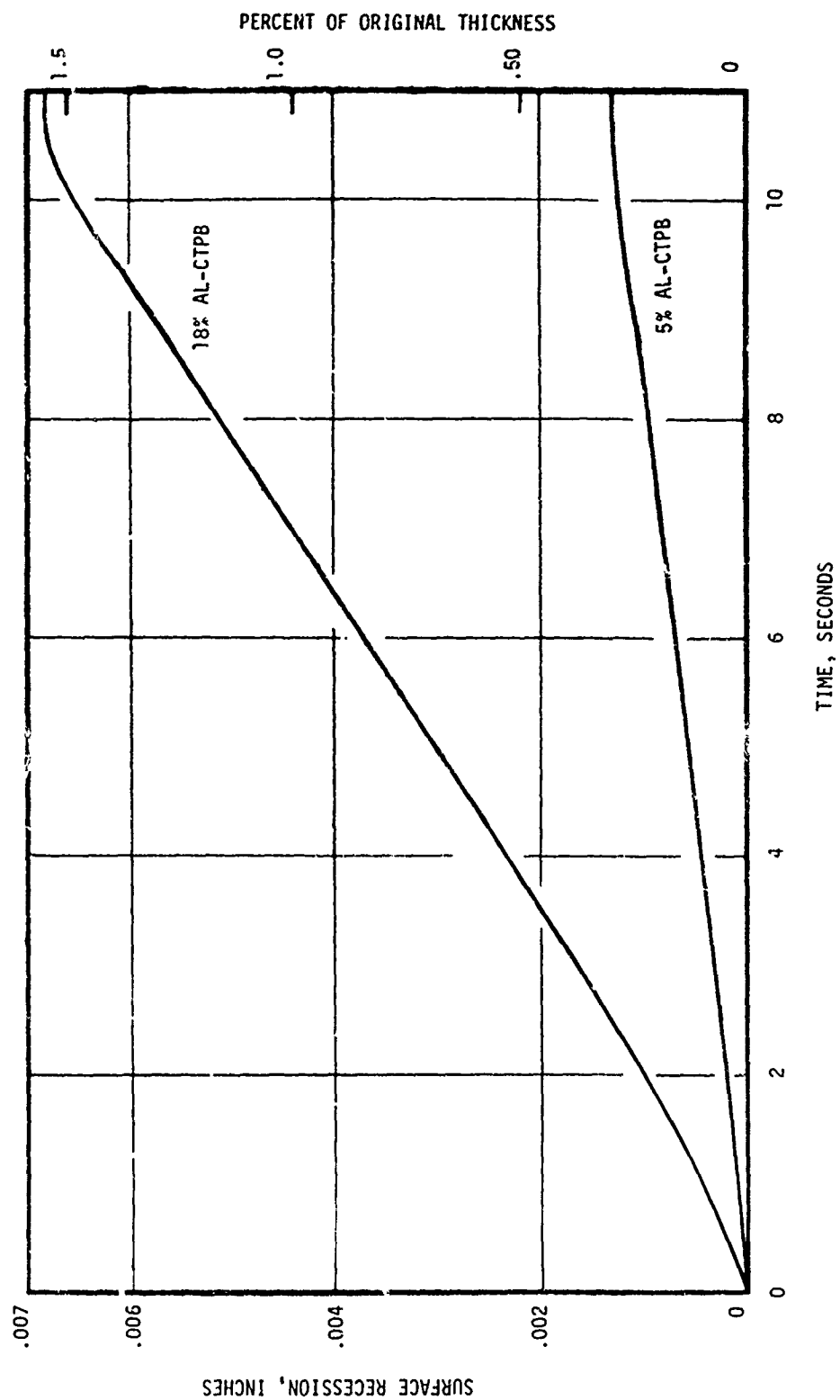


Figure 4-22. Response Histories for Pyrostrand Blast Tube  
A) Surface Recession

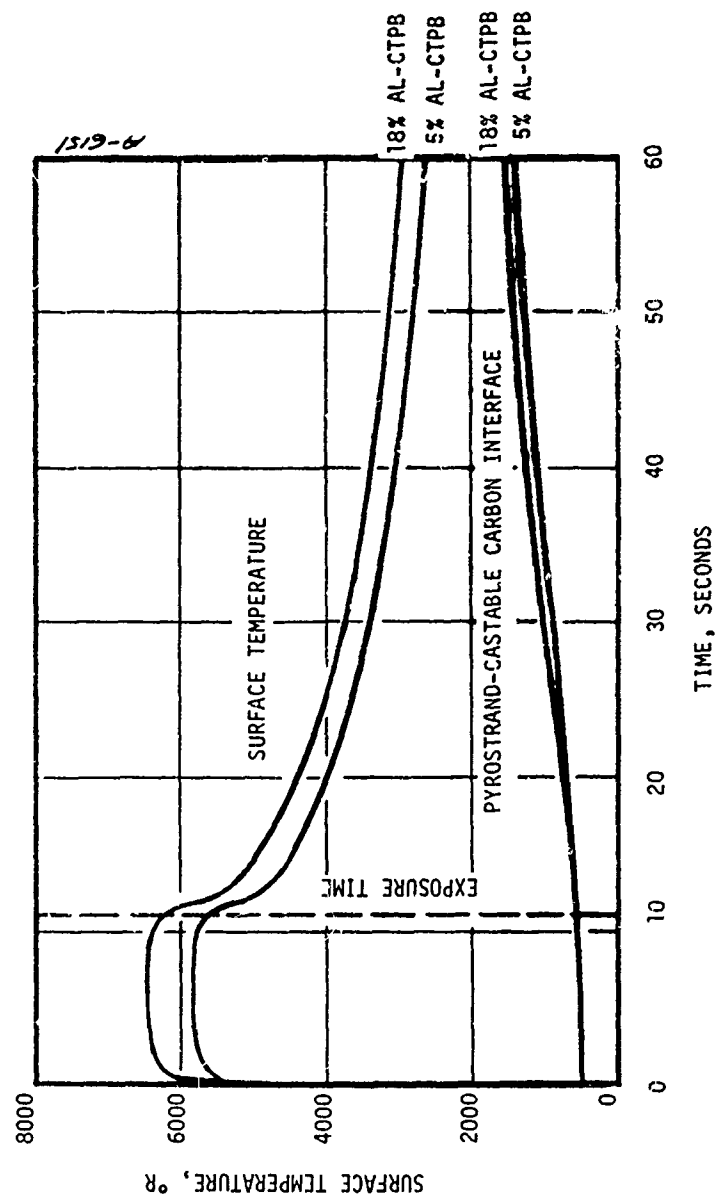


Figure 4-22. Concluded  
B) Surface and Interface Temperatures

## SECTION 5

### NOZZLE THROAT PACKAGE THERMAL RESPONSE PREDICTIONS

The thermochemical screening and in-depth thermal analyses presented in the previous sections provided a rapid but approximate estimate of the thermochemical performance of the candidate materials. To obtain more accurate predictions, in-depth one-dimensional analyses were performed throughout the nozzle using convective heating boundary conditions. This method is considerably more accurate in that it couples the materials response to its environment for transient conditions. These one-dimensional in-depth analyses are suitable for modeling most materials throughout a typical nozzle where two-dimensional conduction effects are negligible. One region in which two-dimensional effects are important is the throat package. In this section, the throat package of the nozzle with a blast tube area ratio of 1.3 and an 18 percent Al-CTPB propellant is analyzed. The ASTHMA computer code was used to assess the two-dimensional effects, and the CMA (one-dimensional) code was used at different locations for comparison.

The input to the ASTHMA code is similar to that used by the CMA code. Propellant data, the flow field analysis, free stream properties, and the heat transfer boundary conditions were all obtained from the information presented in Section 3. Section 5.1 presents the throat package geometry and Section 5.2 summarizes the surface thermochemistry and material property data. The thermal response predictions for the throat package are given in Section 5.3.

#### 5.1 THROAT PACKAGE GEOMETRY

Figure 5-1 illustrates the throat package configuration which was analyzed. It consists of six pyrolytic graphite (PG) washers backed by a section of ATJ graphite which in turn is backed by silica phenolic. The entrance cap is made of G-90 bulk graphite and the retaining ring consists of MX4926 carbon cloth phenolic. Two teflon rings were inserted between three of the PG washers to allow for thermal expansion.

#### 5.2 SURFACE THERMOCHEMISTRY AND MATERIAL PROPERTY DATA

As mentioned in Section 2, the heat conduction solution for a nozzle material using the ASTHMA or CMA codes require a parametric input of surface removal rate as a function of wall temperature and pressure for non-decomposing materials.

These calculations were done using the ACE computer code and are presented in Figure 5-2 for all the materials in the throat package. Note that the PG kinetic curves are based on "old" kinetics. Differences resulting from the "old" kinetics are presented in Section 5.3.2. For materials which exhibit internal decomposition, the surface mass removal rate is also dependent on the pyrolysis off gas rate. Since the ASTHMA code does not model internal decomposition (Section 2), a thermochemistry solution assuming steady state ablation was used for the carbon phenolic retaining ring, and this assumption eliminates the dependence of surface removal rate on the pyrolysis off-gas rate. This solution is also shown in Figure 5-2. In a latter section (Section 5.3.2) it will be shown that this steady state assumption introduces little error into the total surface recession calculations when compared to a one-dimensional CMA solution. The surface thermochemistry calculations for the transient one-dimensional solution are shown in Figure 5-3.

For edge PG and the two bulk graphites, the source of the thermal properties were defined in Section 3. The thermal properties for edge PG and ATJ are presented in Figures 5-4 and 5-5. Since ASTHMA does not account for internal decomposition, the thermal properties for the carbon and silica phenolics were modified to accommodate this. The thermal conductivities are weighted averages between those of virgin and char materials and the specific heats account for energy absorbed by the material during decomposition. For this reason the thermal properties for MX 4926 carbon phenolic and the FM5504 silica phenolic are different for the CMA analysis than for the ASTHMA 2-D analysis. These properties were obtained from Reference 19 and are presented in Figures 5-6 and 5-7. The chamber pressure histories used for the analysis were simplified by UTC and are presented in Figure 5-8.

### 5.3 THERMAL RESPONSE PREDICTIONS

Using the information presented in the previous sections, predictions were made to estimate the thermal response of the components of the throat package. A two-dimensional analysis performed using the ASTHMA code is presented in Section 5.3.1. One-dimensional CMA analyses were done for the throat and MX 4926 retaining ring. These results and their comparisons with the 2-D analysis results are given in Section 5.3.2. Section 5.3.3 presents an analysis of the throat section assuming an insulated boundary condition at the backwall of the PG washers.

### 5.3.1 Two-Dimensional Analysis

Using the geometry, thermochemistry solutions, and material properties given previously, the ASTHMA code was used to predict surface temperatures, in-depth temperatures and surface recession for an 11 second exposure to 18 percent Al-CTPB propellant.

Figure 5-9 presents the predicted isothermal lines generated within the throat package for several elapsed times during the exposure and cooldown. These plots illustrate how the high radial conductivity of the PG washers allows energy to dissipate from the throat surface to the backup materials. Also shown are the insulating effects of the low conductivity carbon phenolic retaining ring. Predicted surface recession is also indicated. In this case the PG washers were predicted to recede 6.3 mils at the throat, an average of 7.7 mils upstream of the throat, and an average of 2.5 mils downstream of the throat. The MX4926 exhibited the most erosion; ranging from .225 inches near the PG washers to .165 inches at the downstream end of the insert. The G-90 bulk graphite was predicted to recede approximately .160 inches.

In calculating the heat transfer coefficient distribution use for this analysis the probable separation of the turbulent boundary layer which occurs downstream of the PG washers was not accounted for. It was assessed that a separation of the flow and subsequent reattachment on the MX4926 insert would result in a higher than calculated heat transfer rate. Figure 5-10 shows the surface contour and isothermal lines in the throat region after the exposure period with an estimate of the gouging caused by the increased heat transfer. All of the isotherm figures illustrate the estimated erosion of the PG washer caused when the upstream G-90 insert recedes faster than the washer. This estimate is necessary since the ASTHMA code accounts only for environmental heating on surfaces parallel to the nozzle centerline.

### 5.3.2 One-Dimensional Analysis Results and Their Comparison to the Two-Dimensional Analysis

Two locations in the throat package were chosen to perform a one-dimensional analysis for comparison to the 2-D results. These locations are at the throat and at the expansion ratio of 1.61 which is in the region of the MX 4926 throat retaining ring.

A total of four one-dimensional analyses were performed at the throat. These correspond to

- 18 percent Al-CTPB, "old" kinetics
- 5 percent Al-CTPB, "old" kinetics
- 18 percent Al-CTPB, "new" kinetics
- 5 percent Al-CTPB, "new" kinetics

The "new" kinetics correspond to the ones currently in the GASKET code and documented in Reference 2.

Figure 5-11 shows the in-depth temperature histories for both the 5 percent and 18 percent Al-CTPB propellant cases using the 1-D analysis and the 18 percent Al-CTPB case using the 2-D analysis. The thermal profiles are shown at the conclusion of the motor firing and at two times during cooldown and are for the "old" kinetics. These results show that the in-depth thermal response given by the one and two dimensional analyses are almost identical. This is due to the highly anisotropic thermal conductivity of the PG washers which allows relatively little energy to flow in the axial direction. Figure 5-11 also illustrates the efficiency of the silica phenolic backup as an insulator. After 60 seconds from startup, the analysis shows that the steel shell is essentially at room temperature. This figure also shows that the 18 percent Al-CTPB propellant results in considerably higher in-depth and surface temperatures than the 5 percent Al-CTPB propellant. This is a direct result of the higher flame temperature of the Al-CTPB propellant.

The corresponding 1-D analysis for both of the propellants using the "new" kinetics showed little effect in the surface and in-depth temperature profiles. For the 18 Al-CTPB propellant, the "new" kinetics led to only a 50°R maximum drop in surface temperature during the firing. The 5 Al-CTPB propellant with the "new" kinetics resulted in only 20°R maximum drop in temperature. Histories for all four 1-D cases and the 2-D case are presented in Figure 5-12. Although the "new" kinetics lead to similar temperatures, the difference in predicted surface recession is significant.

The predicted surface recessions for the throat are shown in Figure 5-13. In general the predicted surface erosion was on the order of 3 to 4 times greater for the "new" kinetics than for the "old" kinetics.



An expansion ratio of 1.61 was chosen to perform one-dimensional CMA analyses for the MX4926 throat retaining ring. This location is shown in Figure 5-9A. These results were used to compare 1-17 2-D results and to determine the accuracy of the ASTHMA code in handling charring ablators. Figure 5-11 presents the in-depth temperature profiles for both the one and two dimensional solutions after an 11 second firing. The CMA analysis gave lower temperatures and a lower surface recession. Since the CMA code was designed to analyze internally decomposing materials, it was felt that the surface recession and temperatures close to the surface were predicted more accurately by this code. Actual 2-D effects near the surface were considered negligible at the analysis location as evidenced by the isothermal lines shown in Figure 5-9. This figure also indicates that 2-D heat conduction effects are sizable at depths greater than the PG washer backwall for an elapsed time of 11 seconds at the location of interest. Physically, the PG washers conduct heat into the ATJ graphite backup which causes axial heat conduction into the neighboring MX4926 retainer. For these reasons, the actual in-depth thermal profile is a combination of the profiles given by the two analyses. This estimate is shown in Figure 5-14.

In-depth thermal profiles predicted by the 2-D analysis for six different times during the motor firing and subsequent cooldown are illustrated in Figure 5-15. This figure indicates that the thermal protection provided by the silica phenolic backup is sufficient to keep the steel shell from a significant rise in temperature. Figures 5-16 and 5-17 compare the surface recessions and surface temperatures given by the 1-D and 2-D analyses. As mentioned above, the one-dimensional analysis gives a better estimate of the surface recession and surface temperature. Both analyses do not account for possible surface gouging caused by flow separation as mentioned in Section 5.3.1. A rough estimate of the total gouging effect was given in Figure 5-10.

### 5.3.3 PG Washer Backwall Insulation Effects

To estimate the effects of the PG backwall boundary condition on the thermal response of the PG washers, a one-dimensional analysis was performed using an insulated PG backwall boundary condition. The sensitivity of the surface recession to this boundary condition is of interest due to the possibility of a gap between the washers and ATJ backup. Results of this study are shown in Figures 5-18 and 5-19. Using the "new" kinetics and the thermochemistry of the 18 percent Al-CTPB propellant the insulated backwall boundary condition caused a small increase in surface temperature and approximately a 25 percent increase in surface recession.

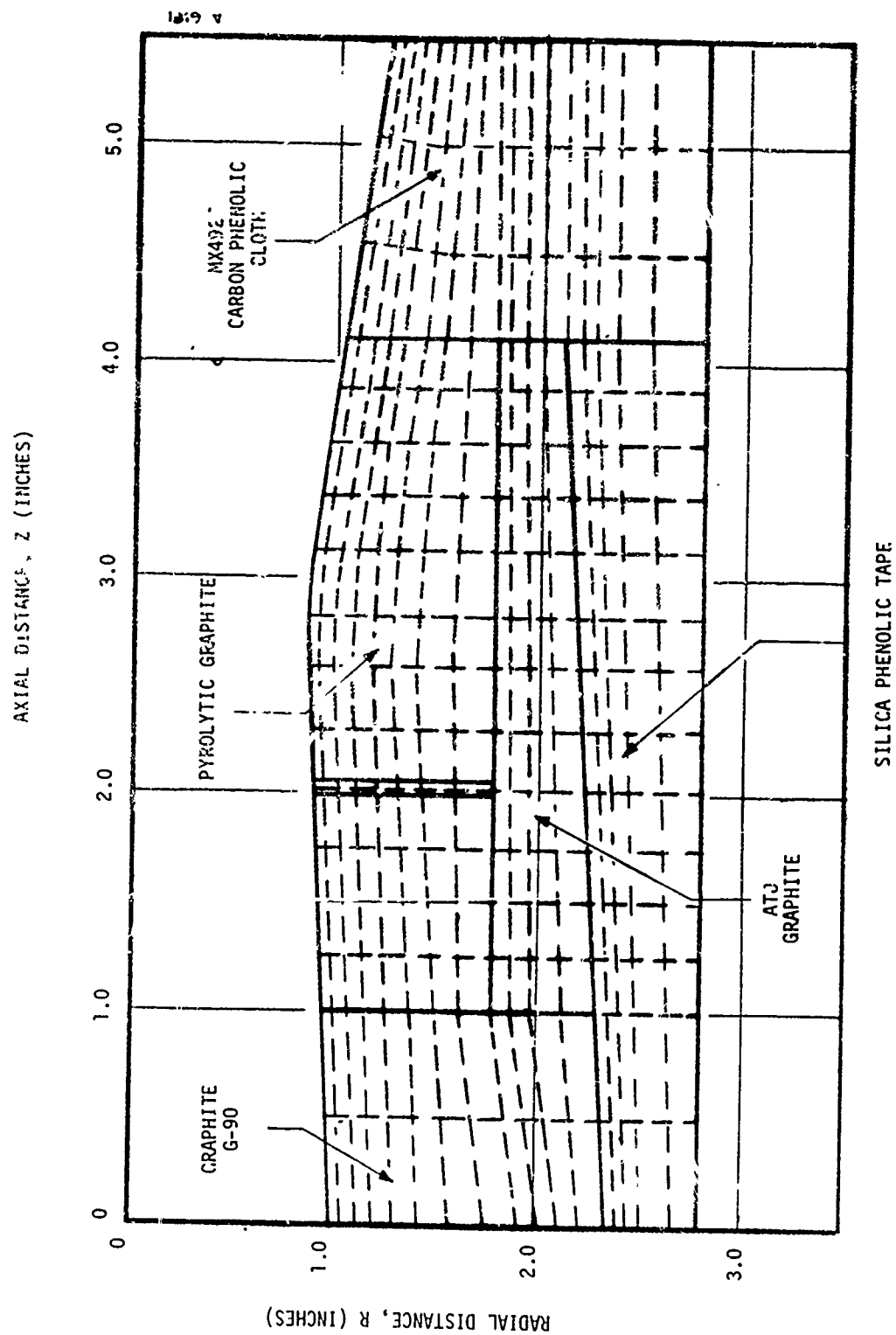


Figure 5-1. Throat Package Geometry for 2-D Analysis

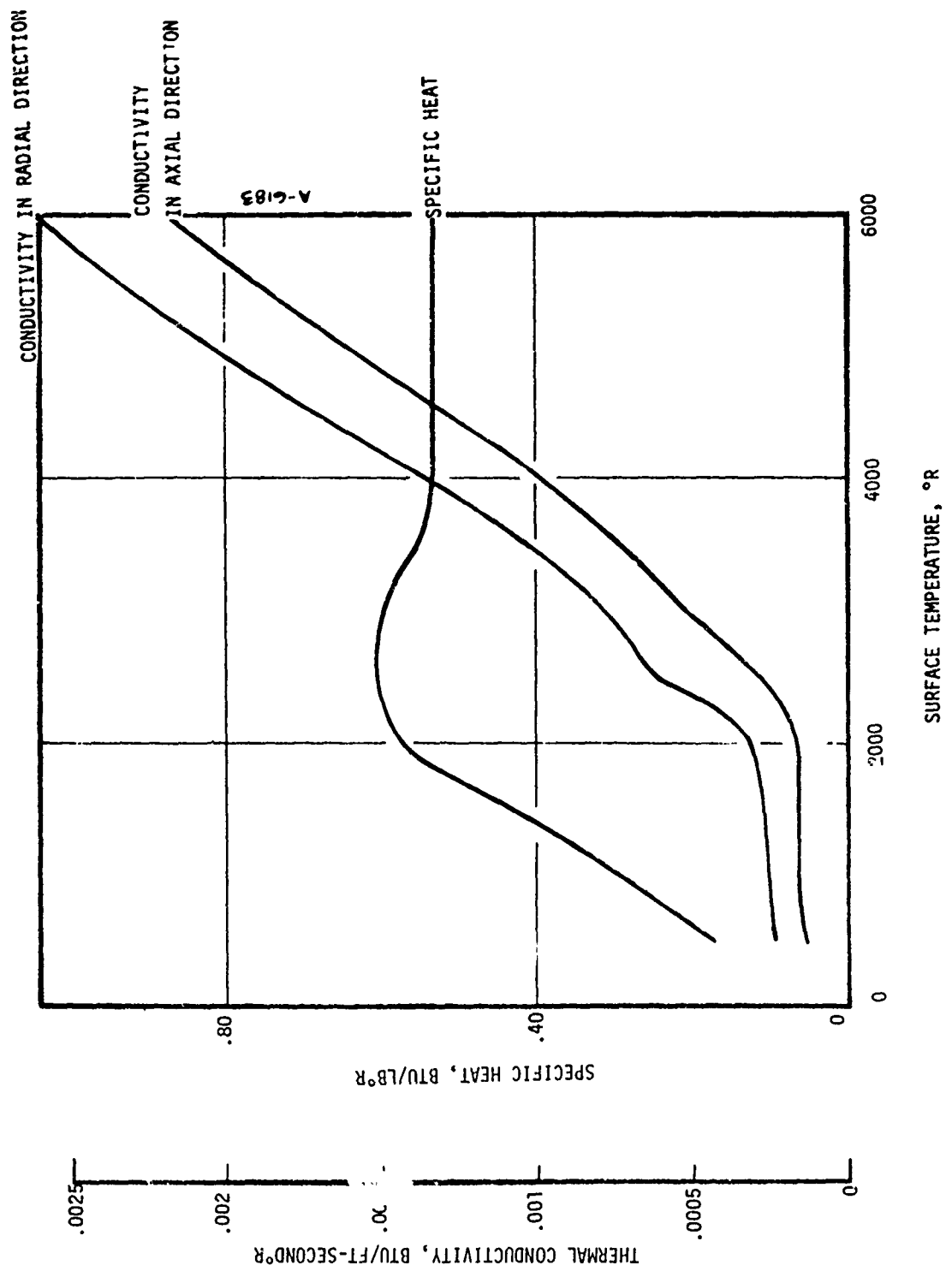


Figure 5-6. Estimated Thermal Properties of MX4926 Accounting For Internal Decomposition

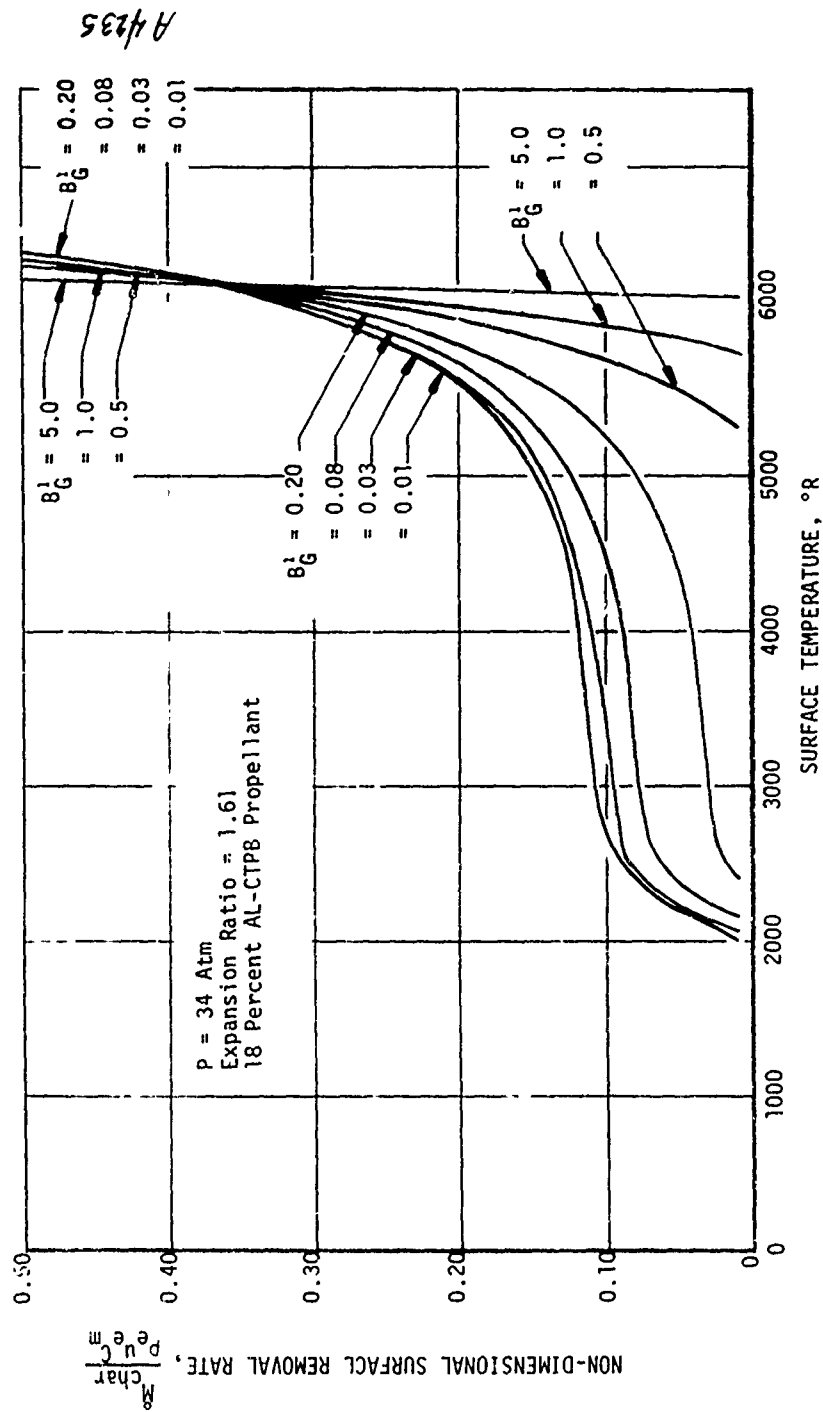


Figure 5-3. Transient Surface Thermochemical Response of MX4926 Carbon-phenolic at the Throat Retaining Ring Location

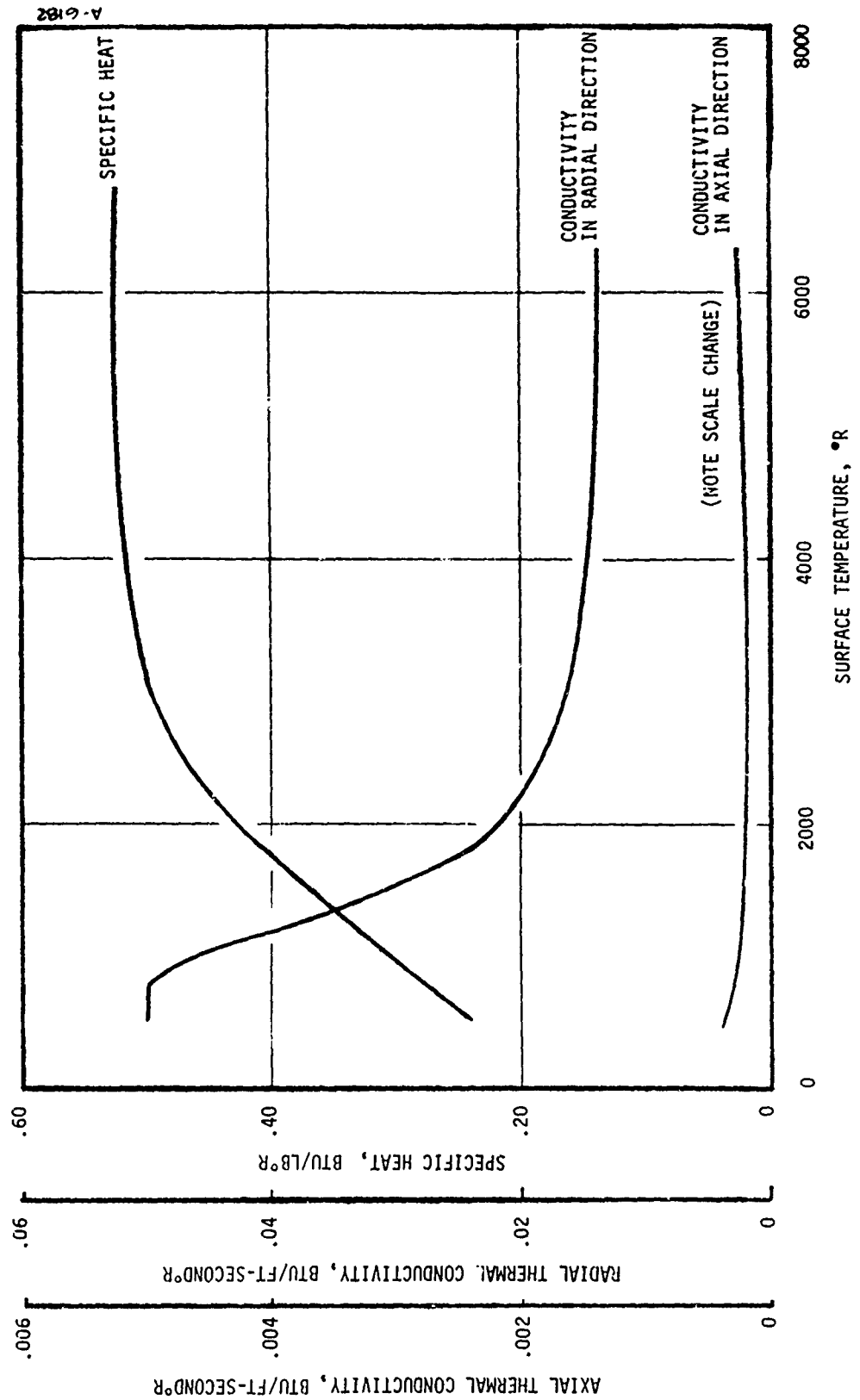


Figure 5-4. Thermal Properties of Edge Oriented Pyrolytic Graphite

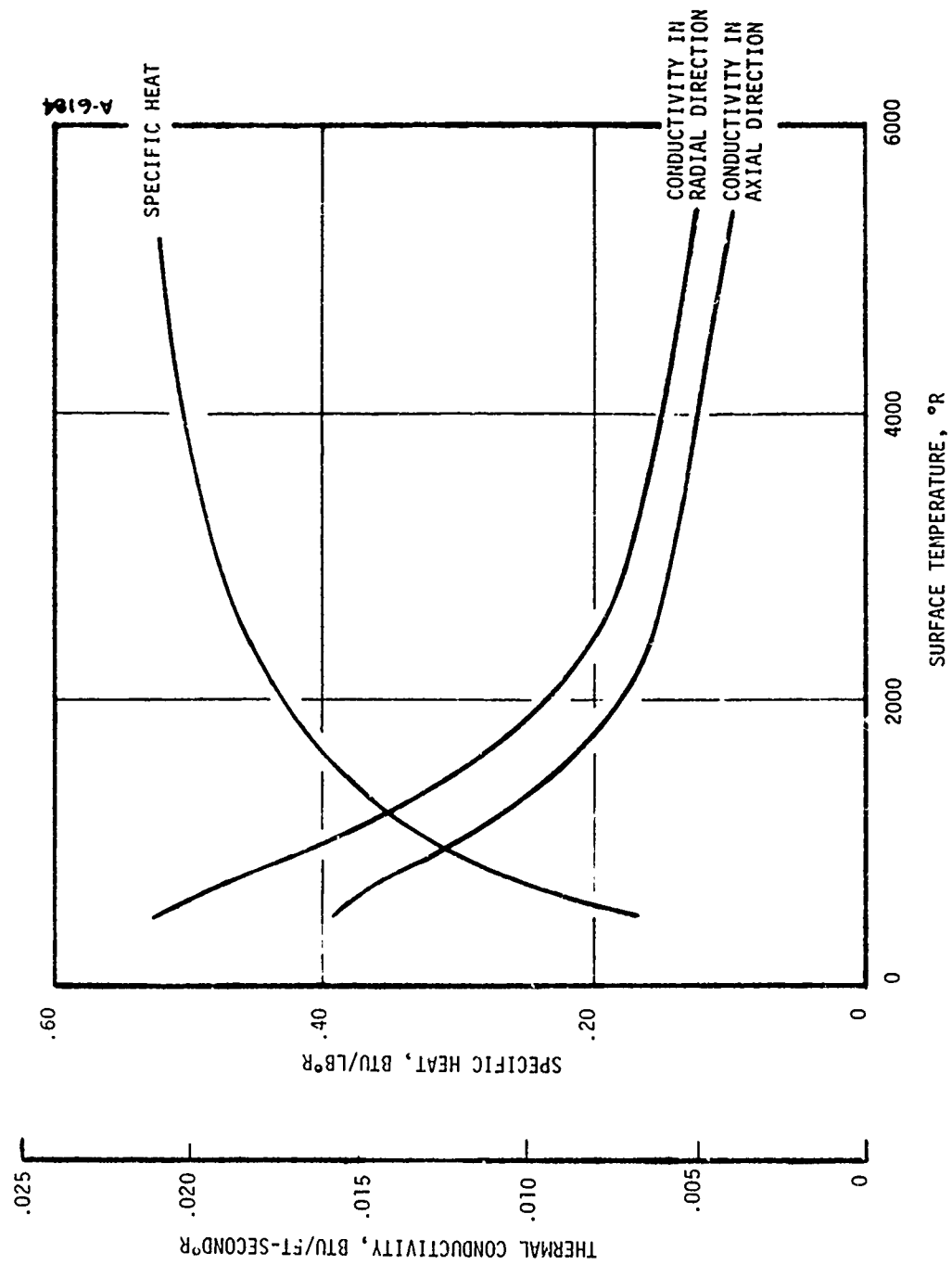


Figure 5-5. Thermal Properties of ATJ Bulk Graphite

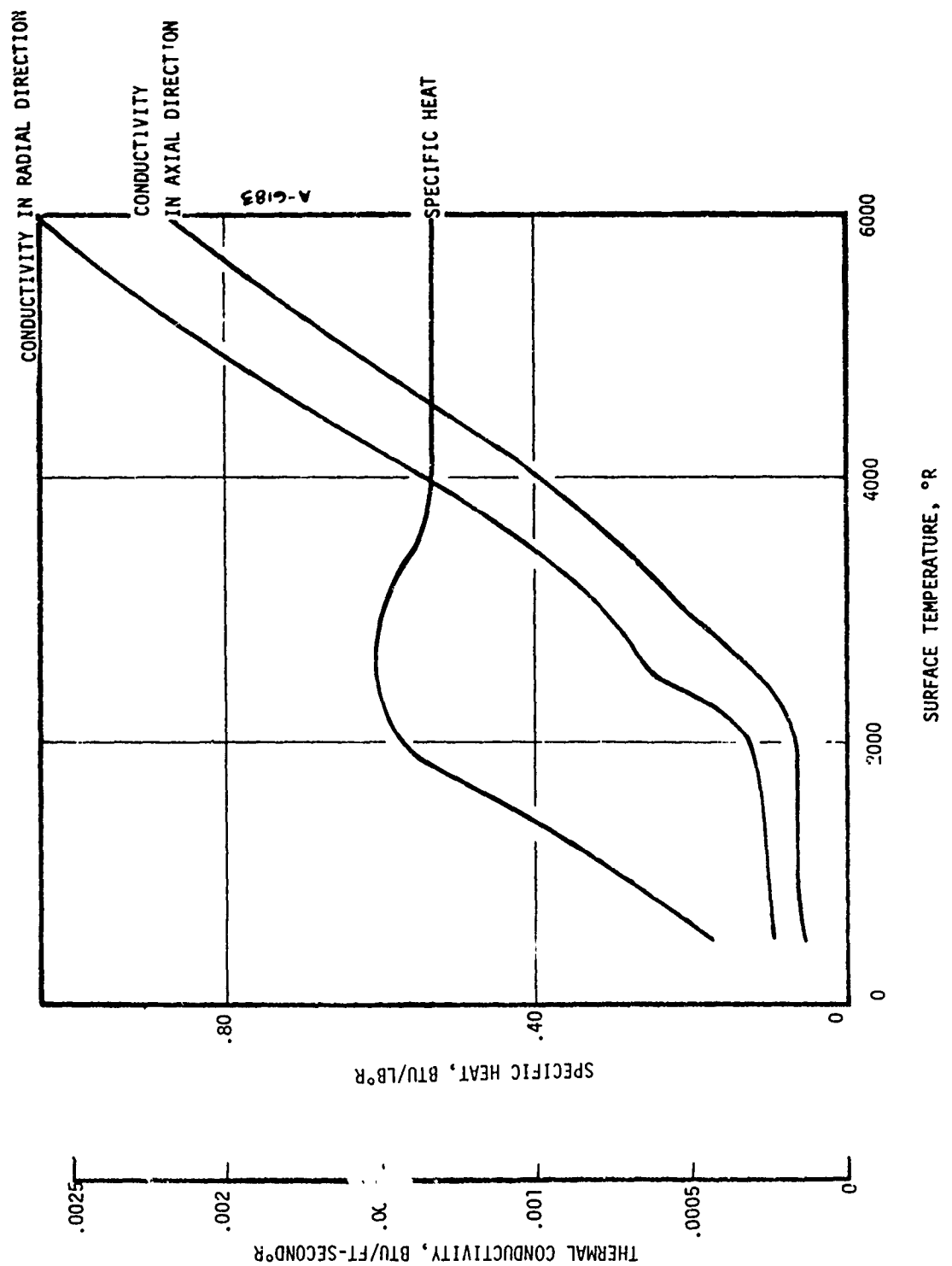


Figure 5-6. Estimated Thermal Properties of MX4926 Accounting For Internal Decomposition

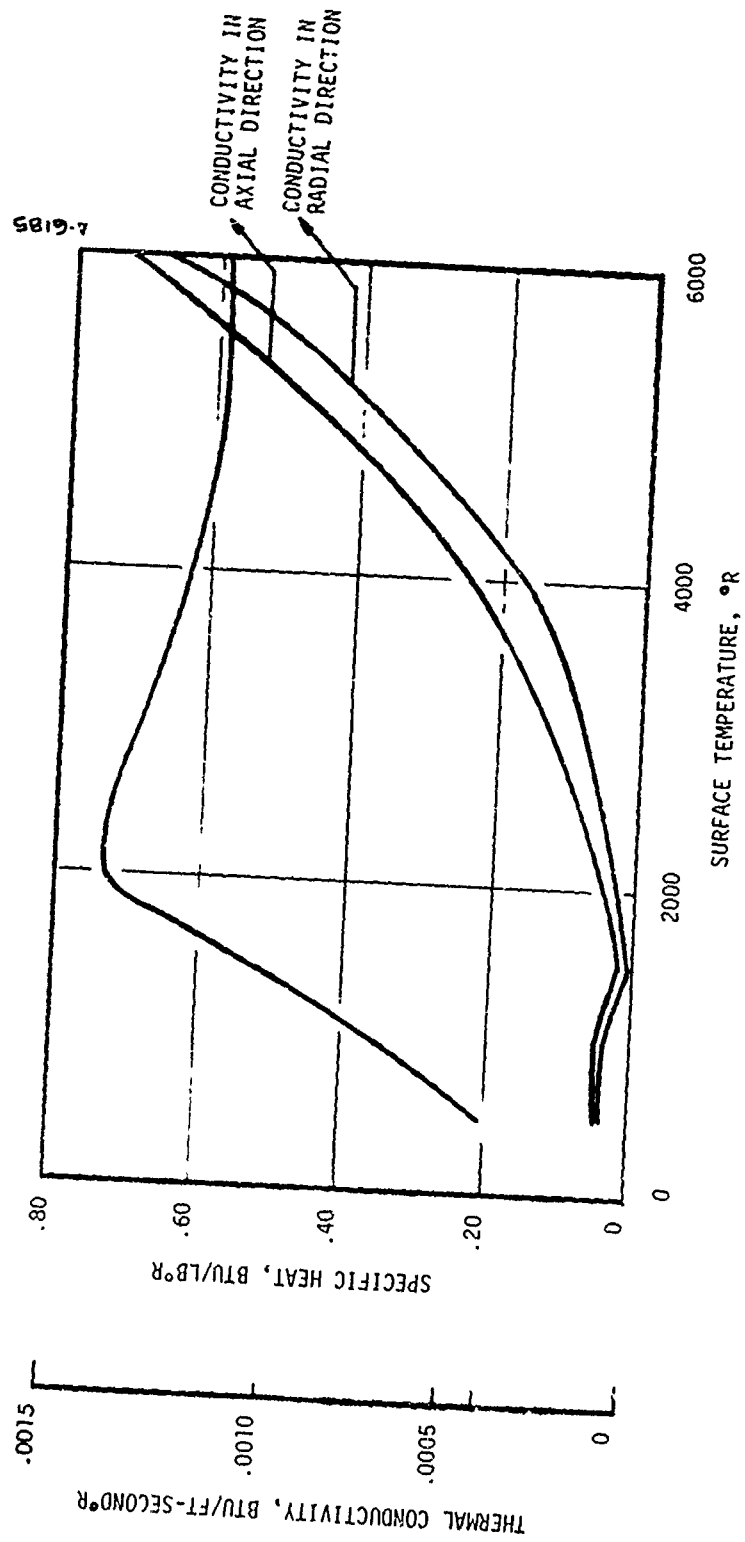


Figure 5-7. Estimated Thermal Properties of Silica Phenolic Accounting for Internal Decomposition



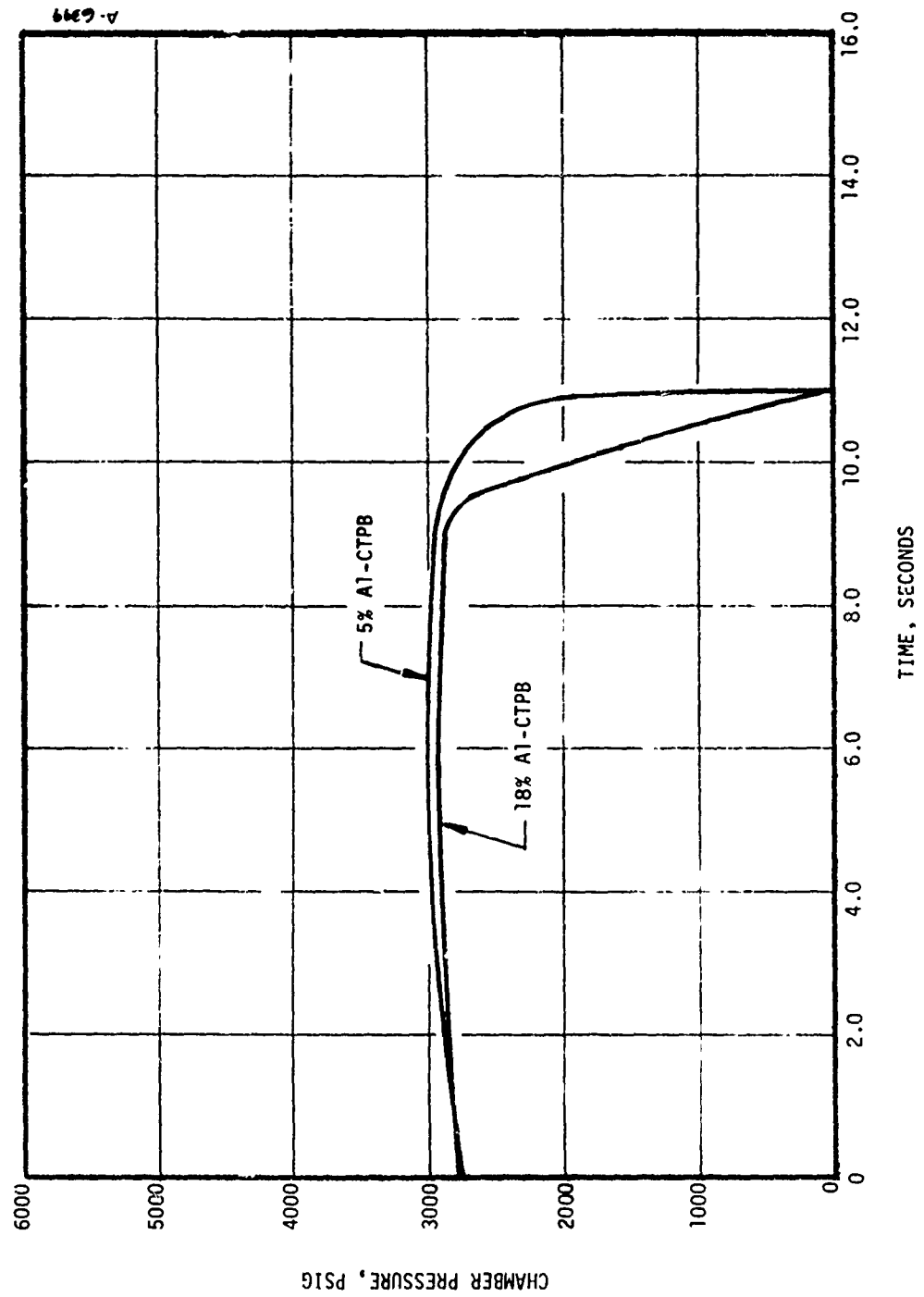


Figure 5-8. Chamber Pressure History for Throat Package Analyses

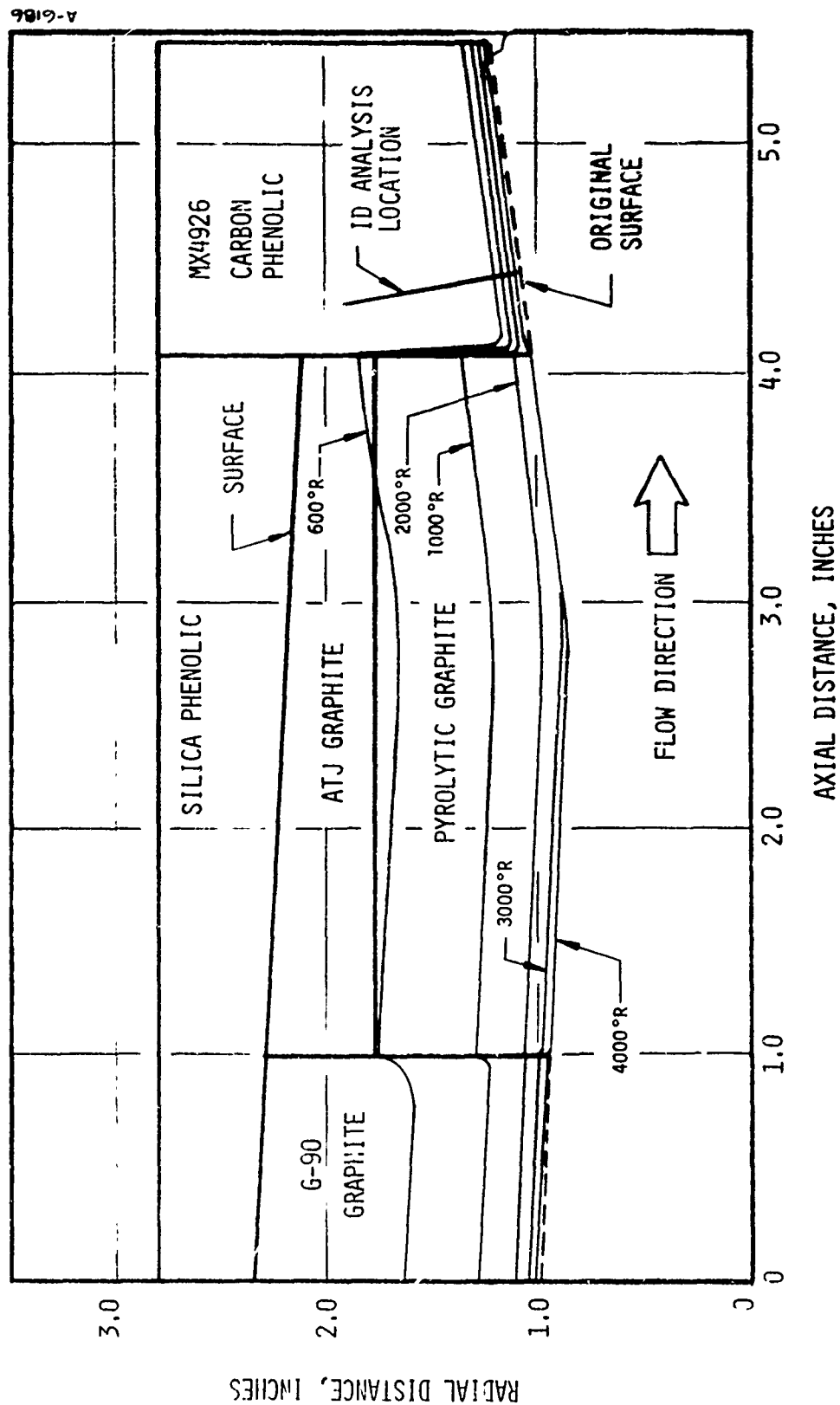


Figure 5-9. Isothermal Locations in Throat Package  
 A) Exposure Time = 0.5 Seconds

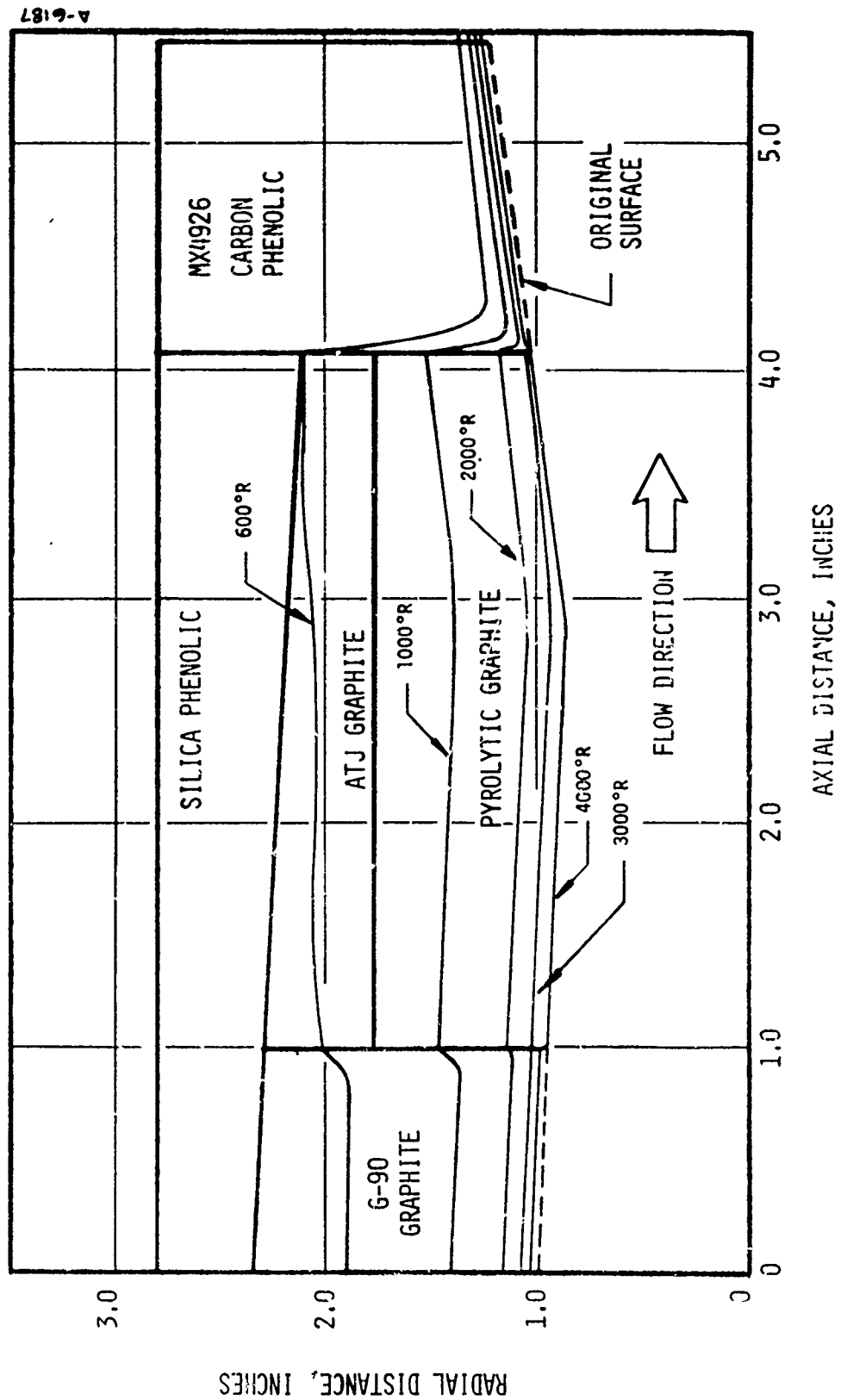


Figure 5-9. Continued

B) Exposure Time = 1.0 Seconds

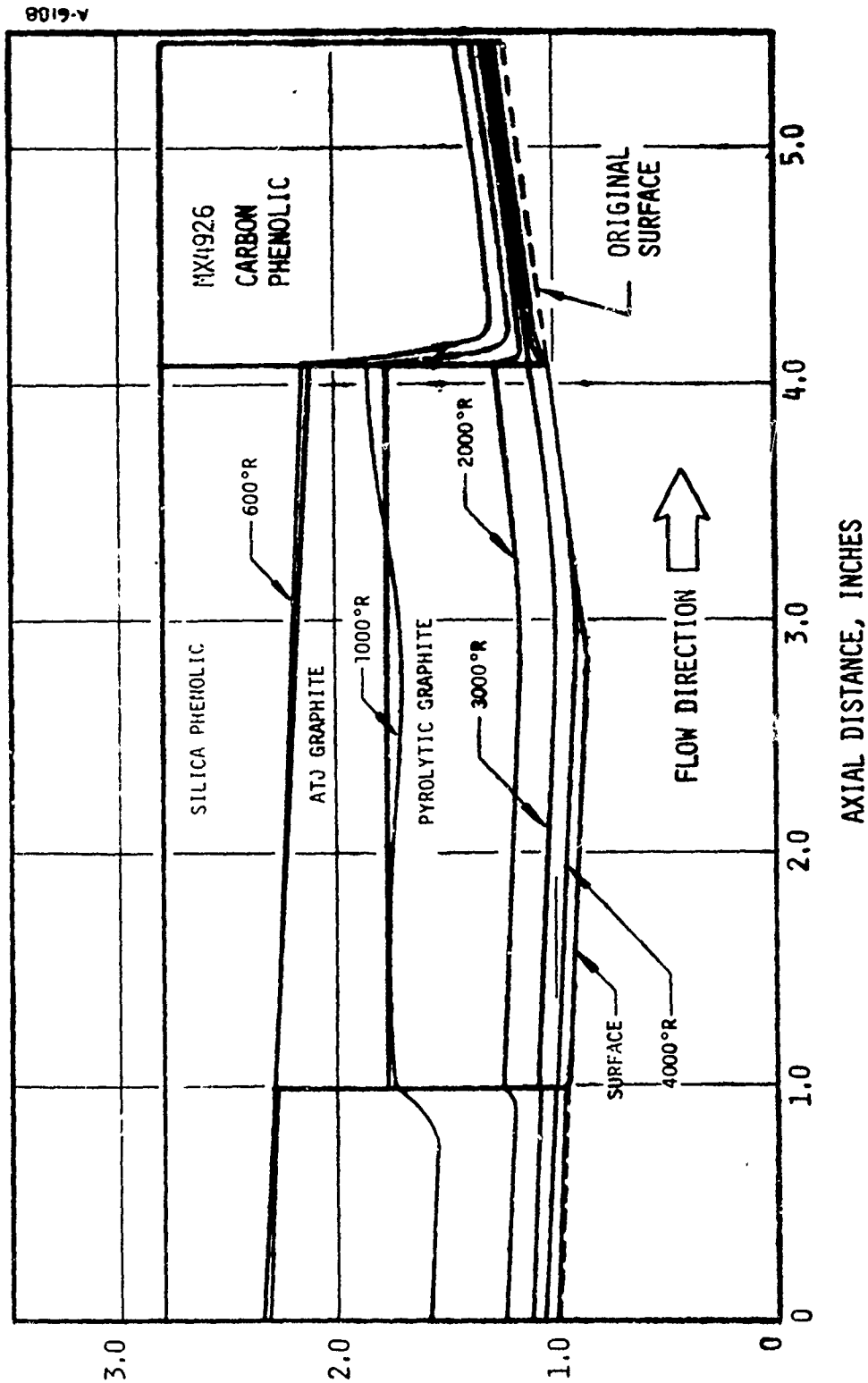


Figure 5-9. Continued

C) Exposure Time = 2.0 Seconds

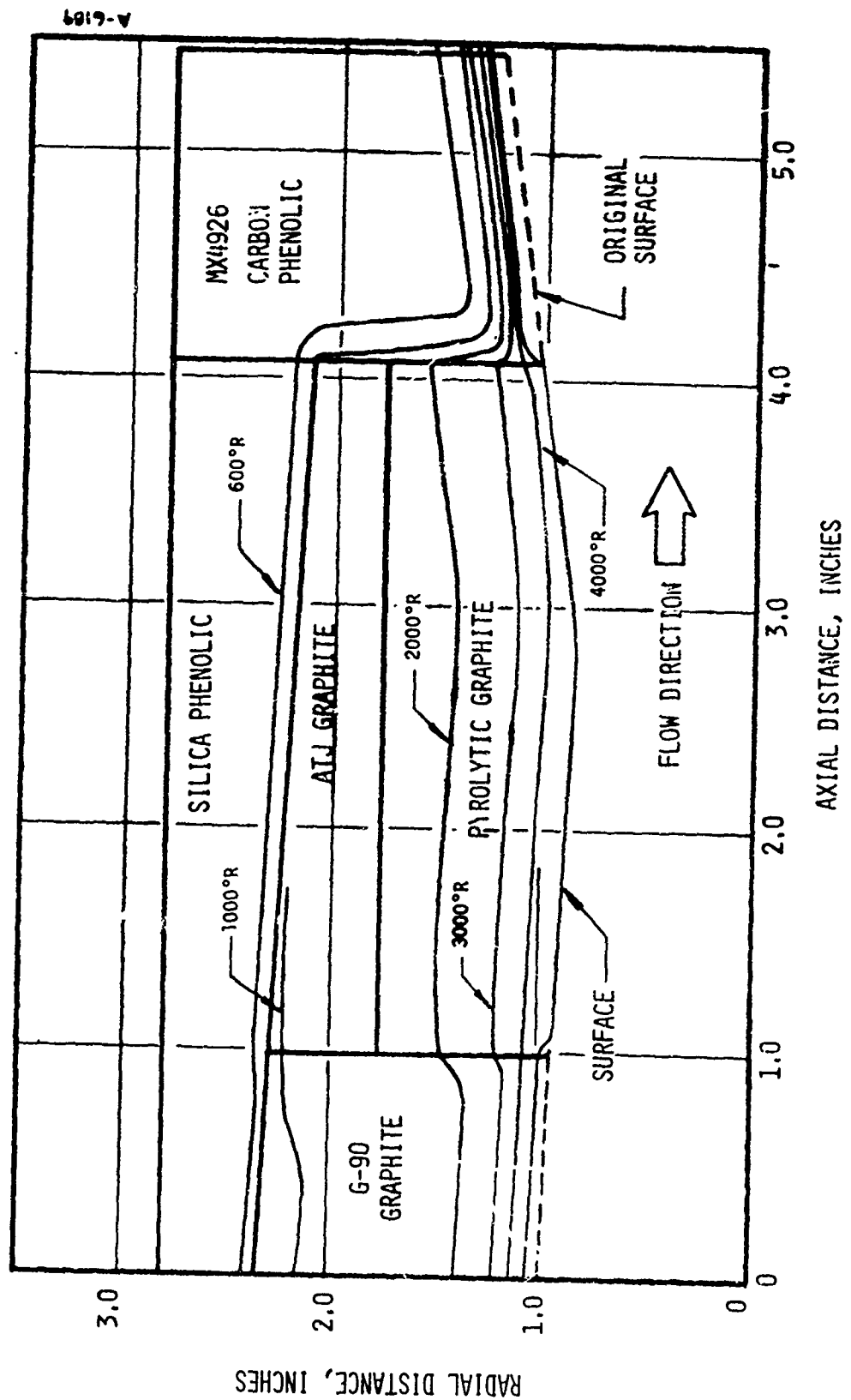


Figure 5-9. Continued

D) Exposure Time = 5.0 Seconds

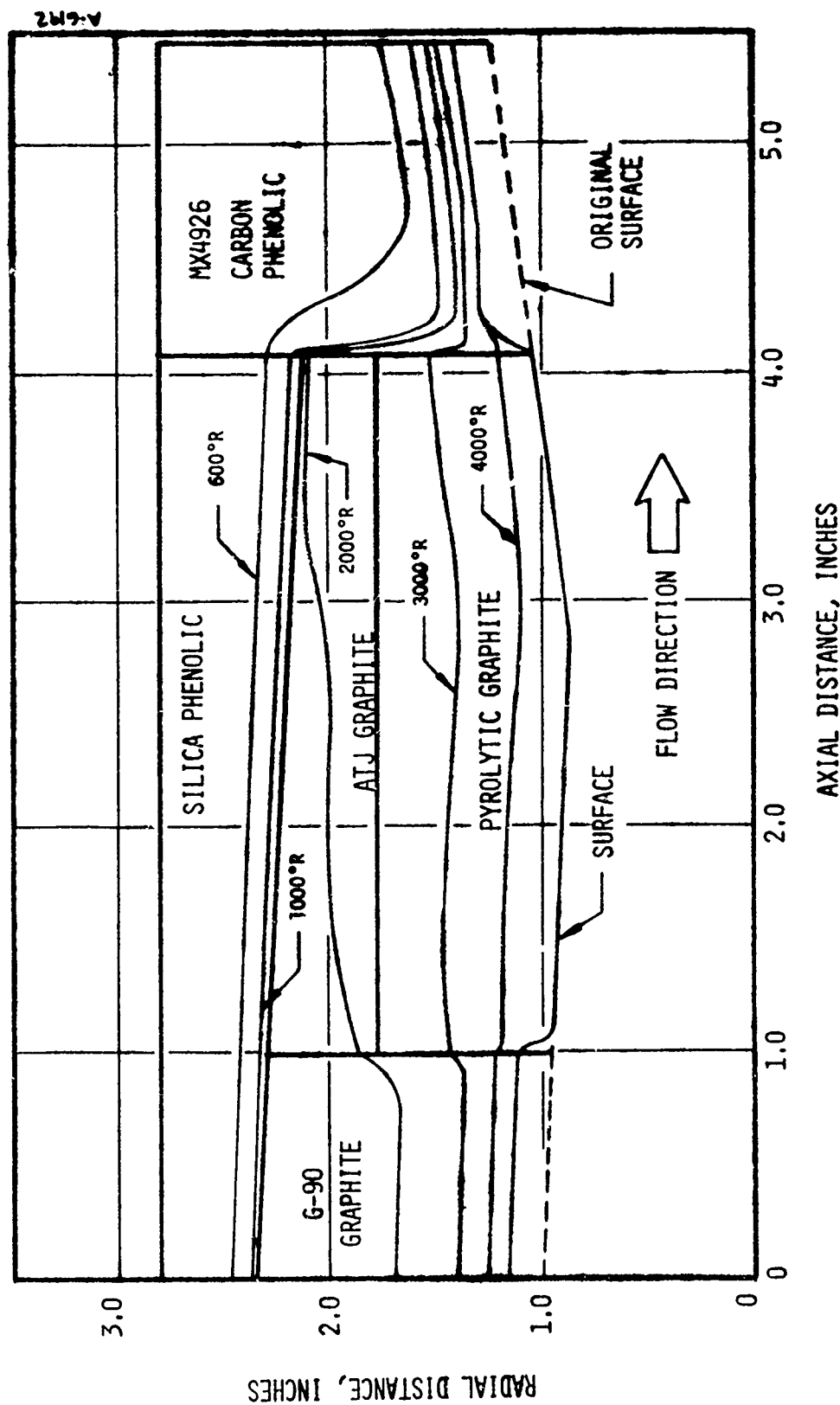


Figure 5-9. Continued

E) Exposure Time = 11.0 Seconds  
(End of Exposure)

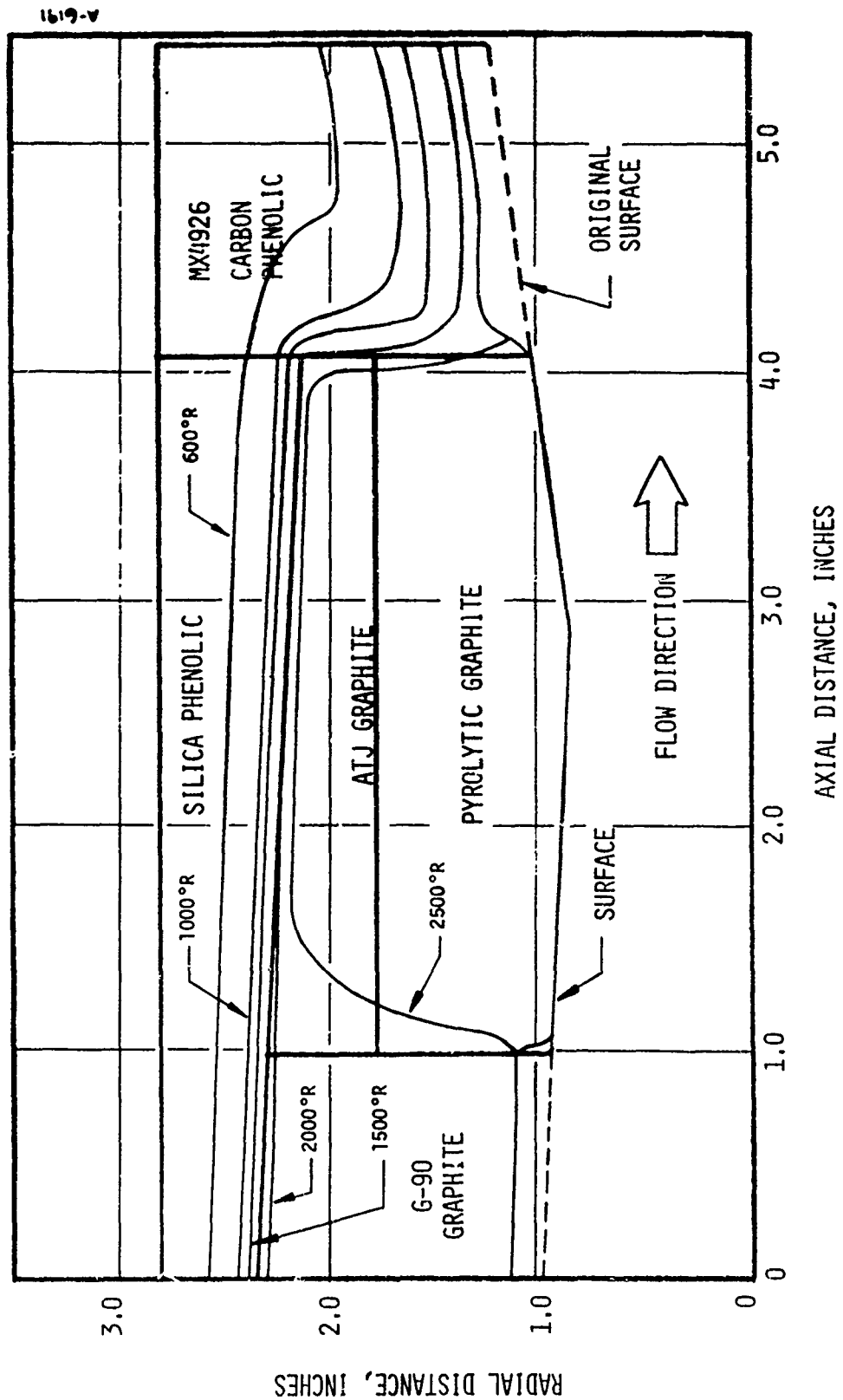


Figure 5-9. Concluded

F) 30 Seconds After Start-Up

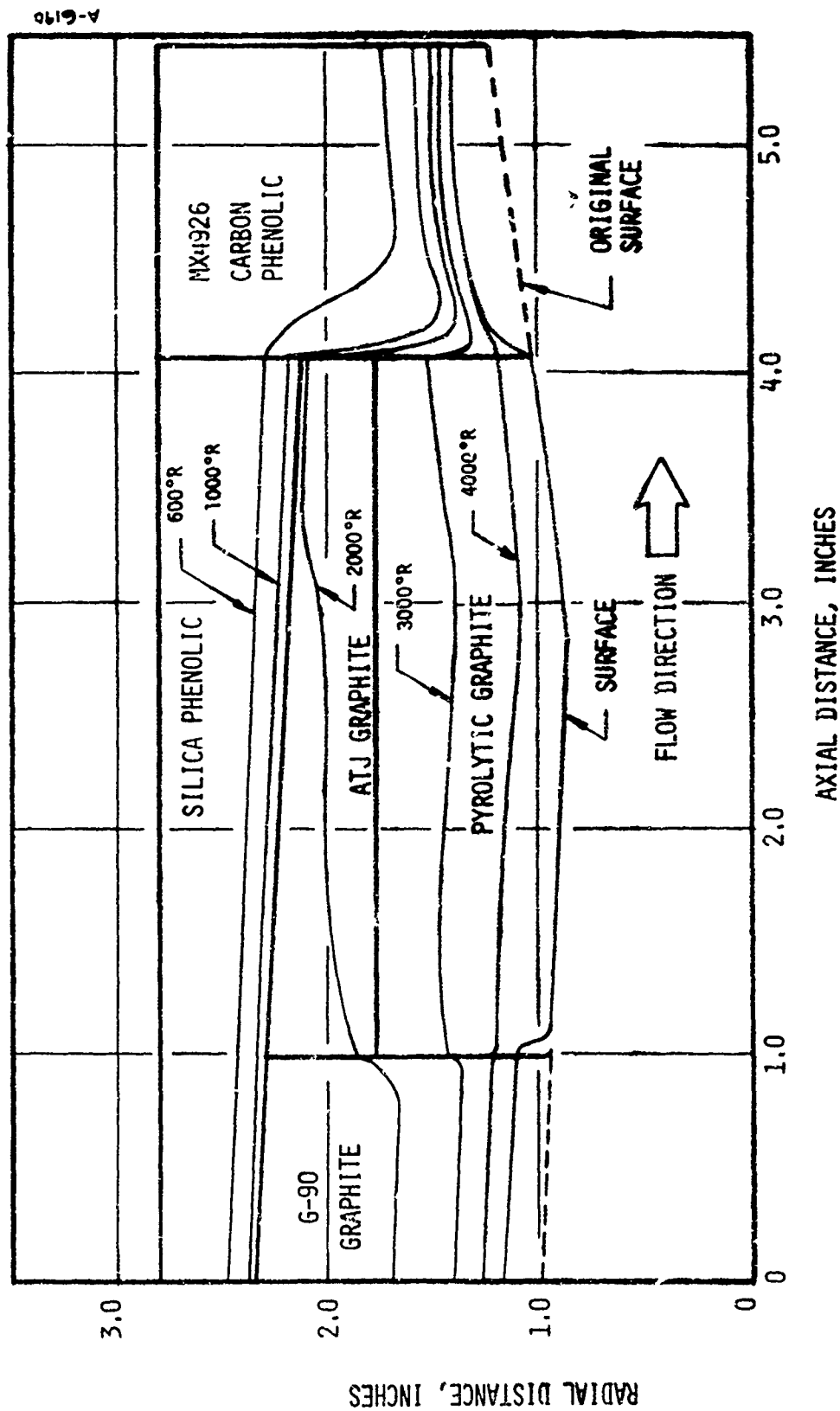


Figure 5-10. Isothermal Locations in Throat Package, Accounting for Estimated Gouging Effects, Exposure Time = 11.0 Seconds



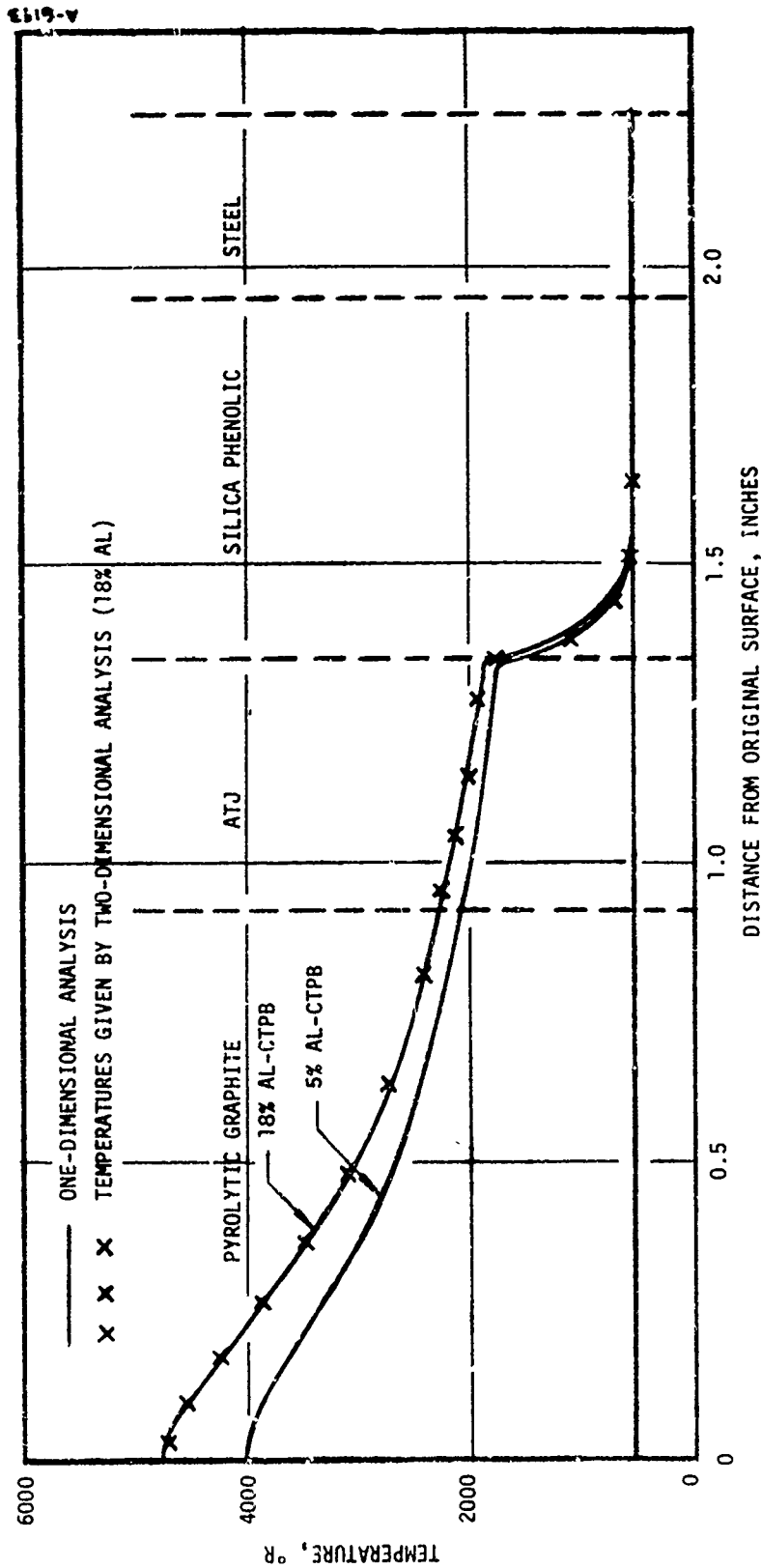


FIGURE 5-11 COMPARISON OF TEMPERATURE PROFILES IN THE THROAT PLANE  
 A. 11.0 SECONDS (END OF EXPOSURE)



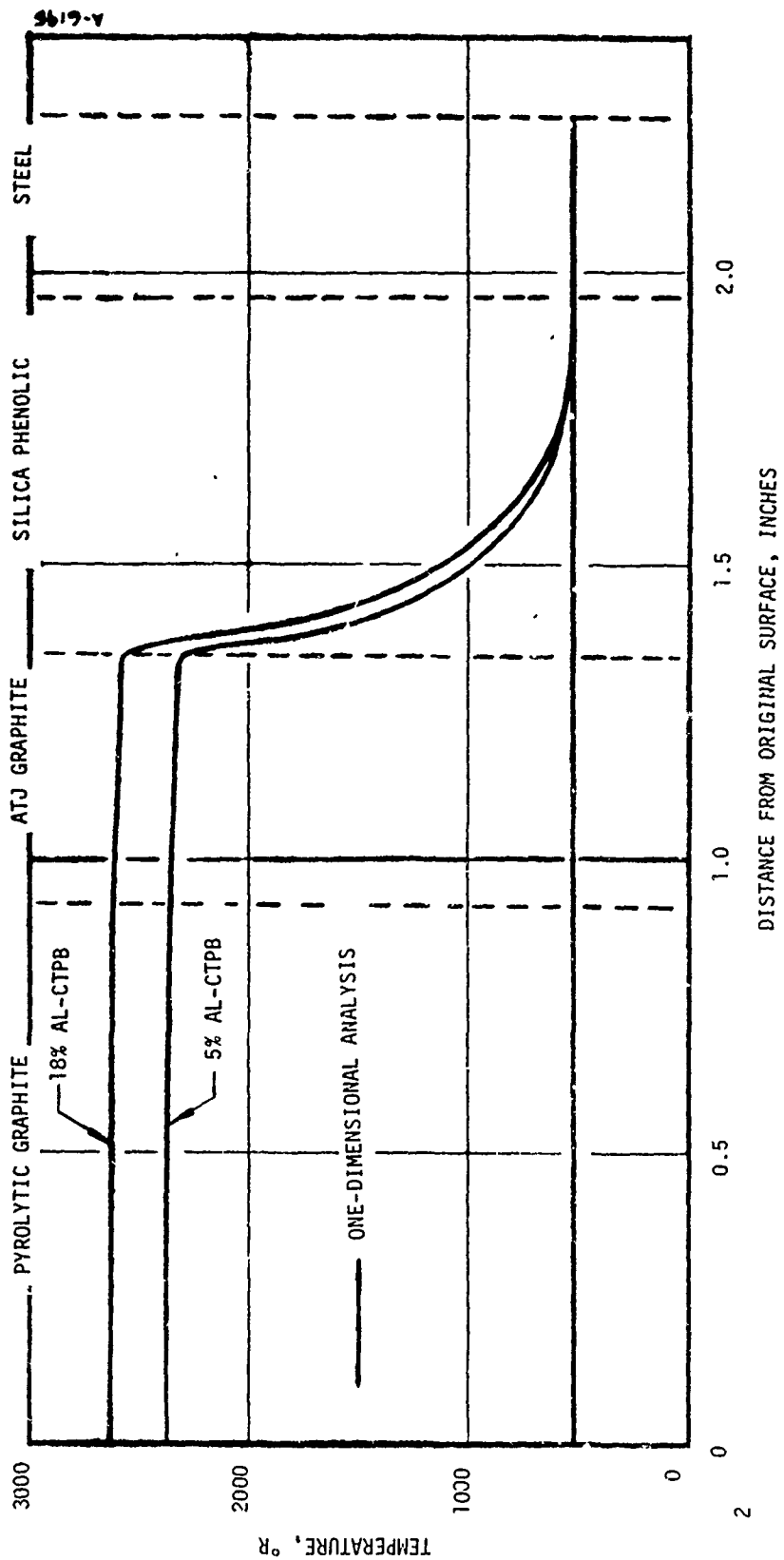


Figure 5-11. Concluded  
C) 60.0 Seconds

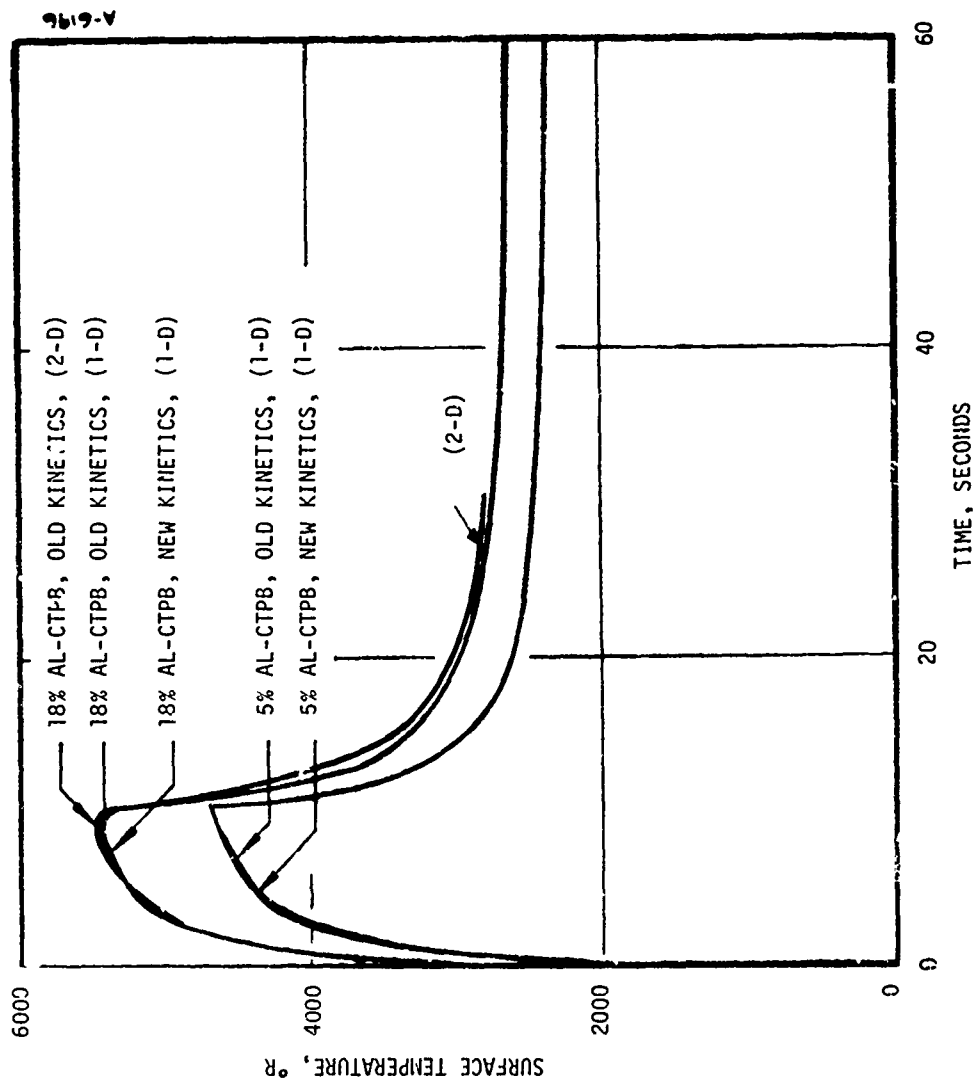


Figure 5-12. Comparison of Predicted Surface Temperatures at the Throat

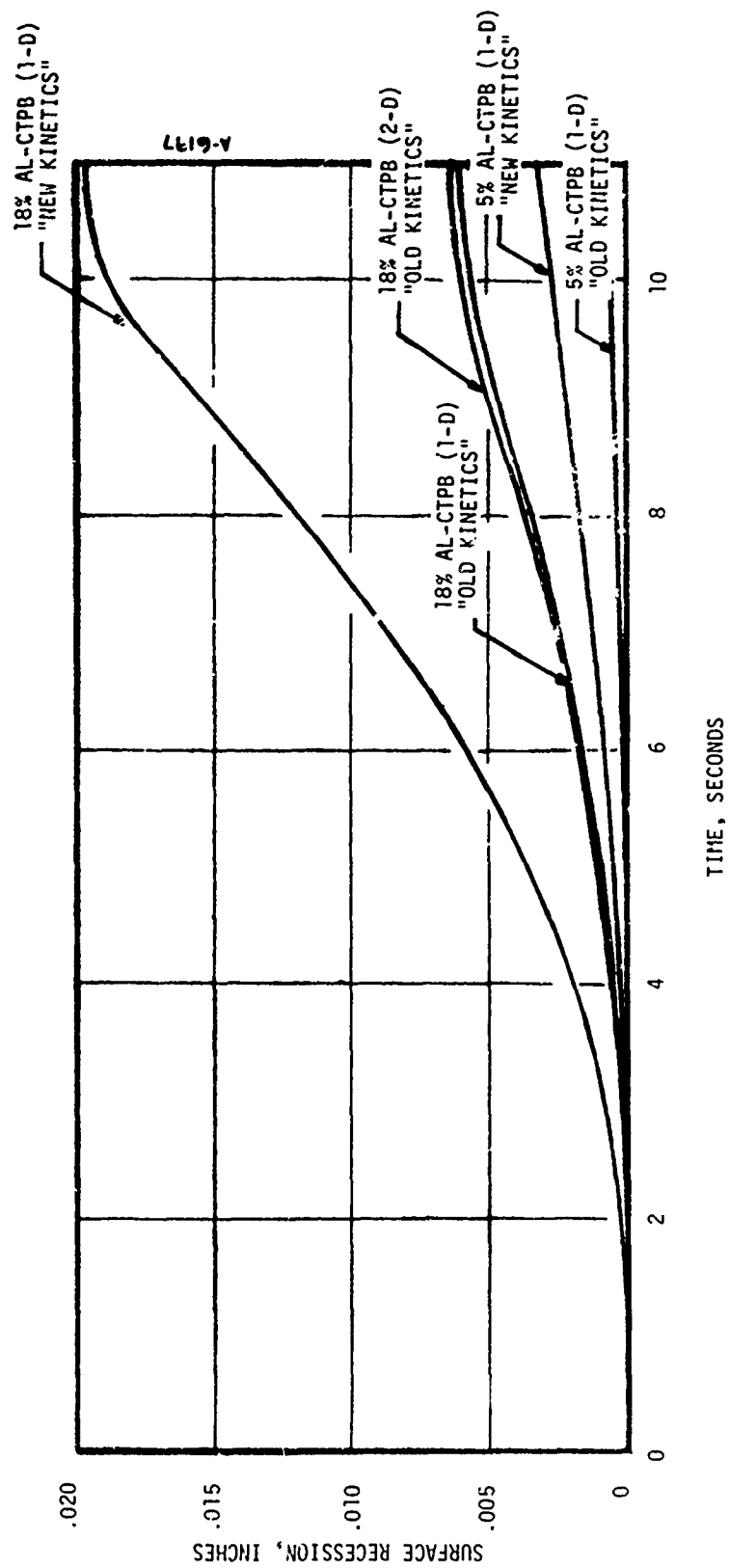


Figure 5-13. Comparison of Predicted Surface Recessions at the Throat

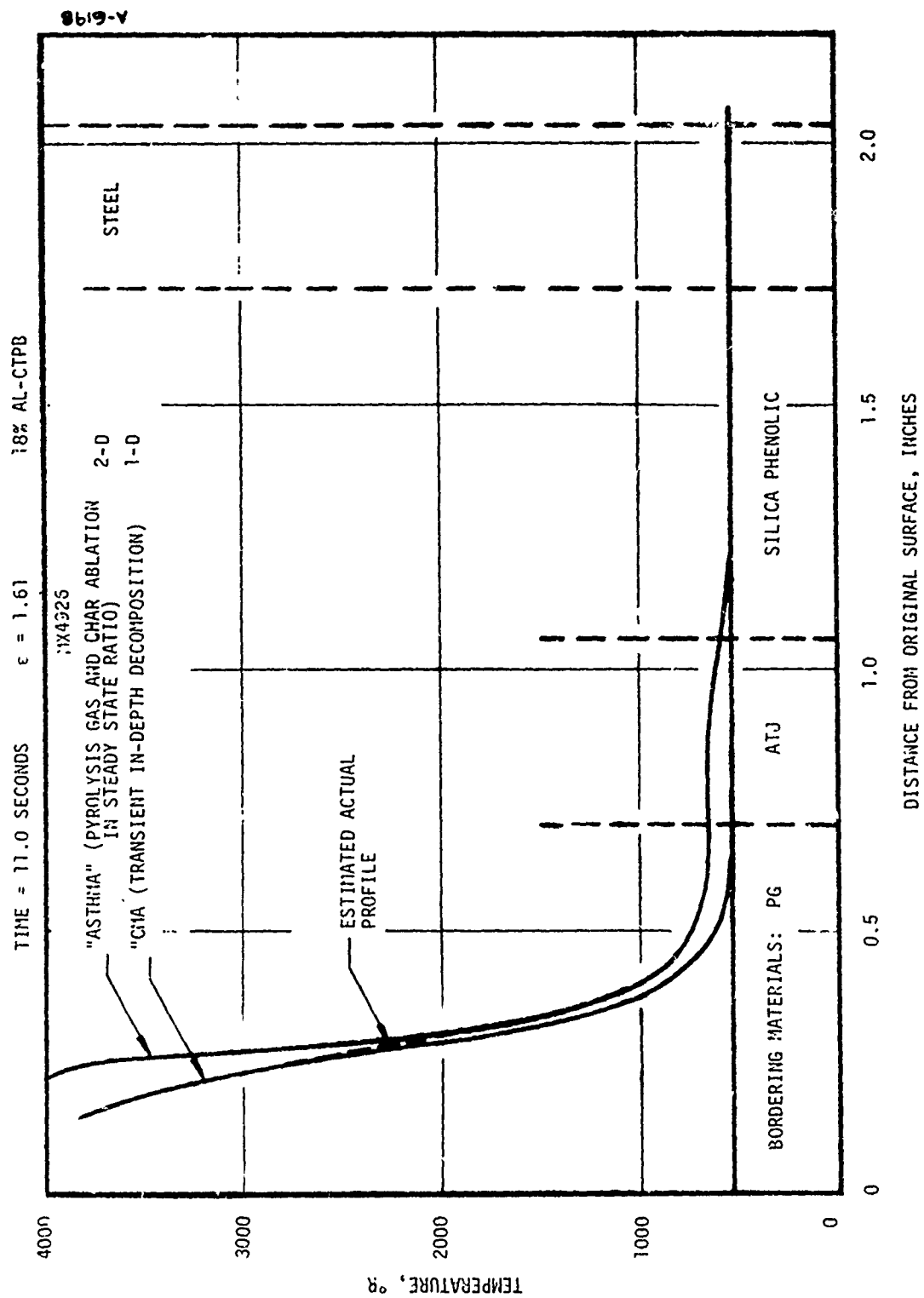


Figure 5-14. Comparison of One and Two Dimensional In-Depth Temperatures for Throat Retaining Ring

MX 4926

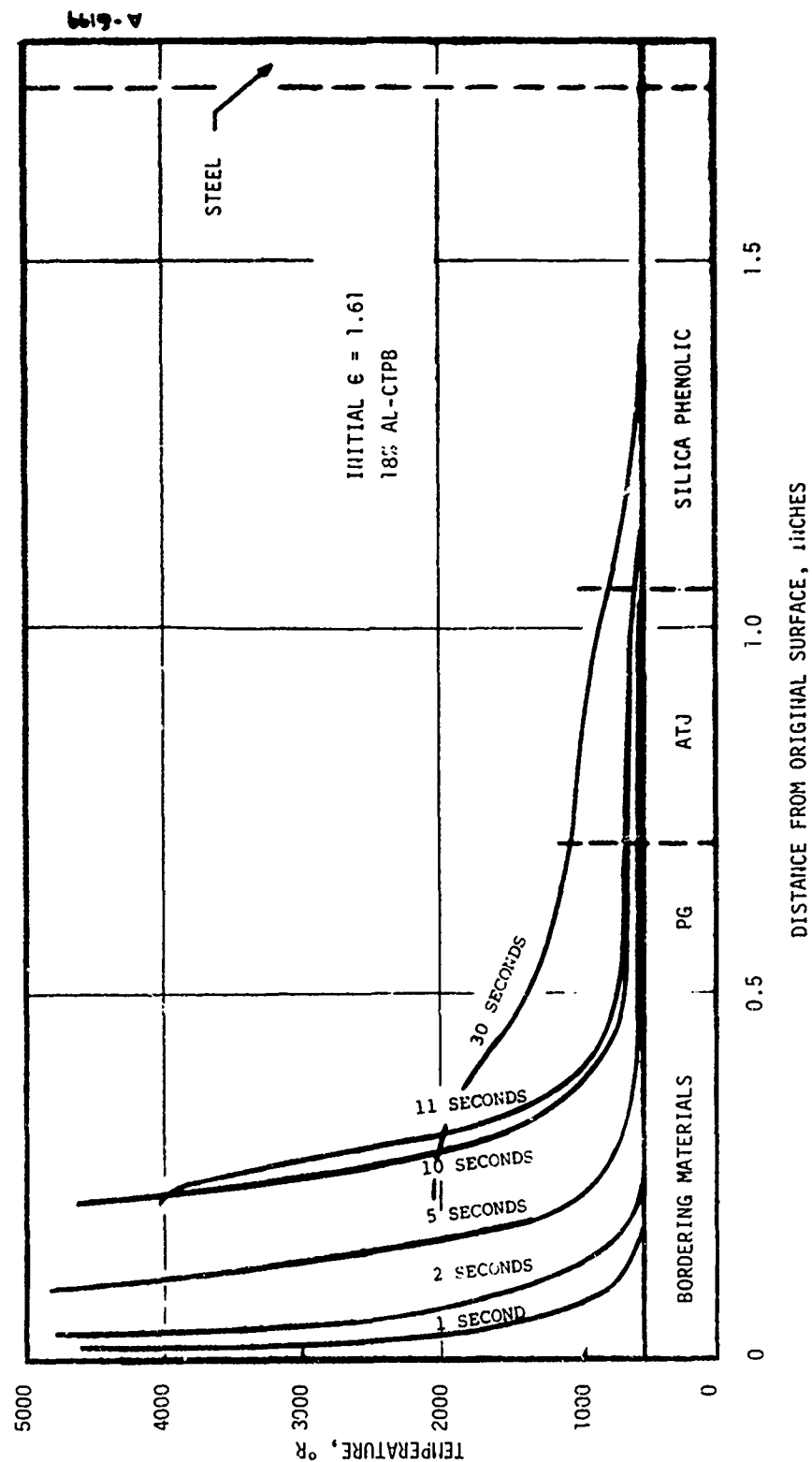


Figure 5-15. Temperature Profiles for MX4926 Throat Retaining Ring, 2-Dimensional Analysis

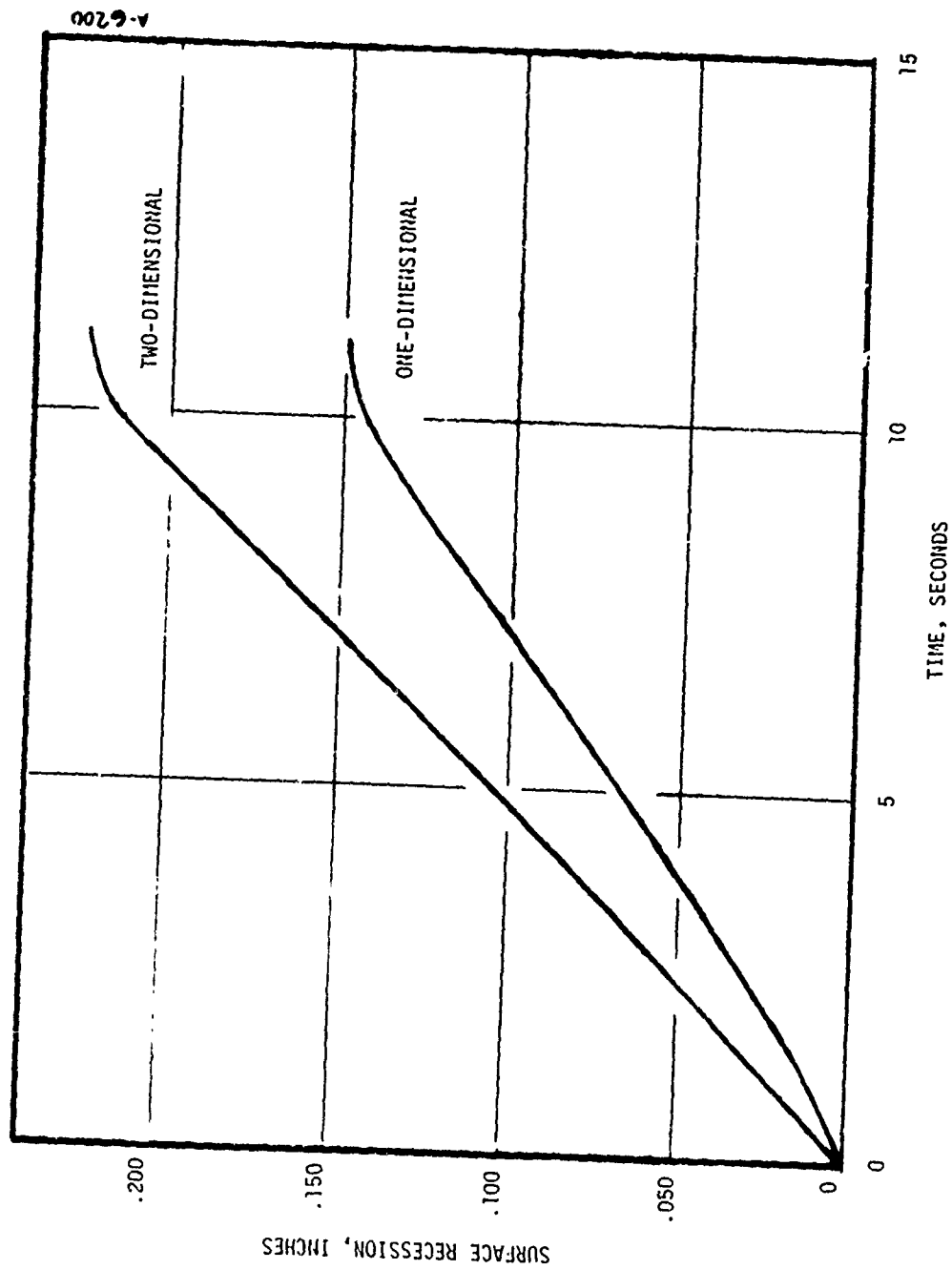


Figure 5-16. Comparison of MX4926 Surface Recessions Given By the One and Two Dimensional Analysis



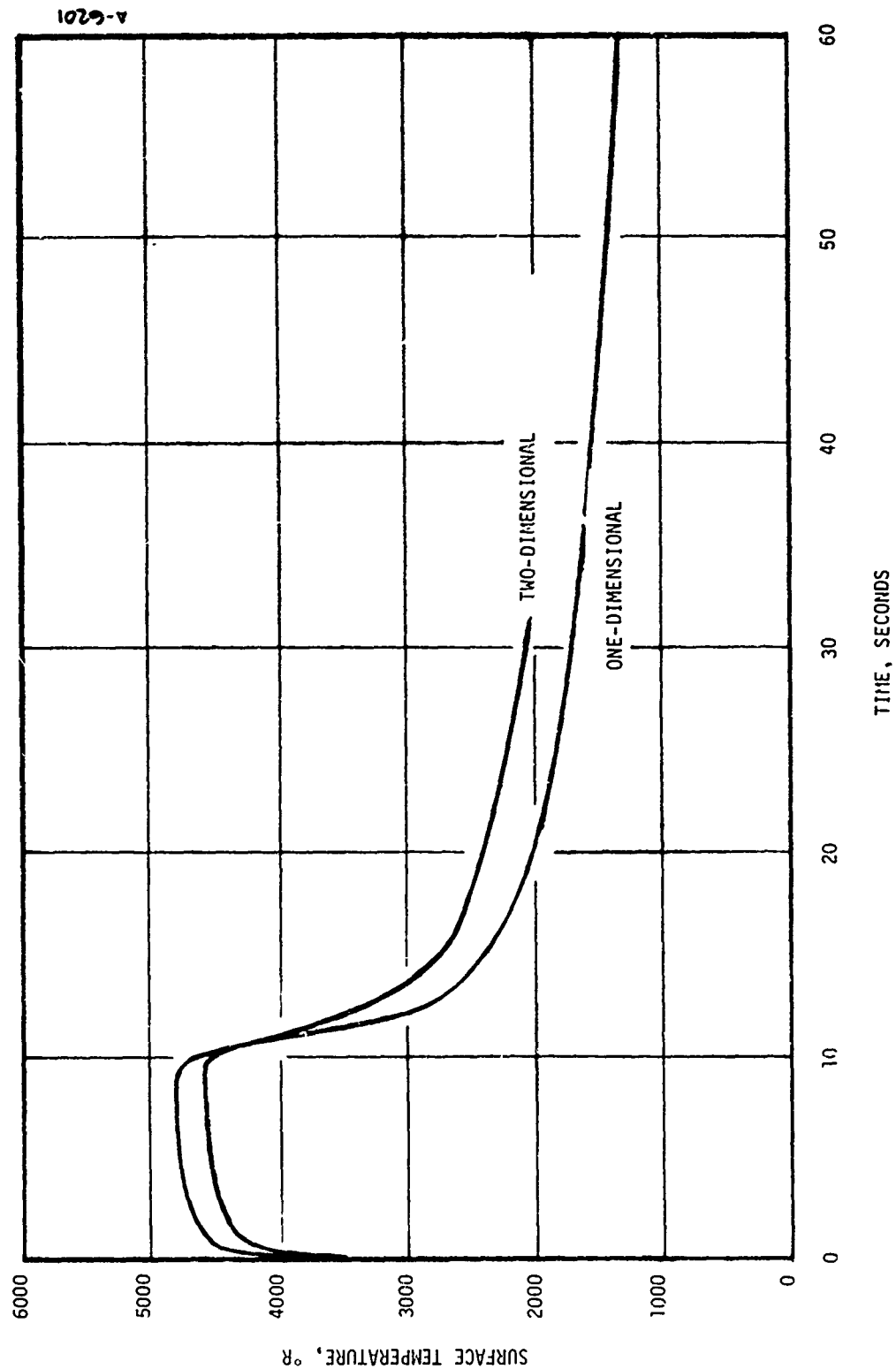


Figure 5-17. Comparison of MX4926 Surface Temperatures Given By The one and Two Dimensional Analysis

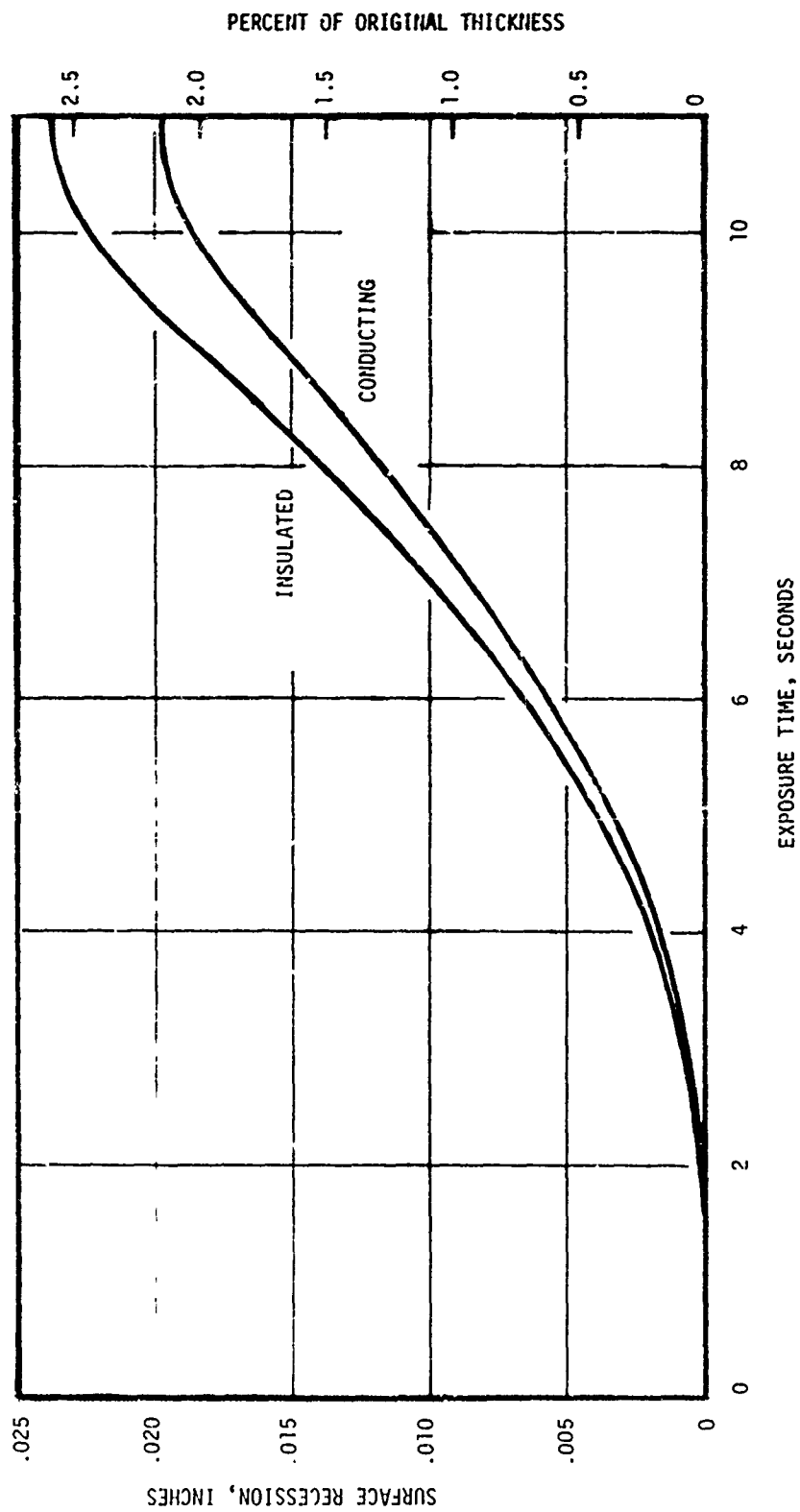


Figure 5-18. Effect of PG Washer Backwall Boundary Condition on Throat Surface Recession

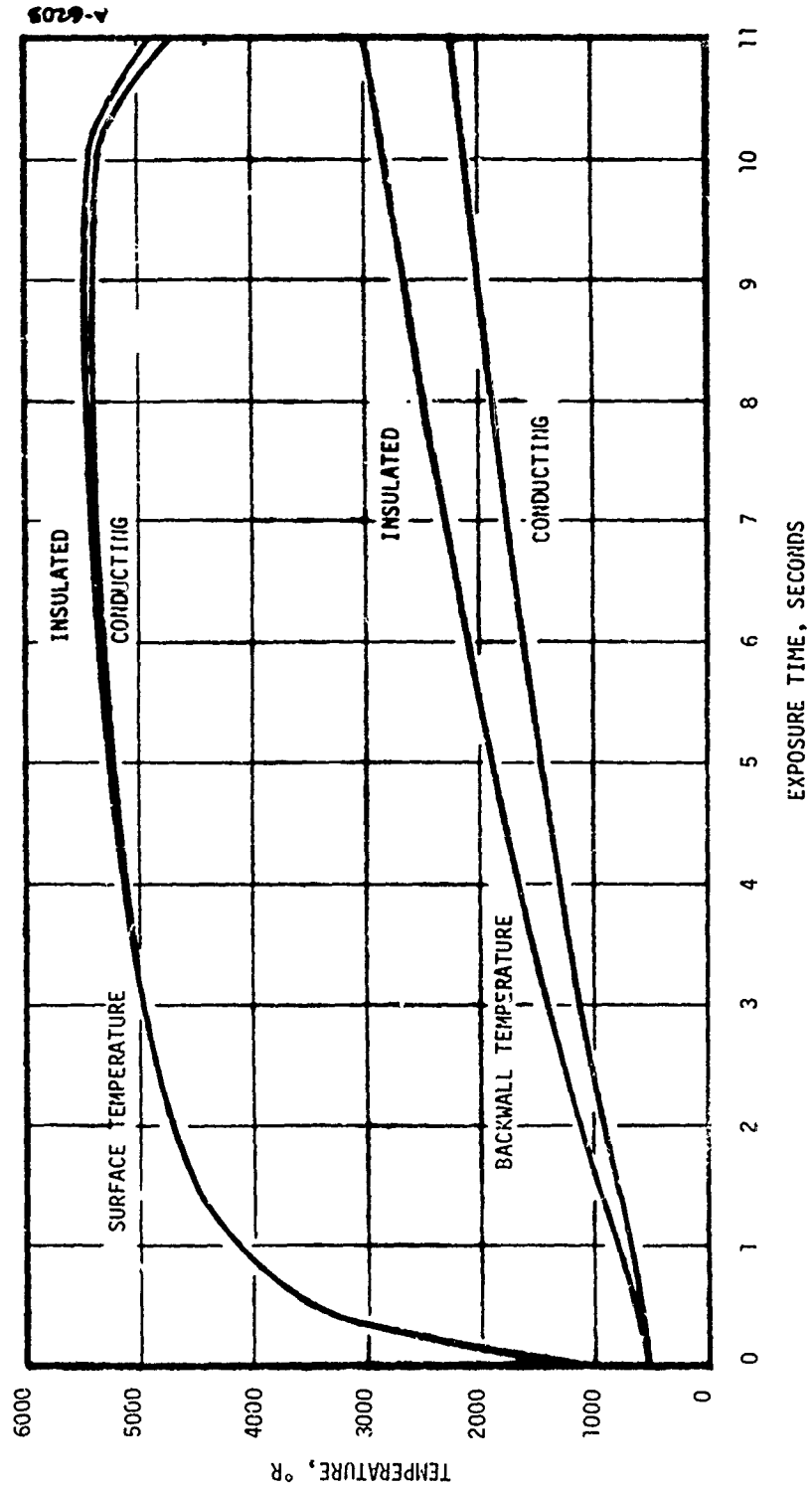


Figure 5-19. Effect of PG Washer Backwall Boundary Condition on Surface and Backwall Temperatures

## SECTION 6

### PRETEST NOZZLE THERMAL RESPONSE PREDICTIONS

One of the objectives of contract F04611-71-C-0051 is to demonstrate the validity of existing analysis techniques for predicting the performance of materials used in high chamber pressure nozzle designs. The criteria used for satisfying this objective was to make pretest predictions at 18 locations in selected nozzles of the initial 13 test firings which were tested by UTC under the above mentioned contract.

Two types of pretest predictions were made. From those locations analyzed for motors S/N 003, S/N 005, and S/N 006, the pretest predictions were made using the predicted chamber pressure history. For the remainder of the locations, the pretest predictions were made using the post test chamber pressure histories. However, the reason that both types of predictions are referred to as "pretest" is because the results of all predictions were transmitted to UTC prior to receiving the post test measurements.

The surface thermochemistry maps required for the predictions are presented in Section 6.1 for all the materials except the PG washer. A summary (except for the PG washer) of the predictions and their comparison to post test measurements of surface recession and char depth are given in Section 6.2. The comparison of the prediction and measured surface recessions for the PG washer is presented in Section 6.3. Finally a summary of the post test char density measurements is presented in Section 6.4.

#### 6.1 SURFACE THERMOCHEMISTRY DATA

The thermochemical calculations performed for the pretest predictions are identified in Table 6-1. This table summarizes the locations, materials, and propellants for which thermochemistry maps were made and their corresponding figures.

The majority of the thermochemistry calculations are for charring ablation materials. For transient analyses, these materials require thermochemistry maps with parametrically varying values of  $B'_g$  as shown in the figures. A transient map was not made for R-155 since sufficient chemical data was not available. A steady state map is given in Figure 4-1 for R-155 and was used to generate a series of steady state response solutions using the SSA computer code. Collectively, these solutions provided a pseudo-transient prediction which was compared to

to the measured test data. Thermochemistry maps for the two non-decomposing materials, G-90 (5 percent and 18 percent AL-CTPB) and Pycobond, are also given in these figures. The maps for G-90 were generated using the GASKET computer code which incorporates reaction kinetics in the surface thermochemistry. (Reference 2). Figure 6-9 shows the surface response of Pycobond to 5 percent AL-CTPB. Reaction kinetics were not incorporated in this map since previous studies (Reference 1) have shown that the surface recession of carbon/carbon composites can be predicted with an accuracy of  $\pm 25$  percent using diffusion controlled thermochemistry.

## 6.2 COMPARISON OF PREDICTED AND MEASURED SURFACE RECESSION, CHAR DEPTHS AND MATERIAL DENSITY PROFILES

This section summarizes the 18 pretest predictions made for a total of six test firings. All but one prediction was made using the CMA computer code. The prediction for R-155 was made by a series of steady state predictions using the SSA computer code. Input for these codes, as before, was derived from the information presented in Section 3. The heat transfer coefficients were obtained from the figures in Section 3.5.1 and were modified by Equation (3-3) which is repeated here.

$$\rho_e u_e C_H = 0.75 \left( \frac{P_c}{2800} \right)^{0.8} \rho_e u_e C_H \text{ ARGEIBL} \quad (3-3)$$

The instantaneous chamber pressure ( $P_c$ ) for each test are presented in Figures 6-13 through 6-18. The actual chamber pressure histories shown for test firings SN 003, SN 005, and SN 006 were not used in making the pre-test predictions, but rather the predicted chamber pressure histories (supplied by UTC) were used. These are shown along with the actual tracings in Figures 6-14 through 6-16. The pressure history for test firing SN 006 (Figure 6-16) shows that at 8 seconds after start-up the pressure decreased rapidly. This was due to the failure and subsequent loss of the throat section. Since predictions were made using the higher predicted pressure history they were not compared to the measured results. Figure 6-18 illustrates the pressure history of test firing 13. This nozzle had a keyhole slotted grain propellant which caused the pressure to reach a maximum immediately after startup and then continuously decrease during the test.

Table 6-2 summarizes the post test measurements made by UTC for the locations at which predictions were made. Surface recession measurements, in general, were made in more than one circumferential location and are averaged to provide a comparison with predictions. In the blast tube, recession

measurements were also averaged over two different axial locations. Additional measurements were provided within 0.25" of the blast tube entrance and exit, but were discarded because of undesirable end effects. Char depth measurements were not obtained at different circumferential locations, but, like recession data, were given at different axial locations in the blast tube. Averages of measurements taken at axial distances of 3.0 and 5.0 inches were used for comparisons with the analytical predictions.

A summary of the pretest predictions and their comparisons to measured data is given in Table 6-3. For the six test firings listed, a total of 18 predictions were made for the various locations and materials shown. The thermochemical recession predictions shown are those obtained from the CMA computer code (SSA computer code for prediction 16) and do not account for char swell. Reference 1 was used to estimate the char swell for MXCE280 and MX4926 (same as FM5055). Char swell information for the other decomposing materials was not available. The predicted net recession shown in Table 6-3 equals the predicted thermochemical recession less the amount of char swell listed. The predicted char depth was also that obtained from the CMA computer program, with the amount of char swell added. Average measured surface recessions are those taken from Table 6-2 except for predictions 5, 10 and 11. The exit cone measurements shown in Table 6-3 are for an area ratio of 5.0 and are interpolated values between those listed in Table 6-2 C for area ratios of 4.2 and 6.7. As mentioned before, the measurements for test firing S/N 006 are not included in this table due to nozzle failure. Test firing S/N 013 used a slotted grain propellant and, as shown in Figure 3-4, the predicted heat transfer coefficient distribution is influenced by the two dimensional flow effects. For this reason, the prediction is dependent on whether the analysis location is in or opposite to the plane of the slot. Also listed in Table 6-3 are the average measured char depths of which those for tests S/N 006 and S/N 0013 were not available.

The last column of Table 6-3 summarizes the comparisons between measured and predicted surface recessions. Excellent agreement with data was found, with most predictions falling within a  $\pm 25$  percent error band about the measured values. Prediction 5 fell below the measured value but it should be noted that the measured surface recession was a relatively small number which had an uncertainty band larger than the average value reported. Predictions 8 and 9 would fall within 5 percent and 28 percent, respectively, if the extremes

of their measured uncertainty bands were considered. The prediction techniques used for the slot plane in test 13 is shown to be reasonably accurate while further studies may be required for modelling the flow field in the plane opposite the slot.

Typical surface recession rate and surface temperature histories are shown in Figure 6-19 for an MXCE280 material in the blast tube. As shown in the figure, the surface recession rate decreases during the motor firing, but the surface temperature remains approximately constant.

### 6.3 PG WASHER SURFACE RECESSION

The surface recession rates for the PG washer nozzle throat are summarized in Figure 6-20 for both the motors tested under the current program (Contract F04611-71-C-0051) which used a CTPB propellant with 5 and 18 percent aluminum loading fractions and those tested under the previous program (Contract F-4611-69-C-0065) which used a PBAN propellant with 16 percent aluminum loading fraction. The difference in the measured surface recession rate for the two types of propellant is obvious. The predicted surface recession rates for both types of propellant are also tabulated on this figure. These rates are based on the "new" kinetics. Good agreement is obtained between the measured and predicted surface recession rates for the PBAN propellant but poor agreement is obtained for the CTPB propellant. Before going into further discussion on this discrepancy a comparison of the thermochemical properties of the two types of propellant might prove beneficial. This comparison is made for the 16 percent aluminum PBAN propellant and the 18 percent aluminum CTPB propellant.

The elemental constituents of the two propellants are summarized in Table 6-4. The gas only elemental constituents, which were obtained by removing the  $Al_2O_3$  particles from the combustion products, are summarized in Table 6-5. The particle concentration was defined by performing an ACE chemical equilibrium solution at the conditions shown in Table 6-6. The propellant ballistics quoted by the manufacturer are summarized in Table 6-7. The remaining thermochemical information for the two propellants is summarized in Table 6-8. This table presents the main gaseous products for the two propellants. These were defined for the conditions summarized in Table 6-6 and were obtained by performing an ACE chemical equilibrium solution. A comparison of the gaseous products for the two propellants shows a maximum difference of approximately 15 percent for the main oxidizing species. As a result, the chemical constituents of the two propellants do not provide an obvious clue to the discrepancy between the predicted and measured surface recession rates. Another possibility is the

difference in temperatures of the two propellants but this is taken into account in the thermochemical predictions. The effect on the surface recession rate resolutions from the difference in the flame temperatures is approximately a factor of two. This factor is based on a change in temperature of approximately 300°R from a temperature of 5000°R (approximate surface temperature). However, the predicted surface recession rate shown in Figure 6-20 is less for the 18° Al-CTPB propellant than the 16° Al-PBAN propellant. This is due to the predictions for the CTPB propellant being used for a 10 second motor firing compared to a 20 second motor firing for the predictions for the PBAN propellant. The longer motor firing time results in a higher average surface temperature which in turn yields a higher average  $B'_c$  and surface recession.

Another possible explanation for the difference is that a step occurs at the junction between the leading PG washer and the G-90 aft entrance cap. This step could have the effect of restarting the boundary layer. A surface recession prediction was made for this condition, and it resulted in a factor of 250% increase in the predicted surface recession rate. This is also considerably less than the measured surface recession rate.

From the above comments, it is apparent that the performance of the PG washer in the CTPB propellant environments is not understood. The large slope of the curves shown in Figure 6-20 suggest that the discrepancy is due to some phenomena other than kinetically controlled surface chemical reactions.

#### 6-4 CHAR DENSITY PROFILE MEASUREMENTS

Additional experimental data which can be used to evaluate the analytical techniques is the post test char density profile. Several attempts were made at making these measurements for the MXCE 280 material in the blast tube of motor S/N 009. As shown in Tabel 6-3, the predicted char depth in this blast tube was only .005 inches which makes the experimental definition of the char density profile extremely difficult.

The shave and weigh method was used in trying to make the char density measurements. This method involves sectioning a sample from the blast tube, weighing the sample, shaving a small amount from the surface, and then reweighing the sample. This process was repeated until the sample was consumed. The sample used for the measurements was taken from a location which was approximately one inch from the upstream end of the blast tube. The sample had a surface area of .234 x .487 inches with the longer length being parallel to the blast tube centerline. Because of the small char depth, only a small amount could be shaved off the



sample during a single step. For the first attempt, a series of 5 mil thick slices was removed from the surface of the sample. The reduced char densities showed considerable scatter due to the weight removed during a single shaving operation being the difference of two relatively large numbers. A second attempt was made with the thickness of the slices being increased to 10 mils. However, the reduced char densities still showed considerable scatter. Further attempts were not made because increasing the thickness of the slices would result in this thickness being a significant fraction of the char depth.

TABLE 6-1  
SUMMARY OF PRETEST THERMOCHEMISTRY MAPS

Location	Material	Propellant (% AL)	Figure No.
Aft Closure	Durez 16771-1	5	6-1
	Durez 16771-1	18	6-2
	MX2625	5	6-3
	R-155	18	4-1
Aft Entrance Cap	G-90	5	6-4
Blast Tube	MXCE 280	5	6-5
	MXCE 280	18	6-6
	MXSE 280	5	6-7
	G-90	18	4-3
	MX4926	5	6-8
	Pycobond	5	6-9
Exit Cone	FM5055	5	6-10
	FM5055	18	6-11
	MX2600	5	6-12

TABLE 6-2  
MEASURED MATERIAL RECESSION AND CHAR DEPTHS  
A) AFT CLOSURE

Test Firing	Mat'l	Area Radio	Circumferential Measurement Location	Measured Recession (in)	Average Measured Recession (in)	Measured Char Depth (in)
3	DUREZ 16771-1	26	TDC	.158	.142 $\pm$ .016	.045
			TDC+45	.126		
5	DUREZ 16771-1	26	TDC	.156	.186 $\pm$ .030	.088
			TDC+45	.215		
6	MX2625	26	TDC	.009	.041 $\pm$ .032	--b
			TDC+45	.073		
13	R-155	27	TDC	.185	--a	--b
			TDC+45	.070		
			TDC+180	- .031		
			TDC+225	- .058		

a average not considered due to asymmetric slotted grain effects

b measurements not available

TABLE 6-2 (Continued)

## MEASURED MATERIAL RECESSION AND CHAR DEPTHS

## B) BLAST TUBE

Test Firing	Area Ratio	Mat'l	Measurement Axial (in)	Location Circum (Deg)	Measured Recession (in)	Average Measured Recession (in)	Measured Char Depth (in)	Average Measured Char Depth (in)
2	2.0	MXCE280	3.0	TDC	.384	.355 <sup>+</sup> .029 -.041	.145	.143 <sup>+</sup> .003
				TDC+45	.347			
			5.0	TDC	.376		.140	
				TDC+45	.314			
3	1.3	MXCE280	3.0	TDC	.440	.456 <sup>+</sup> .014 -.016	.103	
				TDC+45	.455			
				TDC+180	.459			
				TDC+225	.470			
		G-90	5.0	TDC	.193	.196 <sup>+</sup> .004 -.003	N/A	
				TDC+45	.199			
				TDC+180	.200			
				TDC+225	.193			
5	1.3	MXCE280	3.0	TDC+180	.471	.603 <sup>+</sup> .247 -.132	.020	.025 <sup>+</sup> .005
				TDC+225	.565			
			5.0	TDC+180	.526		.030	
				TDC+225	.850			
		MXCE280	3.0	TDC	.422	.561 <sup>+</sup> .139	.025	
				TDC+45	.700			
		MX4926	5.0	TDC	.588	.661 <sup>+</sup> .073	.085	
				TDC+45	.733			
6	2.0	PYCOBOND	3.0	TDC	.200	.203 <sup>+</sup> .015 -.013	N/A	
				TDC+45	.190			
				TDC+180	.209			
				TDC+225	.218			
			5.0	TDC	.197			
				TDC+45	.199			
				TDC+180	.201			
				TDC+225	.211			
9	2.0	MXCE280	3.0	TDC	.356	.350 <sup>+</sup> .026	.110	.105 <sup>+</sup> .005
				TDC+45	.376			
				TDC+180	.347			
				TDC+225	.324			
			5.0	TDC	.346		.100	
				TDC+45	.375			
				TDC+180	.347			
				TDC+225	.325			
13	1.3	MXCE280	3.0	TDC	.491	--a		
				TDC+45	.525			
				TDC+180	-.035			
				TDC+225	.441			
			5.0	TDC	.500			
				TDC+45	.514			
				TDC+180	-.021			
				TDC+225	.443			

a average not considered due to asymmetric slotted grain effects

b distance from entrance to blast tube

c measurements not available

TABLE 6-2 (Concluded)

MEASURED MATERIAL RECESSION AND CHAR DEPTHS  
C) EXIT CONE

Test Firing	Mat'l	Area Ratio	Circumferential Measurement Location	Measured Recession (in)	Average Measured Recession (in)	Measured Char Depth (in)
3	FM5055	4.2	TDC	.223	.148+.075 -.078	.120
			TDC+45	.216		
			TDC+180	.070		
			TDC+225	.082		
		6.8	TDC	-.003	-.005+.002	.150
			TDC+45	-.007		
			TDC+180	-.005		
			TDC+225	-.005		
5	FM5055	4.2	TDC	.122	.123+.001	.065
			TDC+45	.124		
		6.7	TDC	.025	.039+.014	.080
			TDC+45	.053		
	MX2600	4.2	TDC+180	.114	.108+.006	.060
			TDC+225	.102		
		6.7	TDC+180	.032	.032+.000	.080
			TDC+225	.032		

TABLE 6-3  
SUMMARY OF PRETEST PREDICTIONS AND THEIR COMPARISON WITH MEASURED DATA

Pre- diction	Test Firing	Propel- lant (% AL)	Blast Tube Area Ratio	Material	Initial Area Ratio	Location	Predicted Thermo- Chemical Recession (Inches)	Predicted Char Swell (Inches)	Predicted Net Recession (Inches)	Predicted Char Depth (Inches)	Measured Recession (Inches)	Measured Char Depth (Inches)	Predicted Recession (Inches) Measured Recession (Inches)
1	2 <sup>c</sup>	18	2.0	MXCE 280	- 2.0	Blast Tube	.286	.025	.261	.267	.755 <sup>+</sup> .029 -.041	.143	.74
2	3 <sup>b</sup>	18	1.3	Durez 16771-1	-26.0	Aft Closure	.163	--d	.163	.058	.142 <sup>+</sup> .016	.045	1.12
3				MXCE 280	- 1.3	Blast Tube	.377	.022	.355	.227	.456 <sup>+</sup> .014 -.016	.103	.78
4				G-90	- 1.3	↓	.205	N/A	.205	N/A	.196 <sup>+</sup> .004 -.003	N/A	.05
5	▼	↓	▼	FMS055	5.0	Exit Cone	.047	.027	.020	.200	.101 <sup>+</sup> .055 <sup>h</sup>	.131 <sup>h</sup>	.20
6	5b	5	1.3	Durez 16771-1	-26.0	Aft Closure	.182	--d	.182	.056	.196 <sup>+</sup> .030	.088	.98
7				MXCE 280	- 1.3	Blast Tube	.504	.005	.499	.052	.603 <sup>+</sup> .247 -.132	.025	.83
8				MXSE 250	- 1.3	↓	.735	--d	.735	.059	.561 <sup>+</sup> .139	.025	1.31
9				MX4926	- 1.3	↓	.436	.012	.424	.089	.661 <sup>+</sup> .073	.085	.64
10				FMS055A	5.0	Exit Cone	.100	.008	.092	.062	.096 <sup>+</sup> .005 <sup>h</sup>	.070 <sup>h</sup>	.96
11	▼	↓	▼	MX2600	5.0	▼	.082	--d	.082	.100	.084 <sup>+</sup> .004 <sup>h</sup>	.066	.98
12	6 <sup>b</sup>	5	2.0	MX2625	-37.5	Aft Closure	.268	--d	.268	.043	--f	--f	--f
13				Pycobond	- 2.0	Blast Tube	.308	N/A	.308	N/A	--f	N/A	--f
14	↓	▼	▼	G-90	- 1.78	Aft Entrance Cap	.061	N/A	.061	N/A	--f	N/A	--f
15	9 <sup>c</sup>	5	2.0	MXCE 280	- 2.0	Blast Tube	.399	.005	.394	.055	.350 <sup>+</sup> .026	.105	1.13
16	13 <sup>c</sup>	18	1.3	R-155	-26.0	Aft Closure (in slot plane)	.258 <sup>a</sup>	--d	.258 <sup>a</sup>	--e	.185	--9	1.40
17				MXCE 280	- 1.3	Blast Tube (in slot plane)	.284	.023	.261	.240	.495 <sup>+</sup> .005	--9	.53
18	▼	↓	▼	MXCE 280	- 1.3	Blast Tube (in oppo- site plane)	.351	.024	.327	.250	.012 <sup>+</sup> .008	--9	>10

a based on steady state calculations  
b predictions based on predicted chamber pressure history  
c predictions based on measured chamber pressure history  
d char swell factors not available  
e steady state calculation excludes char depth considerations  
f measurements were not comparable to predictions due to nozzle throat failure during testing  
g measurements not available  
h interpolated values

TABLE 6-4

## ELEMENTAL PROPELLANT CONSTITUENTS

Element	Concentration (atomic wt/unit mass)	
	CTPB 18% Al	PBAN 16% Al
H	.03684	.03747
C	.00824	.01030
N	.00602	.00596
O	.02422	.02436
Al	.00663	.00593
Cl	.00601	.00579

TABLE 6-5

## ELEMENTAL PROPELLANT CONSTITUENTS

## GAS ONLY

Element	Concentration (atomic wt/unit mass)	
	CTPB 18% Al	PBAN 16% Al
H	.05359	.05217
C	.01199	.01434
N	.00876	.00831
O	.02186	.02237
Al	.0072	.00056
Cl	.00875	.00806

TABLE 6-6  
CONDITIONS FOR  
PROPELLANT EVALUATIONS

Propellant	Pressure (Atm)	Temperature (°K)
18% Al-CTPB	190.5	3692
16% Al-CTPB	179.0	3485

TABLE 6-7  
PROPELLANT BALLISTICS  
QUOTED BY MANUFACTURER

Propellant	Pressure (psia)	Flame Temperature (°K)	Oxidation Ratio
18% Al-CTPB	1000	3594	1.33
16% Al-CTPB	1000	3420	1.27



TABLE 6-8  
PROPELLANT CONSTITUENTS  
(MOLE FRACTION)

<u>Species</u> <sup>a</sup>	<u>18% Al-CTPB</u>	<u>10% Al-PBAN</u>
Al	$.160 \times 10^{-3}$	-
AlCl	$.526 \times 10^{-2}$	$.364 \times 10^{-2}$
AlCl <sub>2</sub>	$.130 \times 10^{-1}$	$.111 \times 10^{-1}$
AlHO <sub>2</sub>	$.110 \times 10^{-2}$	$.487 \times 10^{-3}$
AlCl <sub>3</sub>	$.368 \times 10^{-3}$	$.362 \times 10^{-3}$
AlO	$.121 \times 10^{-3}$	$.415 \times 10^{-4}$
CHO	$.346 \times 10^{-3}$	$.340 \times 10^{-3}$
CO	$.226 \times 10^0$	$.272 \times 10^0$
CO <sub>2</sub>	$.173 \times 10^{-1}$	$.164 \times 10^{-1}$
Cl	$.110 \times 10^{-1}$	$.692 \times 10^{-2}$
ClH	$.134 \times 10^0$	$.129 \times 10^0$
HO	$.115 \times 10^{-1}$	$.552 \times 10^{-2}$
H	$.340 \times 10^{-1}$	$.239 \times 10^{-1}$
H <sub>2</sub>	$.279 \times 10^0$	$.301 \times 10^0$
H <sub>2</sub> O	$.176 \times 10^0$	$.145 \times 10^0$
NO	$.994 \times 10^{-3}$	$.402 \times 10^{-3}$
N <sub>2</sub>	$.885 \times 10^{-1}$	$.834 \times 10^{-1}$
O	$.785 \times 10^{-3}$	$.250 \times 10^{-3}$
O <sub>2</sub>	$.195 \times 10^{-3}$	-
Al <sub>2</sub> O <sub>3</sub>	$.881 \times 10^{-1}$	$.754 \times 10^{-1}$

<sup>a</sup> Includes only those species with mole fractions equal to or greater than  $.1 \times 10^{-3}$

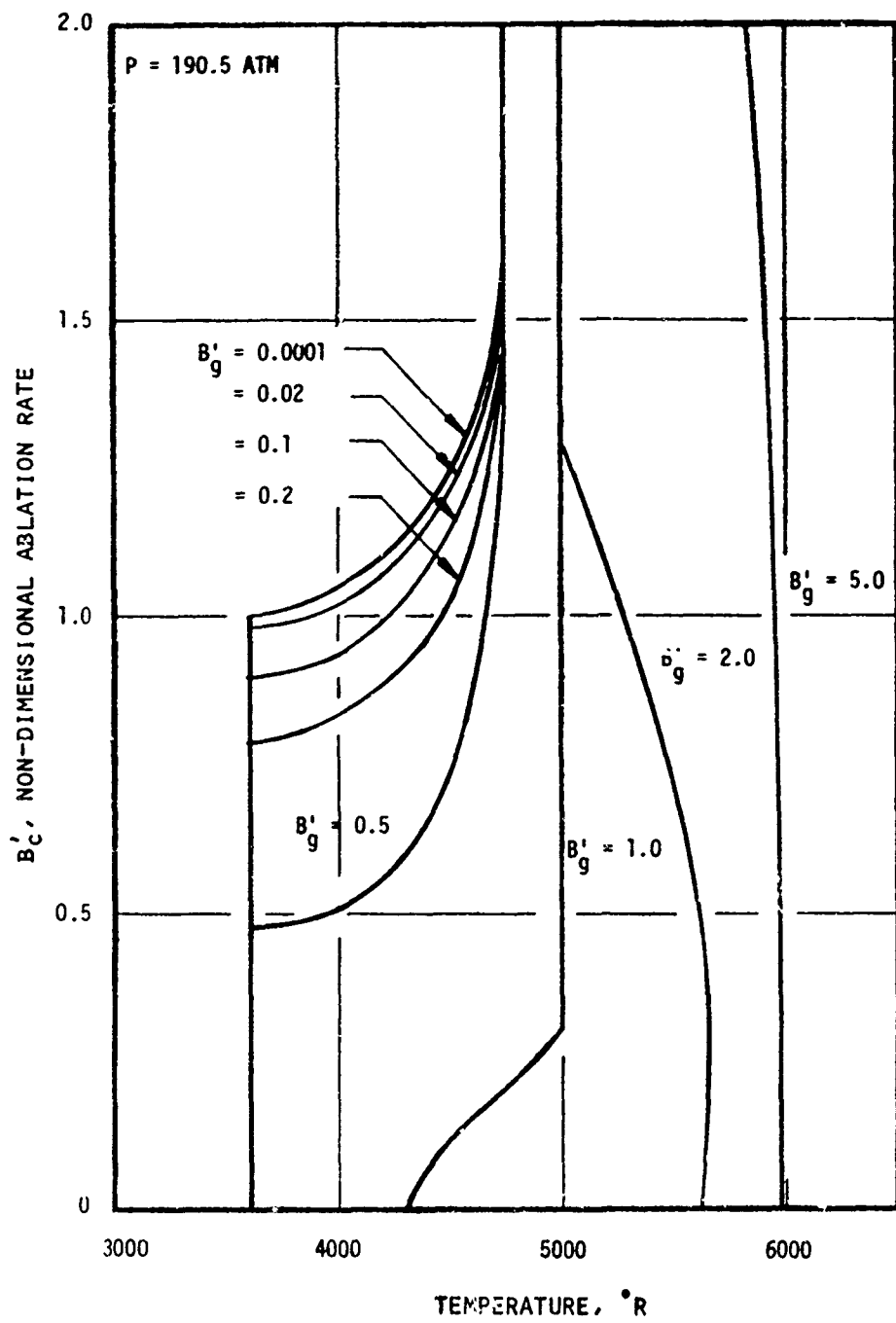


Figure 6-1. Surface Response of Durez 16771 Silica Phenolic to 5% AL-CTPB Propellant

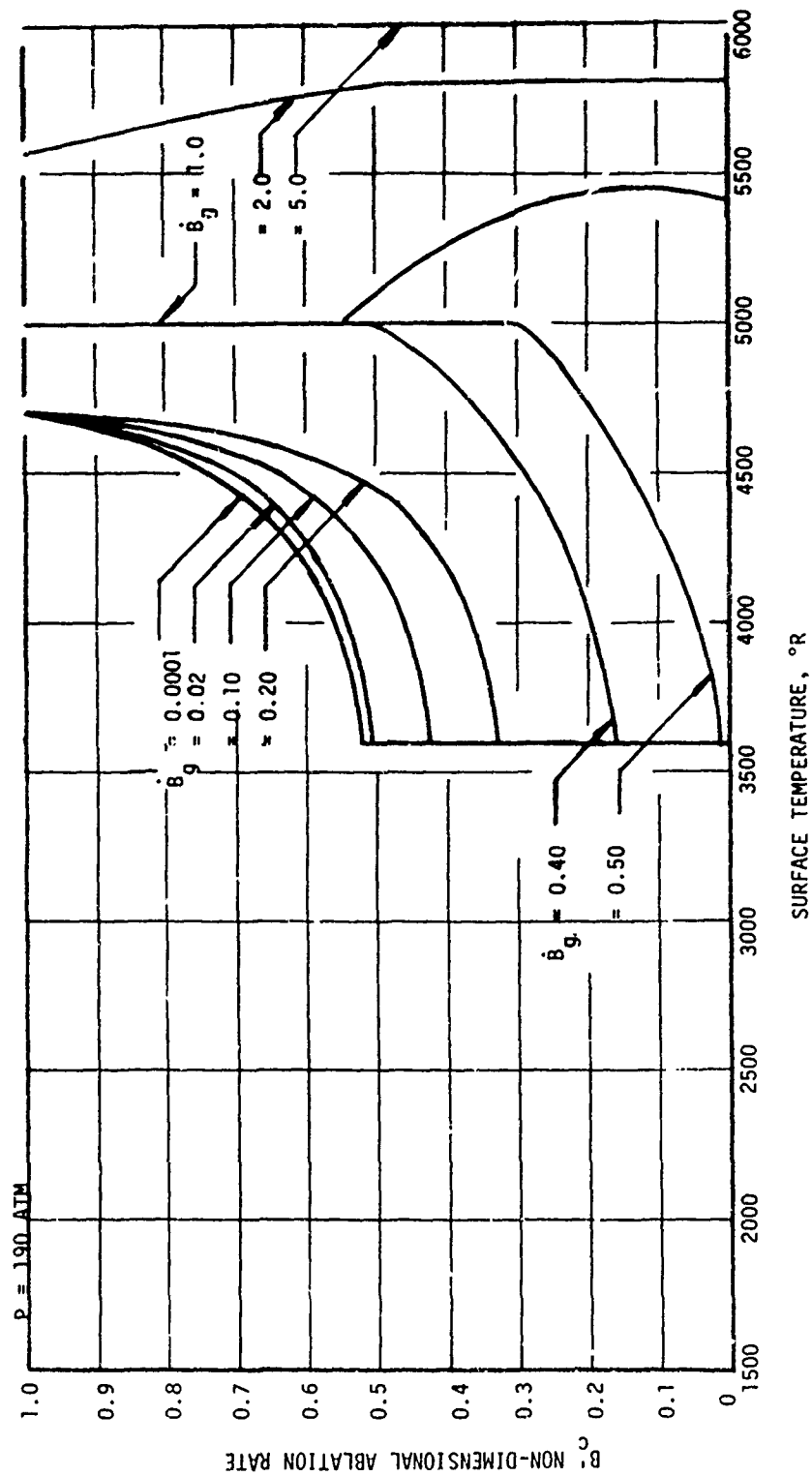


Figure 6-2. Surface Response of Durez 16771 and CTPB 188 Propellant

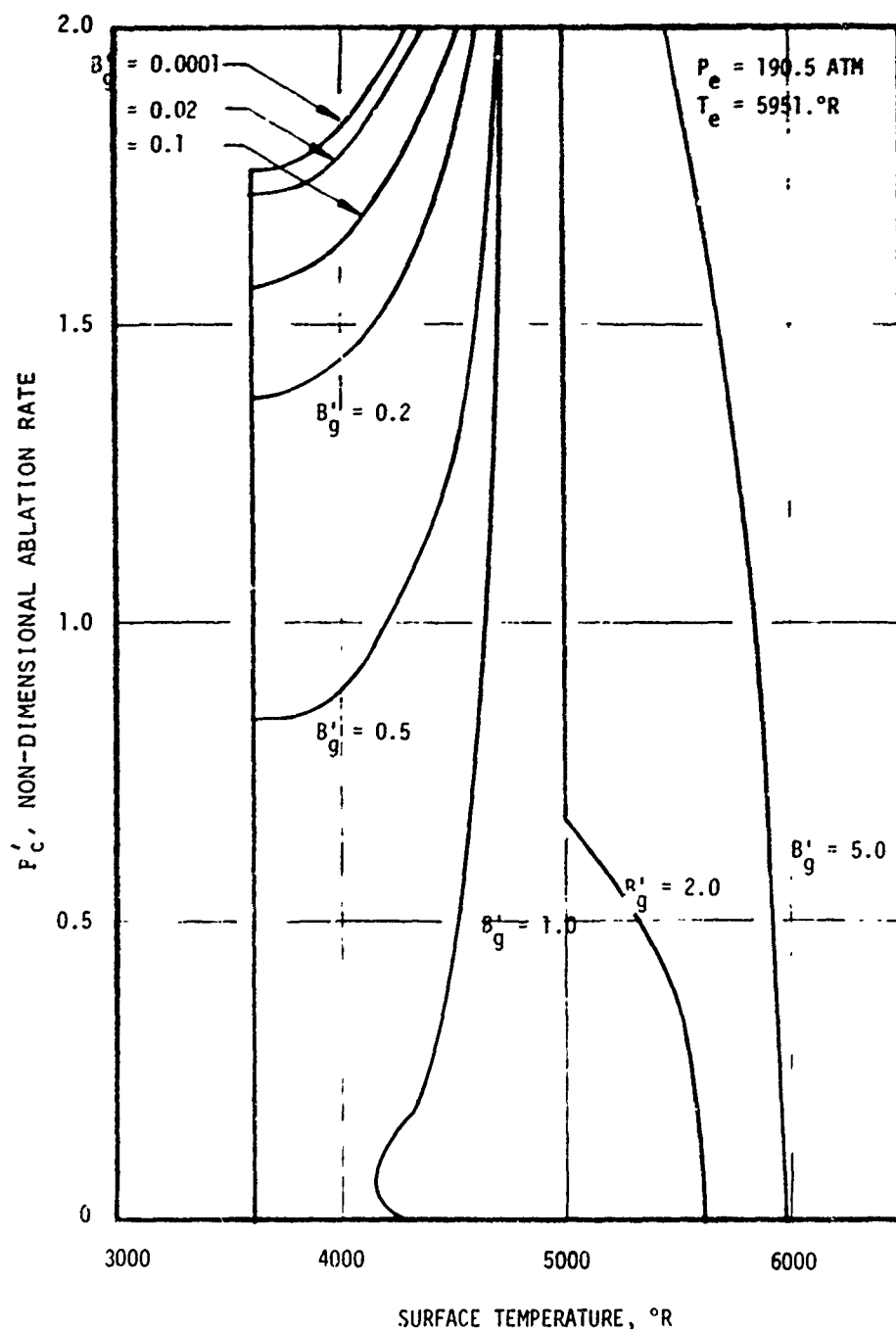


Figure 6-3. Surface Response of MX2625 to 5% AL-CTPB Propellant

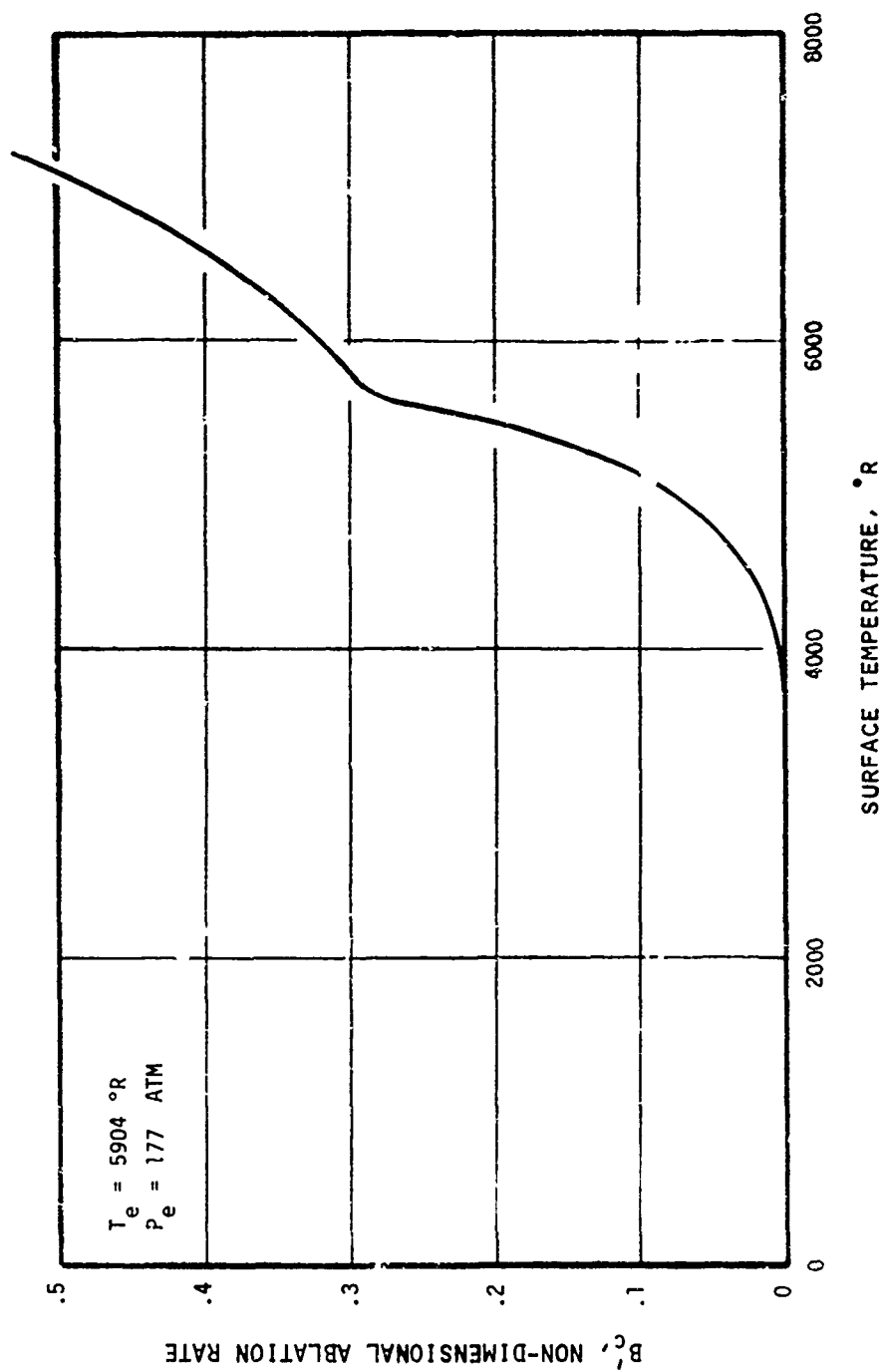


Figure 6-4. Kinetically Controlled Response of G-90 Bulk Graphite to 5% AL-CTPB Propellant

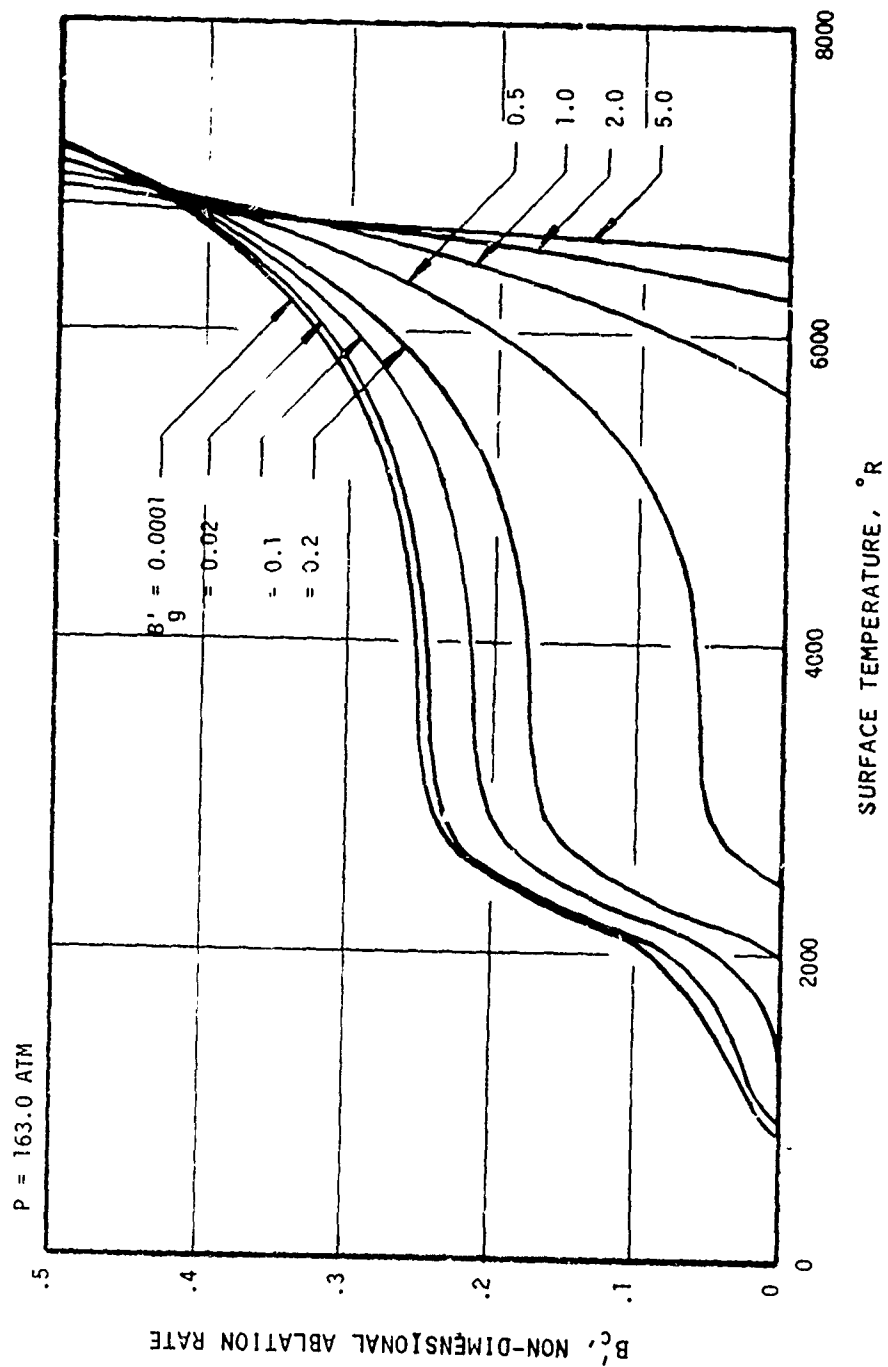


Figure 6-5. Surface Response of MXCE 280 Carbon Phenolic to 5% AL-CTPB Propellant

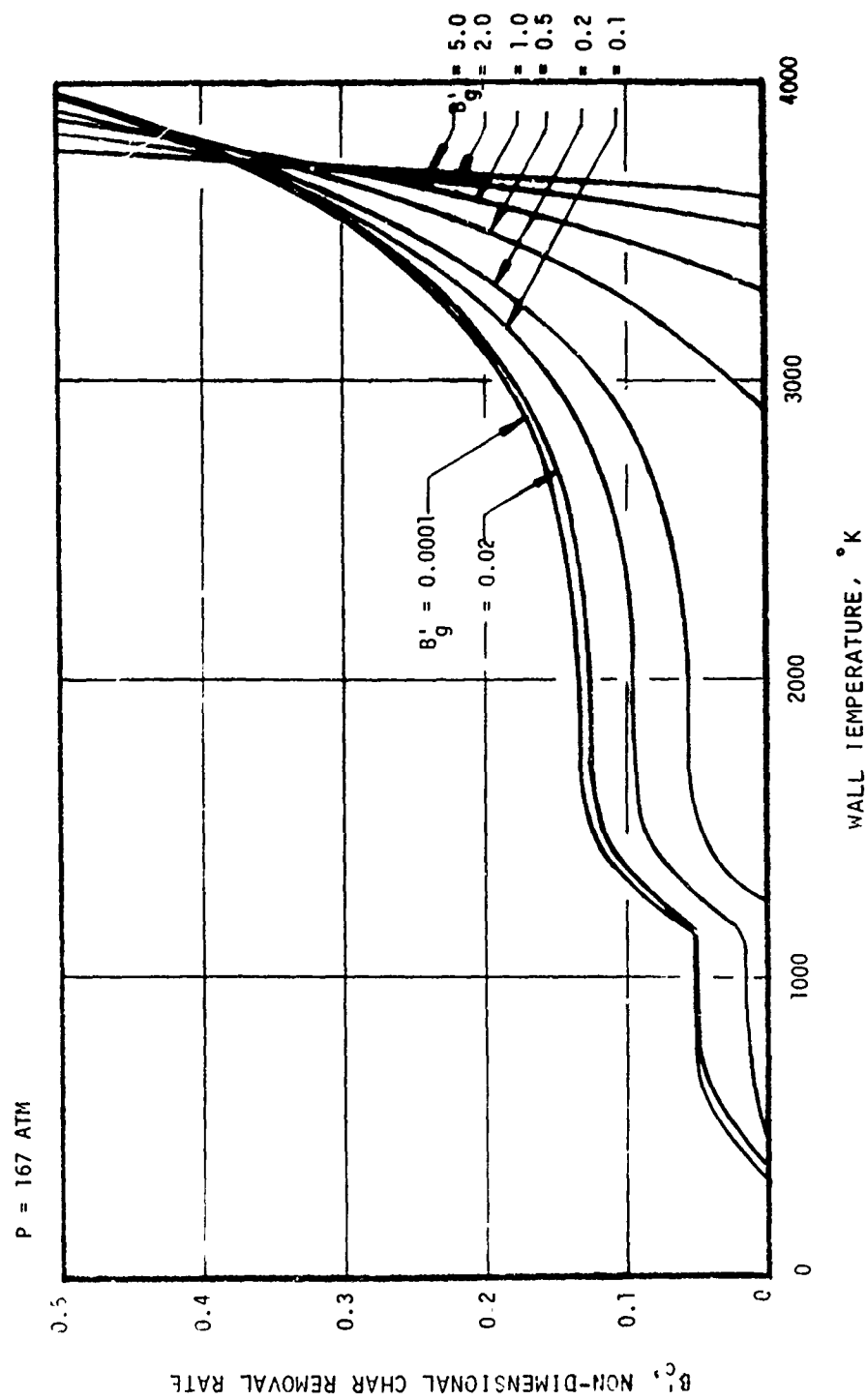


Figure 6-6. Surface Response of MXCE 280 to CTPB 18 Propellant

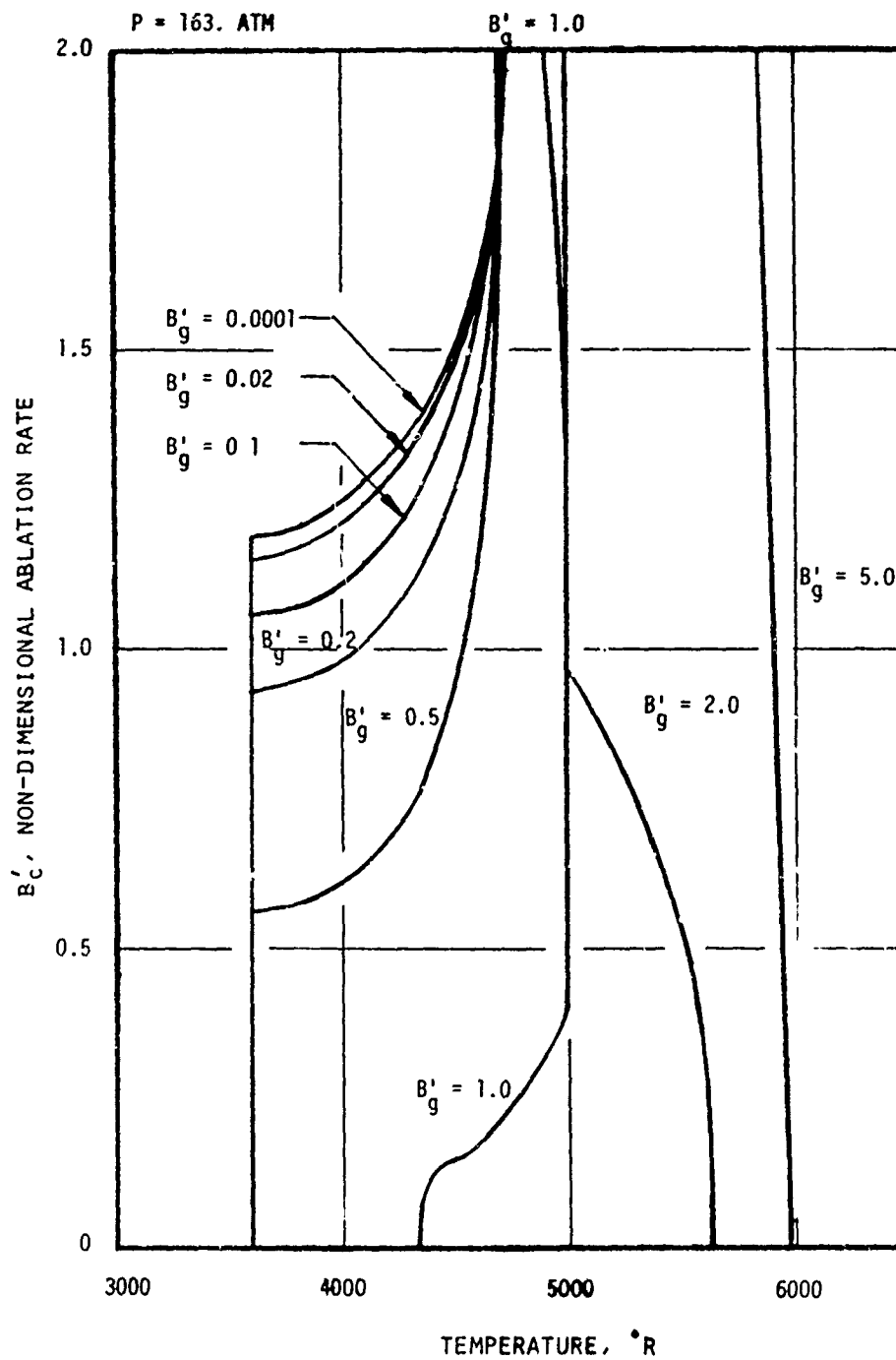


Figure 6-7. Surface Response of MXSE 280 Silica Phenolic to 5% AL-CTPB



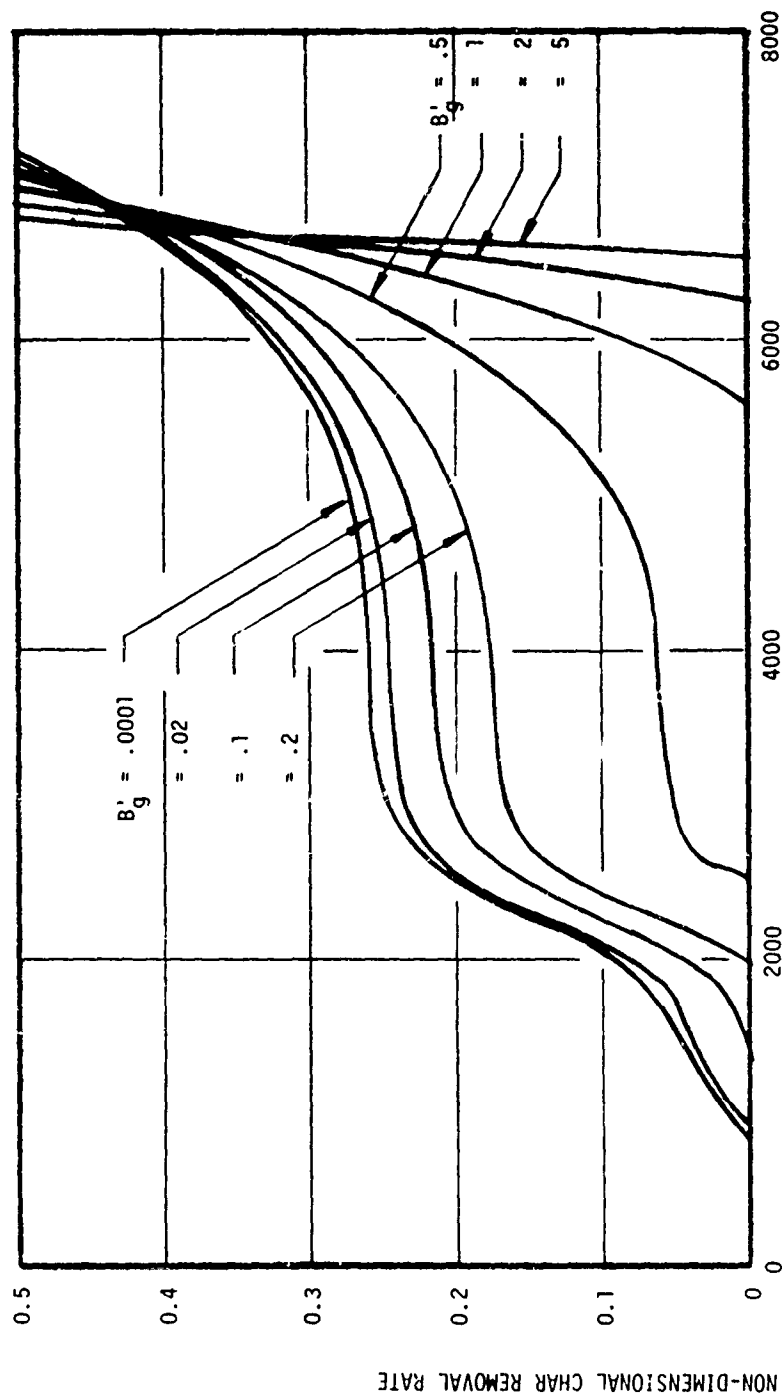


FIGURE 6-8. SURFACE RESPONSE OF MX4926 TO 5% AL-CTPB PROPELLANT

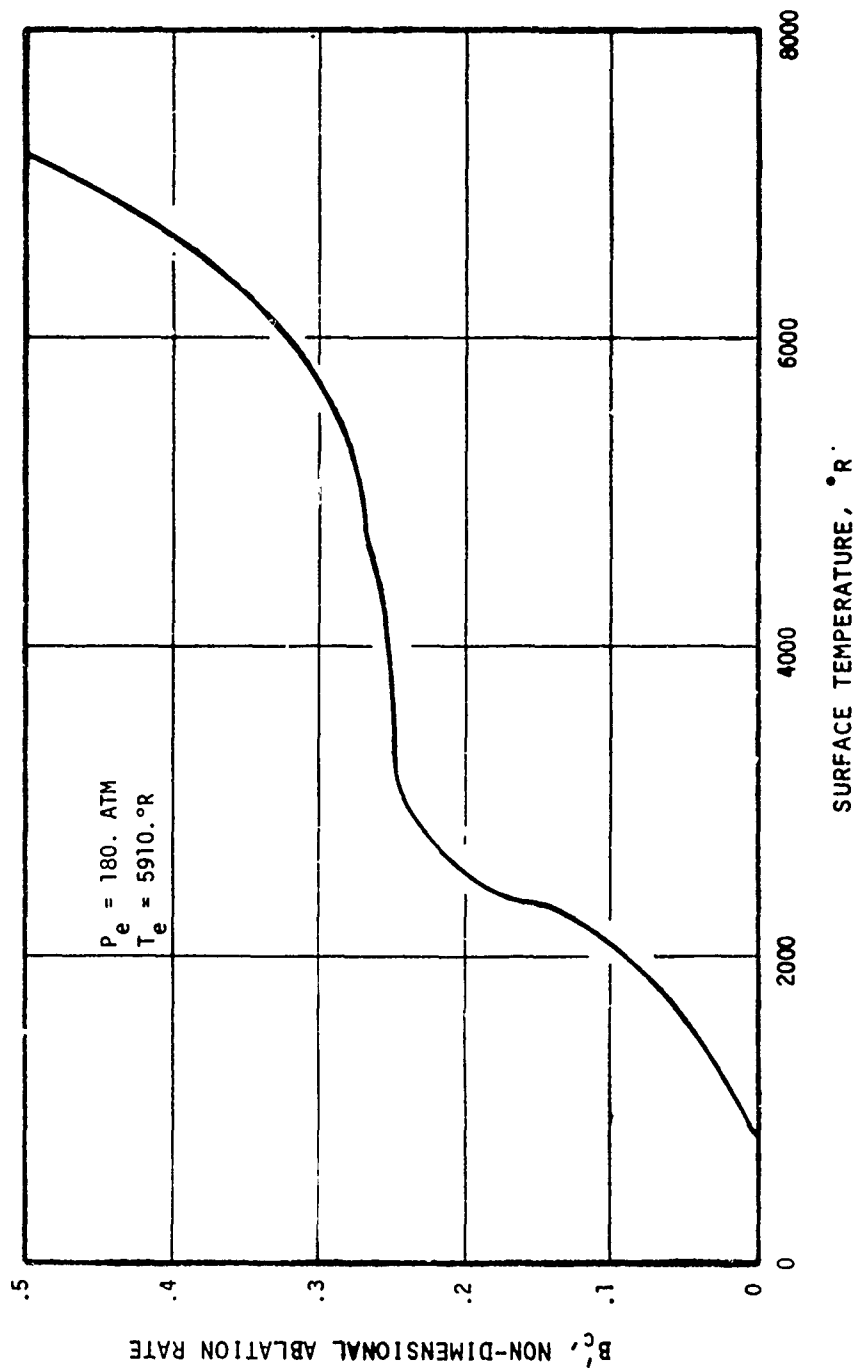


Figure 6-9. Diffusion Controlled Response Pycobond 410-65 to 5% AL-CTPB Propellant

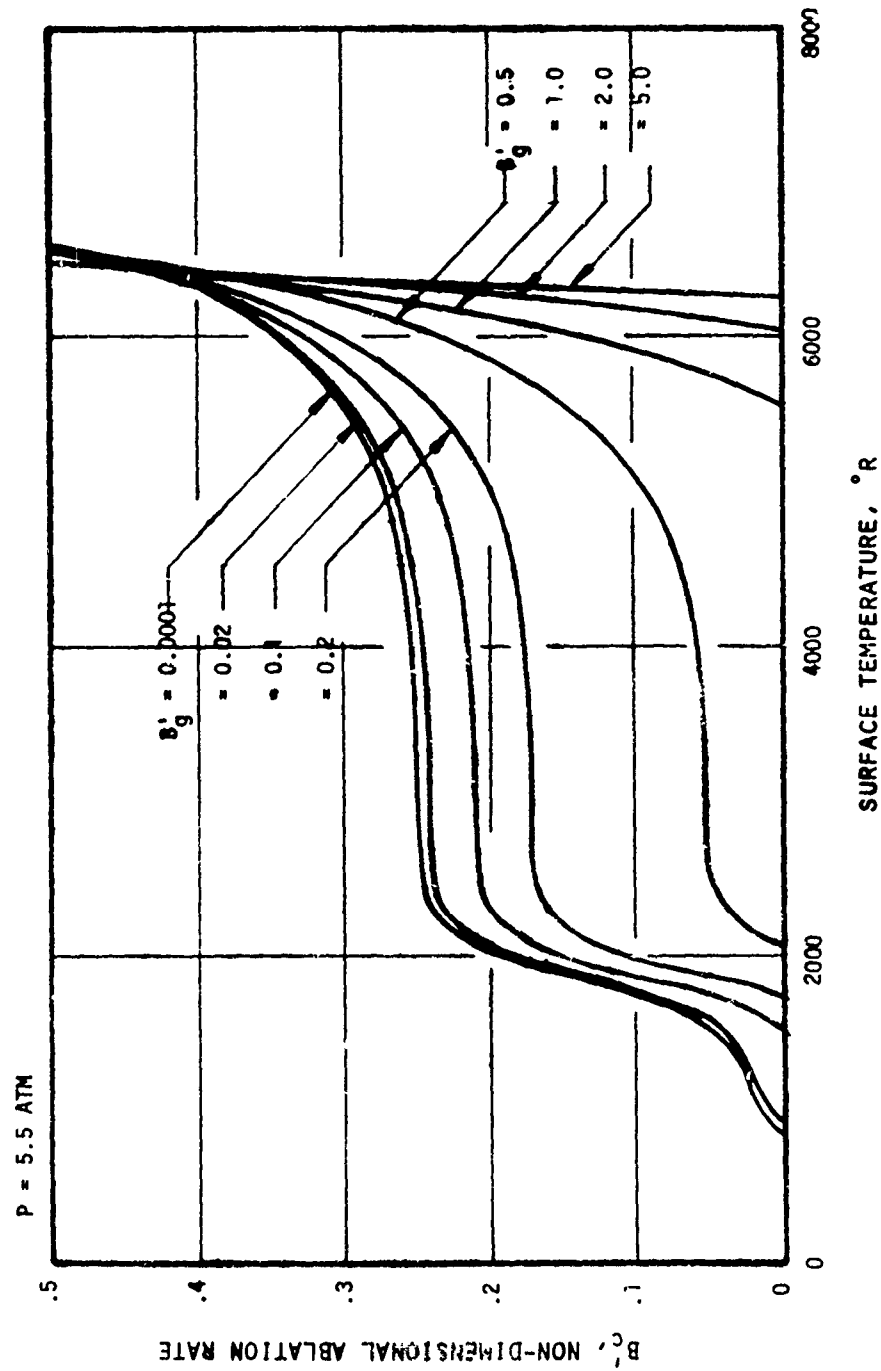


Figure 6-10. Surface Response of FM5055 Carbon Phenolic to 5% AL-CTPB Propellant

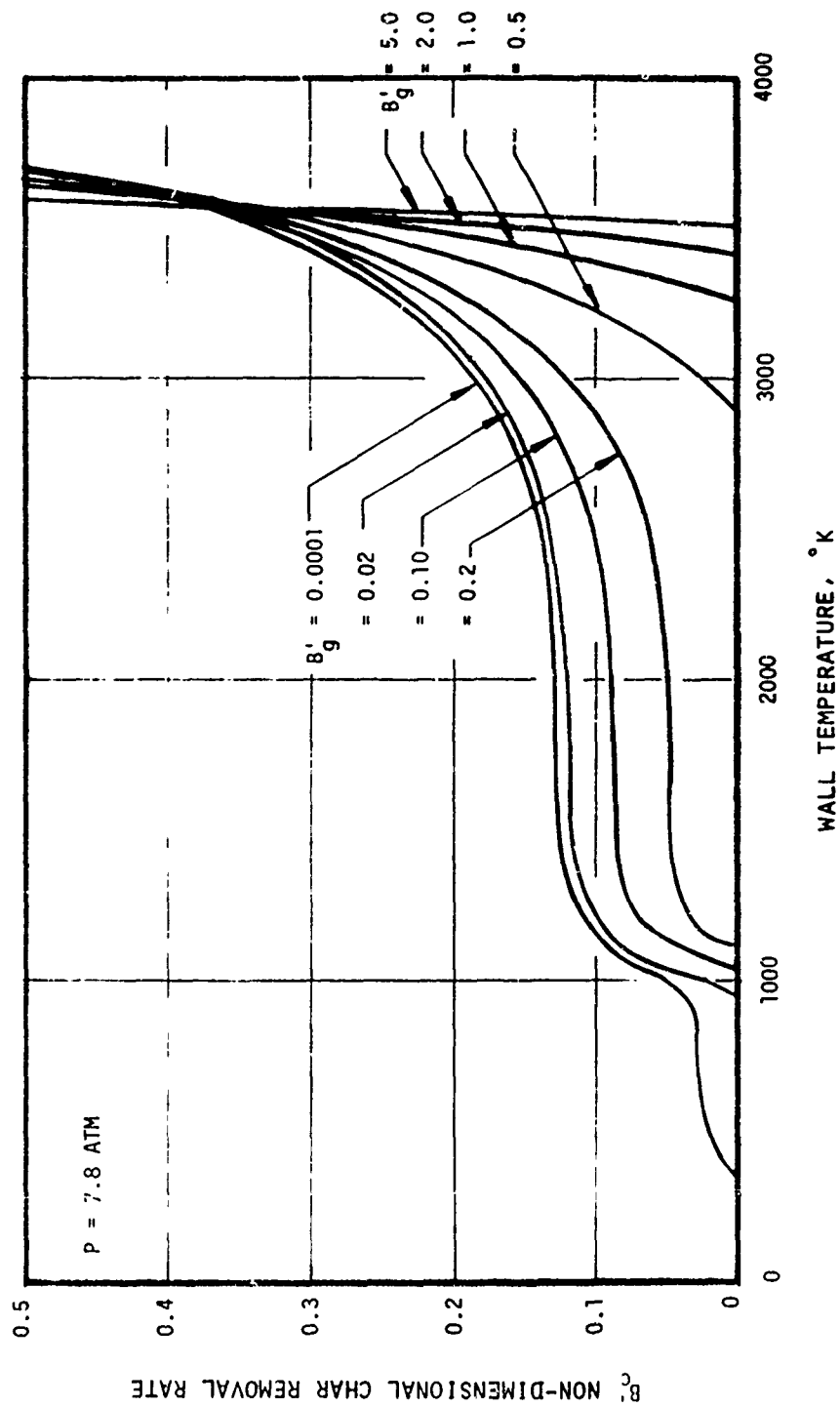


Figure 6-11. Surface Response of FM5055 to CTPB 18% Propellant

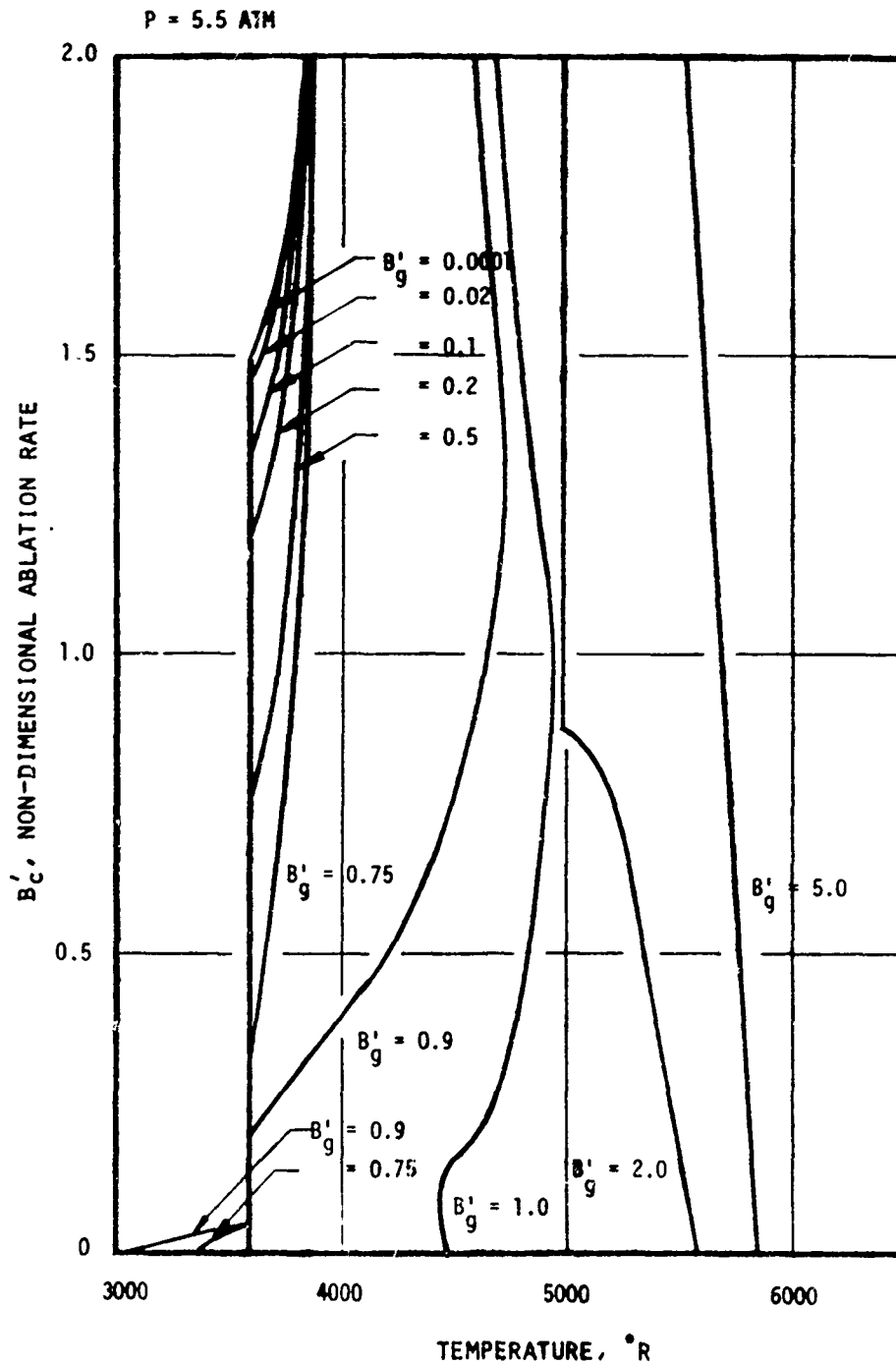


Figure 6-12. Surface Response of MX2600 Silica Phenolic to 5% AL-CTPB Propellant

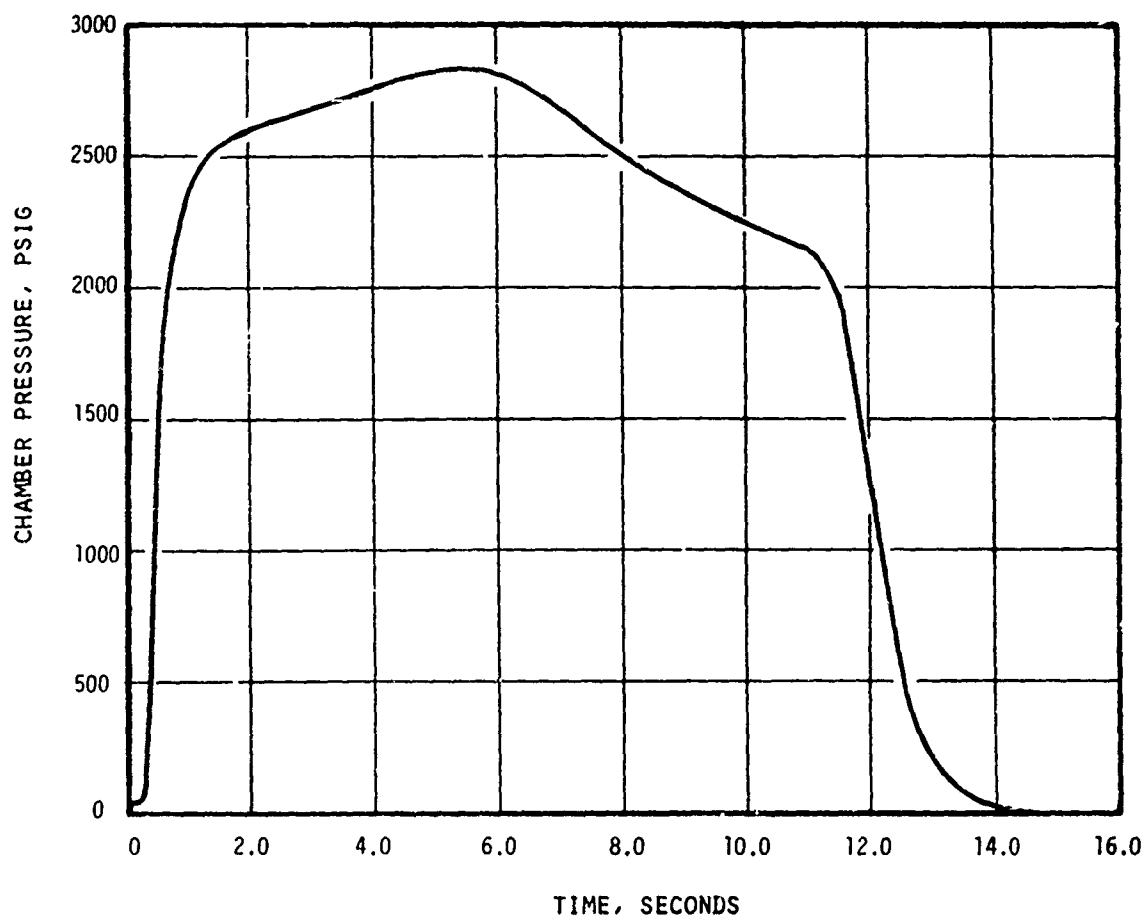


Figure 6-13. Chamber Pressure History For Test Firing 002

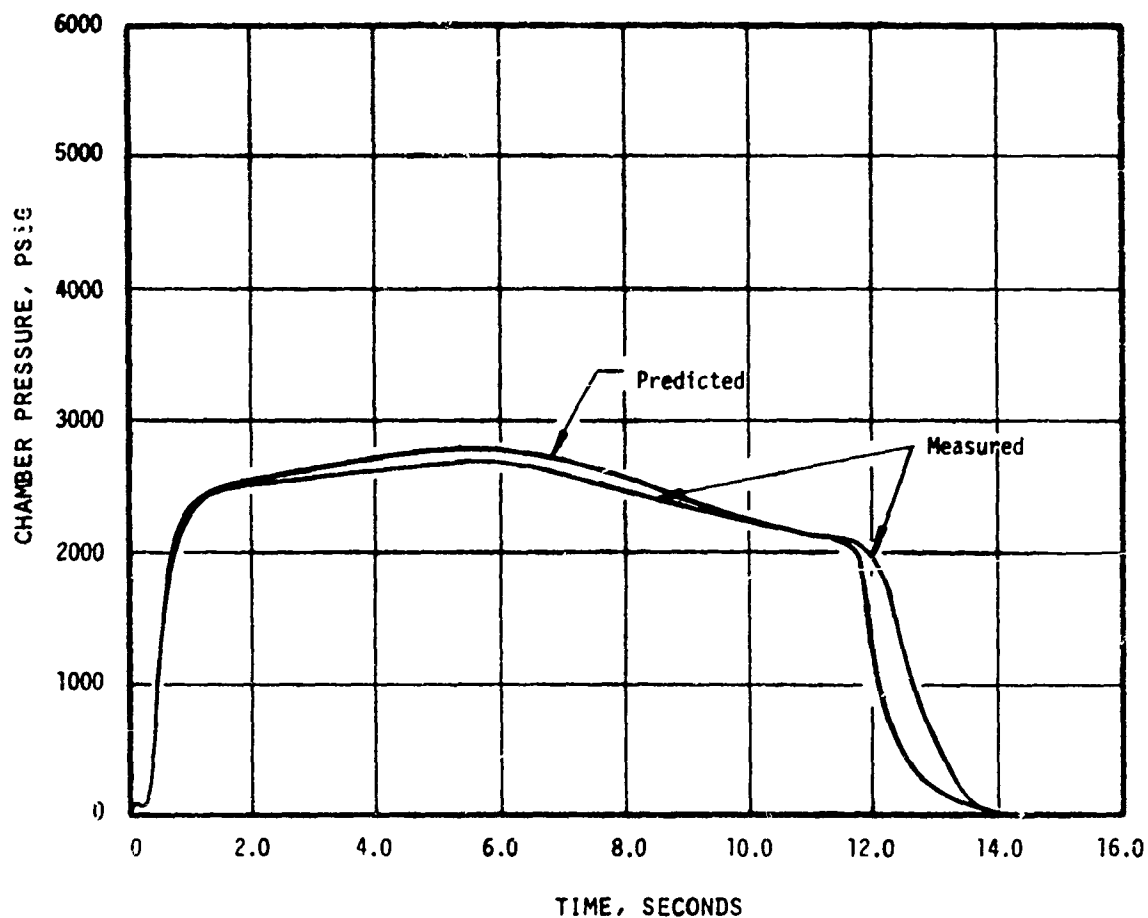


Figure 6-14. Chamber Pressure History For Test Firing 003

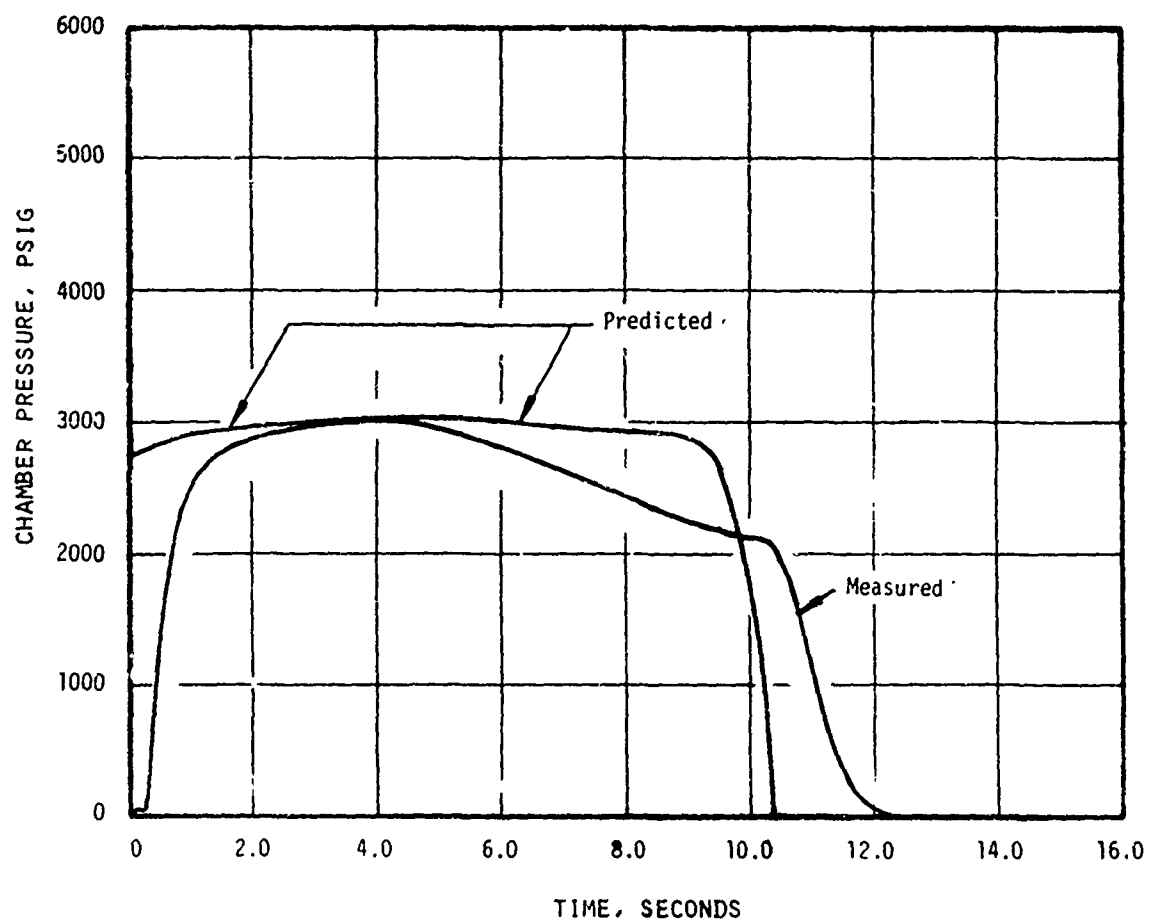


Figure 6-15. Chamber Pressure History For Test Firing 005



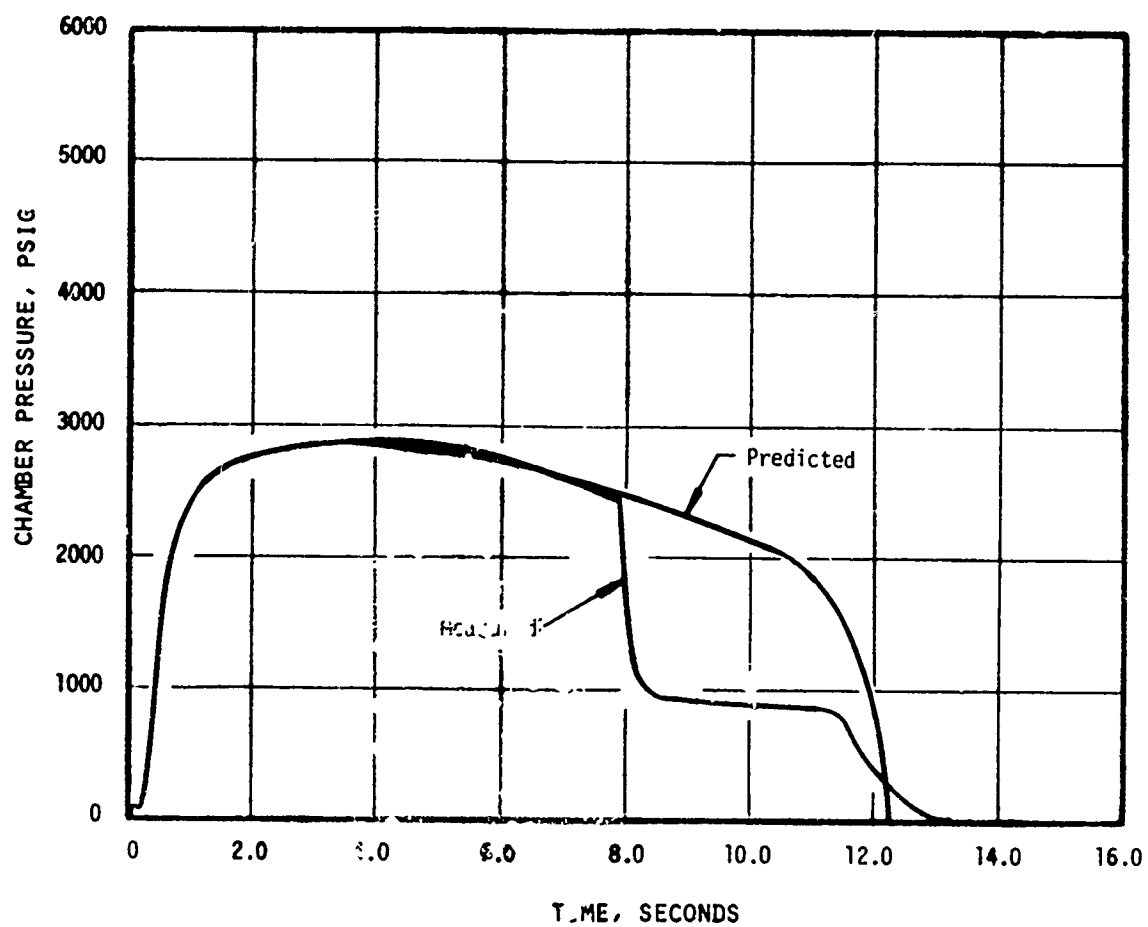


Figure 6-16. Chamber Pressure History For Test Firing 006

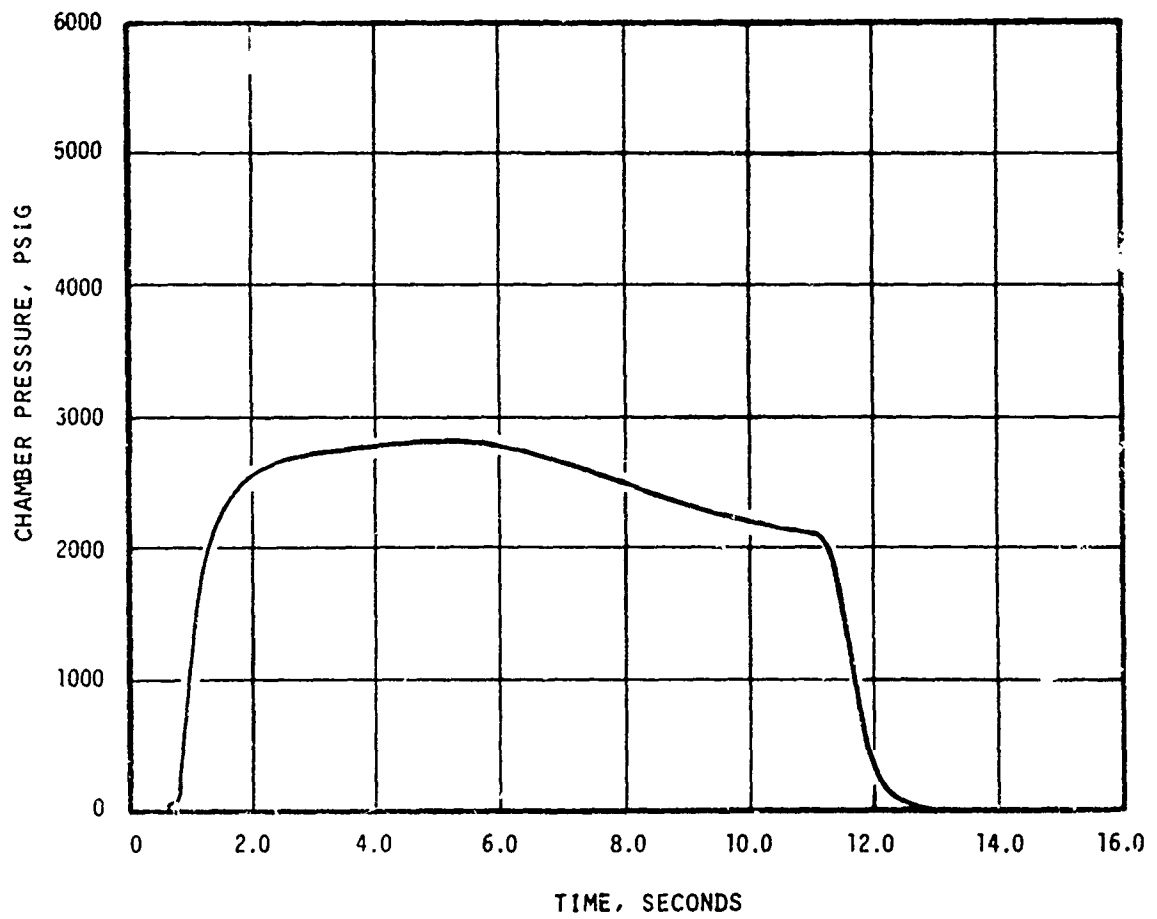


Figure 6-17. Chamber Pressure History For Test Firing 009

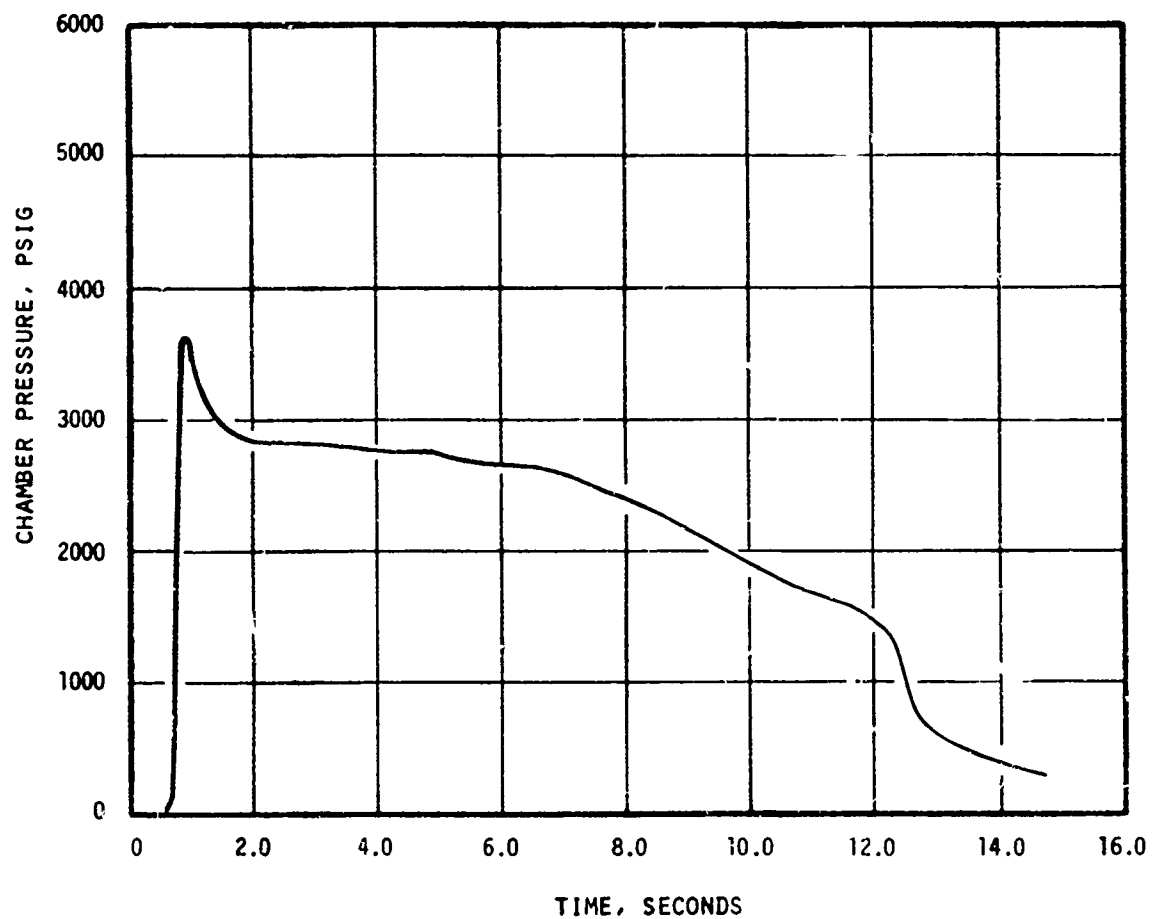


Figure 6-18. Chamber Pressure History for Test Firing 013

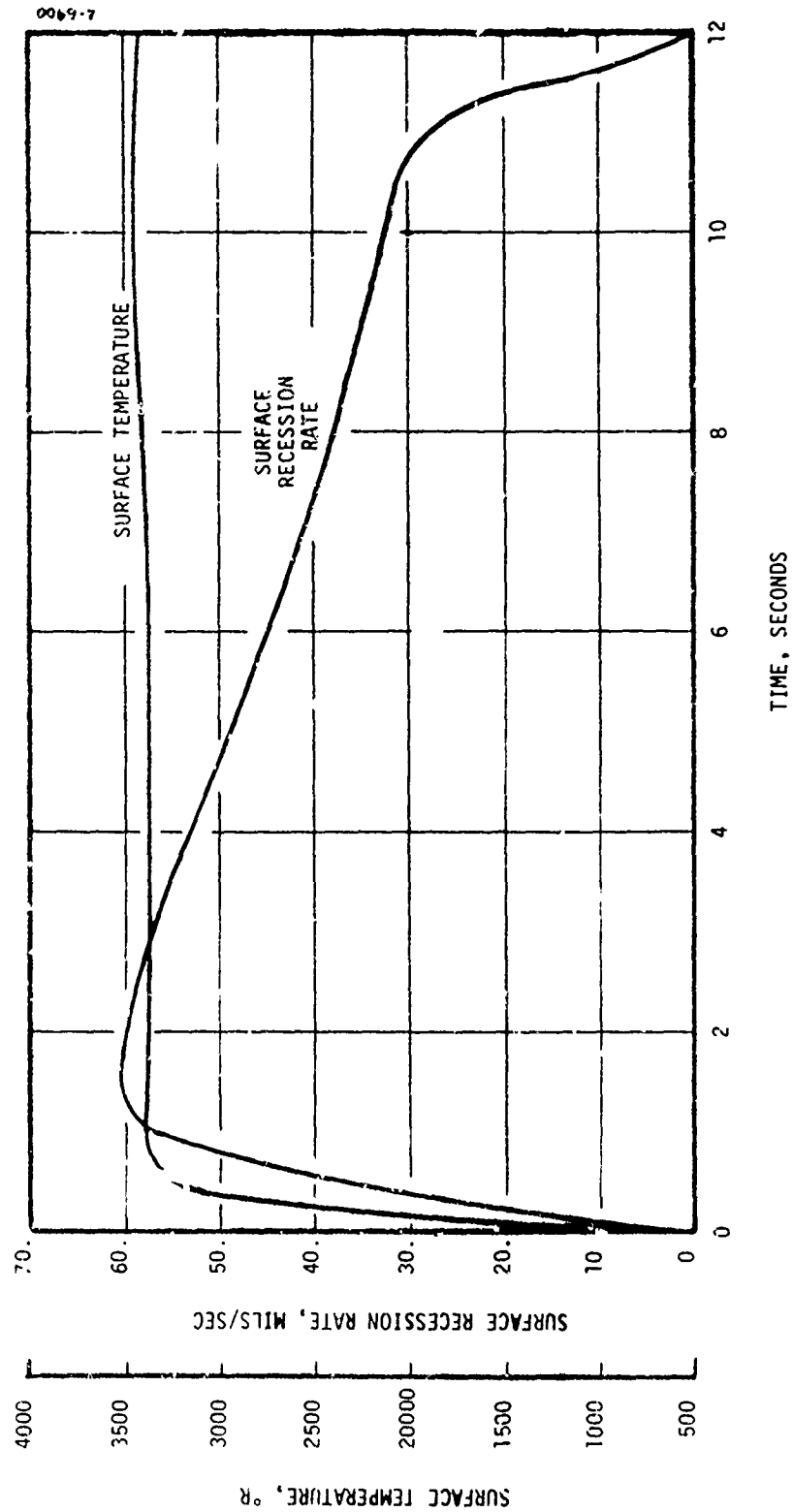


Figure 6-19. Surface Temperature and Recession Rate Histories for the MSCE 280 Blast Tube of Test Firing 5

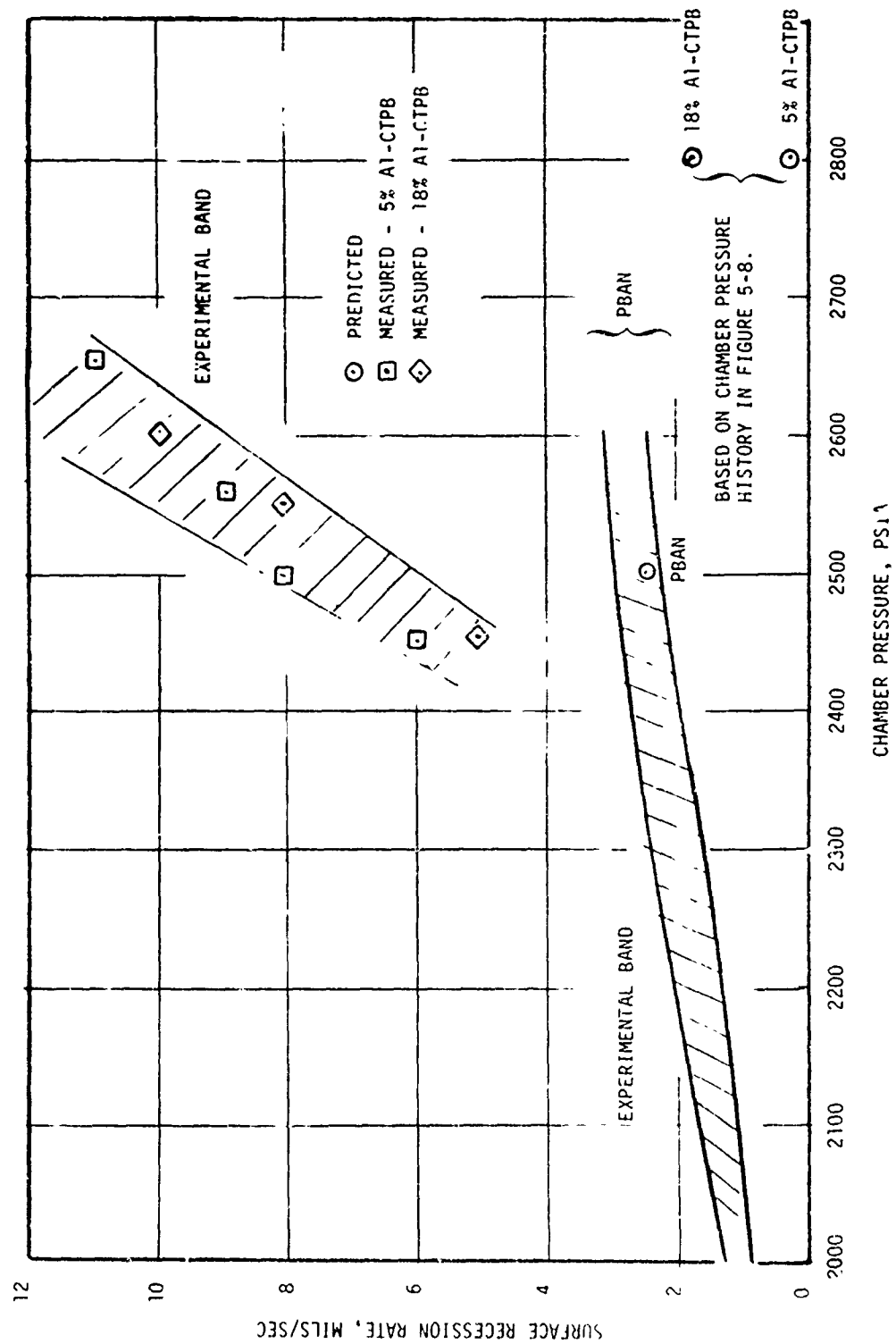


Figure 6-20. Comparison of Predicted and Measured PG Washer Recession Rates

## SECTION 7

### EXPERIMENTAL EVALUATION OF THE HEAT FLUX BOUNDARY CONDITIONS

Total heat flux sensors (or thermocoupled plugs) were installed in the blast tube of rocket motors S/N 005 and S/N 007. The objectives of this instrumentation were to

- Determine experimentally the total heat flux to the nozzle wall and relate this to the convective heat transfer coefficient predicted by the analytical model.
- Determine experimentally the transient surface recession.

The thermal instrumentation systems used to satisfy the above objectives, and then installation into the nozzle components are described briefly in Section 7.1. The data reduction procedure is summarized in Section 7.2, and the experimental data and comparisons between the data and analytical predictions are presented in Section 7.3.

#### 7.1 THERMAL INSTRUMENTATION SYSTEMS

The thermal instrumentation on the high chamber pressure nozzle firings consisted of four total heat flux sensors and three narrow view angle radiometers. The instrumentation was concentrated on motors S/N 005 and S/N 007. This instrumentation is described in considerable detail in References 1, 19, and 20 and, thus, its main features will only be summarized in the following paragraphs. A description of the total heat flux sensor and its installation into the nozzle components will be presented in the following paragraphs.

A schematic of the total heat flux sensor is shown in Figure 7-1. This sensor is 0.500 inches in diameter and is fabricated of the same material at the same layup angle as in the nozzle component in which it is to be installed. Thermocouple lead wires are placed in an isothermal plane at various depths below the surface with the thermocouple junction at the center of the sensor. This junction which is nominally 15 mils in diameter butts up against the sensor material at the interface between the 10 and 20 mil cylindrical holes. The thermocouple leads are placed along the sides of the sensor and are electrically insulated from the sensor by beryllia sleeving which is potted in a boron nitride

slurry. The leads are attached to 30 mil diameter pins located at the back of the sensor. These pins provide terminals for attaching the measurement system leads. The thermocouples are either tungsten 5 percent rhenium/tungsten 26 percent rhenium or Chromel/Alumel and are accurately located using x-ray photographs.

The sensors are installed in the ablative nozzle components prior to the assembly of these components into the structural steel shell. The sensors are bonded to the nozzle component along the cylindrical surface of the sensor, and in addition, the cavity behind the sensor is filled with epoxy to protect the pins and the thermocouple lead wire junctions.

The locations of the total heat flux sensors in the blast tube of the two nozzles are shown in Figure 7-2. The sensors are at the same axial location in the two blast tubes but their radial locations were different due to the difference in the initial blast tube area ratio for the two nozzles.

## 7.2 DATA REDUCTION PROCEDURE

The data reduction procedure for defining the total heat flux to the exposed surface of a solid rocket nozzle is outlined in Figure 2-3. In this procedure, the ACE computer program is used to define the wall enthalpies and the non-dimensional surface thermochemical maps, and the Option 2 version of the CMA computer program is used to determine the in-depth temperatures and the pertinent in-depth energy terms. The in-depth energy terms of interest are the thermal conduction, the adsorption of energy by the pyrolysis gases as they percolate to the surface, and the adsorption of energy in the pyrolysis zone due to material degradation. In the Option 2 version of the CMA program, the surface boundary conditions consist of a specified surface temperature and a specified surface recession rate. As shown in Figure 7-3, these surface boundary conditions are varied until agreement is obtained between the measured and predicted in-depth temperatures. In addition the integral of the specified surface recession rate must be in agreement with the measured surface recession. The surface and in-depth temperatures and the surface recession rate defined from the final iteration using the Option 2 version of the CMA computer code are referred to as "determined" parameters.

As shown in Figure 3.1, the input to the CMA and ACE computer programs require physical, thermal, and chemical material property data. Since this information is used in determining the total heat flux to the surface, the use of the thermocoupled ablative plug as a total heat flux sensor requires that the ablative material be characterized. The material used to fabricate the sensors for the rocket motor firings was MXCE 280. The thermal, physical,

and chemical properties for this material is presented in Reference 1. The surface thermochemical maps and wall and free stream enthalpies which were generated using the ACE computer code are presented in Appendix A. The use of these curves in determining the total surface heat flux is described in detail in Reference 19 and will not be repeated here.

### 7.3 COMPARISONS BETWEEN MEASURED AND PREDICTED SURFACE HEAT FLUX

Experimental thermocouple data were obtained only from the heat flux sensors installed in the blast tube for S/N 005. The determined in-depth temperatures are compared with the measured temperatures in Figure 7-4 for the sensor in the forward end of the blast tube and in Figure 7-5 for the sensor installed in the aft end of the blast tube. The net surface recession rates used in the data reduction analysis to obtain the determined in-depth temperatures are presented in Figure 7-6 for the forward plug (or sensor). The shape of this curve is due to surface recession in the blast tube causing the incident surface heat flux to decrease during the motor firing. A comparison of this determined surface recession (option 2 CMA) and the predicted surface recession (option 1 CMA) is shown in Figure 7-7.

The end result of the data reduction is the determined convective heat transfer coefficient which is compared with the predicted value in Figure 7-8. The comparisons of both the surface recession and the heat transfer coefficient is within 20 percent, and the determined values are generally low. However, the good agreement which is obtained substantiates the analytical techniques being used.



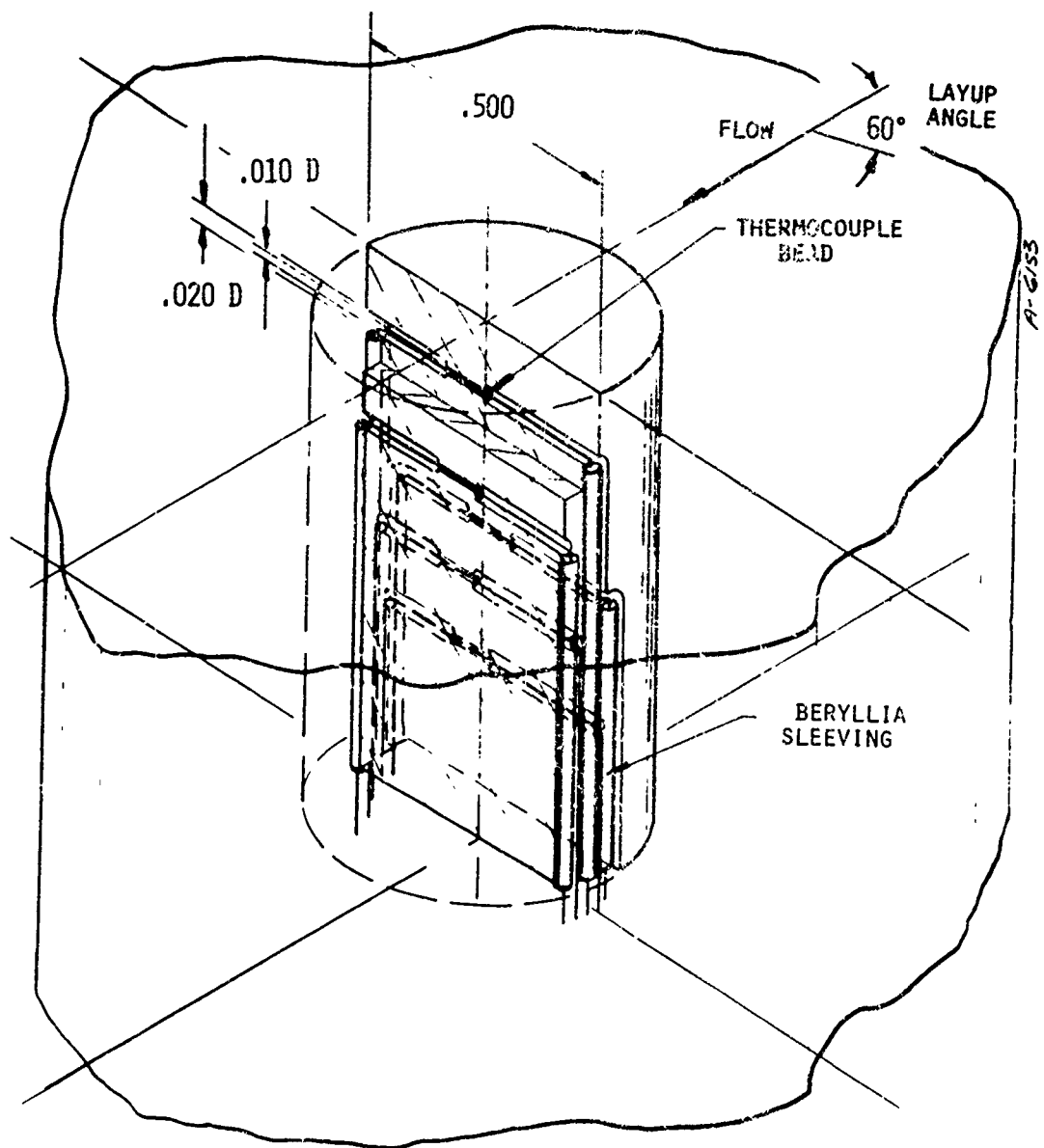


Figure 7-1. Schematic of Total Heat Flux Measurement System Plug

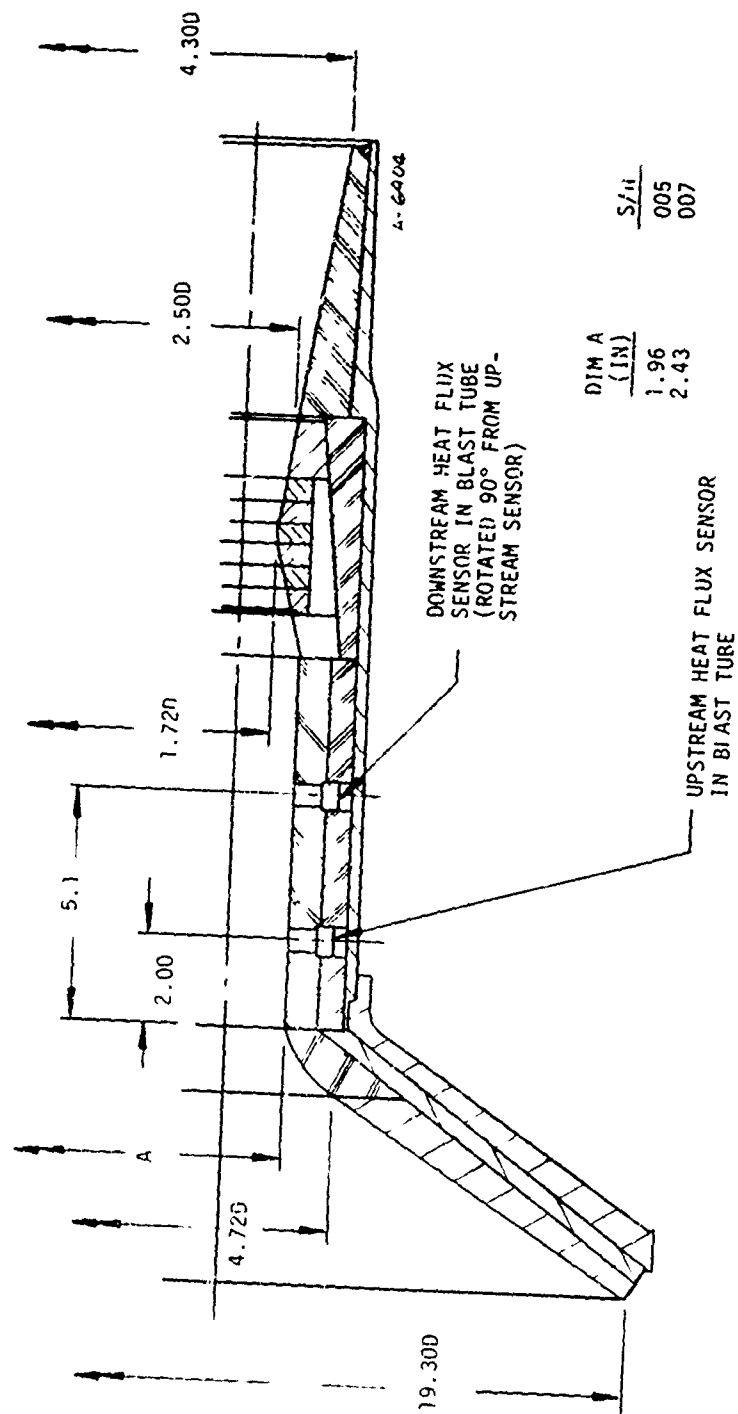


FIGURE 7-2 SCHEMATIC DRAWING SHOWING LOCATIONS OF TOTAL HEAT FLUX SENSORS

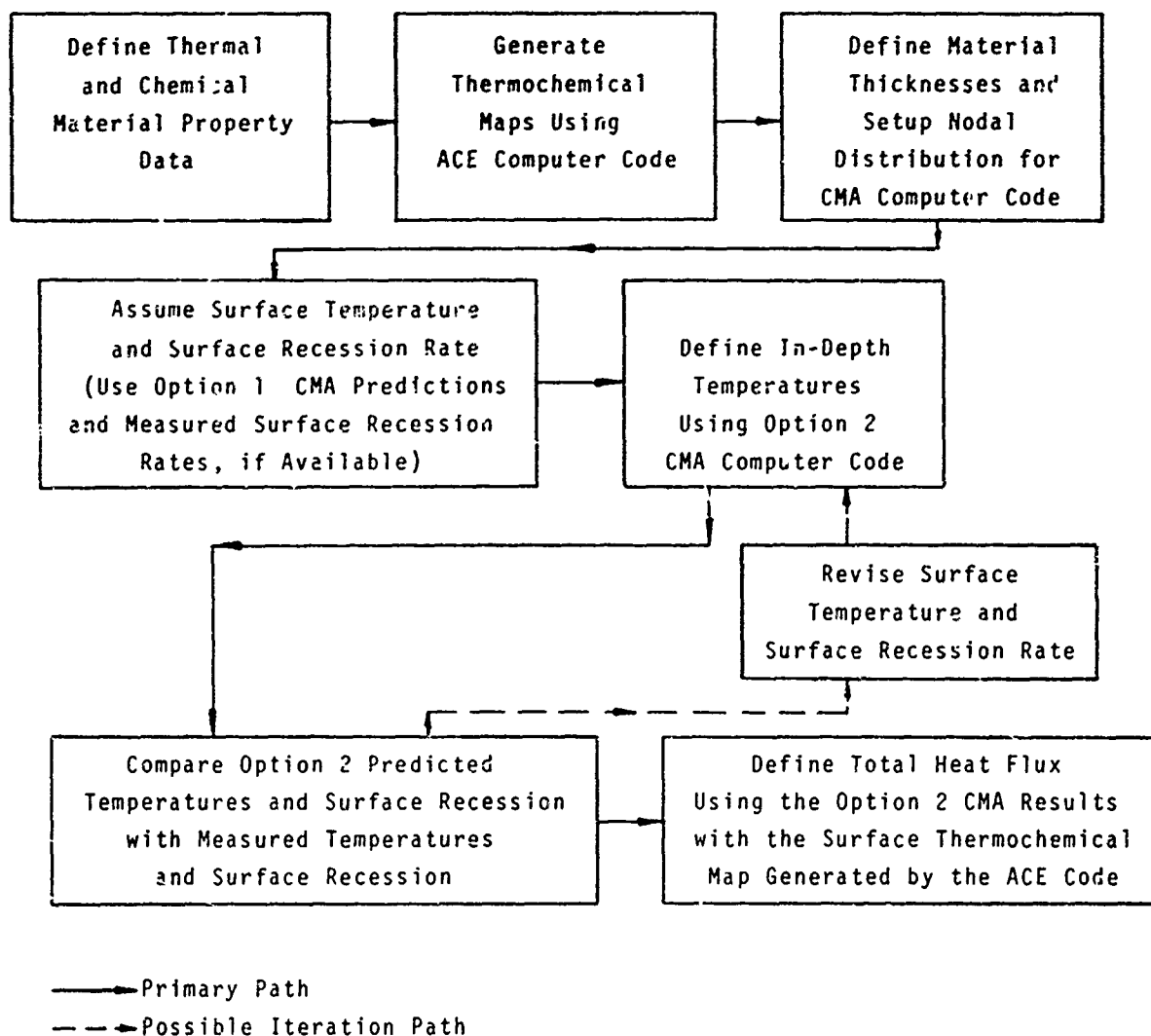


Figure 7-3. Procedure for Defining Total Heat Fluxes Using Measured In-Depth Temperature Histories

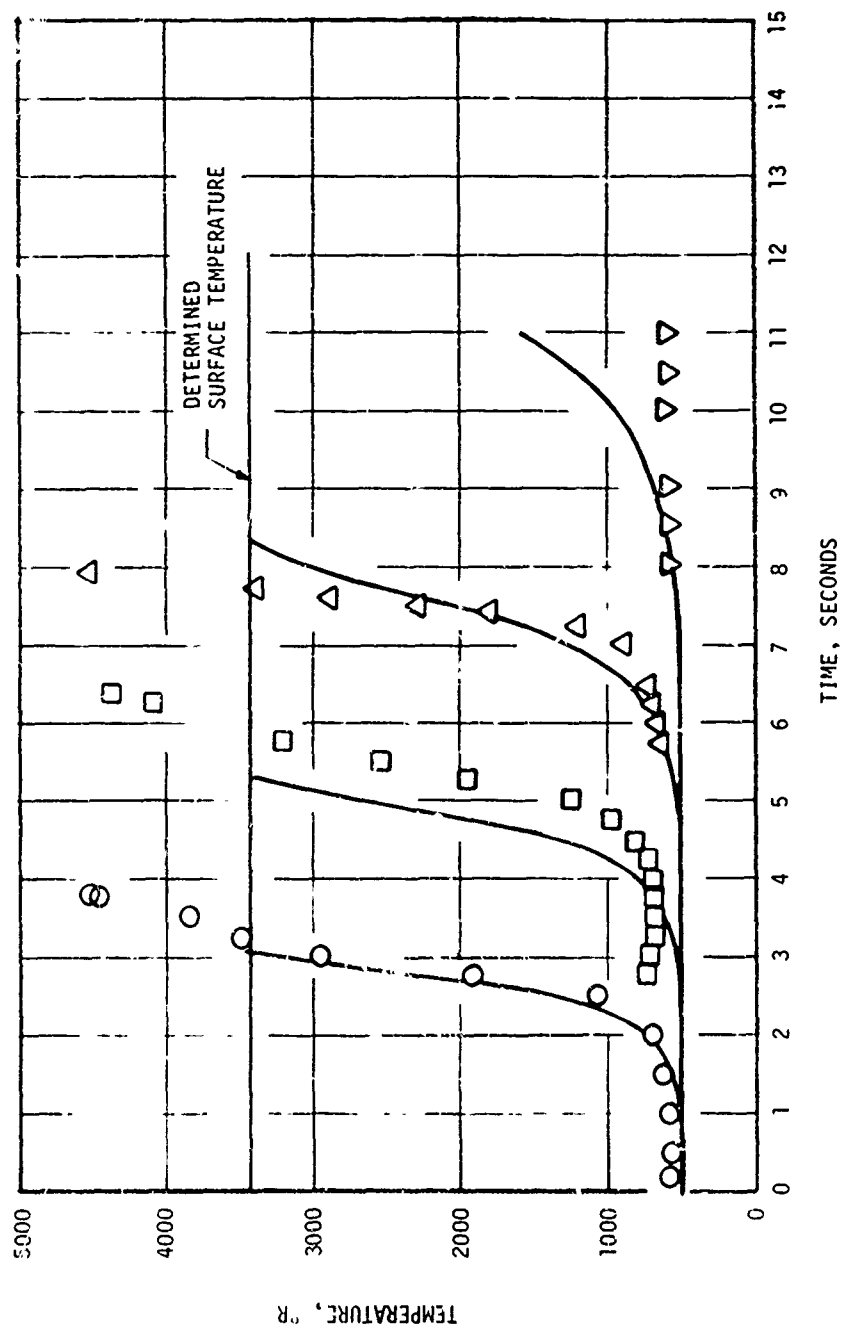


Figure 7-4. Measured and Determined Temperatures for Forward Thermocouple Plug

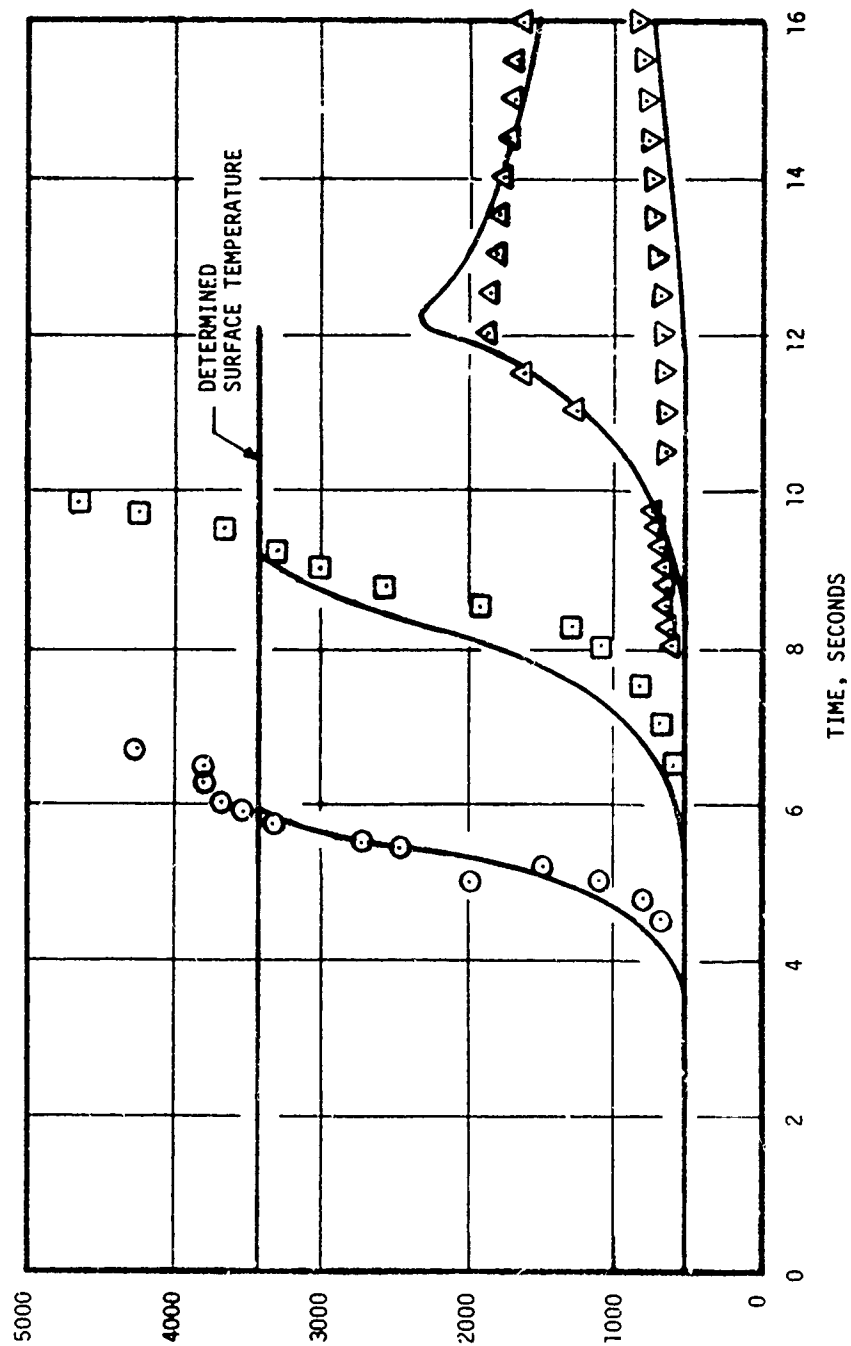


Figure 7-5. Measured and Determined Temperatures  
for Thermocouple  
B) Aft Plug

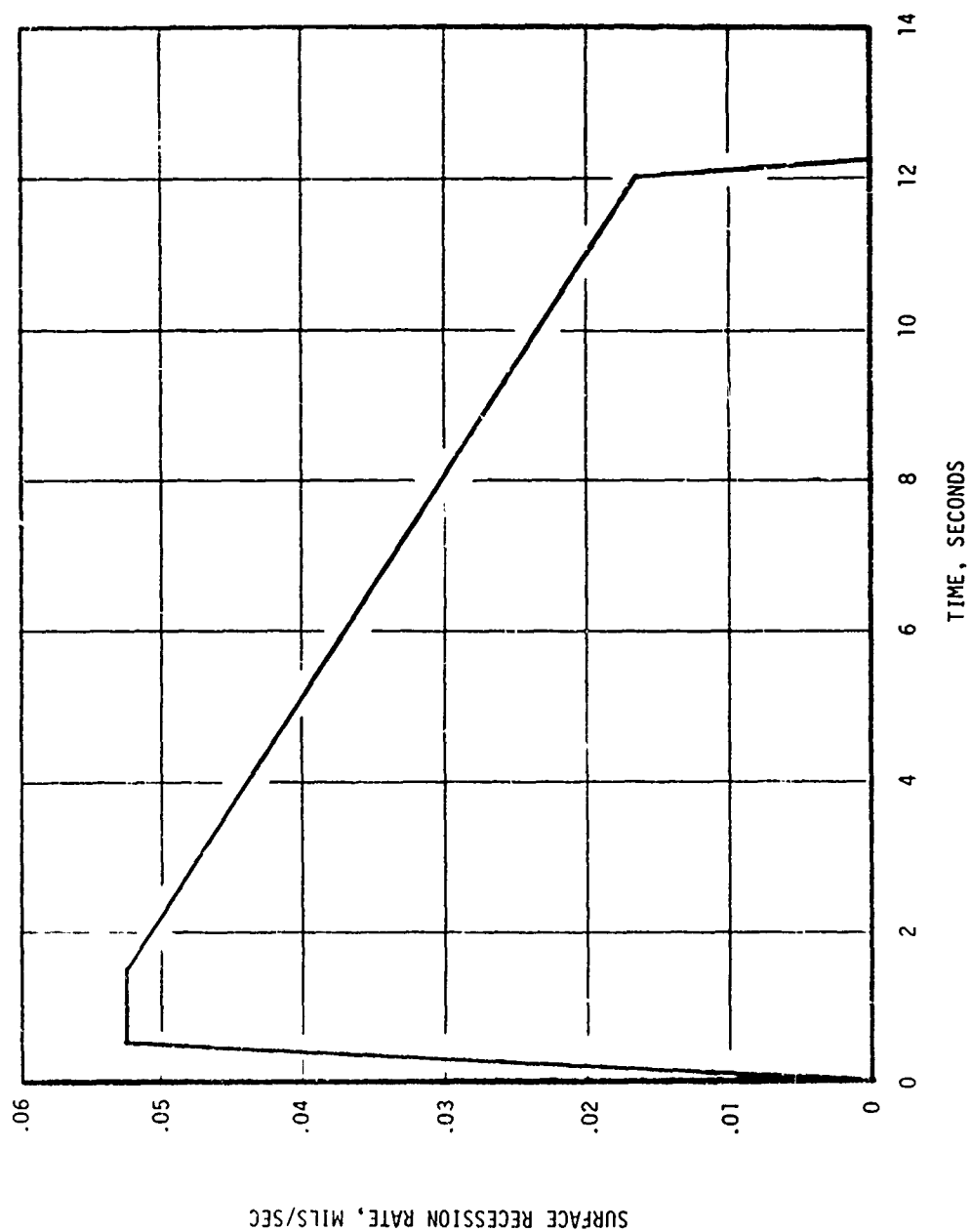


Figure 7-6 . Determined Blast Tube Surface Recession Rate  
A) Forward Plug

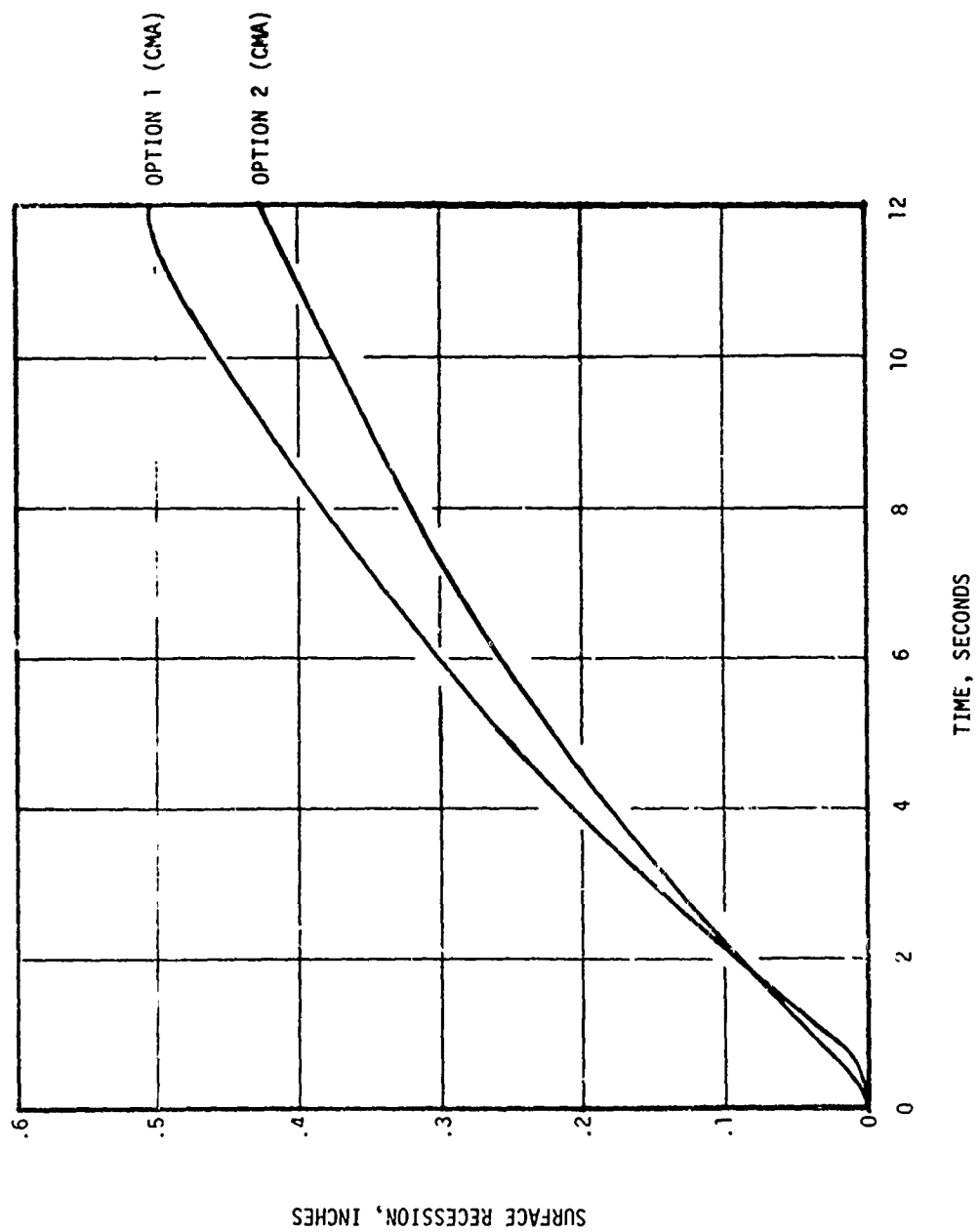


Figure 7-7. Comparison Between Measured, Determined, and Predicted Surface Recession

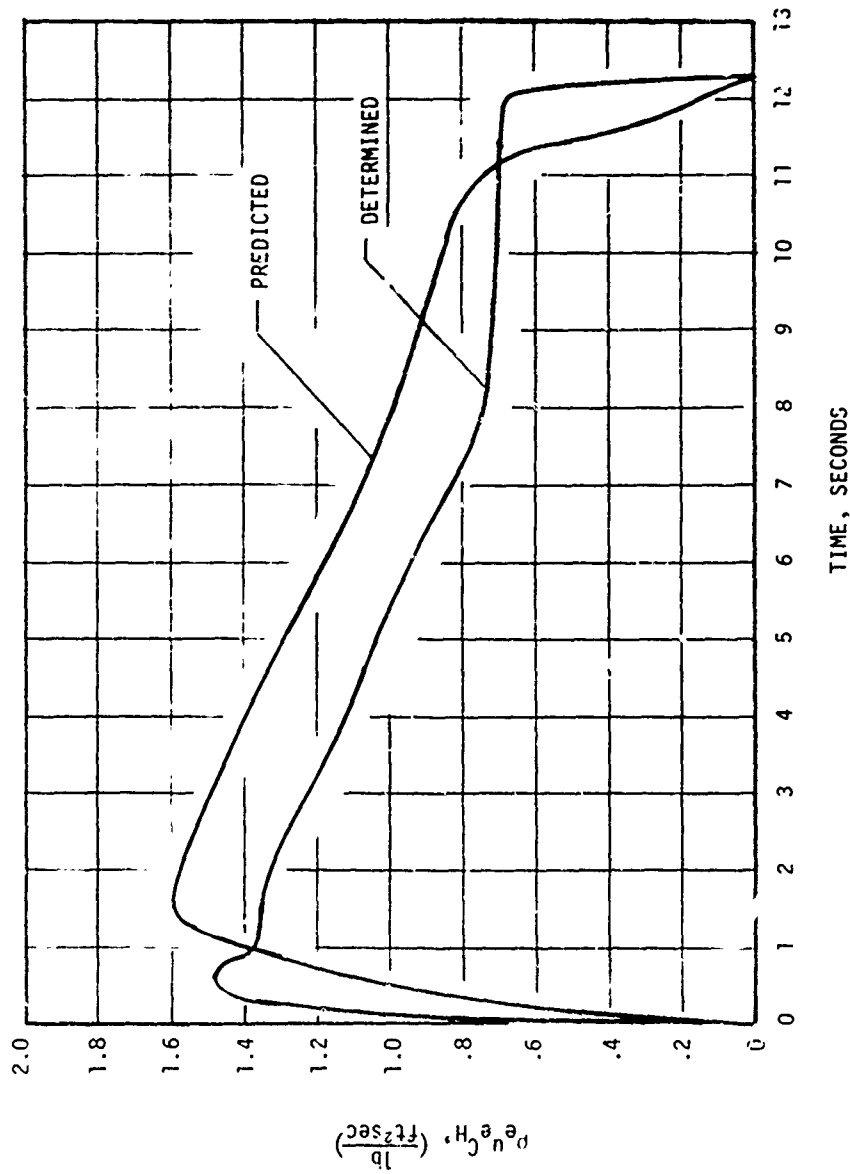


Figure 7-8 . Comparison Between Predicted and Determined Heat Transfer Coefficients for Blast Tube



## SECTION 8

### CONCLUSIONS AND RECOMMENDATIONS

- Aerotherm analysis techniques (ACE, ARGEIBL, CMA, ASTHMA, and GASKET) have been validated for predicting the thermochemical performance of charring ablating and bulk graphite materials.
- The predicted surface recession for the pyrolytic graphite washers at the nozzle throat was low by a factor of at least five for the 18 percent Al-CTPB and 5 percent Al-CTPB propellants. However, the analytical techniques had predicted accurately the surface recession of this material for a 16 percent Al-PBAN propellant at a similar chamber pressure. The exact reason for the discrepancy has not been identified. Because of the severity of the problem, further analytical and experimental efforts should be pursued.
- The predicted circumferential variation in the blast tube surface recession rate was not in good agreement with the experimental measurements for the keyhole port grain configuration. However, this discrepancy is due to the assumption made in the flow field analysis that the two-dimensional flow effects resulting from the keyhole port would be damped out in the upstream end of the blast tube. The experimental data show that the two dimensional flow effects exist along the center length of the blast tube.
- The total heat flux sensors/or thermocouple plugs) provide a reliable and accurate system for defining surface recession rates and in-depth temperatures as well as total incident surface heat flux. The convective heat transfer coefficient determined from these measured data were in good agreement with the predicted values.
- Thermochemical screening provides an economical and practical method for selecting candidate materials.

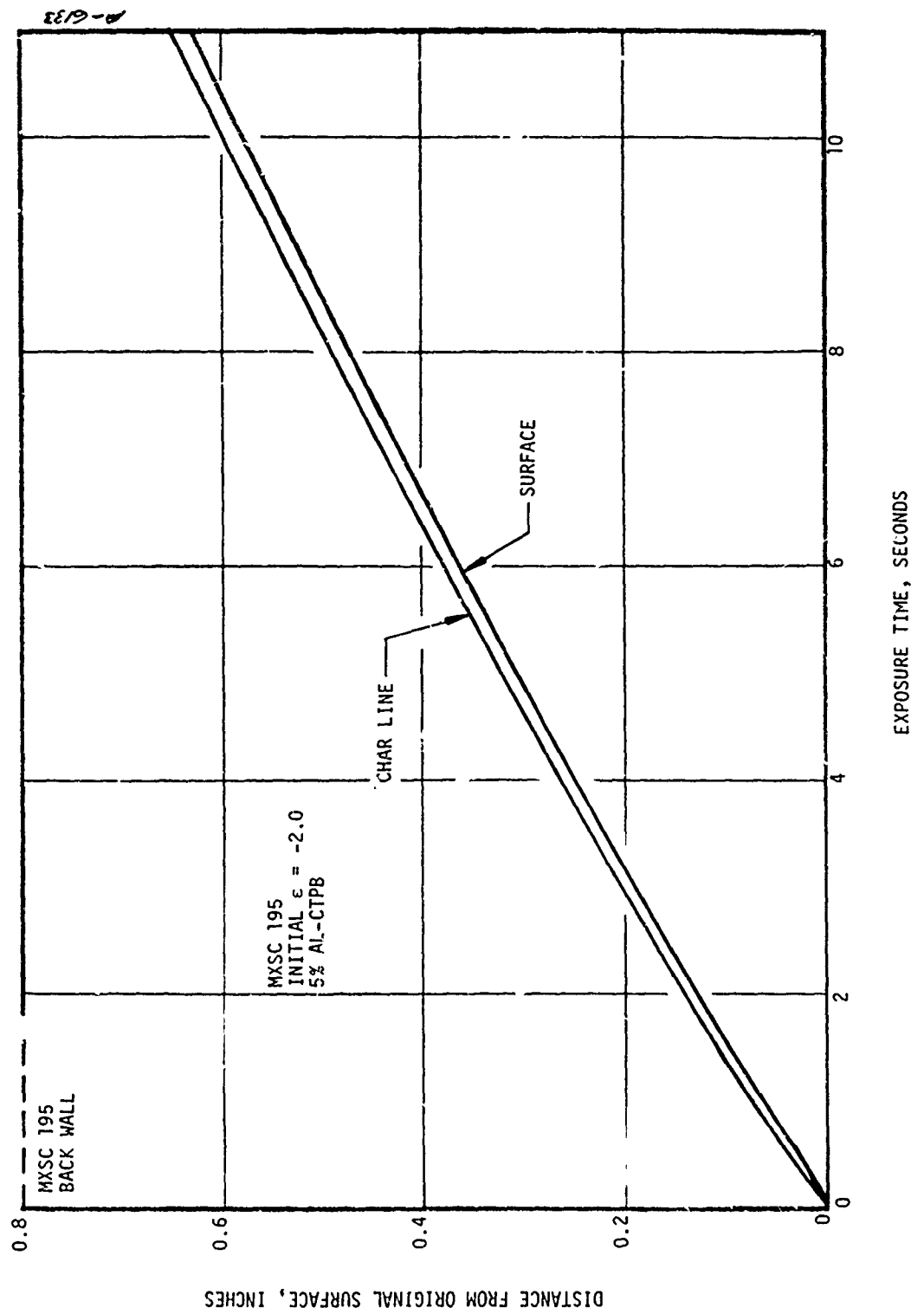


Figure 4-12. Blast Tube Surface and Char Recession Histories

## APPENDIX A

### THERMOCHEMICAL MAPS FOR DEFINING TOTAL SURFACE HEAT FLUX

The thermochemical maps required for defining the total surface heat flux from measured in-depth temperatures are presented in Figures A-1 through A-4 for MXCE 280. The information presented in these figures include the following:

- Relationship between non-dimensional char removal rate,  $(B'_c)$  non-dimensional pyrolysis off gas rate,  $(B'_g)$  ratio of  $B'_g/B'_c$ , and wall temperature
- Relationship between the wall chemical potential, the wall temperature and the non-dimensional pyrolysis off gas rate.
- Relationship between the wall enthalpy, the wall temperature, and the non-dimensional pyrolysis off gas rate.
- Relationship between the freestream chemical potential and the freestream enthalpy with temperature.
- Recovery enthalpy.

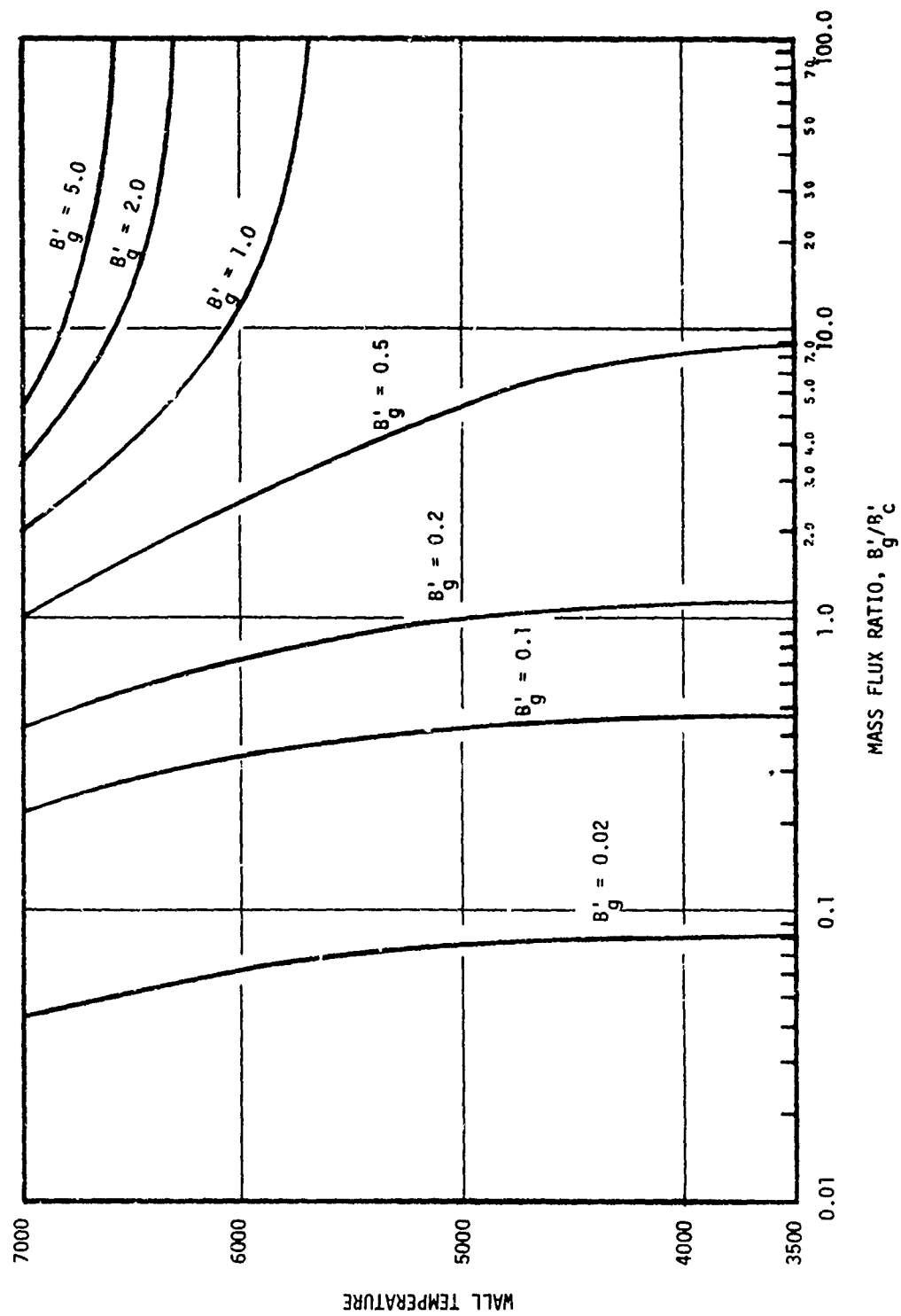


Figure A-1. Wall Temperature as a Function of Mass Flux Ratio for MSCE 280 Blast Tube Sensor

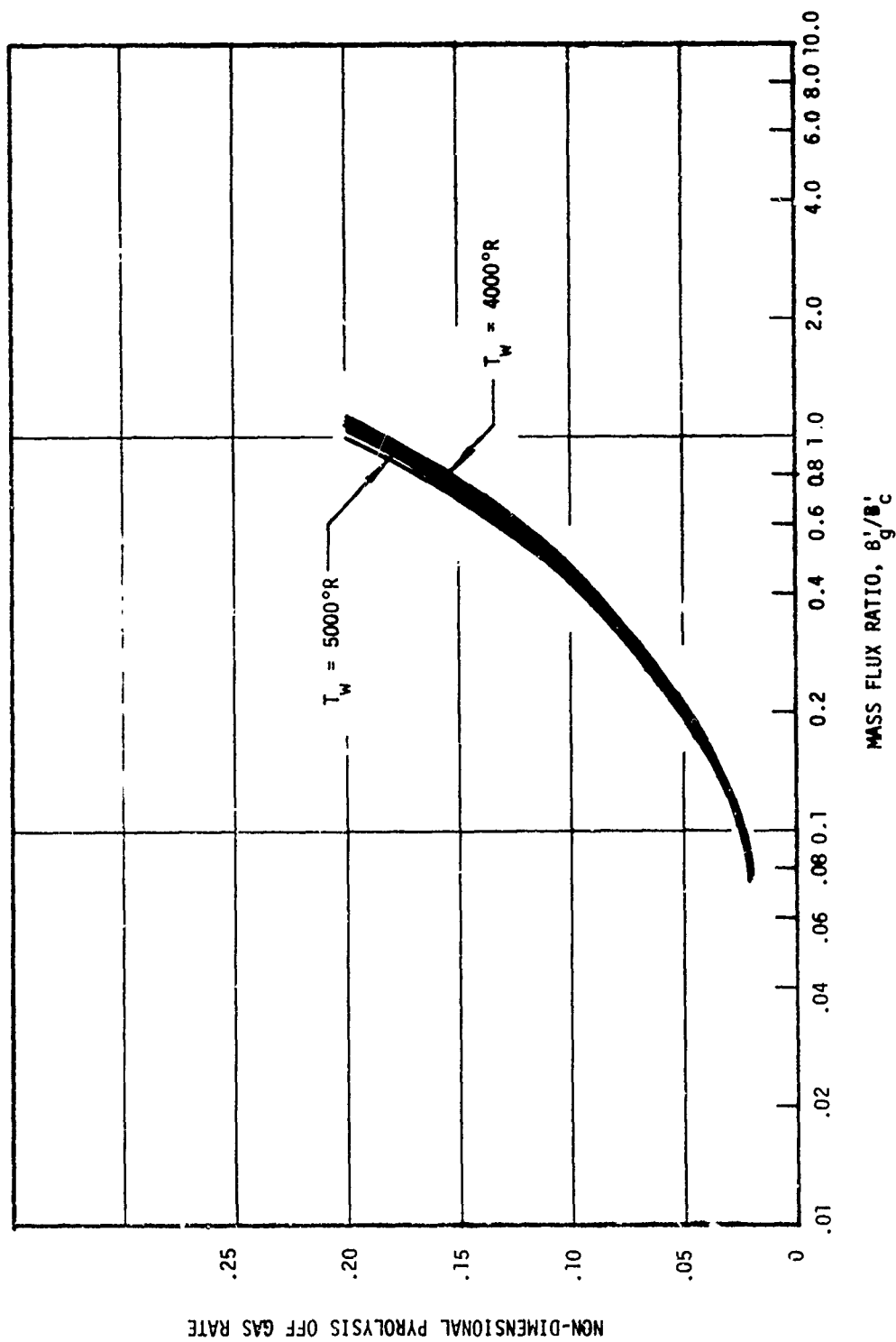


Figure A-2 . Non-Dimensional Pyrolysis Off Gas Rate as a Function of Mass Flux Ratio for MSCE 280 Blast Tube Sensor

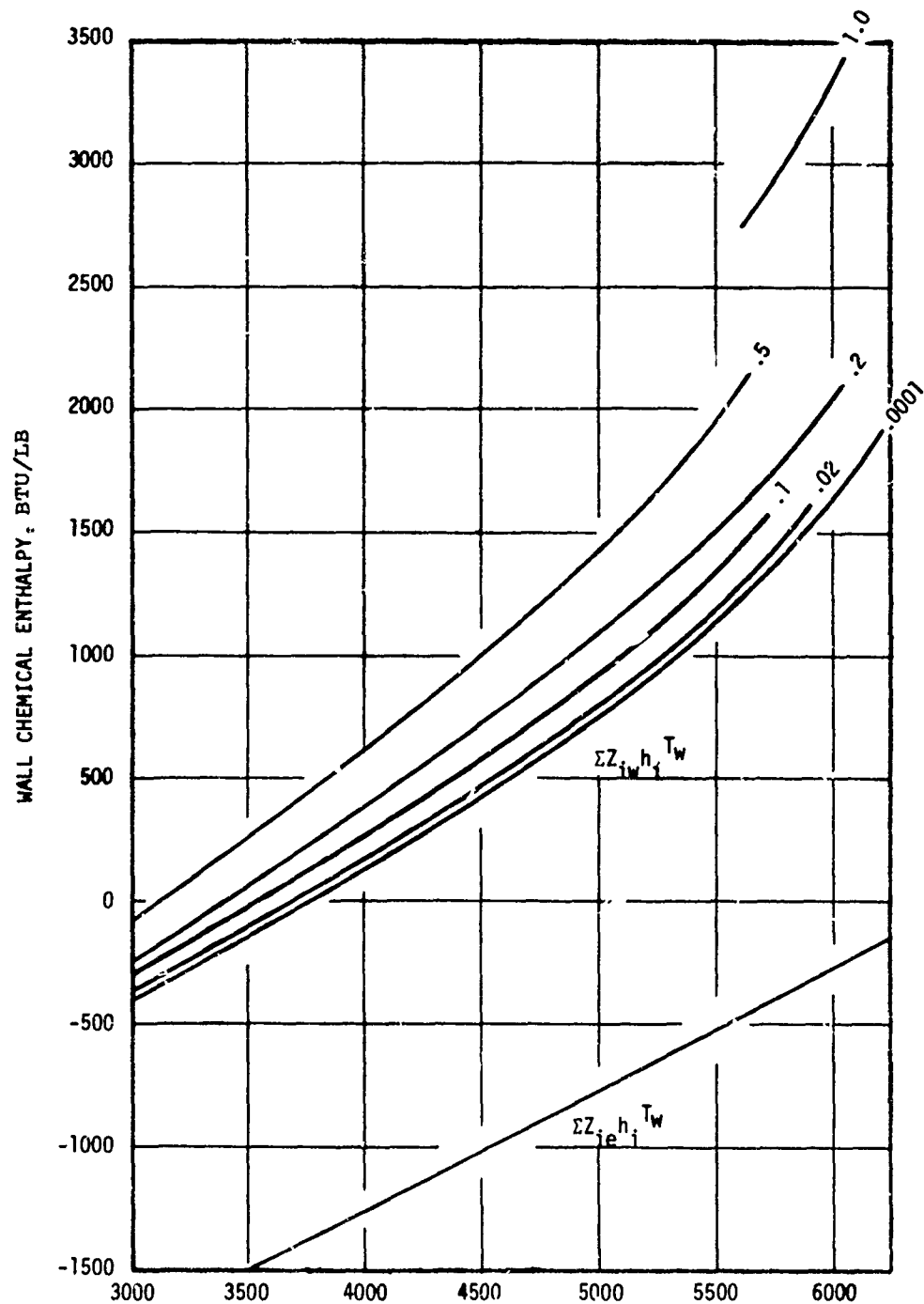


Figure A-3. Freestream and Wall Chemical Potential as a Function of Wall Temperature for MXCE 280 Blast Tube Sensor.

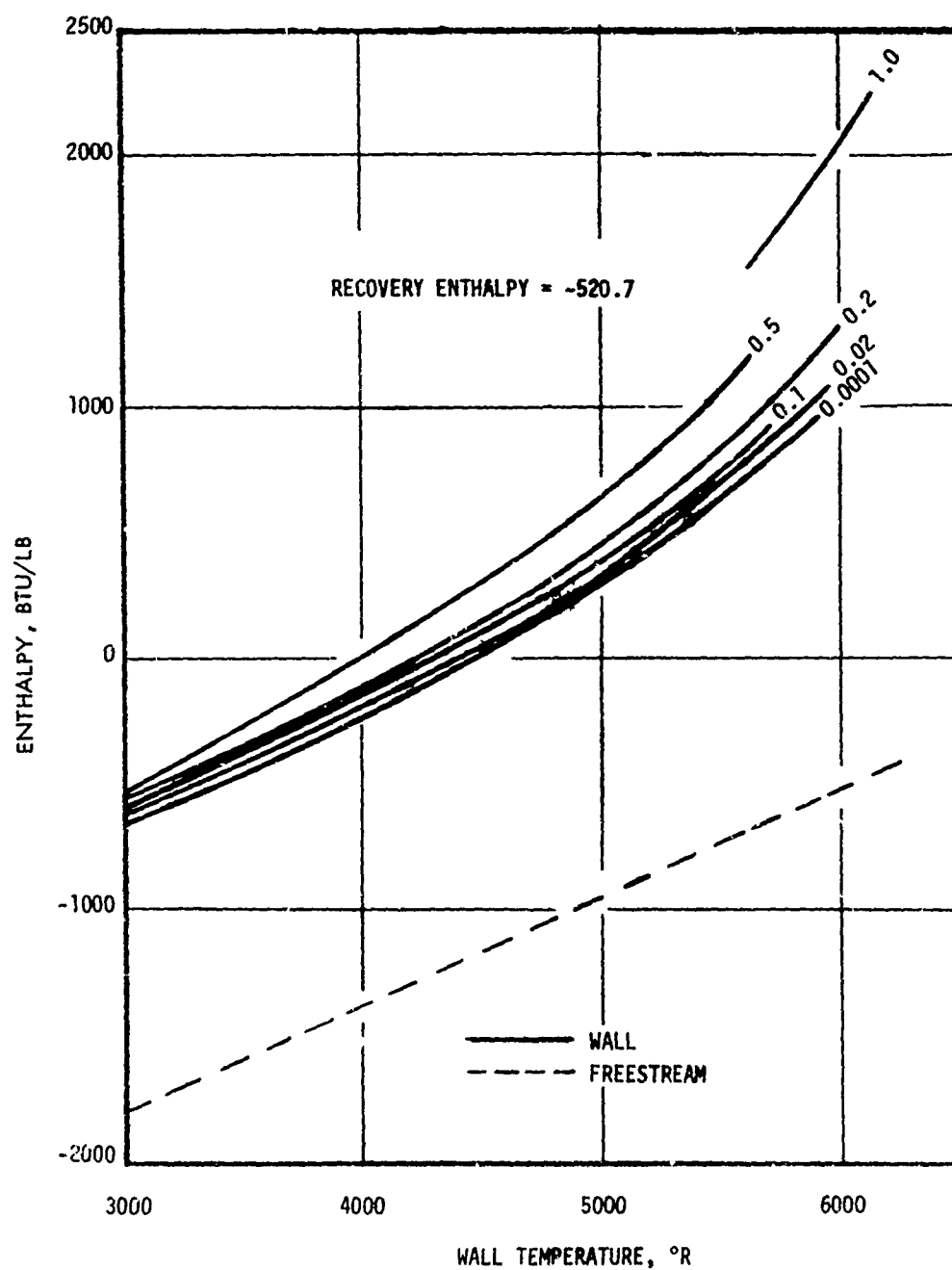


Figure A-4 . Recovery, Freestream, and Wall Enthalpies as a Function of Wall Temperature for MSCE 280 Blast Tube Sensor

## REFERENCES

1. Wool, M. R., Baker, D. L., and Murphy, A. J., "Material Performance of Carbon Phenolic Ablators and Pyrolytic Graphite Coatings in Nozzles Subjected to Multiple Pulse Duty Cycles", AFRDL-TR-71-130 (Aerotherm Final Report 71-43), October, 1971.
2. Wool, M. R., Schaefer, J. W., Murhpy, A. J., Clark, K. J., Reese, Jr, J. J. "Kinetic Responses of Pyrolytic Graphite to Combustion Product Environments." AFRPL-TR-72-22, (Aerotherm Final Report 72-48), April, 1972 (Confidential-Title Unclassified).
3. Baker, D. L., "Development of High Performance Materials for High Chamber Pressure Rocket Motor Application." AFRPL-TR-71-78 DART II Validation of Analytical Design Techniques for Solid Rocket Nozzles at High Pressures (Aerotherm Final Report 71-3), August, 1971. (Confidential-Title Unclassified).
4. Baker, D. L., "Development of High-Performance Materials for High - Part II Evaluation of Thermochemical Analysis Techniques Thermochemical Screening, and Thermal Instrumentation Methods for High Pressure Solid Rocket Motors." AFRPL-TR-69-222, (Aerotherm Interim Report 69-52), September, 1969. (Confidential - Title Unclassified).
5. Schaefer, J. W., and Dahm, T. J., "Studies of Nozzle Ablative Material Performance for Large Solid Boosters." NASA LR-7208 (Aerotherm Report No 66-2), December, 1966.
6. Schaefer, J. W., Dahm, T. J., Rodriguez, D. A., Reese, J. J., Jr., and Wool, M.R.: Studies of Ablative Material Performance for Solid Rocket Nozzle Applications. Aerotherm Final Report No. 68-30, NASA CR-72429, for NASA Lewis Research Center under Contract NAS7-534, March 1, 1968.
7. Baker, D. L., Schaefer, J. W., Wook, M. R.: Thermal Property and Ablative Response Characterization of Pyrolyzed Materials. Aerotherm Final Report No. 69-47, January, 1969.
8. Schaefer, J. W. and Dahm, T. J., "Computer Program Calculation of Ablative Material Performance for Solid Rocket Motor Applications," CPIA Publ. No. 111, Vol. 1, pp 371-395, June, 1966. (Paper presented at the ICRPG/AIAA Solid Propulsion Conference, Washington, D. C., July 19-21, 1966). Aerotherm Corporation, (Confidential - Title Unclassified).
9. User's Manual Aerotherm Equilibrium Surface Thermochemistry Computer Program, Version 3, Aerotherm Corporation, Mountain View, California, Report UM-70-13, April, 1970.
10. User's Manual, Aerotherm Charring Material Thermal Response and Ablation Program, Version 3, Aerotherm Corporation, Mountain View, California, Report No. UM-70-14, April, 1970.
11. User's Manual - Aerotherm Axi-Symmetric Transient Heating and Material Ablation Computer Program (ASTHMA 3). AFRPL-TR-72-24 (Aerotherm Report No. UM-72-26), January, 1972.



12. "User's Manual - Aerotherm Graphite Surface Kinetics Computer Program." AFRPL-TR-72-23 (Aerotherm Report No. UM-72-25), January, 1972.
13. Baker, D. L., "Material Property Characterization of Silica and Carbon Elastomer Modified Phenolic and Carbon/Silica Phenolic Ablative Materials." Aerotherm Final Report No. 70-24, December, 1970.
14. Schaefer, J. W., Dahm, T. J., Rodriguez, D. A., Reese, Jr., J. J., and Wool, M. R., "Studies of Ablative Material Performance for Solid Rocket Nozzle Applications." NASA CR-72429 (Aerotherm Report No. 68-30), 1 March 1968.
15. Bapat, S. G., and Olcott, E. L., "Study of Materials for High Pressure Nozzles. Vol III - Property Determination of Castable Carbon and Graphite Composite." AFRPL-TR-71-18, 4 January 1971.
16. Letter from F. R. Keith (North American Rockwell Corporation) to M. R. Wool (Aerotherm Corporation), Subject: R-155 Composition and Heat of Formation, 14 June 1971.
17. Batchelor, J.D., "Improvements of Pyrolytic Graphite Coated Nozzles for Solid Propellant Rocket Motors," AFRPL-TR-67-245, First Interim Technical Report, Contract F04611-67-C-0047, September 5, 1967.
18. "UCAR Premium Graphite Grade ATJ," Bulletin No. 463-205, Union Carbide Corporation.
19. Baker, D. L., Wool, M. R. and Schaefer, J. W., "Development of Total and Radiative Heat Flux Measurement Systems for Rocket Nozzle Applications," AFRPL-TR-70-82 (Aerotherm Final Report 70-11), August 1970.
20. Wool, M. R., Schaefer, J. W., and Baker, D. L., "Measurement of Convective and Radiative Heat Flux at the Surface of an Ablative Material, ISA Transactions, Vol. 9, No. 2, 1970.